SLAC-R-942

MEASUREMENTS OF DIRECT CP VIOLATION AND CONSTRAINT ON THE CKM TRIANGLE IN $B \to K^*\pi$ DECAYS

A DISSERTATION
SUBMITTED TO THE DEPARTMENT OF PHYSICS
AND THE COMMITTEE ON GRADUATE STUDIES
OF STANFORD UNIVERSITY
IN PARTIAL FULFILLMENT OF THE REQUIREMENTS
FOR THE DEGREE OF
DOCTOR OF PHILOSOPHY

Andrew Phillips Wagner
February 2010

SLAC-Report-942
Work supported by U. S. Department of Energy contract DE-AC02-76SF00515

SLAC National Accelerator Center, 2575 Sand Hill Road, Menlo Park, CA 94309

© Copyright by Andrew Phillips Wagner 2010
All Rights Reserved

I certify that I have read this dissertation and that, in my opinion, it is fully adequate in scope and quality as a dissertation for the degree of Doctor of Philosophy.

(Aaron Roodman) Principal Adviser

I certify that I have read this dissertation and that, in my opinion, it is fully adequate in scope and quality as a dissertation for the degree of Doctor of Philosophy.

(David MacFarlane)

I certify that I have read this dissertation and that, in my opinion, it is fully adequate in scope and quality as a dissertation for the degree of Doctor of Philosophy.

(Michael Peskin)

I certify that I have read this dissertation and that, in my opinion, it is fully adequate in scope and quality as a dissertation for the degree of Doctor of Philosophy.

(Patricia Burchat)

Approved for the University Committee on Graduate Studies.

Abstract

We constrain the apex of the Cabibbo-Kobayashi-Maskawa unitarity triangle with measurements of $B \to K^*\pi$ amplitudes from analyses of $B^0 \to K^+\pi^-\pi^0$ and $B^0 \to K_S\pi^+\pi^-$ decays. This constraint is consistent with the world average. The $B^0 \to K^+\pi^-\pi^0$ decay mode is reconstructed from a sample of 454 million $B^0\overline{B}^0$ events collected by the *BABAR* detector at SLAC. We measure direct CP violation in $B^0 \to K^{*+}\pi^-$ decays at the level of 3σ when measurements from both $B^0 \to K^+\pi^-\pi^0$ and $B^0 \to K_S\pi^+\pi^-$ decays are combined.

Acknowledgement

To my parents Emily and Bradford Wagner, without whose love and support my accomplishments would not be possible, and to my brother George who reminds me to have fun with life. Also to Sarah McMenamin, whose love and friendship have been of immeasurable importance. She has made me both a better scientist and human being. I would like to thank Robin and David Lankton, Scott Diehl and Duncan Hwang for their friendship over the many years we have known each other. Philip Hedges, Mehmet Tepedelenlioglu, Mikol Ryan, Mike Perka and all the other epeeists at Cardinal Fencing deserve thanks for driving me a different kind of crazy during my time as a graduate student. Special thanks are due to my coach Valeriy Naulo. My friends Matt and Tina Jobin, Dzintars Avots, and Jeffrey Chang have provided me countless hours of entertainment for which I am eternally grateful.

The careful criticism, steady guidance and hospitality of Aaron Roodman are the hallmark of both an excellent scientist and advisor. He deserves much thanks for guiding me through my graduate career and making this dissertation possible. I also thank Mathew Graham, and Jose Ocariz for their mentorship in addition to Michael Gronau and Dan Pirjol for their extensive help with the phenomenology motivating this dissertation. I thank Jim MacDonald for his work in setting up a working laboratory and for questions regarding the maintenance of my motorcycle. Mike Kelsey deserves thanks for useful discussions regarding Linux, C++ and the benefits of home ownership. My fellow *BABAR* graduate students: Josh Thompson, Mark Allen, Brian Lindquist, Wells Wulsin, Manuel Franco and Kyle Knoepfel have all been a pleasure to work with. Thanks also go to Vera Luth, Philip Bechtle, Markus Cristinzinziani, Karl Bouldin, Helmut Marsiske, Rainer Bartoldus, Ingrid Ofte, Hojeong Kim, Jochen

Dingfelder, Bernie Culver, Anna Pacheco, Barbara Valdez, Natasha Haulman and everyone else in Group C. Philip Hart, Leonid Sapozhnikov and Lance Simms deserve thanks for introducing me to experimental astrophysics. Finally I would like to thank my reading committee for their time and useful suggestions: David MacFarlane, Michael Peskin, Patricia Burchat, and Tom Devereaux.

Contents

Abstract **v**

Acknowledgement **vi**

1 Introduction **1**

1.1 Outline 3

2 Theory **5**

2.1 The Standard Model 5

2.1.1 Properties of the weak interaction 6

2.1.2 CP violation in weak interactions 8

2.1.3 The CKM triangle 9

2.2 Mesons and SU(n) symmetry 11

2.3 Measurement of CKM parameters 13

2.4 Sensitivity to γ in $B \to K\pi\pi$ decays 15

2.4.1 Corrections from EWP Operators 19

2.4.2 SU(3) expansion of the ratio $r_{\frac{3}{2}}$ 21

2.5 Dalitz Analysis of the Decay $B \to K^+\pi^-\pi^0$ 22

2.5.1 Decay Kinematics 23

2.5.2 Measurement of the isospin weak phase $\Phi_{\frac{3}{2}}$ 31

3 PEP-II and the *BABAR* Detector **34**

3.1 The PEP-II Accelerator 34

3.2 The *BABAR* Detector 36

3.2.1 Silicon Vertex Tracker 38
3.2.2 Drift Chamber 42
3.2.3 Detector of Internally Reflected Cherenkov Light 46
3.2.4 Electromagnetic Calorimeter 49
3.2.5 Trigger 51
3.2.6 The *BABAR* Data Set 52
3.2.7 Monte Carlo Simulation 53

4 Dalitz Analysis of the Decay $B^0 \to K^+\pi^-\pi^0$ 55

4.1 Event Selection 55
4.1.1 Skim Selection 56
4.1.2 Charged Particle Selection and ID 56
4.1.3 π^0 Selection 57
4.1.4 B^0 Canidate Reconstruction 57
4.1.5 Kinematic Variables 58
4.1.6 Multivariate Continuum Suppression 59
4.1.7 Best Candidate Selection 65
4.1.8 Selection Efficiency 66
4.2 Dalitz Coordinates 66
4.3 Mis-Reconstructed Signal Events 68
4.4 B-Related Backgrounds 69
4.5 The Maximum Likelihood Fit 73
4.6 PDF Parametrization 74
4.6.1 Dalitz Plot PDFs 75
4.6.2 Kinematic PDFs 78
4.6.3 Neural Network PDFs 80
4.7 Fit Validation 81
4.7.1 Validation in Samples of Pure Toy MC 82
4.7.2 Validation of the Fit Using Embedded MC 83
4.8 Fit Results 92
4.9 Estimation of Systematic Uncertainty 98

4.9.1 Dalitz Model 98
4.9.2 Line Shapes 99
4.9.3 B-backgrounds 100
4.9.4 Continuum Dalitz Model 101
4.9.5 SCF Fraction 101
4.9.6 PID 102
4.9.7 Fit Bias 102

5 Results **106**
5.1 Constraint on the Apex of the CKM triangle 109
5.2 Evidence of direct CP violation in $B^0 \to K^{*+}\pi^-$ decays 110
5.3 Conclusions 111

A Measurement of $r_{\frac{3}{2}}$ **114**
A.1 Strategy 114
A.2 Measurement 116
A.3 Systematics 117
A.4 Conclusions 118

B B background PDFs **121**

C Correlation Matrix **141**

D Corrections to EMC Resolution in Simulation **148**
D.1 Introduction 148
D.2 Data sample 150
D.3 Smearing method 151
D.4 Results 153
D.5 Validation of the Smearing using $B^0 \to K^{*0}\gamma \to K^+\pi^-\gamma$ 155
D.6 Conclusions 160

Bibliography **161**

List of Tables

2.1 Properties of the $\Upsilon(4S)$ and B mesons. The conjugate mesons B^- and $\overline{B}^0$ are given by the conjugated quark contents of these mesons. . . . 12

2.2 Properties of mesons important in this analysis. The total spin of the meson is given by J and the transformation of the state under $\mathcal{C}$ and $\mathcal{P}$ are given by C, P. Where a meson is not an eigenstate of $\mathcal{C}$ only P is given. Mesons detected directly in *BABAR* are listed as Stable in *BABAR* while others are reconstructed from their decay products. The K^0 is experimentally observed as a linear combination of short and long lived particles, K_S, K_L. The K_L is Stable in *BABAR* and the K_S decays to $\pi^+\pi^-, \pi^0\pi^0$. 14

2.3 Isospin decomposition of $B \to K^*\pi$ amplitudes. The decomposition for $B \to \rho K$ amplitudes follows from the substitutions, $K^* \to K$ and $\pi \to \rho$. 18

2.4 The angular distributions and Blatt-Weisskopf barrier factors for a resonance of spin-J decaying to two pseudoscalar mesons 25

2.5 The *nominal model* for the decay $B^0 \to K^+\pi^-\pi^0$ comprises a non-resonant (NR) amplitude and seven intermediate states. The three types of line shape are described in the text. The masses and widths are from [13], except for the LASS shape [27]. We use the same LASS parameters for both neutral and charged $K\pi$ systems. The *Non-interfering* resonances D^0, D^+ are included in the model and do not affect the relative phases and amplitudes of other states. 30

3.1 Cross-Sections, production and trigger rates for processes at the $\Upsilon(4S)$ resonance and luminosity of $3 \times 10^{33}\,\mathrm{cm}^{-2}s^{-1}$. 52
3.2 Recorded Luminosity at the $\Upsilon(4S)$ resonance and corresponding number of $B\overline{B}$ pairs determined to a precision of 1.1%. Run 7 is not used in this dissertation is not reported. 53

4.1 Fitted values of m_i, w_i which minimize correlations of $\Delta E/\sigma_{\Delta E}$ with the Dalitz plot. 60
4.2 Relative Cut efficiencies 66
4.3 Exclusive neutral B background modes. Modes from each category are taken as a single PDF, as a weighted sum of the individual contributions. Branching fractions ($\mathcal{B}$) are taken from the PDG [13] and, when available, from HFAG [34]. In the cases where only an upper limit exists, we take it as the central value with 100% error. 72
4.4 The fraction of total signal events (f_{sig}) and the DP-averaged SCF fraction ($\langle f_{\mathrm{SCF}} \rangle_{\mathrm{DP}}$) in each tagging category. The fraction of total signal events is determined from a fit to a subset of the *BABAR* data where both B mesons are fully reconstructed known as the BReco dataset. 77
4.5 PDF shape parameters determined from fits to data. 82
4.6 Summary of fit fractions for the resonant amplitudes from 262 toy datasets. μ_{Pull} and σ_{Pull} denote the mean and width of the pull distribution respectively, while the average error is denoted by $\langle \sigma \rangle$. 83
4.7 Summary of fit results for the resonant amplitudes from 100 fully embedded toy samples. μ_{Pull} and σ_{Pull} denote the mean and width of the pull distribution respectively, while the average error is denoted by $\langle \sigma \rangle$. The phases are given in radians. 85
4.8 Fitted event yields for the best solution. Errors are statistical only. The continuum background yields are separated by tagging category. 92

4.9 Results of the four solutions of the fit. The fractions are the CP-averaged isobar fractions (FF_k). The phases Φ for the B^0 decays and $\overline{\Phi}$ for the $\overline{B}^0$ decays are measured relative to $B^0(\overline{B}^0) \to \rho^{\mp}\pi^{\pm}$ in radians. The uncertainties are statistical only. The correlation matrix for Solution-I is given in Appendix C 95
4.10 The line shape parameters of the additional $K_2^{*0}(1430)$, $K_2^{*+}(1430)$, $K^{*0}(1680)$ and $K^{*+}(1680)$ resonances. 99
4.11 Results of the fit to data including the $K_2^{*0}(1430)\pi^0$, $K_2^{*+}(1430)\pi^-$, $K^{*0}(1680)\pi^0$ and $K^{*+}(1680)\pi^-$ amplitudes. The fractions are the CP-averaged isobar fractions (FF_k). The phases Φ for the B^0 decays and $\overline{\Phi}$ for the $\overline{B}^0$ decays are measured relative to $B^0(\overline{B}^0) \to \rho^{\mp}\pi^{\pm}$ in radians. The uncertainties are statistical only. 100
4.12 Summary of systematic uncertainties associated with the $B^0 \to \rho^- K^+$ amplitudes. Uncertainties in the phases are given in radians 103
4.13 Summary of systematic uncertainties associated with the $B^0 \to K^*\pi$ amplitudes. Uncertainties in the phases are given in radians 104
4.14 Summary of systematic uncertainties associated with the NR amplitude and non-interfering D contributions. Uncertainties in the phases are given in radians 105

5.1 The branching fractions are the CP-averaged branching fractions ($\mathcal{B}_k$) defined with the CP asymmetries, $A_{\rm CP}$ in Eq. (2.32). The phases Φ for the B^0 decays and $\overline{\Phi}$ for the $\overline{B}^0$ decays are measured relative to $B^0(\overline{B}^0) \to \rho(770)^{\mp}K^{\pm}$. The first error is statistical and the second is systematic. When the elastic range term is separated from the $K\pi$ S-wave we determine the total NR branching fraction $\mathcal{B}_{\rm NR} = 7.6 \pm 0.5$ (stat.) $\times 10^{-6}$ and the resonant $K_0^*(1430)\pi$ branching fractions $\mathcal{B}_{K_0^*(1430)^+\pi^-} = 27.8 \pm 2.5$ (stat.) $\times 10^{-6}$, $\mathcal{B}_{K_0^*(1430)^0\pi^0} = 7.0 \pm 0.5$ (stat.) $\times 10^{-6}$. 108

A.1 CP-averaged Branching fractions ($\mathcal{B}$) and CP asymmetries for $B \to \rho\pi$ and $B \to K^*K$ decays taken from [34]. Upper limits are quoted for those branching ratios consistent with 0. 115
A.2 Fitted magnitudes and phases from the $B^0 \to (\rho\pi)^0$ Dalitz analysis [39]. The phases Φ for the B^0 decays and $\overline{\Phi}$ for the $\overline{B}^0$ decays are measured relative to $B^0 \to \rho^+\pi^-$ in degrees. The error includes both the statistical and systematic errors from [39]. The amplitudes are comparable to the bilinear interference terms in [39] and are not scaled by the branching fractions listed in Table A.1. 116

C.1 Correlation coefficients between the floated event yields and the B-background and Signal yields. 142
C.2 Correlation coefficients between the floated event yields and the continuum background yields. 143
C.3 Correlation coefficients among the floated isobar parameters for B decays. 144
C.4 Correlation coefficients among the floated isobar parameters for B decays. 145
C.5 Correlation coefficients among the floated isobar parameters for $\overline{B}$ decays. 146
C.6 Correlation coefficients among the floated isobar parameters for $\overline{B}$ decays. 147

D.1 Selection cuts on the $\mu\mu\gamma$ sample applied before smearing 150
D.2 χ^2 values for the fits of the MC to the data 155

List of Figures

1.1 Summary of existing constraints on the CKM triangle as compiled in [7]. 2

1.2 Summary of existing measurements of the CKM angle γ as compiled in [7]. 3

2.1 The CKM triangle. The coordinates of the apex of the triangle are denoted by (ρ, η). 10

2.2 SU(3) spectrum of spin-0 mesons. A separate octet and singlet exist for spin-1 mesons with the substitutions $K \to K^*$, $\pi \to \rho$ and $\eta \to \omega$. Here S denotes the net strangeness of the meson as listed in Table 2.2. 13

2.3 Tree Feynman diagrams contributing to $B \to K^*\pi$ decays. Note that in each case the diagram is sensitive to $V_{ub}^* V_{us} = A\lambda^4(\rho + i\eta)$. 16

2.4 Penguin Feynman diagrams contributing to $B \to K^*\pi$ decays. Note that in each case the diagram is $\propto A\lambda^2\alpha_s$ where $\alpha_s(m_b) \approx 0.22$. The EWP diagrams are identical to the QCD diagrams with the gluon is replaced by a photon. The EWP diagrams are $\propto A\lambda^2\alpha_{\rm em}$ where $\alpha_{\rm em} = 1/137$. 17

2.5 Amplitude and Phase of the $K^{*0}(892)$ line shape as modeled by the RBW. 26

2.6 Amplitude and Phase of the $\rho(770)$ line shape as modeled by the GS. 27

2.7 Amplitude and Phase of the $K\pi$ S-waves as modeled by the LASS parametrization. The cutoff at $m_{K^+\pi^-} = 1.8$ GeV/c^2 is clearly visible. 29

2.8 Isospin triangles and phase differences among $B^0 \to K^*\pi$ amplitudes. 32

3.1 Longitudinal cross section of the *BABAR* detector. The z-axis coincides with the beam axis. The positive y-axis points upward while the positive x-axis points toward the center of the PEP-II rings. ϕ is the angle in the x-y plane and θ is the angle in the z-y plane. Dimensions are in mm. 38
3.2 Longitudinal cross section illustrating the z coverage of the SVT. . . 39
3.3 Transverse cross section illustrating the ϕ coverage of the SVT. 40
3.4 Hit resolution of the layers in the SVT. The z resolution is shown (right) along with the ϕ resolution (left) in μm. 41
3.5 Longitudinal cross section of the DCH. Dimensions are in mm. 43
3.6 Drift cells for the four innermost super-layers. Guard wires are held at an intermediate potential (340 V) to keep showers contained within the cells of a given layer. 44
3.7 Drift cell isochrones spaced by 100ns and shower trajectories (left). Position resolution in the DCH as function of drift distance (right). . 45
3.8 dE/dx as a function of track momentum in the DCH with Bethe-Bloch predictions overlaid (left). Difference between measured and expected dE/dx for Bhabha events (right). The Gaussian fit has a width of 7.5%. 45
3.9 p_t resolution from cosmic events (left). Reconstructed J/ψ mass from muons (right). 46
3.10 Schematic of the DIRC and radiator bar. 47
3.11 Cherenkov angle as a function of track momentum. Predictions for particles of different masses are overlaid. 48
3.12 Efficiency and mis-ID probability for charged kaons as a function of momentum determined from $D^0 \to K^-\pi^+$ decays. 49
3.13 Longitudinal cross section of the EMC (left). Schematic of a wrapped CsI(Tl) crystal and read out package (right). Dimensions are in mm. 50
3.14 Energy resolution in the EMC for photons and electrons from various processes as a function of photon energy (left). Angular resolution of the EMC for photons from π^0 decays (right). 51
3.15 Luminosity delivered and recorded as a function of time. 54

4.1 Distributions for $m_{\rm ES}$ (left) and $\Delta E'$ (right) for signal MC (black), charged B-background (blue) and off-peak data (red). The vertical green lines indicate the selection criteria. The distributions are normalized to have unit area. 59
4.2 $\frac{\Delta E}{\sigma_{\Delta E}}$ distributions for signal events in different m^2_{+-} bins 62
4.3 Neural Network Training Variables 63
4.4 Output distribution for the Neural Network 64
4.5 Number of candidates per event passing all selections except $m_{\rm ES}$ . . 65
4.6 The standard (left) and square (right) Dalitz plots of the selected data sample of 23683 events. The intermediate resonances are more spread out in the square Dalitz plot. The $\overline{D}^0 \to K^+\pi^-$ narrow band is preserved with the choice made for the m' variable. 67
4.7 Selection efficiency, ϵ for TM events (left) and SCF events (right). The maximum efficiency is 1. 68
4.8 The width (RMS) of $m'_{\rm reco} - m'_{\rm truth}$ for SCF events over the Dalitz plot (left). The width (RMS) of $\theta'_{\rm reco} - \theta'_{\rm truth}$ for SCF events over the Dalitz plot (right). The units of the color axis are in 10^{-3}. 78
4.9 The mean (left) and RMS (right) of $\Delta E'$ for TM signal events as a function of the Dalitz Plot. 79
4.10 The NN output for events at low (solid) and high (dashed) $\Delta_{\rm Dalitz}$. . . 80
4.11 $(K\pi)^{*+}_0\pi^-$ $\overline{a}$ (upper left), $\overline{\Phi}$ (lower left), a (upper right) $\overline{a}$ (lower right) Pull distributions of embedded toy fits with Gaussian curves overlaid. 84
4.12 $(K\pi)^{*0}_0\pi^0$ $\overline{a}$ (upper left), $\overline{\Phi}$ (lower left), a (upper right) $\overline{a}$ (lower right) Pull distributions of embedded toy fits with Gaussian curves overlaid. 86
4.13 $K^{*+}(892)\pi^-$ $\overline{a}$ (upper left), $\overline{\Phi}$ (lower left), a (upper right) $\overline{a}$ (lower right) Pull distributions of embedded toy fits with Gaussian curves overlaid. 87
4.14 $K^{*0}(892)\pi^0$ $\overline{a}$ (upper left), $\overline{\Phi}$ (lower left), a (upper right) $\overline{a}$ (lower right) Pull distributions of embedded toy fits with Gaussian curves overlaid. 88
4.15 NR $\overline{a}$ (upper left), $\overline{\Phi}$ (lower left), a (upper right) $\overline{a}$ (lower right) Pull distributions of embedded toy fits with Gaussian curves overlaid. . . . 89

4.16 $\rho^-(1700)K^+$ $\overline{a}$ (upper left), $\overline{\Phi}$ (lower left), a (upper right) $\overline{a}$ (lower right) Pull distributions of embedded toy fits with Gaussian curves overlaid. 90
4.17 $\rho^-(1450)K^+$ $\overline{a}$ (upper left), $\overline{\Phi}$ (lower left), a (upper right) $\overline{a}$ (lower right) Pull distributions of embedded toy fits with Gaussian curves overlaid. 91
4.18 Distributions of the log likelihood for all events (left) and for events excluding the D region $1.8 < m_{K^+\pi^-} < 1.9$ GeV (right). The data are shown as points with error bars. The solid histograms show the projection of the fit result where the signal model includes both TM and SCF contributions.. The dark and light gray shaded areas represent the B background and continuum, respectively. 93
4.19 NN distributions (top left) $m_{\rm ES}$ (top right) and $\Delta E'$ (bottom). The data are shown as points with error bars. The solid histograms show the projection of the fit result where the signal model includes both TM and SCF contributions. The dark and light gray shaded areas represent the B-background and continuum, respectively. 94
4.20 Dalitz projections for: m'(left), θ'(right). The data are shown as points with error bars. The solid histograms show the projection of the fit result where the signal model includes both TM and SCF contributions. The dark and light gray shaded areas represent the B-background and continuum, respectively. 96
4.21 $m_{K^+\pi^-}$ mass distributions for all events (left) and for events in $m_{K^+\pi^-} < 1.8\,\mathrm{GeV}/c^2$ (right). The data are shown as points with error bars. The solid histograms show the projection of the fit result where the signal model includes both TM and SCF contributions. The dark and light gray shaded areas represent the B-background and continuum, respectively. 96

4.22 $m_{\pi^-\pi^0}$ mass distributions for all events (left) and $m_{\pi^-\pi^0} < 2\,\mathrm{GeV}/c^2$ (right). The data are shown as points with error bars. The solid histograms show the projection of the fit result where the signal model includes both TM and SCF contributions. The dark and light gray shaded areas represent the B background and continuum, respectively. 97

4.23 $m_{K^+\pi^0}$ mass distributions for all events (left) and $m_{K^+\pi^0} < 1.8\,\mathrm{GeV}/c^2$ (right). The data are shown as points with error bars. The solid histograms show the projection of the fit result where the signal model includes both TM and SCF contributions. The dark and light gray shaded areas represent the B background and continuum, respectively. 97

5.1 Likelihood Scans for $\Delta\phi_{\frac{3}{2}}$ (left) and $\Phi_{\frac{3}{2}}$ (right). The statistical uncertainty is shown in dashed lines and the total uncertainty is shown in solid. We measure $\Delta\phi_{\frac{3}{2}} = -7^{+15}_{-18}$ (stat.) $\pm$ 15 (syst.)$^\circ$ and exclude the range $-81^\circ < \Phi_{\frac{3}{2}} < -35^\circ$ at the level of 2σ. 110

5.2 Likelihood Scans for $\Delta\Phi_{\rho^-K^+}$ (left) and $\Delta\overline{\Phi}_{\rho^+K^-}$ (right). The statistical uncertainty is shown in dashed lines and the total uncertainty is shown in solid. We measure $\Delta\Phi_{\rho^-K^+} = -33 \pm 22$ (stat.) $\pm$ 20 (syst.)$^\circ$ and $\Delta\overline{\Phi}_{\rho^+K^-} = -39 \pm 25$ (stat.) $\pm$ 20 (syst.)$^\circ$. 111

5.3 The constraint of the apex of the CKM triangle given in Eq. 2.27 for the measured values of $\Phi_{\frac{3}{2}}$ and $r_{\frac{3}{2}}$ in $\sqrt{2\log(L)} = 1, 2$ contours (darkest to lightest). The $\star$ indicates the world average value of the apex of the CKM triangle [7]. 112

5.4 Likelihood Scans for $A_{\mathrm{CP}}(K^{*+}(892)\pi^-)$ using only the $B^0 \to K^+\pi^-\pi^0$ analysis (left) and the combined measurement with the $B^0 \to K_S\pi^+\pi^-$ analysis (right). The statistical uncertainty is shown in dashed lines and the total uncertainty is shown in solid. We measure $A_{\mathrm{CP}}(K^{*+}\pi^-) = -0.24 \pm 0.07$ (stat.) $\pm$ 0.02 (syst.) combining measurements from both $B^0 \to K^+\pi^-\pi^0$ and $B^0 \to K_S\pi^+\pi^-$ analyses (left). 113

A.1 $\sqrt{2\log(L)} = 1, 2, 3, 4, 5$ contours (darkest to lightest) of $|A_\rho|^2$ vs. $|\overline{A}_\rho|^2$. The units are 10^{-6} and are directly comparable to branching fractions. 117

A.2 $\sqrt{2\log(L)} = 1, 2, 3, 4, 5$ contours (darkest to lightest) of $r_{\frac{3}{2}}$. The contour on the right includes statistical errors in addition to a modest estimate of SU(3) breaking ($m_s/m_b \approx 2.5\%$) while the contour on the right illustrates the more conservative $m_s/\Lambda_{\rm QCD} \approx 30\%$ systematic uncertainty [16]. Note the contours are symmetric about the real axis 118
A.3 Likelihood scan of the real part of Eq. (A.3) generated from 4×10^6 randomly sampled $K^{*+}\overline{K}^0$ and $K^+\overline{K}^{*0}$ phases. We take the deviation at 1σ, 0.77 as a systematic error for the real and imaginary parts of $r_{\frac{3}{2}}$. 119

B.1 PDFs for B background Class 1. 122
B.2 PDFs for B background Class 2. 123
B.3 PDFs for B background Class 3. 124
B.4 PDFs for B background Class 4. 125
B.5 PDFs for B background Class 5. 126
B.6 PDFs for B background Class 6. 127
B.7 PDFs for B background Class 7. 128
B.8 PDFs for B background Class 8. 129
B.9 PDFs for B background Class 9. 130
B.10 PDFs for B background Class 10. 131
B.11 PDFs for B background Class 11. 132
B.12 PDFs for B background Class 12. 133
B.13 PDFs for B background Class 13. 134
B.14 PDFs for B background Class 14. 135
B.15 PDFs for B background Class 15. 136
B.16 PDFs for B background Class 16. 137
B.17 PDFs for B background Class 17. 138
B.18 PDFs for B background Class 18. 139
B.19 PDFs for B background Class 19. 140

D.1 E/E_{fit} distribution for data and MC without smearing 151
D.2 Examples of smearing functions 154
D.3 E/E_{fit} resolution plots for the encap 156

D.4 E/E_{fit} resolution plots for the forward barrel 157
D.5 E/E_{fit} resolution plots for the backward barrel 158
D.6 Distributions of ΔE from $K^{*0}\gamma$ for no smearing 159
D.7 Distributions of ΔE from $K^{*0}\gamma$ including smearing 160

Chapter 1

Introduction

In the Standard Model, CP violation in weak interactions is parametrized by an irreducible complex phase in the Cabibbo-Kobayashi-Maskawa (CKM) quark-mixing-matrix [1]. The unitarity of the CKM matrix is typically expressed as a triangle relationship among its parameters where decay amplitudes involving the heaviest generation of quarks are sensitive to the angles of the triangle denoted α, β, γ. Redundant measurements of the parameters of the CKM matrix are an important test of the Standard Model since violation of the unitarity condition would be an indication of new physics processes.

A copious source of heavy quark decays have been supplied by the B factory experiments *BABAR* and BELLE located at SLAC and KEK respectively. In addition to a myriad of other physics topics, these experiments have been enormously successful in measuring the angles β and α. The angle β is measured in decays such as $B^0 \to J/\psi\, K_S$, exploiting the interference of $B^0\overline{B}^0$ mixing, while α may be measured combining information from $B \to \pi\pi$ and $B^0 \to \pi^+\pi^-\pi^0$ decays [2]. A summary of existing constraints on the CKM triangle is shown in Fig. 1.1.

As shown in Fig. 1.1 the measurement of the angle γ remains the most challenging. This angle is measured in the interference of CKM-favored $b \to c$ and CKM-suppressed $b \to u$ transitions contributing to $B^+ \to \overline{D}^0 K^+$ and $B^+ \to D^0 K^+$ decays when the D decays to a CP eigenstate. The method proposed by Gronau, London and Wyler (GLW) [3, 4] consists of reconstructing the D as a CP eigenstate such as

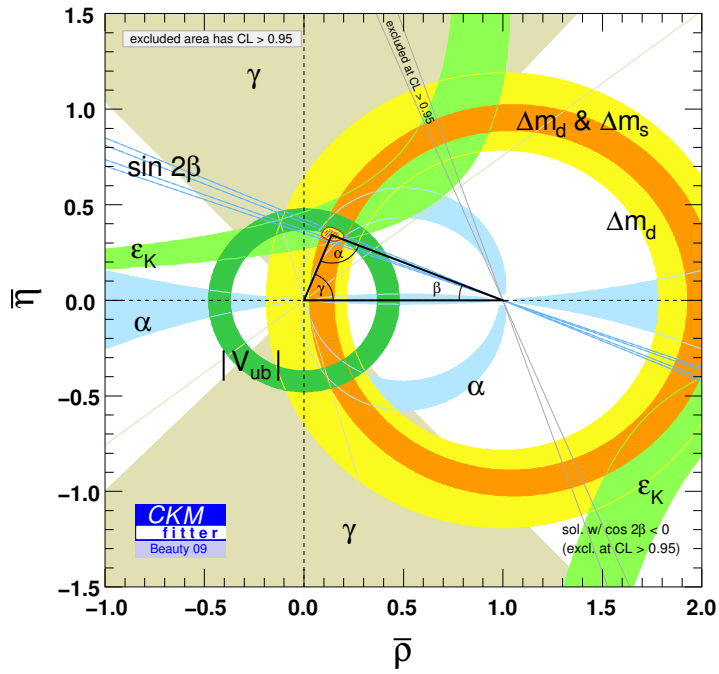

Figure 1.1: Summary of existing constraints on the CKM triangle as compiled in [7].

$\pi^+\pi^-$, so that measurements of the corresponding CP asymmetries and branching fractions can be used to extract γ. The extraction of γ in this case is not independent of the strong phase difference between the $b \to c$ and $b \to u$ transitions or the relative size of the CKM and color-suppressed $b \to u$ transition. Unfortunately, the ratio of amplitudes $|A(B^0 \to D^0K^+)/A(B^0 \to \overline{D}^0K^+)| \approx 0.22$ so that the sensitivity to γ in the GLW method is limited in practice.

It is also possible to gain sensitivity to γ by reconstructing the D as a non CP eigenstate such as $K^+\pi^-$ where the decay $\overline{D}^0 \to K^+\pi^-$ is doubly CKM suppressed (Atwood, Dunietz and Soni (ADS) [5]). This has the advantage of compensating for the small ratio of $B \to DK$ decay amplitudes at the expense of an overall small branching ratio. The most sensitive means of measuring γ to date, however, is to reconstruct the D in the Cabibbo-allowed decays $D^0 \to K_S\pi^-\pi^+$ and $D^0 \to K_SK^+K^-$. Sensitivity to both the ratio of B decay amplitudes and strong phase difference is enhanced by the presence of intermediate resonances interfering in the Dalitz plot (Giri,

Grossman, Soffer, and Zupan (GGSZ) [6]). This technique has been used to measure $\gamma = 76° \pm 22° \pm 5°$ up to a two-fold ambiguity [7]. A summary of existing measurements of γ are show in Fig. 1.2.

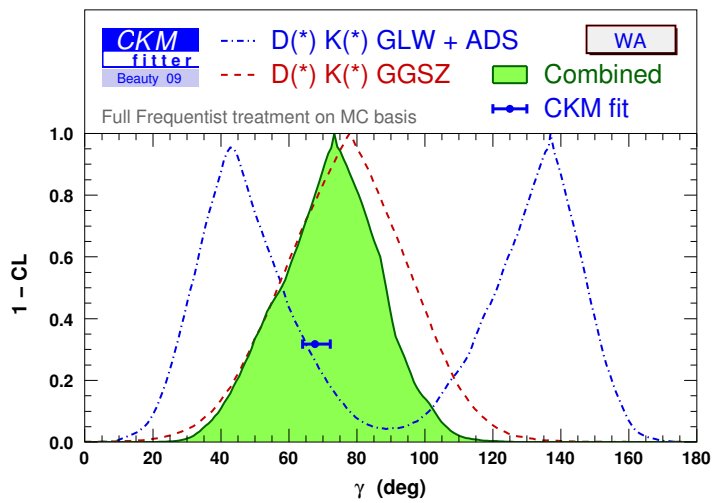

Figure 1.2: Summary of existing measurements of the CKM angle γ as compiled in [7].

This dissertation will discuss how sensitivity to the CKM angle γ can be found using an isospin analysis of loop dominated penguin decays, $B^0 \to K^*\pi$. This novel technique will be shown to be competitive with the GGSZ method given the available *BABAR* dataset, with the additional benefit of sensitivity to new physics processes contributing to $B^0 \to K^*\pi$ amplitudes in penguin processes.

1.1 Outline

In Chapter 2, a theoretical introduction to CP violation is presented in addition to the phenomenology relevant to extracting γ from $B^0 \to K^*\pi$ decays. A description of the *BABAR* detector is included in Chapter 3. The Dalitz analysis of the $B^0 \to K^+\pi^-\pi^0$ decay is presented in Chapter 4. This analysis measures the relative phases and magnitudes of $B^0 \to K^*\pi$ amplitudes contributing to the $B^0 \to K^+\pi^-\pi^0$ final state. In Chapter 5, we combine phases and amplitudes measured in the $B^0 \to$

$K^+\pi^-\pi^0$ and $B^0 \to K_S\pi^+\pi^-$ decays to constraint the CKM triangle. Measurements of direct CP violation in $B^0 \to K^{*+}\pi^-$ decays from both the $B^0 \to K^+\pi^-\pi^0$ and $B^0 \to K_S\pi^+\pi^-$ final states are combined to show evidence of direct CP violation in that decay process.

Chapter 2

Theory

In this chapter we summarize the theoretical description of the Standard Model of particle physics with special attention paid to the subject of CP violation. Flavor symmetry in strong interactions is reviewed in Section 2.2 before the phenomenological description of a means of constraining CKM elements in Section 2.4.

2.1 The Standard Model

The Standard Model (SM) is the theory describing the interactions of fundamental fermions (spin-$\frac{1}{2}$ particles) and forces via an SU(3)$\otimes$SU(2)$\otimes$U(1) gauge symmetry. Each component of the gauge symmetry generates an interaction with a category of fermion. The fermions that couple exclusively to the SU(2)$\otimes$U(1) component are known as leptons, while those that additionally couple to the SU(3) component or strong force, are known as quarks. The fermions in the SM occur in 3 generations each more massive than the last. The members of the lightest generation of quarks are bound by the strong force into protons and neutrons and the lightest leptons are the familiar electron (β particle) and electron-neutrino (ν_e). The forces of the SM are themselves quantized so that the strong force is mediated by particles known as gluons and the electro weak force (SU(2)$\otimes$U(1)) is mediated by the $W^{\pm}$, Z^0 and photon (γ particle). The forces are vector (spin-1) particles.

In addition to the fundamental forces and fermions, it has been proposed that

the particles of the SM acquire mass when a scalar (spin-0) particle coupling to the SU(2)⊗U(1) gauge symmetry has a non-zero vacuum expectation value. This spontaneously breaks the SU(2)⊗U(1) symmetry resulting in massive $W^{\pm}$ and Z^0 bosons and a massless photon. The additional scalar particle is known as the Higgs boson whose direct detection is perhaps the most anticipated measurement in physics. This dissertation will concern itself with the interesting consequences of the weak interaction, which we now describe.

2.1.1 Properties of the weak interaction

The Glashow-Weinberg-Salam model of electroweak interactions describes the interaction of fermion fields via an SU(2)⊗U(1) gauge group in the SM. The covariant derivative for a theory determined by this gauge symmetry is given by

$$D_\mu = \partial_\mu - i\frac{g}{\sqrt{2}}\big(W_\mu^+ T^+ + W_\mu^- T^-\big) - i\frac{g}{\cos\theta_w} Z_\mu\big(T^3 - \sin^2\theta_w Q\big) - ieA_\mu Q, \qquad (2.1)$$

where g is the weak coupling constant and the $W_\mu^{\pm}, Z_\mu$ acquire masses from the Higgs mechanism. The A_μ is the massless photon responsible for the electromagnetic interaction. The electric charge quantum number of a fermion field is given by Q and the weak mixing angle relating the W and Z masses is defined by $m_W = m_Z \cos\theta_w$. T^+, T^- are the raising and lowering operators acting on SU(2) doublets of flavor while the diagonalized generator of SU(2), T^3, returns the value of the SU(2) flavor charge of a fermion field. Note that since the W vector boson couples to SU(2) flavor doublets via the raising and lowering operators this interaction couples up-flavor fermions to down-flavor fermions. This gives rise to charged flavor-changing currents in the SM.

It is interesting to consider how this theory transforms under the discrete symmetries of parity $\mathcal{P}$ and charge conjugation $\mathcal{C}$. The operation of parity (mirror inversion) reflects the spatial coordinates through the origin, $\mathcal{P}\ (t, x, y, z) = (t, -x, -y, -z)$. This inverts the orientation of a particle's spin relative to its momentum, or the handedness. A theory that is invariant under parity makes no distinction between

particles of left and right handedness. The operation of charge conjugation transforms matter fields into antimatter fields in the Lagrangian of the theory. A theory that is invariant under charge conjugation makes no distinction between matter and antimatter. The relative abundance of matter over antimatter in the universe would seem to indicate that a complete theory of particle interactions should violate $\mathcal{C}$; else equal amounts of matter and antimatter would have been created and annihilated in pairs, via the electromagnetic interaction. Additionally, total interaction rates of particles are calculated as sums over the spin states of the final state particles. This implies that the combination of the transformations $\mathcal{CP}$ must also be violated in order to avoid balancing the violation of $\mathcal{C}$ and hence to explain the relative abundance of matter in the universe. The condition that $\mathcal{C}$ and $\mathcal{CP}$ (written CP) be violated separately in order to explain a relative abundance of matter in the universe was first shown by Sakharhov [8].

The concept that weak interactions (those described by the $W^{\pm}$) violate $\mathcal{P}$ was first suggested by Lee and Yang [9] and observed soon after by Wu [10] in the β decay of Co^{60}. Indeed the theory described by Eq. (2.1) would violate both $\mathcal{P}$ and $\mathcal{C}$ if it is required that weak interactions couple only to left-handed matter and right-handed antimatter. This is accomplished by the projection operator $1-\gamma^5$ picking out the left (right) handed components of the matter (antimatter) spinors. This is referred to as the vector axial-vector (V-A) character of the weak interaction. The Lagrangian for such a theory of weak interactions is

$$\mathcal{L}_W = \frac{g}{\sqrt{2}}\big(\overline{\psi}_u\gamma^\mu W^+_\mu(1-\gamma^5)\psi_d + \overline{\psi}_d\gamma^\mu W^-_\mu(1-\gamma^5)\psi_u\big), \tag{2.2}$$

where u and d denote the SU(2) flavor of the fermion fields, $\psi, \overline{\psi}$. Qualitatively it is not difficult to see how Eq. (2.2) violates both $\mathcal{C}$ and $\mathcal{P}$ maximally. $\mathcal{P}$ transforms left-handed matter into right-handed matter while $\mathcal{C}$ transforms left-handed matter into left-handed antimatter; in each case a particle that couples to the weak interaction via Eq. (2.2) is transformed into a particle that does not. This argument also shows that the Lagrangian written in terms of the flavor-eigenstates ψ_u, ψ_d is invariant under the composition $\mathcal{CP}$ since this transforms left-handed matter into right-handed

antimatter. We now proceed to discuss the mechanism for CP violation in weak interactions.

2.1.2 CP violation in weak interactions

Thus far only the vector bosons have explicitly acquired mass from the Higgs mechanism in the theory. The Higgs also couples to the fermions in the theory giving fermion mass terms in the Lagrangian

$$\mathcal{L}_{\mathrm{M}} = -\frac{v}{\sqrt{2}}\big(G_{ij}\overline{\psi}_u^i\psi_u^j + F_{ij}\overline{\psi}_d^i\psi_d^j\big), \tag{2.3}$$

where the vacuum expectation value of the Higgs is $\langle\phi\rangle = v$ and the matrices G_{ij}, F_{ij} are complex coupling constants between fermion fields of generations i, j. We produce a change of basis via the unitary matrices V_d, V_u such that

$$V_d^\dagger\frac{Fv}{\sqrt{2}}V_d = M_d,\ V_u^\dagger\frac{Gv}{\sqrt{2}}V_u = M_u, \tag{2.4}$$

where the mass matrices $M_{u,d}$ are diagonal and real. We now make the change of variables $\overline{\psi}_u \to V_u^\dagger\overline{u},\ \psi_u \to V_u u$ (similarly for the d-type fermions). Making this replacement explicit in Eq. (2.2) gives

$$\mathcal{L}_W = \sum_{i,j}^{n_g}\frac{g}{\sqrt{2}}\big(V_{ij}\overline{u}_i\gamma^\mu W_\mu^+(1-\gamma^5)d_j + V_{ij}^*\overline{d}_j\gamma^\mu W_\mu^-(1-\gamma^5)u_i\big), \tag{2.5}$$

where $V = V_u^\dagger V_d$ and the sum runs over the number of fermion generations n_g in the theory. For each i, j, CP transforms the first term in Eq. (2.5) into the second except that the constants V_{ij}, V_{ij}^* are not transformed. Thus CP is violated for interactions where $V_{ij} \neq V_{ij}^*$ or equivalently where the coupling is not real. Although we have explicitly used the Higgs mechanism to generate masses in the SM, the possibility that this is not the true mechanism nature provides to generate mass in no way violates the spirit of the derivation of the mixing matrix V. So long as the mass and flavor eigenstates of the fermion fields are different a nontrivial mixing matrix may be constructed.

In general an $n_g \times n_g$ unitary complex matrix is given by n_g^2 parameters. It is possible however to transform the phases of the fermion fields $(u,d)_i \rightarrow e^{i\phi_i}(u,d)_i$ (U(1) symmetry) to eliminate $2n_g - 1$ parameters (an overall phase is a necessary convention) in the matrix V. Of the remaining $(n_g-1)^2$ parameters, $\frac{n_g}{2}(n_g-1)$ of them are given by real-valued Euler angles. Thus for a theory of n_g generations of fermions there are $\frac{1}{2}(n_g-1)(n_g-2)$ complex phases in V. Indeed if there were only two generations the matrix would be purely real and CP would not be violated. This fact was first pointed out by Kobayashi and Maskawa [1] before there was experimental evidence for a third generation of matter. Subsequently V is referred to as the Cabibbo-Kobayashi-Maskawa (CKM) mixing matrix (Cabibbo having previously described the mixing in two generations [11]).

2.1.3 The CKM triangle

Written explicitly in terms of the massive quarks the CKM matrix is given by

$$V = \begin{pmatrix} V_{ud} & V_{us} & V_{ub} \\ V_{cd} & V_{cs} & V_{cb} \\ V_{td} & V_{ts} & V_{tb} \end{pmatrix}. \tag{2.6}$$

It is convenient to use the unitarity of the CKM matrix ($V^\dagger V = 1$) to write a relationship between its parameters:

$$V_{ud}V_{ub}^* + V_{cd}V_{cb}^* + V_{td}V_{tb}^* = 0. \tag{2.7}$$

This relationship corresponds to a triangle in the complex plane as shown in Fig. 2.1. The angles of the triangle constructed from the relationship in Eq. (2.7) are given by

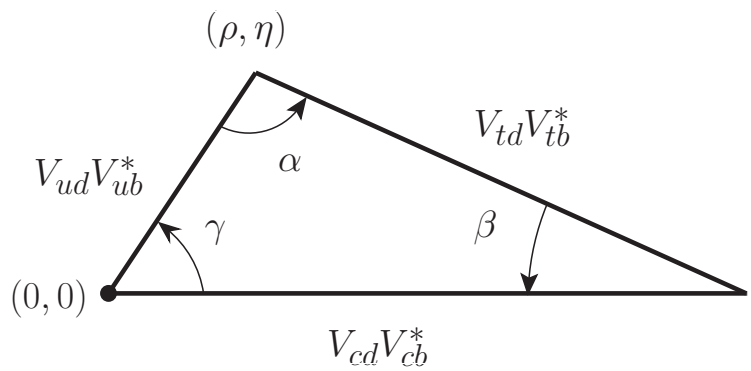

Figure 2.1: The CKM triangle. The coordinates of the apex of the triangle are denoted by (ρ, η).

$$\begin{aligned}
\alpha &= \mathrm{Arg}\left(-\frac{\mathrm{V_{td}V_{tb}^*}}{\mathrm{V_{ud}V_{ub}^*}} \right), \\
\beta &= \mathrm{Arg}\left(-\frac{\mathrm{V_{cd}V_{cb}^*}}{\mathrm{V_{td}V_{tb}^*}} \right), \\
\gamma &= \mathrm{Arg}\left(-\frac{\mathrm{V_{ud}V_{ub}^*}}{\mathrm{V_{cd}V_{cb}^*}} \right),
\end{aligned} \tag{2.8}$$

and satisfy the obvious relationship $\alpha + \beta + \gamma = 180°$. These angles may be measured independently in different particle decays permitting a direct test of the mechanism of CP violation in the SM. If the angles are not found to sum to 180° there must be additional particles and couplings, not in the SM, contributing to the observed decays. Thus the unitarity of the CKM triangle is an extremely powerful prediction, making the study of CP violation a very interesting means of discovering new physics. The measurement of the CKM angle γ will be the subject of this dissertation.

Other than unitarity, the SM places no constraints on the parameters of the CKM matrix though it has been determined experimentally that these parameters are conveniently expressed as an expansion in the value of $|V_{us}| = \lambda = 0.2205 \pm 0.0018$:

$$V \approx \begin{pmatrix} 1-\frac{\lambda^2}{2} & \lambda & A\lambda^3(\rho - i\eta) \\ -\lambda & 1-\frac{\lambda^2}{2} & A\lambda^2 \\ A\lambda^3(1-\rho-i\eta) & -A\lambda^2 & 1 \end{pmatrix}, \tag{2.9}$$

where $A = 0.824 \pm 0.075$ is also relatively well determined from experiment. This scheme is known as the Wolfenstein [12] parametrization of the CKM matrix. The parameters ρ, η [1] are the coordinates of the apex of the CKM triangle in the complex plane and are much less well measured. Constraining these parameters (equivalently, measuring α, β, γ) as redundantly as possible is the primary goal of the B-factory experiments.

Finally, it is interesting to consider the area of the CKM triangle:

$$\frac{1}{2}|V_{cd}V_{cb}^*||V_{ud}V_{ub}^*| \sin\gamma. \tag{2.10}$$

If the CKM matrix was purely real, the area would be 0. Unitarity and the phase invariance of the quark fields constrains the area to a maximum value of $1/(12\sqrt{3}) \approx 0.048$. This provides a constraint on the maximum amount of CP violation in weak interactions. The current experimental value of the area is $\approx 10^{-4}$. Why nature violates CP 3 orders of magnitude less than is absolutely allowable in the weak interaction remains an open question.

2.2 Mesons and SU(n) symmetry

As noted earlier, the quarks of the SM are strongly interacting. They form bound states of pairs (mesons) or triplets (baryons) of quarks that are observed in nature. The decays of mesons mediated by the weak interactions of the bound quarks provide sensitivity to the elements of the CKM matrix and hence CP violation. Of particular interest are the decays of mesons containing b quarks since these are sensitive to V_{qb} in tree decays (See Fig. 2.3) and V_{tq} in loop (penguin) diagrams (See Fig. 2.4). The

[1] It is common to illustrate the constraints on the CKM triangle on the rescaled axes $\overline{\rho} = \rho(1-\frac{\lambda^2}{2})$ and $\overline{\eta} = \eta(1-\frac{\lambda^2}{2})$ as done in Fig. 1.1

B mesons are listed in Table 2.1.

Table 2.1: Properties of the $\Upsilon(4S)$ and B mesons. The conjugate mesons B^- and $\overline{B}^0$ are given by the conjugated quark contents of these mesons.

meson	Quark content	Mass (GeV/c^2)	Lifetime (10^{-12} s)
$\Upsilon(4S)$	$\overline{b}b$	10.58 ± 0.0035	10^{-8}
B^+	$\overline{b}u$	5.2789 ± 0.0018	1.62 ± 0.06
B^0	$\overline{b}d$	5.2798 ± 0.0016	1.56 ± 0.06
B_s^0	$\overline{b}s$	5.3696 ± 0.0024	1.61 ± 0.10

The $\Upsilon(4S)$ resonance is especially important experimentally. This resonance decays almost completely to $B^0\overline{B}^0$ and B^+B^- pairs (50% each) and may be copiously produced in e^+e^- collisions such as those at SLAC and KEK. The large sample of B decays recorded in this way is necessary to measure the small effects of CP violation with precision.

To the extent that the quark masses are much less than the strong interaction energy scale the continuous symmetry acting on the n lightest quarks, SU(n), is respected. This is known as isospin or SU(2) symmetry for the u and d quarks and SU(3) when the more massive s quark is included. The u, d, s quarks belong to the $\mathbf{3}$ representation of SU(3) while the anti-quarks belong to the $\overline{\mathbf{3}}$ representation. The observed spectra of mesons may be constructed by taking the tensor product of these representations to obtain $\mathbf{3} \otimes \overline{\mathbf{3}} = \mathbf{8} \oplus \mathbf{1}$ the octet and singlet depicted in Fig. 2.2. Note that states of the same strangeness occupy SU(2) (isospin) subgroup representations of the larger SU(3) representation. From this it is clear that the K^+, K^0 and $K^-, \overline{K}^0$ belong to spinor ($I = \frac{1}{2}$) representations of SU(2) while the π^+, π^-, π^0 belong to the isovector ($I = 1$) representation and the η, η' are isosinglets ($I = 0$). A table of the mesons relevant to this analysis is given in Table 2.2. A detailed description of meson properties and explanation of the decomposition of representations of SU(n) is included in Section 37 of the PDG [13].

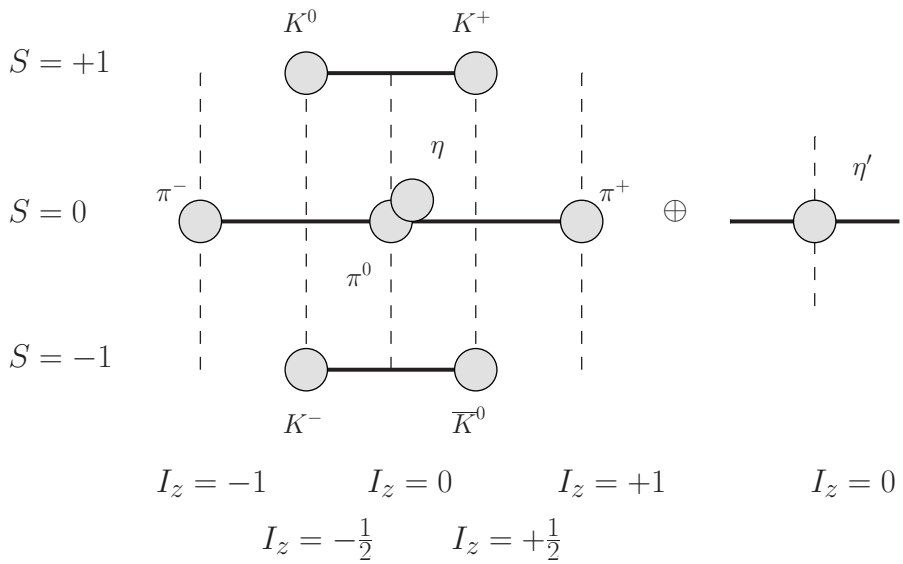

Figure 2.2: SU(3) spectrum of spin-0 mesons. A separate octet and singlet exist for spin-1 mesons with the substitutions $K \to K^*$, $\pi \to \rho$ and $\eta \to \omega$. Here S denotes the net strangeness of the meson as listed in Table 2.2.

2.3 Measurement of CKM parameters

The decay amplitude of a meson can be written as the sum of contributions from different decay processes leading to the same final state f. Each decay process is depicted diagrammatically as a Feynman graph. A general B decay amplitude is given by

$$A(B \to f) = \sum_{j=1}^{n} A_j e^{i(\delta_j + \phi_j)}, \tag{2.11}$$

where the δ_j parametrize the phase contribution of CP conserving processes and ϕ_j the contribution of CP violating processes. In the SM the CP violating processes are due to weak interactions and the ϕ_j correspond to the CKM angles α, β, γ, depending on the decay. Since CP acts like complex conjugation on the CKM parameters, the conjugate decay amplitude is given by

Table 2.2: Properties of mesons important in this analysis. The total spin of the meson is given by J and the transformation of the state under $\mathcal{C}$ and $\mathcal{P}$ are given by C, P. Where a meson is not an eigenstate of $\mathcal{C}$ only P is given. Mesons detected directly in *BABAR* are listed as Stable in *BABAR* while others are reconstructed from their decay products. The K^0 is experimentally observed as a linear combination of short and long lived particles, K_S, K_L. The K_L is Stable in *BABAR* and the K_S decays to $\pi^+\pi^-, \pi^0\pi^0$.

meson	Quark content	Mass (MeV/c^2)	J^{PC}	Principle Decay
$\pi^\pm$	$u\overline{d}, d\overline{u}$	139.57	0^-	Stable in *BABAR*
π^0	$1/\sqrt{2}(u\overline{u} - d\overline{d})$	134.98	0^{-+}	$\gamma\gamma$
$K^\pm$	$\overline{s}u, \overline{u}s$	493.68	0^-	Stable in *BABAR*
$K^0, \overline{K}^0$	$\overline{s}d, s\overline{d}$	497.65	0^-	See caption
$\rho^\pm$	$u\overline{d}, d\overline{u}$	775.8	1^-	$\pi^\pm\pi^0$
ρ^0	$1/\sqrt{2}(u\overline{u} - d\overline{d})$	775.8	1^{--}	$\pi^+\pi^-$
$K^{*\pm}$	$\overline{s}u, \overline{u}s$	891.66	1^-	$K^\pm\pi^0$, $\overset{(-)}{K}{}^0\pi^\pm$
$K^{*0}, \overline{K}^{*0}$	$\overline{s}d, s\overline{d}$	896.1	1^-	$K^\pm\pi^\mp$, $\overset{(-)}{K}{}^0\pi^0$

$$\overline{A}(\overline{B} \to \overline{f}) = \sum_{j=1}^{n} A_j e^{i(\delta_j - \phi_j)}. \tag{2.12}$$

The squares of decay amplitudes are proportional to the measurable branching fractions so the CP asymmetry (expanded for two interfering contributions),

$$\frac{|\overline{A}(\overline{B} \to \overline{f})|^2 - |A(B \to f)|^2}{|\overline{A}(\overline{B} \to \overline{f})|^2 + |A(B \to f)|^2} = \frac{2A_1A_2\sin(\delta_1 - \delta_2)\sin(\phi_1 - \phi_2)}{A_1^2 + A_2^2 + 2A_1A_2\cos(\delta_1 - \delta_2)\cos(\phi_1 - \phi_2)}, \tag{2.13}$$

provides a direct measure of CP violation in a given B decay. This quantity has been measured precisely for many different decay processes since many experimental uncertainties cancel in the ratio of amplitudes. Unfortunately, the A_j, δ_j cannot be reliably calculated, so despite the precision with which direct CP asymmetry can be measured, it is very difficult to extract CKM parameters from these asymmetries.

One strategy to overcome this difficulty is to take advantage of the fact that the mass and CP eigenstates of neutral B mesons are not the same so that the B^0 and

$\overline{B}^0$ mesons mix with each other over time; *i.e.*, $B^0 \to \overline{B}^0, \overline{B}^0 \to B^0$. The amplitude of the now time-dependent CP asymmetry is sensitive to a single weak phase rather than a weak and strong phase difference:

$$\frac{|\overline{A}(t)(\overline{B} \to f_{\rm CP})|^2 - |A(t)(B \to f_{\rm CP})|^2}{|\overline{A}(t)(\overline{B} \to f_{\rm CP})|^2 + |A(t)(B \to f_{\rm CP})|^2} = \frac{2\eta_f \mathrm{Im}\left(e^{-2i\beta}\frac{\overline{A}_f}{A_f}\right)}{1+\left|\frac{\overline{A}_f}{A_f}\right|^2}\sin(\Delta m_d t) + \frac{1-\left|\frac{\overline{A}_f}{A_f}\right|^2}{1+\left|\frac{\overline{A}_f}{A_f}\right|^2}\cos(\Delta m_d t), \quad (2.14)$$

where $\eta_f = \pm 1$ is the CP eigenvalue of the final state and Δm_d is the mass difference between the heavy and light B mass eigenstates. This method is of such importance that both the *BABAR* and BELLE detectors are designed specifically to exploit it; time-dependent CP asymmetries have been measured precisely to extract the CKM angle β [14].

Rather than extracting CKM parameters from CP asymmetries, it is possible in certain decay processes to measure the relative phases of intermediate amplitudes contributing to a common final state. This occurs in 3-body decays where the final state $B \to abc$ receives contributions from several intermediate resonances; *i.e.*, $B \to r_{ab}c$, and $B \to ar_{bc}$ where $r_{ab} \to ab$ and $r_{bc} \to bc$. The relative phases of these amplitudes can be measured in their interference over the available phase space of the $B \to abc$ decay or Dalitz plot (See Section 2.5). In Section 2.4 we explain how this strategy can be used to extract the CKM angle γ from the interference of $B^0 \to K^{*+}\pi^-$ and $B^0 \to K^{*0}\pi^0$ decays to the common final state $B^0 \to K^+\pi^-\pi^0$.

2.4 Sensitivity to γ in $B \to K\pi\pi$ decays

The tree contribution in B decays via the transition $\overline{b} \to \overline{u}u\overline{s}$ provides sensitivity to the CKM angle γ. This is the case for the decays $B^0 \to K^{*+}\pi^-$ and $B^0 \to K^{*0}\pi^0$ shown in Fig. 2.3. If the tree diagram was the sole contribution to the decay amplitude in these cases one could use Eq. (2.12) to show that

$$\gamma = -\frac{1}{2}\mathrm{Arg}\left(\frac{\overline{A}(\overline{B} \to \overline{K}^{*0}\pi^0)}{A(B \to K^{*0}\pi^0)}\right), \tag{2.15}$$

where the phase of the $B^0 \to K^{*0}\pi^0$ decay amplitude is determined relative to the $B^0 \to K^{*+}\pi^-$ amplitude via interference on the $B^0 \to K^+\pi^-\pi^0$ Dalitz plot. The phase difference between $\overline{B}^0 \to K^{*-}\pi^+$ and $B^0 \to K^{*+}\pi^-$ also necessary to evaluate Eq. (2.15), would be determined from the interference of these decays on the $B^0 \to K_S\pi^+\pi^-$ Dalitz plot.

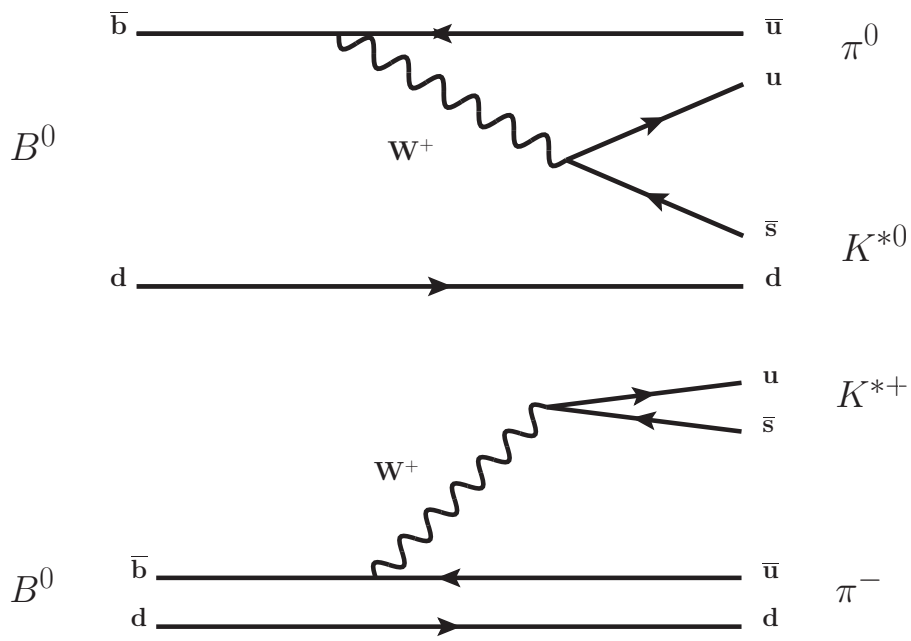

Figure 2.3: Tree Feynman diagrams contributing to $B \to K^*\pi$ decays. Note that in each case the diagram is sensitive to $V_{ub}^*V_{us} = A\lambda^4(\rho + i\eta)$.

The total amplitude for $B \to K^*\pi$ decays; however, is dominated by doubly CKM enhanced quantum chromodynamic (QCD) and electroweak (EW) loop order diagrams (penguins) shown in Fig. 2.4. These contributions prevent a model-independent measurement of γ using Eq. (2.15).

It is possible to eliminate the QCD penguins from consideration by noting that isospin is a good symmetry of the strong interaction, so the QCD penguin contributions must be $\Delta I = 0$. Decomposing $B \to K^*\pi$ amplitudes in an isospin basis one can

construct a linear combination of $B^0 \to K^{*0}\pi^0$ and $B^0 \to K^{*+}\pi^-$ decay amplitudes is pure $\Delta I = 1$ and hence free of QCD penguin contributions [15]. The remaining tree contribution is sensitive to γ, while the EW penguin (EWP) contribution may be independently measured via an SU(3) decomposition of operators and strangeness conserving B^+ decay amplitudes [16].

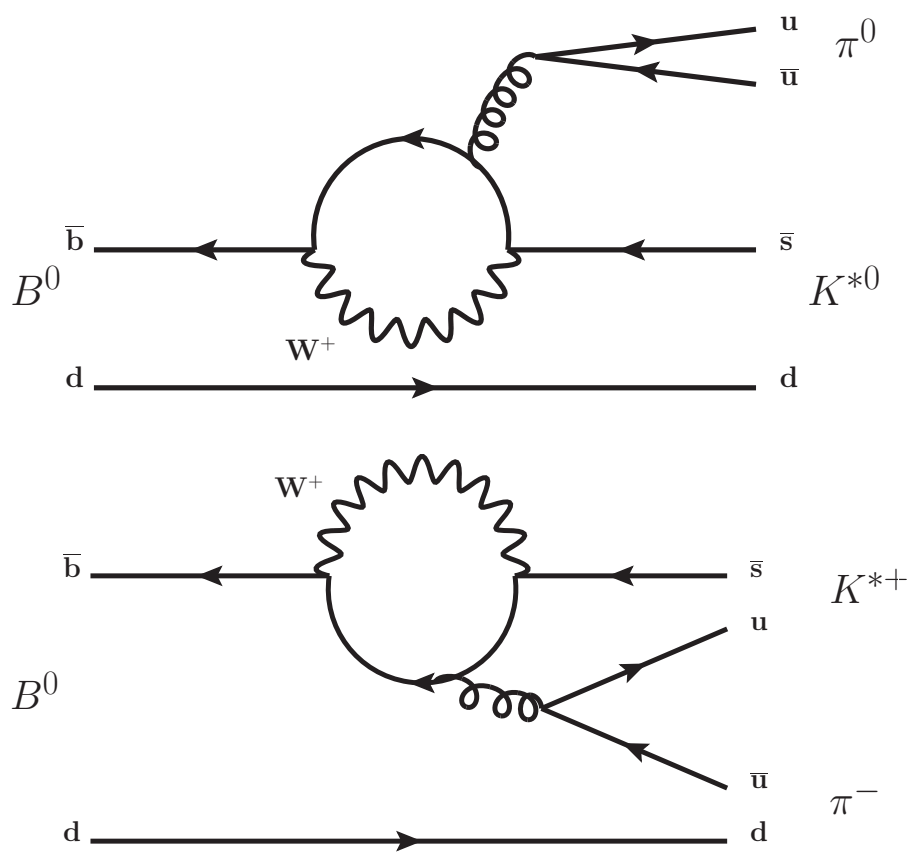

Figure 2.4: Penguin Feynman diagrams contributing to $B \to K^*\pi$ decays. Note that in each case the diagram is $\propto A\lambda^2\alpha_s$ where $\alpha_s(m_b) \approx 0.22$. The EWP diagrams are identical to the QCD diagrams with the gluon is replaced by a photon. The EWP diagrams are $\propto A\lambda^2\alpha_{\rm em}$ where $\alpha_{\rm em} = 1/137$.

Recall from Section 2.2 that B and K^* mesons transform as $I = \frac{1}{2}$ states while π and ρ mesons transform as $I = 1$. We expand $K^*\pi$ and ρK states in an isospin basis by taking the tensor product of isospin states for each particle contributing to the final state. For instance, a $K^{*+}\pi^-$ state may be expanded as

$$|K^{*+}\pi^-\rangle = \left|\frac{1}{2}1;\frac{1}{2}-1\right\rangle = \frac{1}{\sqrt{3}}\left|\frac{1}{2}1;\frac{3}{2}\frac{-1}{2}\right\rangle + \sqrt{\frac{2}{3}}\left|\frac{1}{2}1;\frac{1}{2}\frac{-1}{2}\right\rangle, \tag{2.16}$$

where the Clebsch-Gordon coefficients are described in Section 35 of the PDG [13]. The decay amplitude operators can similarly be expanded in an isospin basis as

$$O^{\Delta I} = \sum_{I_z=-\Delta I}^{\Delta I} \langle \Delta I, I_z|. \tag{2.17}$$

The operators contributing to a transition from an $I = \frac{1}{2}$ state (B meson) to a combination of $I = \frac{1}{2}$ and $I = \frac{3}{2}$ states are $O^{\Delta I=1}$ and $O^{\Delta I=0}$. Note that only the $\Delta I = 1$ operator can contribute to a transition from a B meson to an $I = \frac{3}{2}$ state so this isospin state must be free of QCD penguin contributions. We expand $B \to K^*\pi$ amplitudes in an isospin basis in Table 2.3 using Eq. (2.17) and final state decompositions as in Eq. (2.17).

Table 2.3: Isospin decomposition of $B \to K^*\pi$ amplitudes. The decomposition for $B \to \rho K$ amplitudes follows from the substitutions, $K^* \to K$ and $\pi \to \rho$.

$$\begin{aligned}
A(B^+ \to K^{*0}\pi^+) &= \tfrac{\sqrt{2}}{3}A^1_{\frac{3}{2}} - \tfrac{\sqrt{2}}{3}A^1_{\frac{1}{2}} + \sqrt{\tfrac{2}{3}}A^0_{\frac{1}{2}} \\
A(B^+ \to K^{*+}\pi^0) &= \tfrac{2}{3}A^1_{\frac{3}{2}} + \tfrac{1}{3}A^1_{\frac{1}{2}} - \sqrt{\tfrac{1}{3}}A^0_{\frac{1}{2}} \\
A(B^0 \to K^{*+}\pi^-) &= \tfrac{\sqrt{2}}{3}A^1_{\frac{3}{2}} - \tfrac{\sqrt{2}}{3}A^1_{\frac{1}{2}} - \sqrt{\tfrac{2}{3}}A^0_{\frac{1}{2}} \\
A(B^0 \to K^{*0}\pi^0) &= \tfrac{2}{3}A^1_{\frac{3}{2}} + \tfrac{1}{3}A^1_{\frac{1}{2}} + \sqrt{\tfrac{1}{3}}A^0_{\frac{1}{2}}
\end{aligned}$$

The upper index of the isospin amplitudes in Table 2.3 denotes the ΔI of the transition and the lower index denotes the isospin I of the final state. We seek to solve for $A^1_{\frac{3}{2}}$ (where we drop the unambiguous $\Delta I = 1$ upper index) in terms of B decay amplitudes whose relative phases are observable and whose CP-violating weak phase may be extracted via the interference of CP conjugate amplitudes to a common final state. Expressions for $A_{\frac{3}{2}}$ in terms of $K^*\pi$ and ρK decay amplitudes satisfying these conditions are

$$A_{\frac{3}{2}} = \frac{1}{\sqrt{2}}A(B^0 \to K^{*+}\pi^-) + A(B^0 \to K^{*0}\pi^0), \tag{2.18}$$
$$A_{\frac{3}{2}} = \frac{1}{\sqrt{2}}A(B^0 \to K^{+}\rho^-) + A(B^0 \to K^{0}\rho^0).$$

This disseration will concern itself primarily with the measurement of $B \to K^*\pi$ decays though it is important to note that sensitivity to γ is also possible via the measurement of $B \to \rho K$ decay amplitudes. We now define the CP-violating weak phase $\Phi_{\frac{3}{2}}$ in analogy with Eq. (2.15) as

$$\Phi_{\frac{3}{2}} = -\frac{1}{2}\mathrm{Arg}\left(\frac{\overline{A}_{\frac{3}{2}}}{A_{\frac{3}{2}}}\right), \tag{2.19}$$

which is equal to γ in the limit that EWP diagrams do not contribute to the decay amplitudes. In Section 2.4.1 we discuss how EWP contributions affect the extraction of CKM parameters from measurements of $\Phi_{\frac{3}{2}}$ and how they can be independently measured.

2.4.1 Corrections from EWP Operators

The CKM enhancement of the EWP largely compensates its α_{em} suppression, resulting in a contribution roughly comparable to that of the tree. This fact means the EWP contribution must be measured independently before $\Phi_{\frac{3}{2}}$ can be related to the CKM angle γ. The effective Hamiltonian describing $\overline{b} \to \overline{u}u\overline{s}$ transitions is given by

$$H = \frac{G_F}{\sqrt{2}}\left(V_{ub}^*V_{us}[c_1O_1 + c_2O_2] - V_{tb}^*V_{ts}\sum_{i=3}^{10} c_iO_i\right) \tag{2.20}$$

in the Operator Product Expansion [17]. The operators $O_{1,2}$ have the flavor content $(\overline{b}u)_{V-A}(\overline{u}s)_{V-A}$ and $(\overline{b}s)_{V-A}(\overline{u}u)_{V-A}$, respectively, and correspond to the tree diagrams in Fig. 2.3. The penguin operators are given by the $O_{i=3...10}$ where the $i = 3...6$ describe the QCD penguins and the $i = 7...10$ describe the EWP contributions. The dominant EWP operators are proportional to the tree operators via the relationships

$$O_{9,10} = \frac{3}{2}O_{1,2} + (\Delta I = 0 \text{ operators}). \tag{2.21}$$

The isospin amplitude $A_{\frac{3}{2}}$ may now be expressed in terms of CKM elements and tree operators as

$$A_{\frac{3}{2}} = \langle f_{\frac{3}{2}}|H^{\Delta I=1}|B\rangle = \frac{G_F}{\sqrt{2}}\sum_{i=+,-}(V_{ub}^*V_{us}C_i - \frac{3}{2}V_{tb}^*V_{ts}C_i^{\text{EWP}})\langle f_{\frac{3}{2}}|O_i^{\Delta I=1}|B\rangle. \tag{2.22}$$

where $O_{\pm}^{\Delta I=1} = \frac{1}{2}(O_1^{\Delta I=1} \pm O_2^{\Delta I=1})$, $C_{\pm} = c_1 \pm c_2$, $C_{\pm}^{\text{EWP}} = c_9 \pm c_{10}$. The $I = \frac{3}{2}$ final state $f_{\frac{3}{2}}$ enforces the $\Delta I = 1$ constraint on the operators. Consequently, the QCD penguin operators do not appear in Eq. (2.22). We have also neglected the EWP operators $O_{7,8}$ involving small Wilson coefficients. We can substitute the Wolfenstein parameters for the CKM elements into Eq. (2.22) and use a relationship between Wilson coefficients following the convention of [16]

$$\frac{C_+^{\text{EWP}}}{C_+} = -\frac{C_-^{\text{EWP}}}{C_-}, \tag{2.23}$$

to express the amplitude in an especially simple form:

$$A_{\frac{3}{2}} \propto (\overline{\rho} + i\overline{\eta})(1 + r_{\frac{3}{2}}) + C(1 - r_{\frac{3}{2}}), \text{ where} \tag{2.24}$$

$$C = \frac{3}{2}\frac{C_+^{\text{EWP}}}{C_+}\frac{1-\frac{\lambda^2}{2}}{\lambda^2}, \; r_{\frac{3}{2}} = \frac{\langle f_{\frac{3}{2}}|C_-O_-^{\Delta I=1}|B\rangle}{\langle f_{\frac{3}{2}}|C_+O_+^{\Delta I=1}|B\rangle}. \tag{2.25}$$

In terms of tree and penguin amplitudes the isospin amplitude is given by $A_{\frac{3}{2}} = Te^{i\gamma} - P_{\text{EWP}}$ so from Eq. (2.24), the ratio of penguin to tree amplitudes is

$$\frac{P_{\text{EWP}}}{T} = \frac{-C}{\sqrt{\overline{\rho}^2 + \overline{\eta}^2}}\frac{(1 - r_{\frac{3}{2}})}{(1 + r_{\frac{3}{2}})}. \tag{2.26}$$

An expression for $\Phi_{\frac{3}{2}}$ can be derived using Eq. (2.19) and Eq. (2.24)

$$\Phi_{\frac{3}{2}} = -\frac{1}{2}\arctan\left(\frac{I_- R_- - R_+ I_+}{R_+ R_- + I_+ I_-}\right), \text{ where} \tag{2.27}$$

$$\begin{aligned} R_\pm &= \overline{\rho} + C + (\overline{\rho} - C)\mathrm{Re}(r_{\frac{3}{2}}) \pm \overline{\eta}\mathrm{Im}(r_{\frac{3}{2}}), \\ I_\pm &= (\overline{\rho} - C)\mathrm{Im}(r_{\frac{3}{2}}) \pm \overline{\eta}(\mathrm{Re}(r_{\frac{3}{2}}) + 1). \end{aligned} \tag{2.28}$$

Since knowledge of the ratio of hadronic matrix elements $r_{\frac{3}{2}}$ and $C = -0.27 \pm 0.007$ [16] is required to evaluate Eq. (2.27), measurements of $\Phi_{\frac{3}{2}}$ will be used to constrain the apex of the CKM triangle $\overline{\rho}, \overline{\eta}$ rather than as an explicit measurement of the angle γ. It now remains to determine a strategy for measuring $r_{\frac{3}{2}}$. Such a strategy is possible due to an SU(3) expansion of the operators and states appearing in Eq. (2.25) [16] which we disscus in Appendix A.

2.4.2 SU(3) expansion of the ratio $r_{\frac{3}{2}}$

The $\overline{b} \to \overline{u}u\overline{s}$ transition operators may be expanded in an SU(3) basis much in the same way they are expanded in an SU(2) basis. Such operators are given by $\overline{\mathbf{3}} \otimes \overline{\mathbf{3}} \otimes \mathbf{3} = \overline{\mathbf{15}} \oplus \mathbf{6} \oplus \overline{\mathbf{3}} \oplus \overline{\mathbf{3}}$ expressed as a direct sum of irreducible SU(3) representations. The linear combinations of operators, $O_-^{\Delta I=1}$ and $O_+^{\Delta I=1}$, transform as $\mathbf{6}$ and $\overline{\mathbf{15}}$ respectively since only the $\mathbf{6}$ and $\overline{\mathbf{15}}$ representations contain SU(2) subgroup representations transforming as $\Delta I = 1$ [18]. The tensor product of SU(3) octet states, $K^*\pi$, is decomposed as $\mathbf{8} \otimes \mathbf{8} = \mathbf{27} \oplus \overline{\mathbf{10}} \oplus \mathbf{10} \oplus \mathbf{8} \oplus \mathbf{8} \oplus \mathbf{1}$ where the $I = \frac{3}{2}$ linear combination of $K^*\pi$ states, $A_{\frac{3}{2}}$, simplifies to $\mathbf{27} \oplus \mathbf{10}$. B mesons transform as the fundamental representation $\mathbf{3}$. An expression for $r_{\frac{3}{2}}$ in terms of SU(3) amplitudes is given by

$$r_{\frac{3}{2}} = -\frac{C_-}{C_+}\frac{\langle \mathbf{10}|\mathbf{6}|\mathbf{3}\rangle}{\langle \mathbf{27}|\overline{\mathbf{15}}|\mathbf{3}\rangle}, \tag{2.29}$$

where the SU(3) decompositions for the amplitudes and operators have been substituted into Eq. (2.25) and a table of SU(3) Clebsch-Gordon coefficients [18] has been

used to simplify the expression. It is useful to note that a similar decomposition of amplitudes is possible for ρK states. A relative minus sign between expressions for $r_{\frac{3}{3}}$ using $K^*\pi$ and ρK states appears due to the fact that the $\langle \mathbf{10}|\mathbf{6}|\mathbf{3}\rangle$ amplitude is anti-symmetric under the exchange of quarks between vector and pseudoscalar mesons in the SU(3) decomposition.

A table of SU(3) decompositions of amplitudes analogous to Table 2.3 [18] can be used to express the SU(3) amplitudes appearing in Eq. (2.29) in terms of $\Delta S = 0$, B^+ decay amplitudes where the EWP contribution is suppressed. Substituting these decompositions into Table 2.3 [16] gives

$$r_{\frac{3}{2}} = \frac{[A_{\rho^+\pi^0} - A_{\rho^0\pi^+}] - \sqrt{2}[A_{K^{*+}\overline{K}^0} - A_{K^+\overline{K}^{*0}}]}{A_{\rho^+\pi^0} + A_{\rho^0\pi^+}}. \tag{2.30}$$

This expression permits the measurement of $r_{\frac{3}{2}}$ from the B^+ decay amplitudes discussed in Appendix A, and is generalizable to $I = \frac{3}{2}$ amplitudes constructed from any excited K^* intermediate state by replacing the ρ with the corresponding resonance in the same SU(3) octet as the excited K^*.

2.5 Dalitz Analysis of the Decay $B \to K^+\pi^-\pi^0$

In order to use the expressions in Eq. (2.18) to construct $I = \frac{3}{2}$ amplitudes useful in producing a constraint on the CKM triangle, we must measure the interference of the $B^0 \to K^*\pi$ (or $B^0 \to \rho K$) amplitudes over the kinematic phase space of their decay to a common final state. Such an analysis is possible by constructing the two dimensional distribution of $B^0 \to K^+\pi^-\pi^0$ decays in the invariant mass pairs $m^2_{K^\pm\pi^\pm} = (p_{K^\pm} + p_{\pi^\mp})^2$ and $m^2_{K^\pm\pi^0} = (p_{K^\pm} + p_{\pi^0})^2$, typically denoted as x, y respectively [2]. The two dimensional, kinematic distribution of B decays is referred to as a Dalitz plot. Dalitz analyses are commonly used to study the dynamics of 3-body final states where the interference of several intermediate resonances contributing to the final state are of interest. The relative phases and amplitudes of the resonances are measured by modeling the total decay amplitude as a sum of isobars k, each given

[2] We use natural units where $\hbar = c = 1$ in our algebraic equations

by

$$A_k = a_k e^{i\Phi_k} \int_{DP} f_k(J, x, y)\ dx\ dy. \tag{2.31}$$

where a_k, Φ_k are the amplitude and phase respectively. The decay kinematics of a spin-J resonance are specified by $f_k(J, x, y)$. The isobar fraction FF_k (CP-averaged over B and $\overline{B}$), and CP asymmetry, $A^k_{\rm CP}$ are given by

$$\begin{aligned} FF_k &= \frac{|A_k|^2 + |\overline{A}_k|^2}{|\sum_j A_j|^2 + |\sum_j \overline{A}_j|^2}, \\ A_{\rm CP}(k) &= \frac{\overline{a}_k^2 - a_k^2}{\overline{a}_k^2 + a_k^2}. \end{aligned} \tag{2.32}$$

Due to interference, the fractions FF_k do not in general add up to unity. The nominal Dalitz model for the decay $B^0 \to K^+\pi^-\pi^0$ includes seven resonant intermediate states: $\rho^-(770)K^+$, $\rho^-(1450)K^+$, $\rho^-(1700)K^+$, $K^{*+}(892)\pi^-$, $K^{*0}(892)\pi^0$, $(K\pi)^{*+}_0\pi^-$, $(K\pi)^{*0}_0\pi^0$ and a non-resonant contribution, uniformly distributed over the Dalitz plot. The notation for the $(K\pi)^*_0$ isobar components, introduced by the *BABAR* experiment [19], denotes each phenomenological amplitude describing the neutral and charged $K\pi$ scalar resonances by a superposition of an elastic effective range term, and the $K^*_0(1430)$ scalar resonance. The kinematic parametrization of the resonances, $f_k(J, x, y)$, are described in Section 2.5.1 and summarized in Table 2.5.

2.5.1 Decay Kinematics

The kinematic phase space available to an intermediate resonance (Dalitz distribution) are specified by the $f_k(J, x, y)$ where the relative momenta of particles a and b in the ac rest frame are defined as $\vec{p}$ and $\vec{q}$ respectively, in a general 3-body decay $B \to abc$. The angle between $\vec{p}$ and $\vec{q}$ is the helicity angle defined as $\cos\theta_H = \vec{p}\cdot\vec{q}/(|\vec{p}||\vec{q}|)$.

We expand the kinematic distribution as a sum over the helicity states, denoted by λ, of the intermediate resonance. For instance, a K^{*0} resonance (formed in the

$K^+\pi^-$ system) is expressed as

$$\begin{aligned} f_{K^{*0}}(J,x,y) &= \sum_\lambda \langle K^+\pi^-|K^{*0}_\lambda\rangle R_{K^{*0}}(x)\langle\pi^0 K^{*0}_\lambda|B^0\rangle \\ &= Z(J,\vec{p},\vec{q})B_B(L,\vec{p})B_{K^{*0}}(L,\vec{q})R_{K^{*0}}(x), \end{aligned} \tag{2.33}$$

where $R_{K^{*0}}(x)$ is the K^{*0} mass distribution or line shape, $Z(J,\vec{p},\vec{q})$ describes the angular dependence of the decay, and $B_B(L,\vec{p})$, $B_{K^{*0}}(L,\vec{q})$ are Blatt-Weisskopf barrier factors [20] for the transitions $B^0 \to K^{*0}\pi^0$ and $K^{*0} \to K^+\pi^-$ of orbital angular momentum L. The momenta of the π^0 and K^+ in the $K^+\pi^-$ rest frame are given by $\vec{p}$ and $\vec{q}$, respectively.

Angular Distribution

We use the Zemach tensor formalism [21] for the angular distribution $Z(J,\vec{p},\vec{q})$ of a process by which a pseudoscalar B meson produces a spin-J resonance in association with a bachelor pseudoscalar meson. For a spin-0 resonance the decay distribution is isotropic and $Z(0,\vec{p},\vec{q}) = 1$ while for a spin-1 resonance the distribution is derived as [22]

$$\begin{aligned} Z(1,\vec{p},\vec{q}) &= (p_{B^0}+p_c)_\mu \sum_\lambda \epsilon^{*\mu}_\lambda \epsilon^\nu_\lambda (p_a-p_b)_\nu \\ &= (p_{B^0}+p_c)_\mu \Big[-g_{\mu\nu} + \frac{(p_a+p_b)^\mu(p_a+p_b)^\nu}{m^2_{ab}}\Big](p_a-p_b)_\nu \\ &= (m^2_{bc}-m^2_{ac}) + \frac{(m^2_{B^0}-m^2_c)(m^2_a-m^2_b)}{m^2_{ab}} \\ &= -2|\vec{p}||\vec{q}|\cos\theta_H, \end{aligned} \tag{2.34}$$

where ϵ denotes the polarization vectors of the intermediate resonance and the helicity state of a spin-1 resonance are $\lambda = +1, 0, -1$. The 4-momenta of the particles in the decay $B^0 \to abc$ are given by p_j where $j = B^0, a, b, c$. The angular distributions and Blatt-Weisskopf barrier factors for resonances of spin-$0, 1, 2$ are shown in Table 2.4.

Barrier Factor

The Schrödinger equation for a wave scattering from a potential $V(r)$ can be expressed in spherical coordinates and solved in terms of partial waves of definite angular momentum L. This formulation introduces an effective potential in the Schrödinger equation from which the wave scatters:

$$U_L(r) = V(r) + \frac{\hbar^2 L(L+1)}{2Mr^2} \text{ (for r > R)}, \tag{2.35}$$

where M and R are the mass and radius of the scattering center (resonance). Since the resonances decay to two pseudoscalar particles, the orbital angular momentum of the final state, L, must be equal to the spin of the resonance, J. As a result the transition amplitudes of waves scattering from the effective potential in Eq. (2.35) acquire the Blatt-Weisskopf barrier factors listed in Table 2.4.

Table 2.4: The angular distributions and Blatt-Weisskopf barrier factors for a resonance of spin-J decaying to two pseudoscalar mesons

Spin-J	$Z(J,\vec{p},\vec{q})$	$B(J,\vec{q})$
0	1	1
1	$-2\lvert\vec{p}\rvert\lvert\vec{q}\rvert\cos\theta_H$	$\sqrt{\frac{1+z_o^2}{1+z^2}}$
2	$\frac{4}{3}\lvert\vec{p}\rvert^2\lvert\vec{q}\rvert^2(3\cos^2\theta_H - 1)$	$\sqrt{\frac{9+3z_o^2+z_0^4}{9+3z^2+z^4}}$

The Blatt-Weisskopf barrier factors are normalized so as to be equal to 1 when $m_{ab} = M$. We parametrize the barrier factors in terms of $z = |\vec{q}|R$ and $z_0 = |\vec{q}_0|R$ where $|\vec{q}_0|$ is the value of $|\vec{q}|$ when $m_{ab} = M$.

Line Shapes

The line shapes of the $K^{*+}(892)$ and $K^{*0}(892)$ resonances are described by the relativistic Breit-Wigner (RBW) distribution:

$$R^{\mathrm{RBW}}(x, J, M, \Gamma^0) = \frac{1}{M^2 - x - iM\Gamma(x, J, \Gamma^0)}. \tag{2.36}$$

The Dalitz-dependence of the total width $\Gamma(x, J, \Gamma^0)$ can be ignored for high-mass states. For the low-mass states which decay almost elastically, it is defined by

$$\Gamma(x, J, \Gamma^0) = \Gamma^0 \frac{M}{\sqrt{x}} \left(\frac{|\vec{q}|}{|\vec{q}_0|} \right)^{2J+1} B(J, |\vec{q}|)^2, \tag{2.37}$$

where $\Gamma^0 = \Gamma(M^2, J, \Gamma^0)$. The RBW line shape is illustrated in Fig. 2.5 for the $K^{*0}(892)$ resonance.

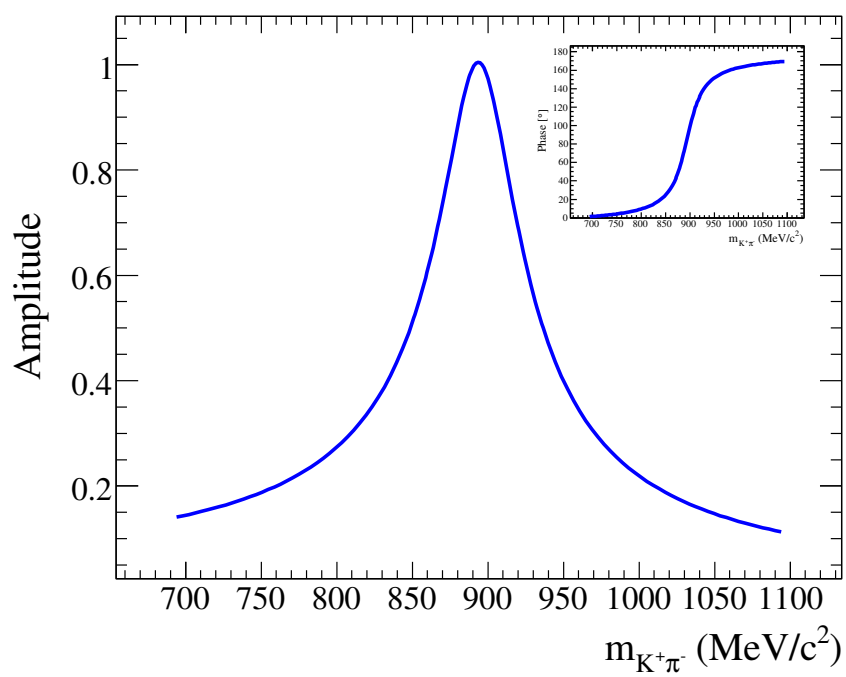

Figure 2.5: Amplitude and Phase of the $K^{*0}(892)$ line shape as modeled by the RBW.

The Gounaris-Sakurai (GS) parametrization [23] is used to describe the Dalitz distribution of the broad $\rho^-(770)$, $\rho^-(1450)$ and $\rho^-(1700)$ resonances decaying to two

pions:

$$R^{\mathrm{GS}}(x, J, M, \Gamma^0) = \frac{1 + \frac{d\Gamma^0}{M}}{M^2 + g(x) - x - iM\Gamma(x, J, \Gamma^0)}, \tag{2.38}$$

where the Dalitz-dependent width $\Gamma(x, J, \Gamma^0)$ is defined in Eq. (2.37). The expressions of the constant d and the function $g(x)$ in terms of M and Γ^0 are given in [23]. The parameters of the ρ line shapes, R, M, Γ^0 are taken from τ decay and $\pi\pi$ scattering in [24] and [25]. The GS line shape is illustrated in Fig. 2.6 for the $\rho(770)$ resonance.

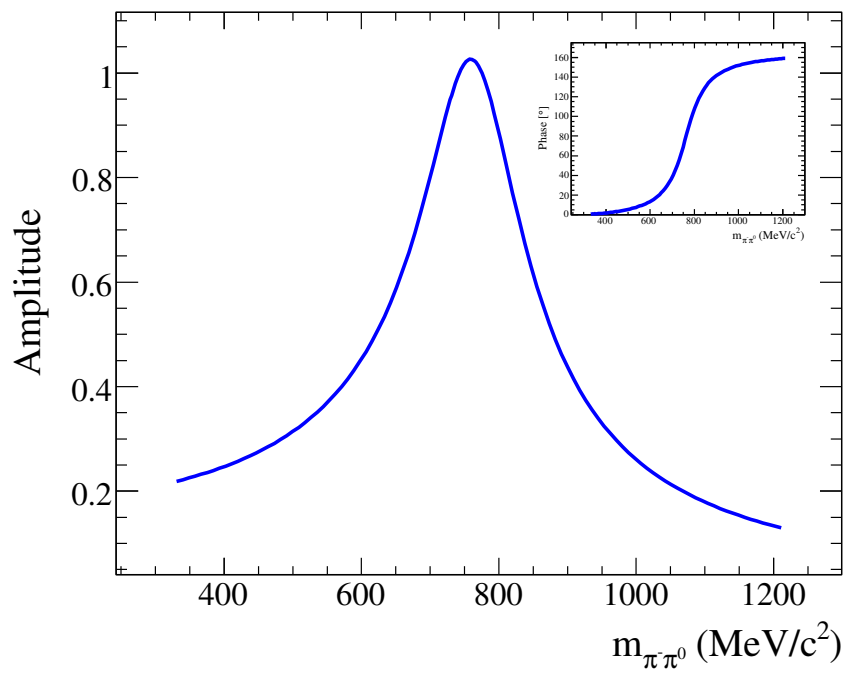

Figure 2.6: Amplitude and Phase of the $\rho(770)$ line shape as modeled by the GS.

An effective-range parametrization was suggested [26] for the $K\pi$ scalar ($J = 0$) amplitudes, $(K\pi)_0^{*+}$ and $(K\pi)_0^{*0}$ which dominate for $m_{K\pi} < 2$ GeV/c^2, to describe the slowly increasing phase as a function of the $K\pi$ mass. We use the parametrization as in the LASS experiment [27], tuned for B decays:

$$R^{\mathrm{LASS}}(x, M, \Gamma^0, a, r) = \frac{\sqrt{x}}{|\vec{q}| \cot \delta_B - i|\vec{q}|} + e^{2i\delta_B} \frac{M\Gamma^0 \frac{M}{|\vec{q}_0|}}{M^2 - x - iM\Gamma(x, 0, \Gamma^0)}, \tag{2.39}$$

where

$$\cot \delta_B = \frac{1}{a|\vec{q}|} + \frac{1}{2}\, r\, |\vec{q}|\,, \tag{2.40}$$

a is the scattering length, and r the effective range (Table 2.5). We impose a cutoff for the $K\pi$ S-waves at $\sqrt{x} = 1.8$ GeV/c^2 so that

$$R^{\mathrm{LASS}}(\sqrt{x} > 1.8 \text{ GeV}/c^2, M, \Gamma^0, a, r) = e^{2i\delta_B} \frac{M\Gamma^0 \frac{M}{|\vec{q}_0|}}{M^2 - x - iM\Gamma(x, 0, \Gamma^0)}. \tag{2.41}$$

The LASS line shape is illustrated in Fig. 2.7 for the $(K\pi)_0^{*0}$ S-wave. The effect of the cutoff at $\sqrt{x} = 1.8$ GeV/c^2 is clearly visible.

The parameters describing the resonances contributing to the nominal Dalitz model are summarized in Table 2.5. The D^0, D^+ resonances which also contribute to the $K^+\pi^-\pi^0$ final state are included as non-interfering amplitudes. These resonances are are narrower than the detector resolution so their line shapes are modeled as gaussians to good approximation. The D^+ line shape is taken from a fit to simulated data.

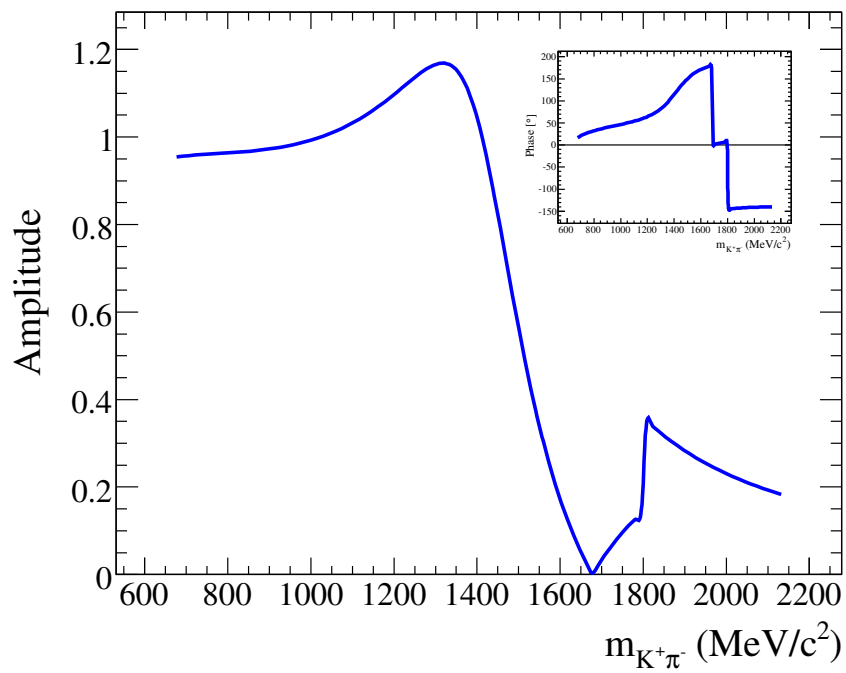

Figure 2.7: Amplitude and Phase of the $K\pi$ S-waves as modeled by the LASS parametrization. The cutoff at $m_{K^+\pi^-} = 1.8$ GeV/c^2 is clearly visible.

Table 2.5: The *nominal model* for the decay $B^0 \to K^+\pi^-\pi^0$ comprises a non-resonant (NR) amplitude and seven intermediate states. The three types of line shape are described in the text. The masses and widths are from [13], except for the LASS shape [27]. We use the same LASS parameters for both neutral and charged $K\pi$ systems. The *Non-interfering* resonances D^0, D^+ are included in the model and do not affect the relative phases and amplitudes of other states.

Resonance	Line shape	Parameters
	Spin-$J = 1$	
$\rho^-(770)$	GS	$M = 768.5$ MeV/c^2
		$\Gamma^0 = 148.2$ MeV
		$R = 0$ (GeV)$^{-1}$
$\rho^-(1450)$	GS	$M = 1439$ MeV/c^2
		$\Gamma^0 = 550$ MeV
		$R = 0$ (GeV)$^{-1}$
$\rho^-(1700)$	GS	$M = 1795$ MeV/c^2
		$\Gamma^0 = 278$ MeV
		$R = 0$ (GeV)$^{-1}$
$K^{*+}(892)$	RBW	$M = 891.6$ MeV/c^2
		$\Gamma^0 = 50$ MeV
		$R = 3.4$ (GeV)$^{-1}$
$K^{*0}(892)$	RBW	$M = 891.6$ MeV/c^2
		$\Gamma^0 = 50.5$ MeV
		$R = 3.4$ (GeV)$^{-1}$
	Spin-$J = 0$	
$(K\pi)_0^{*+}$, $(K\pi)_0^{*0}$	LASS	$M = 1415$ MeV/c^2
		$\Gamma^0 = 300$ MeV
		cutoff $m_{K\pi} = 1800$ MeV/c^2
		$a = 2.07$ (GeV/c)$^{-1}$
		$r = 3.32$ (GeV/c)$^{-1}$

NR	Constant	
	Non-interfering Components	
D^0	$M = 1862.3$ MeV/c^2	Double Gaussian
	$\Gamma^0 = 7.1$ MeV/c^2	(From Data)
D^+	$M = 1864.4$ MeV/c^2	Double Gaussian
	$\Gamma^0 = 9.9$ MeV/c^2	(From MC)

2.5.2 Measurement of the isospin weak phase $\Phi_{\frac{3}{2}}$

We now develop expressions for the isospin weak phase $\Phi_{\frac{3}{2}}$ using equations Eq. (2.18) and Eq. (2.19) in terms of observable amplitudes and phases given the isobar parametrization described in Section 2.5. These expressions will be used in the analysis Section 5.1 to produce a constraint on the CKM triangle.

Measurement of $\Phi_{\frac{3}{2}}$ in $B^0 \to K^*\pi$ decays

Applying the isobar parametrization of amplitudes Eq. (2.31) to the isospin triangle relationship for $B^0 \to K^*\pi$ decays in Eq. (2.18) gives

$$\begin{aligned} \overline{A}_{\frac{3}{2}} &= \frac{1}{\sqrt{2}}|\overline{A}_{K^{*-}\pi^+}|e^{i\overline{\Phi}_{K^{*-}\pi^+}} + |\overline{A}_{\overline{K}^{*0}\pi^0}|e^{i\overline{\Phi}_{\overline{K}^{*0}\pi^0}}, \\ A_{\frac{3}{2}} &= \frac{1}{\sqrt{2}}|A_{K^{*+}\pi^-}|e^{i\Phi_{K^{*+}\pi^-}} + |A_{K^{*0}\pi^0}|e^{i\Phi_{K^{*0}\pi^0}}. \end{aligned} \tag{2.42}$$

Since the relative phase between $B^0 \to K^{*\pm}\pi^\mp$ and $B^0 \to K^{*0}\pi^0$ is observable the $K^{*\pm}\pi^\mp$ phase is factored from the expressions in Eq. 2.42:

$$\begin{aligned} \overline{A}_{\frac{3}{2}} &= (\frac{1}{\sqrt{2}}|\overline{A}_{K^{*-}\pi^+}| + |\overline{A}_{\overline{K}^{*0}\pi^0}|e^{i\Delta\overline{\Phi}})e^{i\overline{\Phi}_{K^{*-}\pi^+}}, \\ A_{\frac{3}{2}} &= (\frac{1}{\sqrt{2}}|A_{K^{*+}\pi^-}| + |A_{K^{*0}\pi^0}|e^{i\Delta\Phi})e^{i\Phi_{K^{*+}\pi^-}}. \end{aligned} \tag{2.43}$$

where $\Delta\Phi = \Phi_{K^{*0}\pi^0} - \Phi_{K^{*+}\pi^-}$ and $\Delta\overline{\Phi} = \overline{\Phi}_{\overline{K}^{*0}\pi^0} - \overline{\Phi}_{K^{*-}\pi^+}$. We now substitute the expressions in Eq. (2.43) into Eq. (2.19) using the identity $a+ib = \sqrt{a^2+b^2}e^{i\arctan\left(\frac{b}{a}\right)}$ and find

$$\Phi_{\frac{3}{2}} = \frac{1}{2}\left(\arctan\left(\frac{\sin\Delta\Phi}{\frac{|A_{K^{*+}\pi^-}|}{\sqrt{2}|A_{K^{*0}\pi^0}|} + \cos\Delta\Phi}\right) - \arctan\left(\frac{\sin\Delta\overline{\Phi}}{\frac{|\overline{A}_{K^{*-}\pi^+}|}{\sqrt{2}|\overline{A}_{\overline{K}^{*0}\pi^0}|} + \cos\Delta\overline{\Phi}}\right) - \Delta\phi_{K^*\pi}\right). \tag{2.44}$$

The phase difference $\Delta\phi_{K^*\pi} = \overline{\Phi}_{K^{*-}\pi^+} - \Phi_{K^{*+}\pi^-}$ is measured in the Dalitz analysis of

the decay $B^0 \to K_s\pi^+\pi^-$ where the charge conjugated $K^*\pi$ amplitudes interfere. This phase difference fixes the relative orientation of the isospin triangles shown in Fig. 2.8. The remaining expression in Eq. 2.44, that we define as

$$\Delta\phi_{\frac{3}{2}} = \arctan\left(\frac{\sin\Delta\Phi}{\frac{|A_{K^{*+}\pi^-}|}{\sqrt{2}|A_{K^{*0}\pi^0}|} + \cos\Delta\Phi}\right) - \arctan\left(\frac{\sin\Delta\overline{\Phi}}{\frac{|\overline{A}_{K^{*-}\pi^+}|}{\sqrt{2}|\overline{A}_{\overline{K}^{*0}\pi^0}|} + \cos\Delta\overline{\Phi}}\right), \qquad (2.45)$$

is expressed only in terms of the amplitudes and phases measured in the $B^0 \to K^+\pi^-\pi^0$ Dalitz analysis. The algebraic relationship between the $B \to K^*\pi$ amplitudes and $\Phi_{\frac{3}{2}}$ in Eq. (2.44) is illustrated in Fig. 2.8.

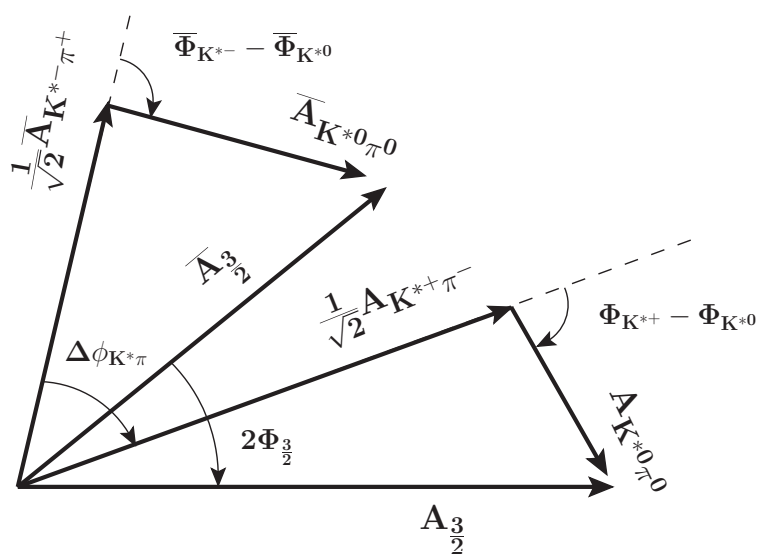

Figure 2.8: Isospin triangles and phase differences among $B^0 \to K^*\pi$ amplitudes.

Measurement of $\Phi_{\frac{3}{2}}$ in $B^0 \to \rho K$ decays

The isospin phase $\Phi_{\frac{3}{2}}$ may also be measured using the interference of $B^0 \to \rho K$ intermediate states, though the measurement here is somewhat more subtle since the $B^0 \to \rho^- K^+$ and $B^0 \to \rho^0 K^0$ amplitudes do not share a common final state. Expressing Eq. (2.18) in terms of the isobar amplitudes and phases gives

$$\overline{A}_{\frac{3}{2}} = \frac{1}{\sqrt{2}}|\overline{A}_{\rho^+K^-}|e^{i\overline{\Phi}_{\rho^+K^-}} + |\overline{A}_{\rho^0\overline{K}^0}|e^{i\overline{\Phi}_{\rho^0\overline{K}^0}}, \tag{2.46}$$
$$A_{\frac{3}{2}} = \frac{1}{\sqrt{2}}|A_{\rho^-K^+}|e^{i\Phi_{\rho^-K^+}} + |A_{\rho^0K^0}|e^{i\Phi_{\rho^0K^0}}.$$

Since $B^0 \to \rho^-K^+$ and $B^0 \to \rho^0K^0$ both interfere with $B^0 \to K^{*+}\pi^-$ we factor $\Phi_{K^{*+}\pi^-}$ from the expressions in Eq. 2.46. At this point, an argument identical to that used construct $\Phi_{\frac{3}{2}}$ from $B^0 \to K^*\pi$ amplitudes may be used to show

$$\Phi_{\frac{3}{2}} = \frac{1}{2}\Bigg(\arctan\left(\frac{|A_{\rho^-K^+}|\sin\Delta\Phi_{\rho^-K^+} + \sqrt{2}|A_{\rho^0K^0}|\sin\Delta\Phi_{\rho^0K^0}}{|A_{\rho^-K^+}|\cos\Delta\Phi_{\rho^-K^+} + \sqrt{2}|A_{\rho^0K^0}|\cos\Delta\Phi_{\rho^0K^0}}\right)$$
$$- \arctan\left(\frac{|\overline{A}_{\rho^+K^-}|\sin\Delta\overline{\Phi}_{\rho^+K^-} + \sqrt{2}|\overline{A}_{\rho^0\overline{K}^0}|\sin\Delta\overline{\Phi}_{\rho^0\overline{K}^0}}{|\overline{A}_{\rho^+K^-}|\cos\Delta\overline{\Phi}_{\rho^+K^-} + \sqrt{2}|\overline{A}_{\rho^0\overline{K}^0}|\cos\Delta\overline{\Phi}_{\rho^0\overline{K}^0}}\right) - \Delta\phi_{K^*\pi}\Bigg), \tag{2.47}$$

where $\Delta\Phi_{\rho^-K^+} = \Phi_{\rho^-K^+} - \Phi_{K^{*+}\pi^-}$, $\Delta\overline{\Phi}_{\rho^+K^-} = \overline{\Phi}_{\rho^+K^-} - \overline{\Phi}_{K^{*-}\pi^+}$, $\Delta\Phi_{\rho^0K^0} = \Phi_{\rho^0K^0} - \Phi_{K^{*+}\pi^-}$, and $\Delta\overline{\Phi}_{\rho^0\overline{K}^0} = \overline{\Phi}_{\rho^0\overline{K}^0} - \overline{\Phi}_{K^{*-}\pi^+}$. Unlike the expression of $\Phi_{\frac{3}{2}}$ in terms of $B^0 \to K^*\pi$ amplitudes, expressions involving amplitudes measured in $B^0 \to K^+\pi^-\pi^0$ and $B^0 \to K_s\pi^+\pi^-$ cannot be easily isolated in Eq. (2.47). Measuring $\Phi_{\frac{3}{2}}$ in this way will require simultaneous knowledge of the correlations among the isobar amplitudes in both the $B^0 \to K^+\pi^-\pi^0$ and $B^0 \to K_s\pi^+\pi^-$ Dalitz analyses.

Chapter 3

PEP-II and the *BABAR* Detector

In this section we describe the PEP-II accelerator and the *BABAR* detector comprising the SLAC B factory. As discussed in Section 2.2 the $\Upsilon(4S)$ resonance decays almost exclusively to $B^0, \overline{B}^0$ and B^+B^- mesons whose decays can in turn be used to study CP violation. The goal of the PEP-II accelerator is to supply e^+, e^- beams at the $\Upsilon(4S)$ resonance with as high a luminosity as possible. The *BABAR* detector is designed to identify and reconstruct the decays of the resulting B mesons with both high efficiency and accuracy. The content of this section is described in detail in [28].

3.1 The PEP-II Accelerator

The PEP-II storage rings are supplied with electrons and positrons (e^+, e^-) from the 3 km long Stanford Linear Accelerator (linac). Electrons are generated from a thermionic cathode gun and are accelerated to an energy of 9 GeV via a process designed to reduce their emittance. One third of the electron bunches emitted from the gun are diverted to a tungsten target where pairs of electrons and positrons are produced. The positrons are filtered from the electrons, returned to the beginning of the linac, and accelerated to 3.1 GeV. The 9 GeV electron beam is transported to the high energy storage ring (HER) while 3.1 GeV positrons are stored in the low energy ring (LER) of PEP-II. The e^+, e^- beams are collided with each other at an interaction region (IR) surrounded by the *BABAR* detector.

The 9 GeV electron and 3.1 GeV positron beams collide with a center-of-mass (c.m.) energy of 10.58 GeV, the mass of the $\Upsilon(4S)$ resonance (*on-peak*). The asymmetric energy of the beams results in a Lorentz boost $\beta\gamma = 0.56$ to the $\Upsilon(4S)$ resonance, making measurements of the relative lifetimes of the short lived $B^0, \overline{B}^0$ mesons possible. Measurements of the relative lifetimes of $B^0, \overline{B}^0$ mesons where one is reconstructed as a CP eigenstate and the other as a tagged flavor eigenstate permit the measurement of the time dependent CP asymmetry discussed in Section 2.3. The design of the *BABAR* detector is optimized with the asymmetric production of B mesons in mind. Approximately 10% of the data collected by *BABAR* are at energies 40 MeV below the $\Upsilon(4S)$ resonance (*off-peak*) so that samples of $e^+e^- \rightarrow q\overline{q}(q = u, d, s)$ background events can be studied independently of samples containing B mesons.

The term B factory implies that PEP-II is able to supply steady beams at high luminosity in order to acquire the statistics necessary to study rare CP-violating decay processes. This requirement has led to a design with high beam currents (or many bunches) of electrons (positrons) circulating in the HER (LER). The principle radio frequency (RF) of the accelerator is 476 MHz, but due to the need to avoid parasitic crossings of the beams away from the IR only every other bucket is filled. This results in a bunch spacing of 4 ns. The need to maintain stability of the closely spaced bunches in each beam has necessitated that the higher order RF modes in the cavities be damped by wave guides terminating in ferrite loads. In addition to this a feedback system detects the phase error of each of 1600 bunches with respect to the master RF oscillator and applies a signal which corrects for their positions and energies. Finally, the need to refill the storage rings, which originally required a 6 minute interruption in data collection every hour has been overcome using a continuous (*trickle*) injection scheme. This permits the luminosity to be maintained at its peak value for long periods of time without the interuption of data collection. The efforts of the PEP-II accelerator group have been responsible for supplying the high luminosities (up to $1.5 \times 10^{34}/\text{cm}^2/\text{s}$) and subsequently large dataset (See Table 3.2) without which this analysis would not be possible.

3.2 The *BABAR* Detector

BABAR is a general purpose particle detector optimized for the study of CP-violation in B meson decays. The detector is designed around a solenoidal magnetic field geometry and is optimized to measure the properties of particles resulting from the asymmetric collision of e^+e^- beams in the laboratory frame. The small branching fraction of B mesons to CP eigenstates in the presence of significant continuum backgrounds places the following requirements on the detector design:

- Large acceptance of particles down to small angles relative to the boost direction, necessitating an asymmetric design of detector elements.
- Excellent reconstruction efficiency for both charged and neutral particles.
- Very good energy and momentum resolution for all particles in order to discriminate B meson signal decays from the continuum background. Dalitz analyses require good energy and momentum resolution in order to accurately reconstruct the phase space of B meson decays.
- Excellent vertex resolution, both parallel and transverse to the beam axis.
- Efficient and reliable identification of particles resulting from B meson decays. Especially important in this analysis is the identification of charged K (kaon) and π (pion) mesons.
- A reliable trigger system capable of selecting events of interest with high efficiency while rejecting background.

The detector subsystems relevant to this analysis ordered from the interior to exterior of the *BABAR* experiment are as follows:

- The silicon vertex tracker (SVT) consists of five layers of double-sided silicon strip detectors used to precisely reconstruct the verticies of B meson decays. The SVT additionally provides some measurement of the ionization energy loss, dE/dx used in particle identification.

- The drift chamber (DCH) is a multi-wire proportional chamber used to measure the momenta of charged particles in the solenoidal magnetic field. The DCH also provides a measurement of dE/dx used in particle identification.

- The detector of internally reflected Cherenkov light (DIRC) provides a measurement of the velocities of charged particles from the measured angle of emitted Cherenkov light in a fused Silica bar. This novel subsystem permits discrimination between kaon and pion mesons from momenta of 500 MeV/c up to the kinematic limit of 4.5 GeV/c. Accurate kaon and pion identification is crucial to this analysis.

- The electro-magnetic calorimeter (ECAL) consists of CsI scintillators measuring the energy of ionizing radiation. The ECAL additionally provides measurements of the position of neutral pions and photons.

- The instrumented flux return (IFR) consists of resistive plate chambers (RPCs) used to identify muons and other long-lived particles. The IFR is described in detail in [28].

A schematic of the *BABAR* detector is shown in Fig. 3.1 and a detailed description of the detector subsystems relevant to this analysis are included in the following sections.

The Super Conducting Solenoid

The measurement of the momenta of charged particles is facilitated by a 1.5T magnetic field in which the particles are bent. The solenoidal field is supplied by superconducting niobium-titanium filaments wound into strands and finally into cables measuring a total 10.3 km in length. The super conductor is cooled by Liquid Helium circulated in channels welded to the support structure of the solenoid. The longitudinal component of the field is uniform to within 2.5% and the azimuthal component is not greater than 1mT inside the tracking volume.

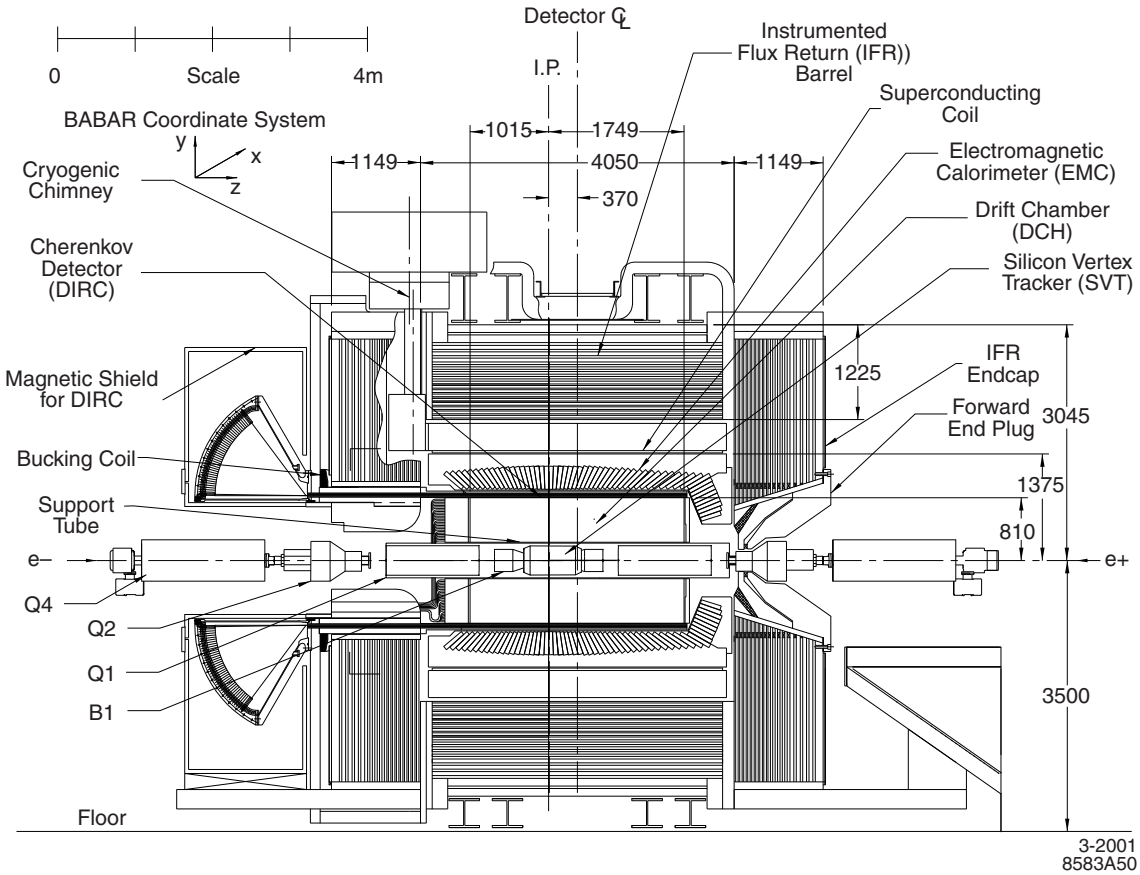

Figure 3.1: Longitudinal cross section of the *BABAR* detector. The z-axis coincides with the beam axis. The positive y-axis points upward while the positive x-axis points toward the center of the PEP-II rings. ϕ is the angle in the x-y plane and θ is the angle in the z-y plane. Dimensions are in mm.

3.2.1 Silicon Vertex Tracker

The SVT provides precise measurements of charged particle trajectories (tracks) and the decay verticies of B mesons close to the IR. The SVT additionally provides some amount of particle identification via the measurement of dE/dx. The SVT provides this information by measuring the charge taken from (deposited on) p^+ (n^+) type strips on a 300μ thick n-type substrate due to the creation of electron-hole pairs from the passage of ionizing radiation. The p^+ and n^+ type strips are located on opposite sides of the substrate and are oriented orthogonally to each other. The ϕ strips are

oriented parallel to the beam direction while the z strips are transverse to the beam direction. The strips are spaced between $10 - 15\mu m$ (inner layers) and $40\mu m$ (outer layers) apart on the substrate in order to provide the vertexing resolution required for CP asymmetry measurements in B decays.

Individual double sided strip detectors are arranged in 5 layers around the beam axis. The inner 3 layers are relatively close to the beam pipe and are designed to provide the precise vertexing measurements necessary to study CP asymmetry in B meson decays. The position information from the outer 2 layers is used to reconstruct the tracks of particles with low momenta transverse to the beam (low p_t). The tracking information from the outer layers is also combined with that from the DCH to improve overall track reconstruction. The SVT covers 90% of the total solid angle in the c.m. frame while corresponding to only 4% of a radiation length of traversed material. Transverse and longitudinal cross sections of the SVT are shown in Fig. 3.2 and Fig. 3.3.

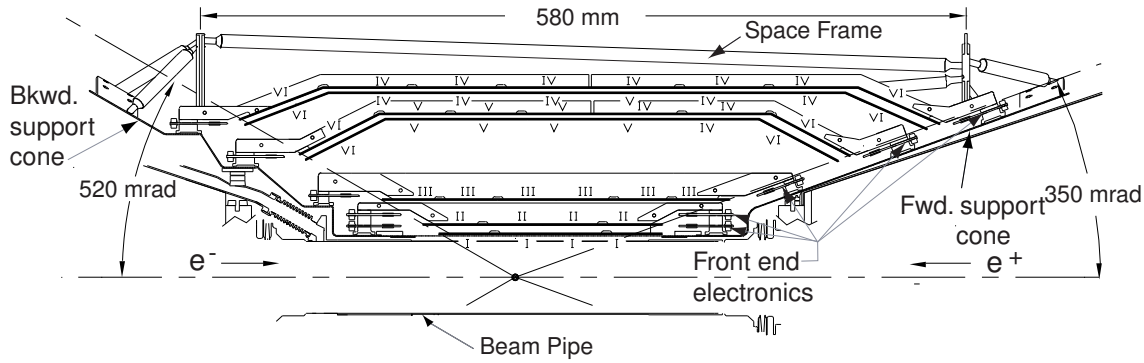

Figure 3.2: Longitudinal cross section illustrating the z coverage of the SVT.

The SVT is read out by a custom IC, the ATOM (A Time-Over-Threshold Machine). Charge pulse signals are readout from the SVT and sent to a programmable threshold comparator which records the width of the pulse over threshold (Time-Over-Threshold or ToT) in a circular memory buffer. Pulses are sampled at a rate of 15Mhz. The ToT, time and strip address are readout upon receipt of the Level 1

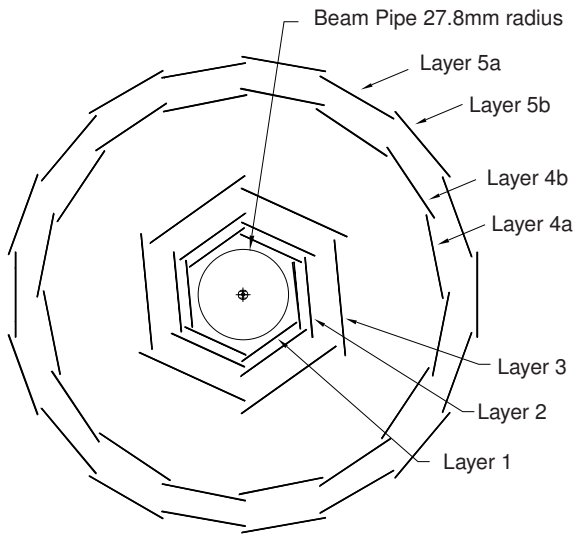

Figure 3.3: Transverse cross section illustrating the ϕ coverage of the SVT.

accept command from the data acquisition system.

In order to accurately reconstruct the tracks of charged particles the 340 individual strip sensors comprising the SVT must be aligned relative to each other. The local alignment of the sensors is performed with a sample of $e^+e^- \rightarrow \mu^+\mu^-$ events and cosmic muons. Tracks from these events are fit using only the hit information from the SVT. These hits and associated tracks are then used to fit for the most likely value of the position and orientation of each sensor. The local alignment is relatively stable and has been performed only rarely. Once the local alignment is complete the SVT must also be globally aligned relative to the DCH since it is not structurally supported by the rest of the *BABAR* detector. The global alignment is performed by minimizing the difference between track parameters fit with only hits from the SVT and DCH separately. Diurnal fluctuations of order .1mm in the relative position of the SVT and DCH require the global alignment to be performed every 2-3 hours.

The resolution of the SVT is determined by measuring the distance between the SVT hits used to reconstruct a given track and the track trajectory (in the plane of the sensor) as determined by a fit to hits recorded in both the SVT and DCH. The z and ϕ resolutions for track hits as a function of incident angle θ are shown in Fig. 3.4. The measured resolution meets the requirements of CP violation studies

in B decays. The ToT measurement may be used to obtain the pulse height in charge from a look-up table of measured pulse heights. The pulse height directly corresponds to the ionization energy loss dE/dx and provides a 2σ separation between kaons and pions up to 500 MeV/c and between kaons and protons above 1 GeV/c.

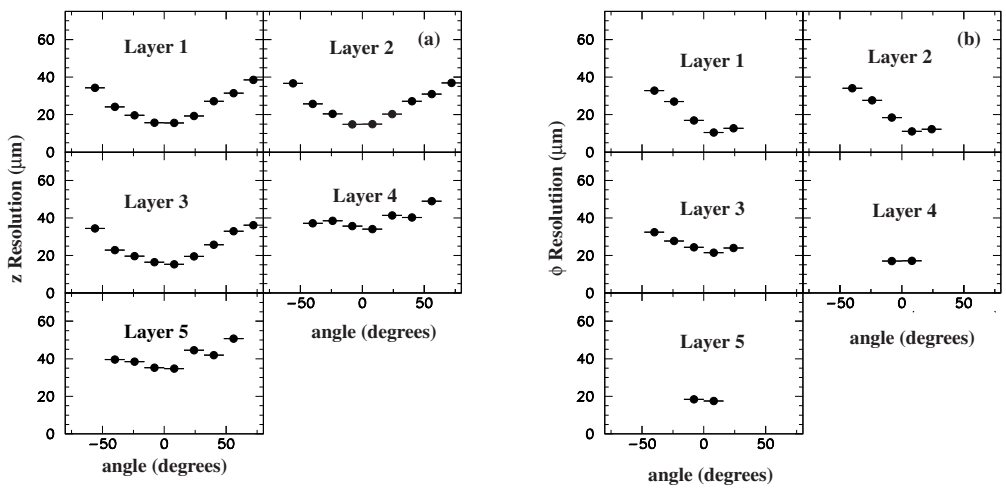

Figure 3.4: Hit resolution of the layers in the SVT. The z resolution is shown (right) along with the ϕ resolution (left) in μm.

3.2.2 Drift Chamber

The DCH is a multi-wire proportional chamber designed to provide precise measurements of the momenta of charged particles in addition to particle identification from measurements of dE/dx. The DCH measures the trajectory of charged particles by the ionization of an inert gas mixture as the particle passes through the detector. The ionized electrons from the gas drift towards the sense wires in the chamber held at high voltage, and as they are accelerated ionize other molecules of gas producing a shower of negative charge deposited on the sense wire. The sense wires are surrounded by grounded field wires in a hexagonal pattern which attract the positively ionized gas molecules produced in the shower. As the shower propagates toward the wire the electrons are accelerated over increasingly small potential differences so that the average potential drop of an electron is only 50V while the sense wire is held at 1960V. Conversely the positive ions in the shower are accelerated over increasingly large potential differences (up to the sense wire potential), so that most of the current read out from sense wire is induced from the motion of the positive charges. The width of the current pulse is a measure of the position of charged particle as it passed through the drift cell while the integral (total charge induced on the wire) is a measure of the ionization energy loss, dE/dx. A longitudinal cross section of the DCH is shown in Fig. 3.5. A transverse cross section illustrating the arrangement of hexagonal drift cells is shown in Fig. 3.6.

The *BABAR* DCH uses a helium:isobutane mixture in an $80:20$ ratio. This choice of gas and low mass aluminum field wires results in a contribution of less than .2% of a radiation length of material. The hexagonal drift cells are 11.9 and 19 mm along the radial and azimuthal directions respectively, as shown in Fig. 3.6. The DCH consists of 7104 such cells arranged in 40 clyindrical layers. The layers are grouped into 10 superlayers where two of the 4 layers in each superlayer are set at small stereo angles relative to the other two axial layers. This arrangement permits the measurement of both the z and ϕ trajectories of charged particles. The signals from the sense wires are read out by a custom amplifier IC producing a discriminator output output signal for the drift time and a shaped analog signal for the measurement of dE/dx.

Samples of cosmic muons and $e^+e^- \rightarrow e^+e^-, \mu^+\mu^-$ events are used to calculate

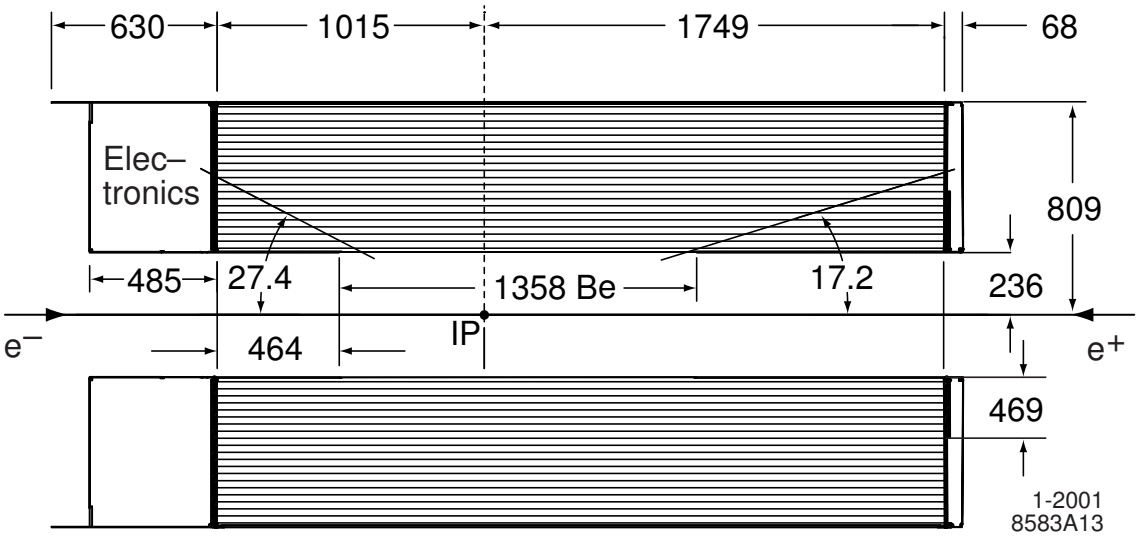

Figure 3.5: Longitudinal cross section of the DCH. Dimensions are in mm.

isochrones (distances of equal drift time) from which the drift time to distance relation is determined Fig. 3.7. The measurement of dE/dx as a function of momentum is shown in Fig. 3.8 with Bethe-Bloch curves for particles of different masses superimposed. The dE/dx resolution, also shown in Fig. 3.8, is calculated for a sample of $e^+e^- \to e^+e^-$ (Bhabha) events and is 7.5%.

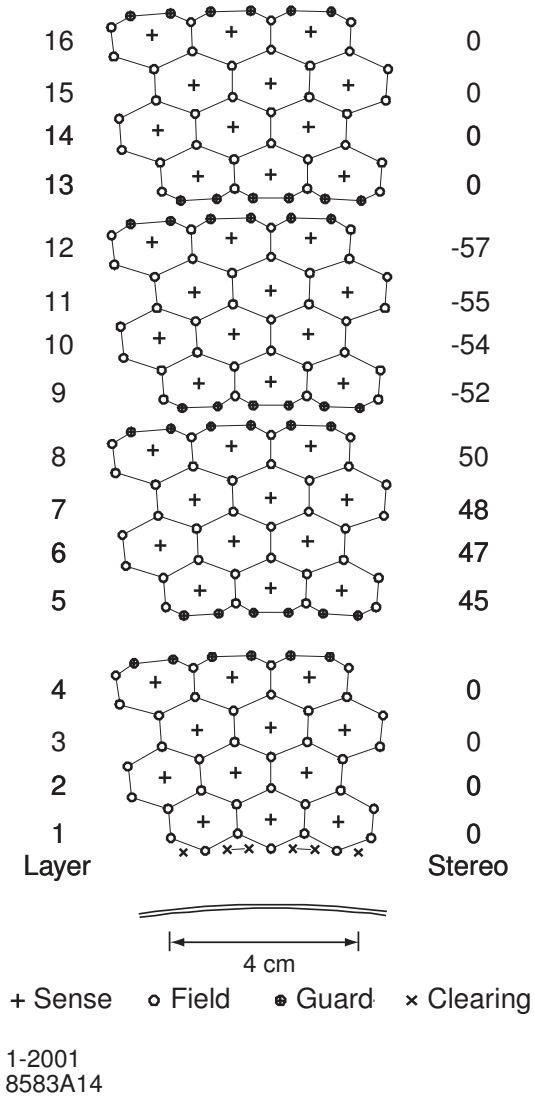

Figure 3.6: Drift cells for the four innermost super-layers. Guard wires are held at an intermediate potential (340 V) to keep showers contained within the cells of a given layer.

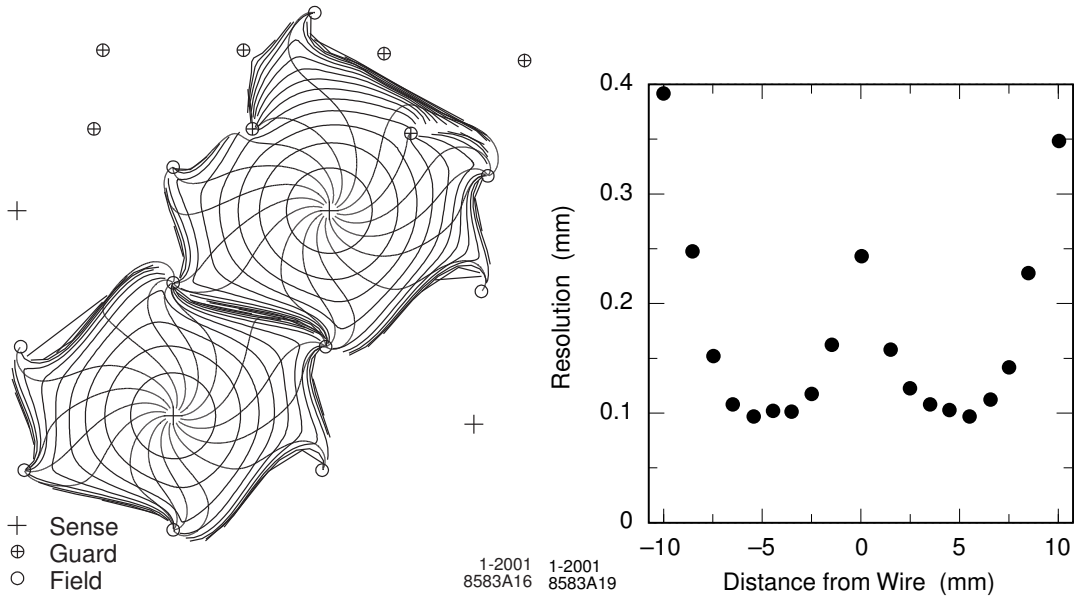

Figure 3.7: Drift cell isochrones spaced by 100ns and shower trajectories (left). Position resolution in the DCH as function of drift distance (right).

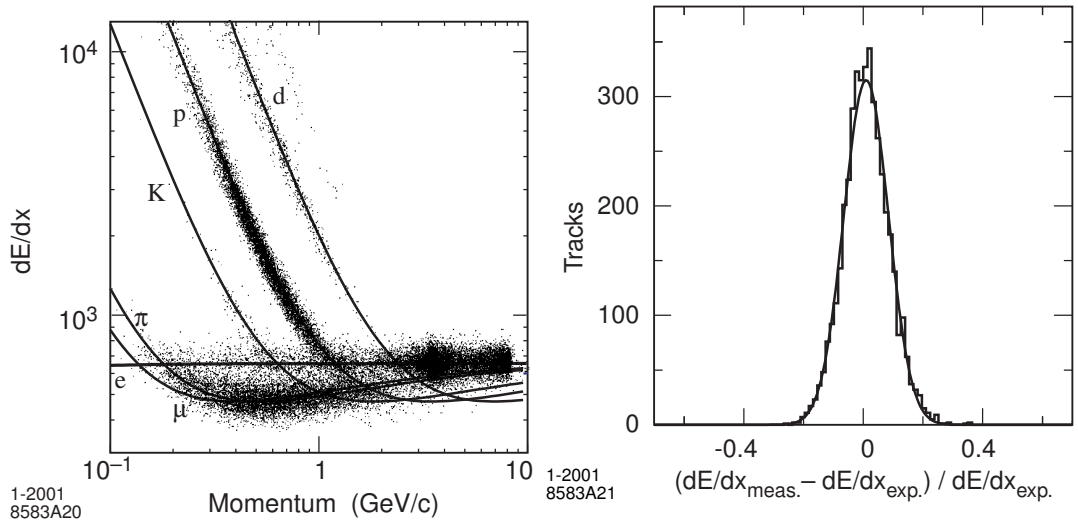

Figure 3.8: dE/dx as a function of track momentum in the DCH with Bethe-Bloch predictions overlaid (left). Difference between measured and expected dE/dx for Bhabha events (right). The Gaussian fit has a width of 7.5%.

The drift distance resolution obtained in Fig. 3.7 permits the trajectory of charged particles with momenta transverse to the magnetic field to be measured with high precision. The track position measurements (z,ϕ) near the IP are dominated by the SVT while the p_t measurement is dominated by the DCH drift distance resolution. The resolution of p_t for cosmic muons is well described by a linear function:

$$\frac{\sigma_{p_t}}{p_t} = (0.13 \pm .01)\%\ p_t + (0.45 \pm 0.03)\%. \tag{3.1}$$

The momentum resolution of cosmic muons and the invariant mass resolution of $J/\psi \rightarrow \mu^+\mu^-$ decays from $B\overline{B}$ events are shown in Fig. 3.9. Good momentum resolution is required to accurately reconstruct the phase space of B decays (Dalitz plot) and is extremely important in this analysis.

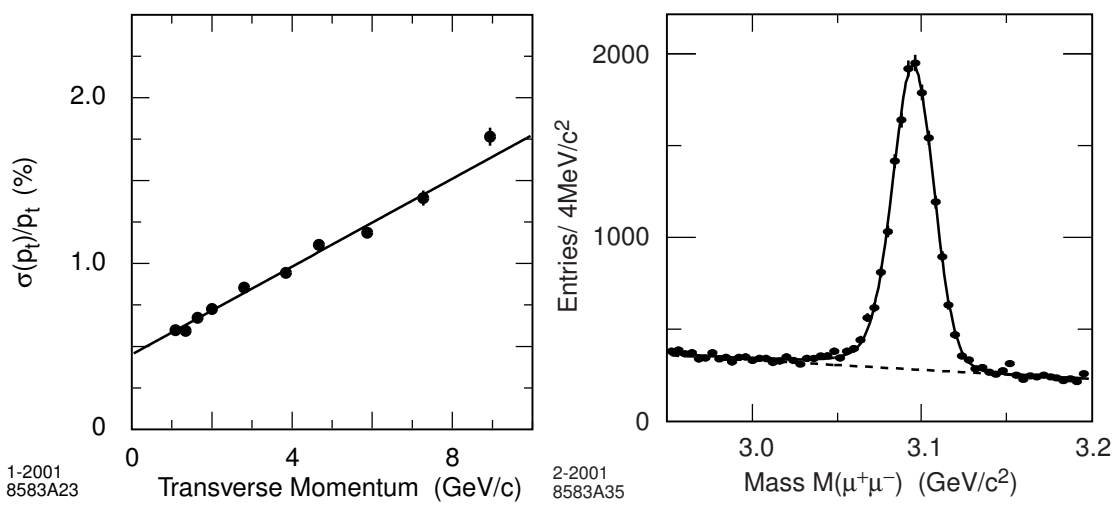

Figure 3.9: p_t resolution from cosmic events (left). Reconstructed J/ψ mass from muons (right).

3.2.3 Detector of Internally Reflected Cherenkov Light

Charged particles of momenta greater than 700 MeV/c are identified in the *BABAR* experiment by a novel device known as the DIRC. The DIRC exploits the fact that charged particles traveling faster than the local phase velocity of light radiate photons (Cherenkov Light) at an angle θ_c relative to the momentum of the particle. The

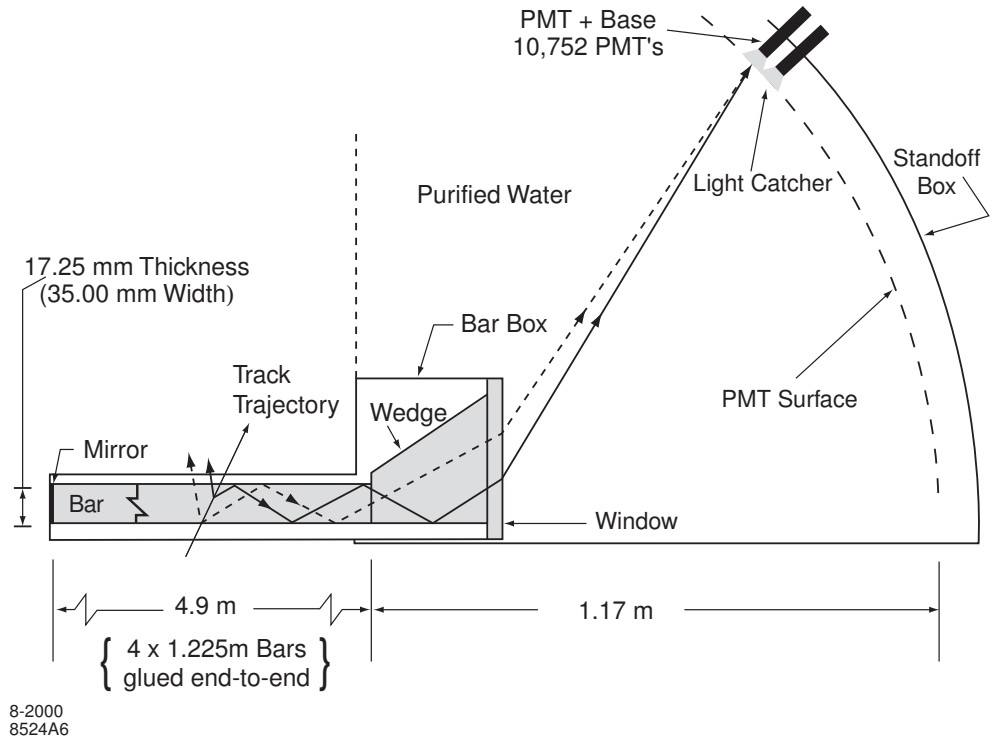

Figure 3.10: Schematic of the DIRC and radiator bar.

Cherenkov angle of emitted photons in a medium of index of refraction n for a particle of velocity v is given by

$$\cos\theta_c = \frac{1}{n\beta}, \text{ where } \beta = \frac{v}{c}. \tag{3.2}$$

The DIRC consists of long thin bars of fused silica ($n = 1.473$) in which charged particles emit Cherenkov light. For relativistic particles ($\beta \approx 1$) some photons will always lie within the incident angle of internal reflection for fused silica and be transported to either end of the silica bars. Photons propagate through the silica until they reach the end of the bar where they enter a water-filled expansion called the standoff box. The standoff box exists to measure the Cherenkov angle, θ_c projected over a long distance. Water is chosen to fill this distance since it has an index of refraction close to that of fused silica and is readily available. A mirror is placed at the end opposite the standoff box to collect light internally reflected toward the opposite end of the

detector. The end of the standoff box is densely packed with photomultiplier tubes (PMTs) which record the Cherenkov angle modified by refraction at the water-silica exit boundary. Signals from the PMTs are amplified by an analog IC, and a digital pulse timed with the peak of the PMT pulse is used to record the arrival time of each Cherenkov photon. A schematic of the DIRC is shown in Fig. 3.10.

The measured Cherenkov angle as a function of momentum for charged tracks is shown in Fig. 3.11. The efficiency for correctly identifying a kaon traversing the DIRC and the probability of mis-identifying a pion as a kaon as a function of momentum are shown in Fig. 3.12. The measurements of kaon efficiency and kaon-pion mis-ID are determined from $D^0 \to K^-\pi^+$ decays, kinematically selected from inclusive D^* events. This selection guarantees that the sign of the charged particle correctly identifies it as a kaon or pion, permitting the mis-ID and efficiency to be measured.

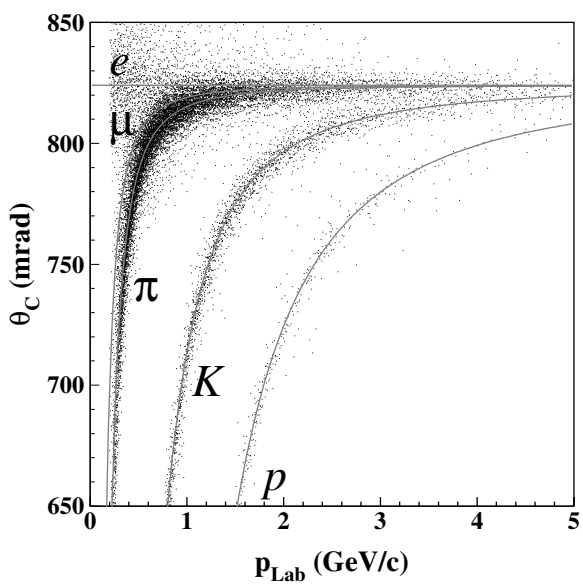

Figure 3.11: Cherenkov angle as a function of track momentum. Predictions for particles of different masses are overlaid.

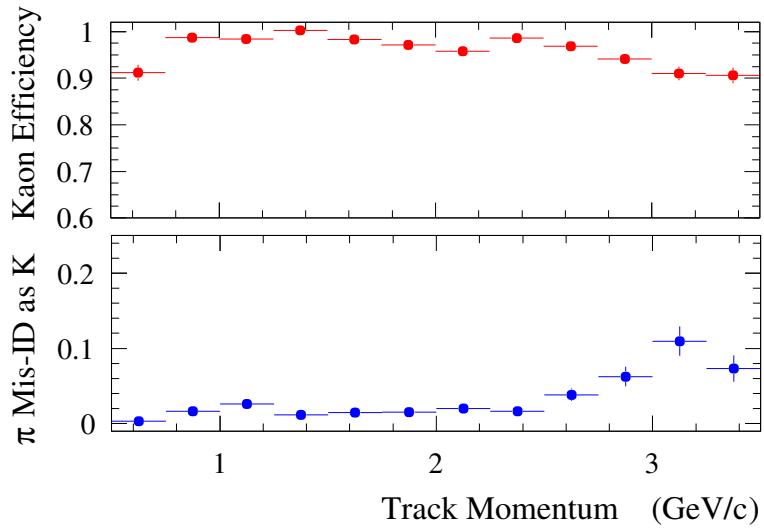

Figure 3.12: Efficiency and mis-ID probability for charged kaons as a function of momentum determined from $D^0 \to K^-\pi^+$ decays.

3.2.4 Electromagnetic Calorimeter

The EMC is designed to measure the energy of particles by producing an electromagnetic shower from their passage through a scintillator. Ideally, all of the energy of a particle should be converted to a shower of photons from this process. The *BABAR* EMC consists of an array of 6580 finely segmented thallium doped cesium iodide (CsI(Tl)) crystals. These crystals permit the efficient measurement of electromagnetic showers with high resolution over the range from 20 MeV to 9 GeV. The fine segmentation of the calorimeter permits the accurate measurement of the angular positions (θ, ϕ) of photons from the decays of neutral particles π^0, η. The accurate reconstruction of neutral particles is critical for the study of rare B decays containing one or more neutral mesons (e.g. $B^0 \to K^+\pi^-\pi^0$).

The CsI(Tl) crystals are arranged in a cylindrical barrel and conical endcap. The full coverage of this system corresponds to 90% of the total solid-angle in the c.m. frame. Individual crystals are machined into trapezoids measuring 4.7×4.7 cm^2 on the front face and 6.1×6.0 cm^2 on the back. The crystals range from 29.6 cm to 32.4 cm in length. CsI(Tl) has a high light yield producing $50,000$ photons per MeV of particle energy. Scintillation photons produced in the crystals are detected with

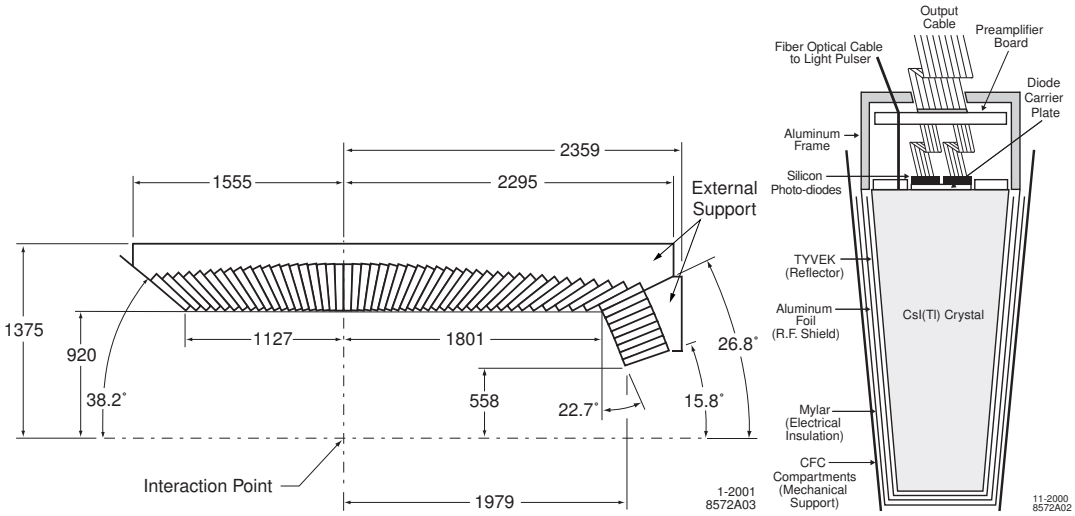

Figure 3.13: Longitudinal cross section of the EMC (left). Schematic of a wrapped CsI(Tl) crystal and read out package (right). Dimensions are in mm.

two silicon PIN diodes glued to the back of each crystal. A diagram illustrating the arrangement of crystals in EMC and read out of individual crystals is shown in Fig. 3.13.

The photo-electric charge yield of the PIN diodes is converted into a measurement of energy by calibrating the EMC with two sources at opposite ends of the energy sensitivity range. A 6.13 MeV photon source, radioactive Fluorinert, is used to calibrate the EMC at low energy. The known relationship between the energy and polar angle of Bhabha events is used to calibrate the EMC at high energy ($3 - 9\,\mathrm{GeV}$). Corrections to the calibrated energy due to imperfect containment and absorption of the shower are derived at low energies ($E < .8\,\mathrm{GeV}$) from π^0 decays, constraining the two-photon mass to be equal to the nominal π^0 mass, and from $e^+e^- \to e^+e^-\gamma$ events at high energies ($.8 < E < 9\,\mathrm{GeV}$). A correction applied to Monte Carlo simulations of the calorimeter response is developed from $e^+e^- \to \mu^+\mu^-\gamma$ events and is discussed in Appendix D.

The radioactive source, Bhabha events, and π^0 mass are also used to determine the resolution of the calorimeter. A fit to the energy dependence of the resolution in Fig. 3.14 gives

$$\frac{\sigma_E}{E} = \frac{(2.32 \pm .3)\%}{\sqrt[4]{E(\,\mathrm{GeV})}} \oplus (1.85 \pm .12)\%. \tag{3.3}$$

The two-photon invariant mass from π^0 and η decays is used to infer the energy dependence of the angular resolution shown in Fig. 3.14. The angular resolution as a function of energy is given by

$$\sigma_{\phi,\theta} = \frac{3.87 \pm 0.07}{\sqrt{E(\,\mathrm{GeV})}}\ \mathrm{mrad}. \tag{3.4}$$

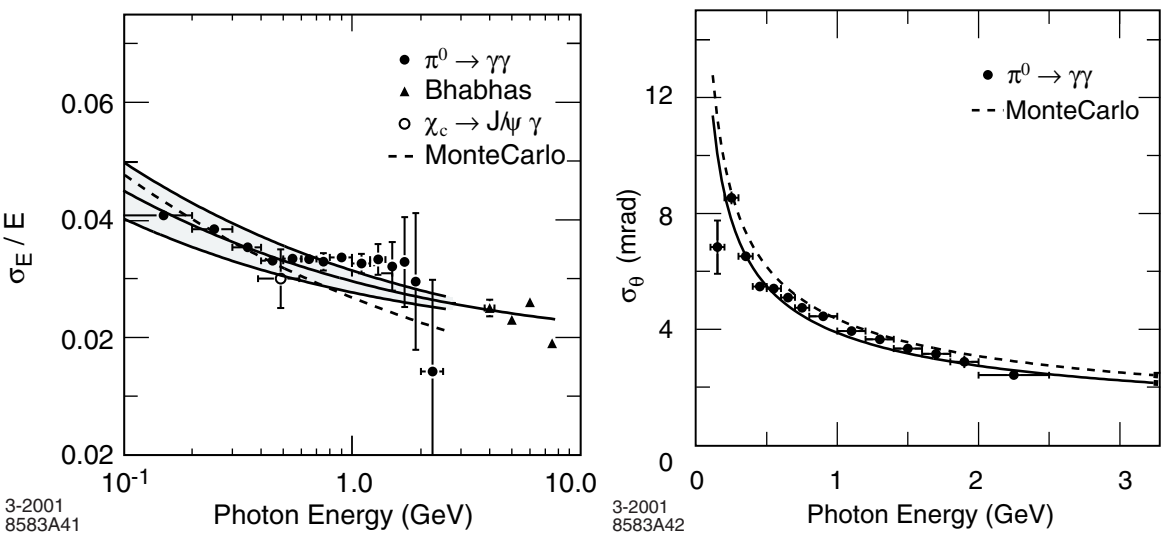

Figure 3.14: Energy resolution in the EMC for photons and electrons from various processes as a function of photon energy (left). Angular resolution of the EMC for photons from π^0 decays (right).

3.2.5 Trigger

In order to record events at the manageable rate of 120 Hz *BABAR* implements a trigger system designed to select events of interest with high efficiency while rejecting beam-induced background. Events are processed in a two tier trigger system consisting of a Level 1 (L1) hardware trigger followed by a Level 3 (L3) software trigger. The total trigger efficiency is greater than 99% for $B\overline{B}$ events and 95% for other $q\overline{q}$ (continuum)

events. Nominally, the L1 trigger reduces the 20 kHZ beam-induced background rate to an output rate of 1-5 kHz while the L3 performs a second stage rate reduction to 120 Hz. Approximately 75% of the events triggered by L3 are of physical interest while the remaining 25% are collected for the determination of luminosity, calibration and diagnostics.

Table 3.1: Cross-Sections, production and trigger rates for processes at the $\Upsilon(4S)$ resonance and luminosity of $3 \times 10^{33}\,\mathrm{cm}^{-2}s^{-1}$.

Event Type	Cross-Section (nb)	Production Rate (Hz)	L1 trigger Rate (Hz)
$b\overline{b}$	1.1	3.2	3.2
$u\overline{u}, d\overline{d}, c\overline{c}, s\overline{s}$	3.4	10.2	10.1
e^+e^-	53	159	156
$\mu^+\mu^-$	1.2	3.5	3.1
$\tau^+\tau^-$	0.9	2.8	2.4

The L1 consists of a drift chamber trigger (DCT) and calorimeter trigger (EMT) based on information from those sub-systems respectively. The DCT performs a fast reconstruction of tracks from drift times and hits in the DCH. The output of the DCT categorizes events by number and length of tracks in the event, in addition to the number of tracks above a high transverse momentum threshold ($p_t > 800\,\mathrm{MeV}/c$). The EMT divides the calorimeter into 280 towers reporting the position and energy in each tower summed for crystal energies greater than 20 MeV. Information from the DCT and EMT is sent to a global trigger every 134 ns identifying events of physical interest with specific triggers. Events which generate a L1 accept trigger are read out in full to an online computer farm where a more complete event reconstruction and analysis is performed (L3 trigger). The L3 executable takes on average 8.5 ms per event per farm computer to complete before it is finally written out or rejected.

3.2.6 The *BABAR* Data Set

The PEP-II B factory at SLAC recorded data from October 1999 to April 2008 divided into several periods of extended data collection known as Runs. The period of time in between Runs was typically used for maintenance and upgrades of the accelerator

and BABAR detector. The final Run period (Run 7) of data collection was used to explore other Υ resonances, besides the $\Upsilon(4S)$. This dissertation is based on the data collected in Runs 1-6. A summary of the data collected by the BABAR experiment is shown in Table 3.2, and a plot illustrating the luminosity delivered by PEP-II and recorded by BABAR as a function of time is shown in Fig. 3.15.

Table 3.2: Recorded Luminosity at the $\Upsilon(4S)$ resonance and corresponding number of $B\overline{B}$ pairs determined to a precision of 1.1%. Run 7 is not used in this dissertation is not reported.

Run	Dates	On-peak (fb^{-1})	Off-peak (fb^{-1})	$N_{B\overline{B}} \times 10^6$
1	Oct 1999-Oct 2000	20.4	2.6	22.4
2	Feb 2001-June 2002	61.1	6.9	67.4
3	Dec 2002-June 2003	32.3	2.47	35.56
4	Sep 2003-July 2004	100.3	10.1	110.45
5	Apr 2005-Aug 2006	133.3	14.5	147.2
6	Jan 2007-Sep 2007	66.1	4.6	71.4
Total	-	**413.4**	**41.2**	**454**

3.2.7 Monte Carlo Simulation

In addition to the recorded data, simulated events known as Monte Carlo (MC) are used to validate the analysis procedure and develop event selection criteria. MC is generated using Version 4 of the `GEANT` [29] program to simulate the propagation of particles in the detector given their known properties, so that the simulated events may be reconstructed and selected in an identical manner to data. This permits selection and reconstruction criteria to be developed so as to maximize the efficiency of correctly reconstructing signal events while minimizing backgrounds.

We generate large samples of $B^0 \to K^+\pi^-\pi^0$ decays with the model of interfering resonances described in Section 2.5 to both develop selection criteria and validate the analysis procedure. It is worth noting that the analysis software `RooThreeBodyDalitz`, shares the `EvtGen` package in common with the MC generator so that the means of generating the kinematic distributions of B decays and fitting them are identical.

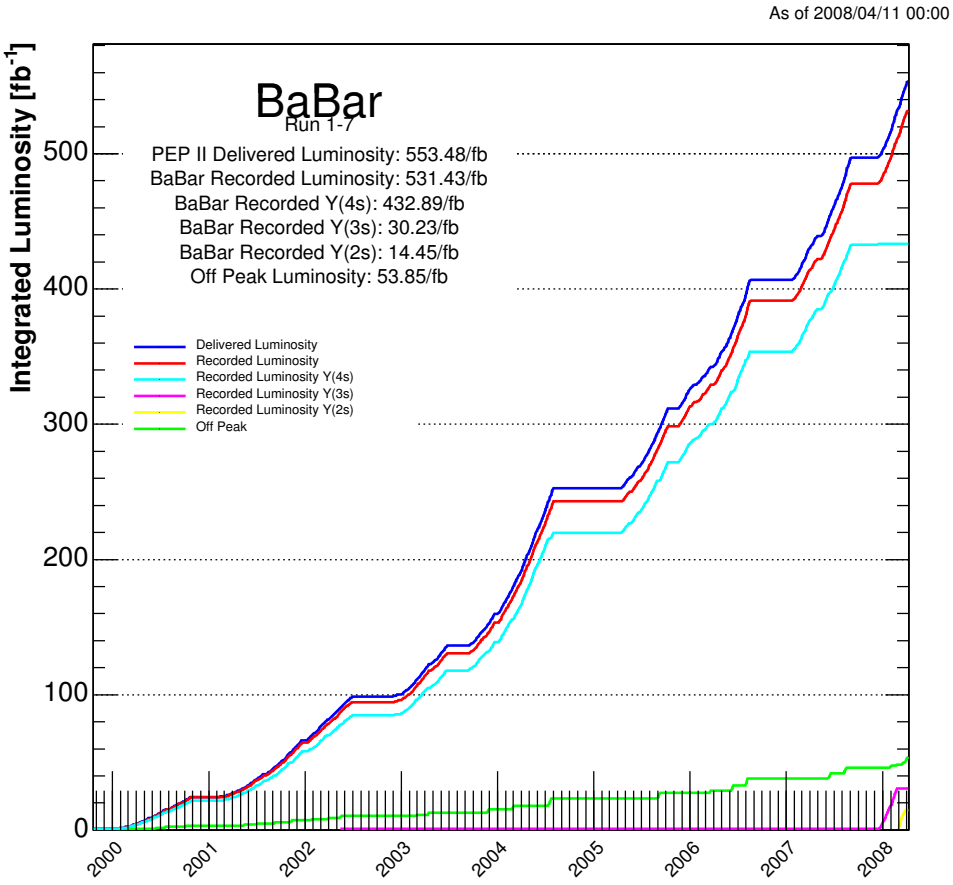

Figure 3.15: Luminosity delivered and recorded as a function of time.

This permits a robust validation of the analysis procedure by guaranteeing that the fitted distribution of decays is identical to the generated distribution.

Backgrounds are studied in a large sample of $B^0\overline{B}^0$ and B^+B^- simulated decays. Backgrounds contributing a large number of expected events are further studied in higher statistics samples of decays simulated with the specific background. These are listed in Table 4.3 along with the simulation production (SP) catalog number used to identify the collection of events.

Chapter 4

Dalitz Analysis of the Decay $B^0 \to K^+\pi^-\pi^0$

In this section the reconstruction and analysis of the phase space of the decay $B^0 \to K^+\pi^-\pi^0$ is presented using the *BABAR* dataset. The reconstruction and selection of $B^0 \to K^+\pi^-\pi^0$ decays is described in the first sections. The fit procedure used to exact the amplitudes and phases of the intermediate amplitudes contributing to the final state is described in the later half. This analysis is an update of the *BABAR* analysis presented in [30] including Runs 5, 6 of the *BABAR* dataset. The $B^0 \to K_s\pi^+\pi^-$ Dalitz analysis, also necessary to produce the constraint on the CKM triangle suggested in [15] is described in [31].

4.1 Event Selection

Hadronic *continuum* events produced via the non-resonant processes $e^+e^- \to q\overline{q}$ ($q = u, d, s, c$) at the $\Upsilon(4S)$ energy would overwhelm the number of resonantly produced B decays in the absence of measurable quantities capable of discriminating between events reconstructed from the two processes. In order to maximize the sensitivity of the analysis to the magnitudes and phases of the interfering amplitudes contributing to the final state, we develop a set of criteria that preferentially selects $B^0 \to K^+\pi^-\pi^0$ decays from the continuum background. The criteria should also limit the number

of events that are mis-reconstructed, both from other B decay modes, known as *B-backgrounds*, and from the signal decay process itself, known as *self cross-feed* (SCF). In this section we describe the process of event reconstruction and the selection criteria used in this analysis.

4.1.1 Skim Selection

Since it is impractical to apply a set of selection criteria to the entire *BABAR* dataset, a series of sub-sets have been created that loosely match the criteria of various B decays. These sub-sets are known as skims. We apply our selection criteria to events which have first passed the `BToCPP` skim, requiring events to contain three particles from lists of charged track and π^0 candidates. The $m_{\rm ES}$ (See Section 4.1.5) of the candidate is required to be greater than $5.2\,\mathrm{GeV}/c^2$ and the total energy of the candidate in the c.m. frame is required to be $4.99 < E^* < 5.59\,\mathrm{GeV}$. The skim passes nearly 100% of signal decays and yet comprises only about 2% of the total *BABAR* dataset. More stringent requirements of the particles used to reconstruct the B candidate are made after events pass the skim.

4.1.2 Charged Particle Selection and ID

The charged kaon and pion daughter particles are selected from lists of reconstructed particles meeting criteria that ensure the particle's momenta are well measured. We select charged tracks taken from the `GoodTracksLoose` list, which requires that tracks have, $100\,\mathrm{MeV}/c < p_t < 10\,\mathrm{GeV}/c$, $|z_0| < 10\,\mathrm{cm}$, $|d_0| < 1.5\,\mathrm{cm}$ and at least 12 hits in the DCH.

Measurements of dE/dx in both the DCH and SVT (See Fig. 3.8) in addition to the measurement of the Cherenkov angle in DIRC (See Fig. 3.11) are combined to produce a likelihood estimator for the probability of a charged particle to be a kaon, pion, or proton. We require that the kaons and pions used to reconstruct the $K^+\pi^-\pi^0$ final state pass the `KaonLHTight` and `PionLHTight` selectors respectively. The kaon selector requires that $L_K/(L_K + L_\pi) > .9$, $L_K/(L_K + L_p) > .2$ while the

pion selector requires $L_K/(L_K + L_\pi) < .5,\ L_p/(L_p + L_\pi) < .98$ [1] where L_K, L_π, L_p are the likelihoods for a particle to be a kaon, pion or proton respectively. The selectors also require that both the kaon and pion are not identified as electrons.

4.1.3 π^0 Selection

The π^0 is selected from the `pi0AllLoose` list, requiring the two-photon mass of candidates to be loosely consistent with the nominal π^0 mass, $100 < m_{\pi^0} < 160\,\mathrm{MeV}/c^2$ and a c.m. energy greater than 200 MeV. It is important to note that B candidates with a mis-reconstructed π^0 are a significant source of SCF events. In order to reduce the number of SCF candidates we additionally require

- The invariant mass of a π^0 candidate to be consistent with nominal π^0 mass at the level of 3σ, $|\frac{m_{\pi^0} - m_{\mathrm{PDG}}}{\sigma_{m_{\pi^0}}}| < 3$.
- The modulus of the cosine of the angle the decay photons make with the π^0 momentum vector, $|\cos\theta^*_{\pi^0}|$, to be less than 0.95.

4.1.4 B^0 Canidate Reconstruction

B^0 candidates are reconstructed by requiring that the K^+, π^- and π^0 originate from a common vertex within the beam spot. The 4-momenta of the K^+, π^- and π^0 are fit with this constraint, or vertexed, using the `TreeFitter` [32] algorithm given the mass hypothesis of the daughter particles. The 4-momenta are fit a second time with the additional constraint that that their invariant mass be consistent with the B mass. The mass constrained 4-momenta are necessary to ensure that particles occupy only physically allowed regions of the Dalitz plot, and are used to construct the Dalitz distribution of the B^0 decays.

It is important to note that the decay $B^0 \to K^+\pi^-\pi^0$ is flavor specific. The charge of the K or π determines the flavor of the B. This fact permits the flavor of the other B produced in the decay of the $\Upsilon(4S)$ to be used as additional input in the analysis. Events where the opposite B flavor has been reliably determined are less

[1] The selection cuts for particles of momenta greater than $2.5\,\mathrm{GeV}/c$ are functions of momentum.

likely to be either continuum background or SCF. A neural network is trained using a large sample of MC events with output into seven exclusive categories identifying the flavor of the B. In order of purity from highest to lowest these are: `Lepton, KaonI, KaonII, KaonPion, Pion, Other,` and `Notag`. The tagging categories identify the flavor of the B in decay processes involving leptons, charged kaons and pions or other charged particles whose sign indicates the B flavor. Each event is identified with the tagging category of the other B determined from the neural network.

4.1.5 Kinematic Variables

At the $\Upsilon(4S)$ resonance, B mesons are characterized by two nearly independent kinematic variables, the beam energy substituted mass $m_{\rm ES}$, and the energy difference between the reconstructed B and beam, ΔE:

$$m_{\rm ES} = \sqrt{(s/2 + \vec{p_0} \cdot \vec{p_B})^2/E_0^2 - p_B^2}, \tag{4.1}$$

$$\Delta E = E_B^* - \sqrt{s}/2, \tag{4.2}$$

where E and p are energy and momentum, the subscripts 0 and B refer to the e^+e^--beam system and the B candidate respectively; s is the square of the center-of-mass energy and the asterisk labels the c.m. frame. We require that $5.272 < m_{\rm ES} < 5.2875\,{\rm GeV}/c^2$.

In order to reliably fit the isobar amplitudes on the Dalitz plot it is important to minimize and correct for any correlations of these kinematic variables with the momenta of the daughter particles. The energy resolution of π^0 particles varies as a function of the π^0 energy (See Fig. 3.14) or equivalently, the $K^+\pi^-$ invariant mass, $m_{K^+\pi^-}$. This variation can be partially corrected by dividing ΔE by the per event error $\sigma_{\Delta E}$. Fig. 4.2 shows the $\Delta E/\sigma_{\Delta E}$ distributions for different bins of the Dalitz Plot.

The curves in Fig. 4.2 correspond to fits to the $\Delta E/\sigma_{\Delta E}$ distribution with a Gaussian and 1st order polynomial. The width of the Gaussian varies from .98 (high-energetic π^0's) to 1.18 (low-energetic π^0's). We account for this dependence by translating the

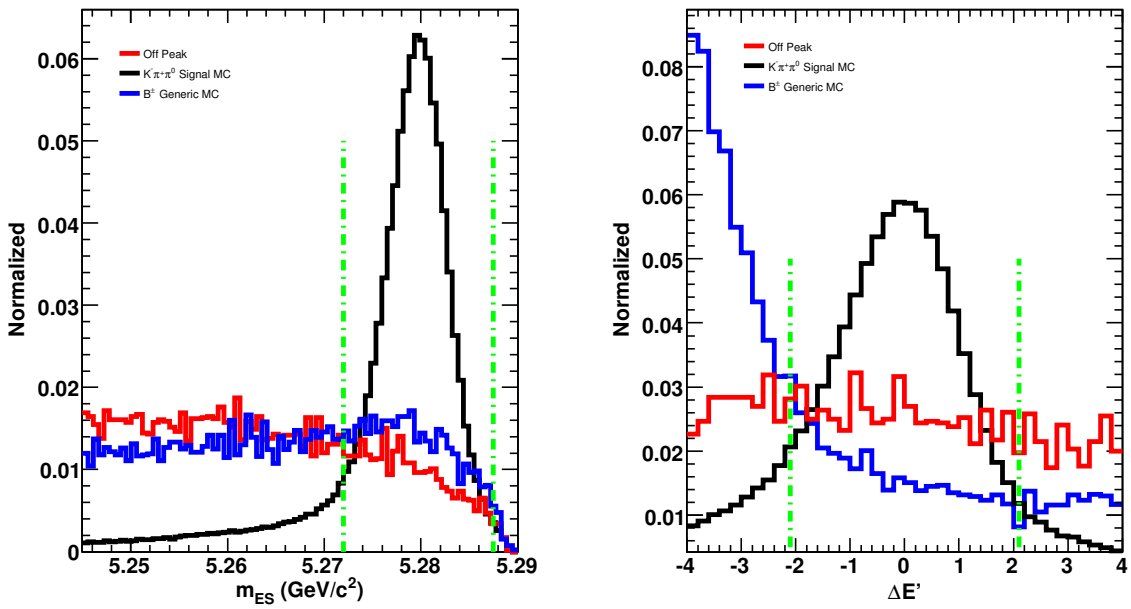

Figure 4.1: Distributions for $m_{\rm ES}$ (left) and $\Delta E'$ (right) for signal MC (black), charged B-background (blue) and off-peak data (red). The vertical green lines indicate the selection criteria. The distributions are normalized to have unit area.

mean and modulating the width of the distribution as 3rd order polynomial functions of $m^2_{K^+\pi^-}$. We introduce the dimensionless quantity $\Delta E'$:

$$\Delta E' = \frac{\dfrac{\Delta E}{\sigma \Delta E} + m_0 + m_1 x + m_2 x^2 + m_3 x^3}{w_0 + w_1 x + w_2 x^2 + w_3 x^3}\,, \tag{4.3}$$

where $x = m^2_{K^+\pi^-}$ and the coefficients, m_i, w_i are determined from fits to high statistics signal MC. We require $|\Delta E'| \leq 2.1$. The fitted values of m_i, w_i which minimize correlations with the Dalitz plot are shown in Table 4.1. Distributions of the kinematic variables $m_{\rm ES}$ and $\Delta E'$ are shown in Fig. 4.1.

4.1.6 Multivariate Continuum Suppression

To further enhance discrimination between signal and continuum, we train a neural network (NN) [33] with six discriminating variables:

- The angle between the B momentum and e^+ beam direction, $\theta_{B,z}$.

Table 4.1: Fitted values of m_i, w_i which minimize correlations of $\Delta E/\sigma_{\Delta E}$ with the Dalitz plot.

i	$m_i \times 10^{-3}$	$w_i \times 10^{-3}$
0	246.36	1055.09
1	−2.72968	6.85963
2	1.14497	0.658859
3	−0.047	−0.025

- The angle between the B thrust axis and e^+ beam direction, $\theta_{T,z}$ [2].
- The angle between the thrust axis of the rest of the event (ROE) and e^+ beam direction, $\theta_{\mathrm{ROE},z}$ [2].
- The Legendre moments L_0 and L_2 defined as

$$L_n = \sum_{i=\mathrm{ROE}} |\vec{p_i^*}| \times |\cos(\theta_i)|^n, \tag{4.4}$$

  where $\vec{p_i^*}$ is the momentum of a particle i, in the event whose angle with the B thrust axis is θ_i. The sum runs over all charged and neutral particles in the event except for those in the B candidate.
- The flight distance between the two B mesons scaled by the error, $\Delta z/\sigma_{\Delta z}$.

The Legendre moments and angles, $\theta_{B,z}$, $\theta_{T,z}$ and $\theta_{\mathrm{ROE},z}$ effectively discriminate signal from continuum since B mesons are produced nearly at rest in the c.m. frame, and consequently the angular distribution of its decay is relatively isotropic. Continuum events in contrast are relatively jet like. The variable $\Delta z/\sigma_{\Delta z}$, measures the characteristic life time of B mesons in the detector and has a relatively narrow distribution for continuum events as compared to B events. Since the selection variables must be uncorrelated with the Dalitz plot, the Dalitz positions of events are not used in the NN. Distributions for the training variables are shown in Fig. 4.3.

[2] The trust axis maximizes the projection of the longitudinal momenta of the particles in question.

The NN training has been performed using off-peak data and correctly reconstructed signal MC events. The $K^\pm$ candidates in the off-peak events are required to pass the `KLHTight` PID selector. The NN output distribution for truth matched signal events and off-peak data are plotted in Fig. 4.4, where the cut displayed is chosen both to enhance signal purity and ensure that a manageable number of events enter the ML fit. We require $0.6 < NN$ which removes 90% of the continuum background while keeping 81% of the signal.

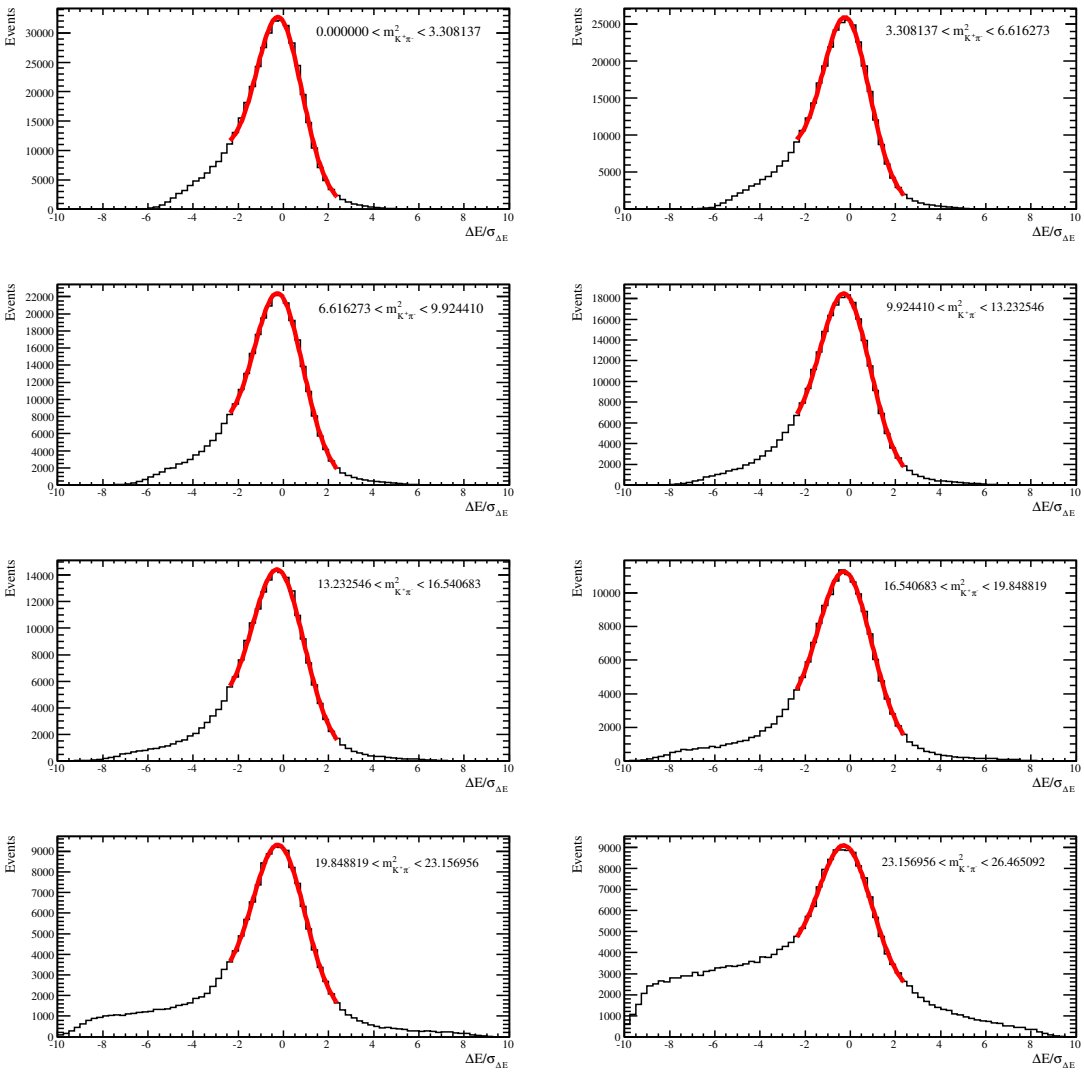

Figure 4.2: $\Delta E/\sigma_{\Delta E}$ distribution for correctly reconstructed MC events in different bins of $m^2_{K^+\pi^-}$ (estimator of the π^0 energy) fit with a Gaussian and a linear polynomial.

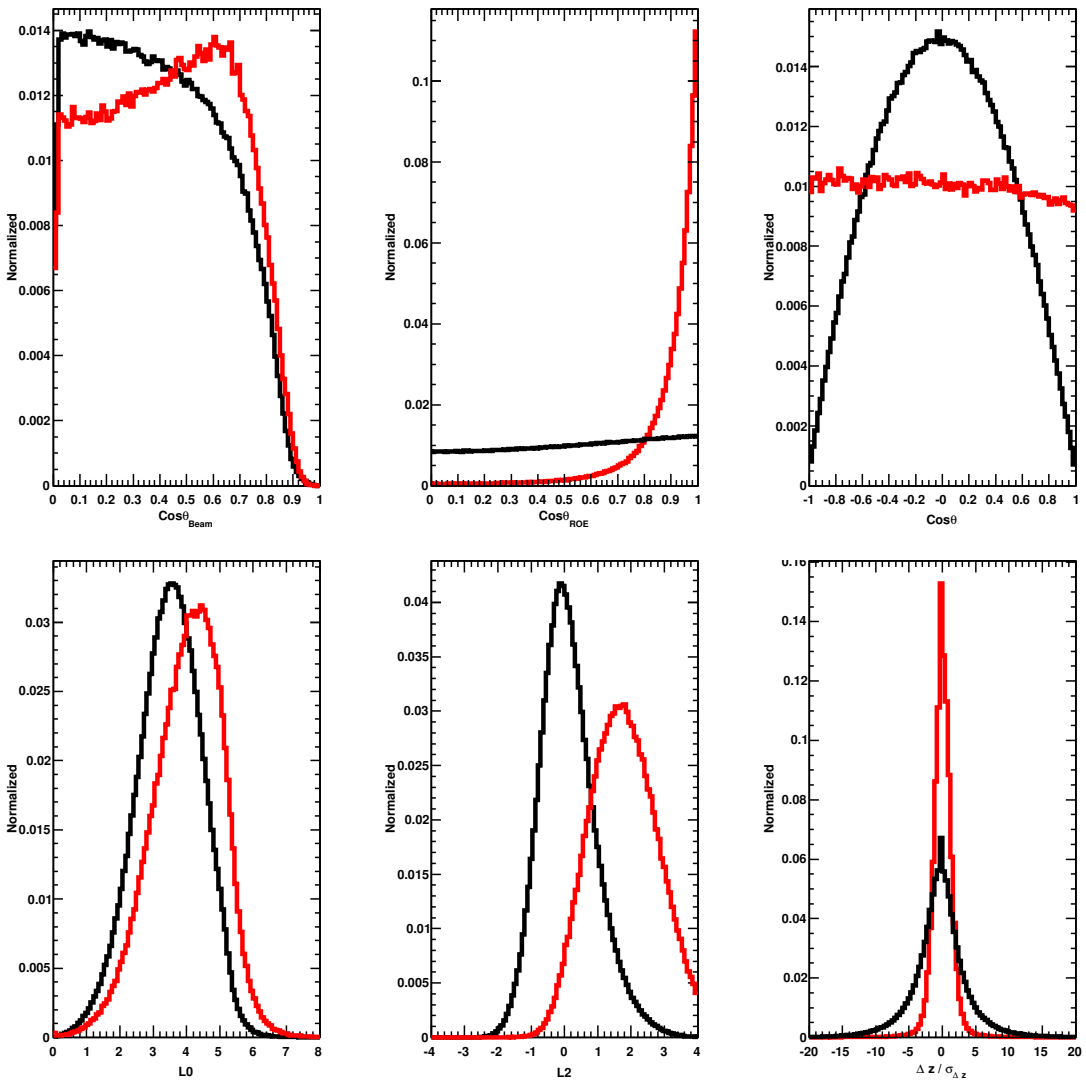

Figure 4.3: The distribution of $\cos\theta_{T,z}$ (upper left), $\cos\theta_{\mathrm{ROE},z}$ (upper middle), $\cos\theta_{B,z}$ (upper right) L_0 (lower left), L_2 (lower middle) and $\Delta z/\sigma_{\Delta z}$ (lower right). MC signal events are shown in black, and off-peak data are shown in red.

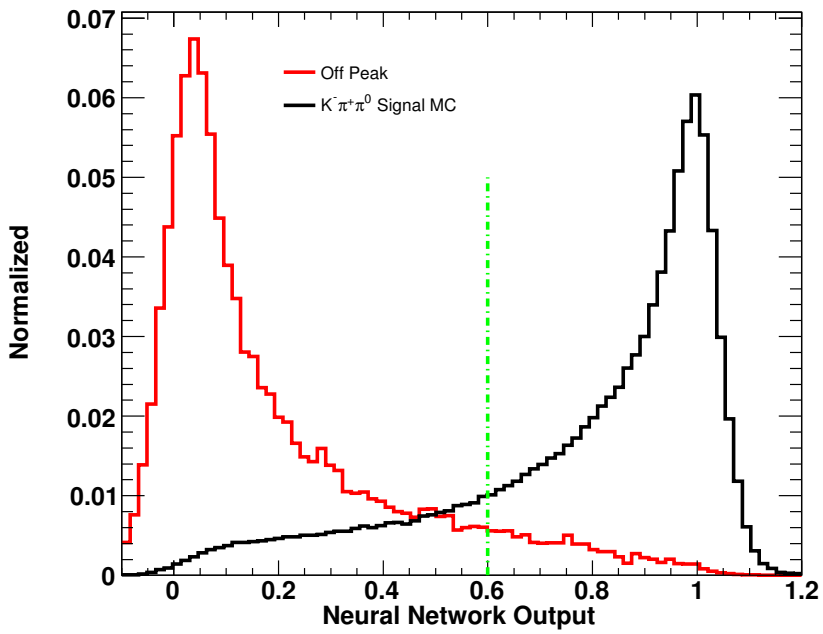

Figure 4.4: Output distribution for the Neural Network, using the 6 discriminating variables defined in the text. MC signal are shown in black, and off-peak data are shown in red. The vertical green line indicates the cut applied, $0.6 < NN$.

4.1.7 Best Candidate Selection

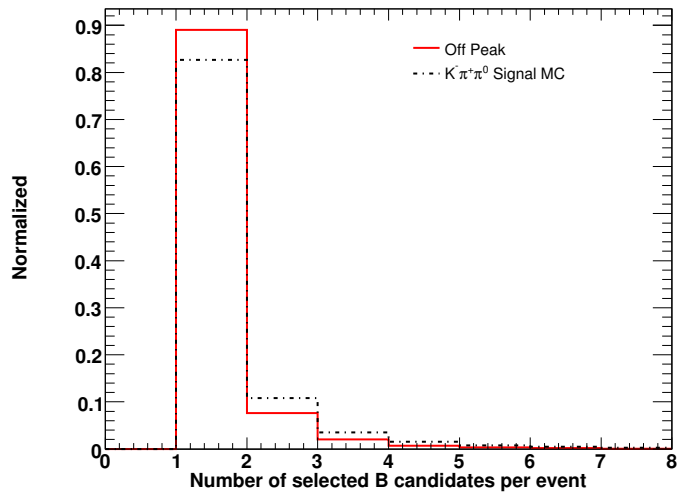

Figure 4.5: Number of B candidates per event passing all selections, except $m_{\rm ES}$.

Approximately 17% of the signal MC events which have B candidates passing all selections except $m_{\rm ES}$, contain multiple B candidates as shown in Fig. 4.5. Since the continuum Dalitz plot is modeled from the $m_{\rm ES}$ sideband ($5.2 \leq m_{\rm ES} \leq 5.272$) of on-peak data, the $m_{\rm ES}$ cut is not applied in selecting the best B candidate. On average such events contain 1.3 B candidates. Due to the specific kinematics of multi-candidate events, their occurrence strongly depends on the location of the event in the Dalitz plot. To prevent biasing the distributions (PDFs) of the variables that will enter the maximum likelihood (ML) fit, we select the candidate with the minimum value of

$$\chi^2 = \left(\frac{m_{\pi^0} - m_{\pi^0}^{\rm PDG}}{\sigma_{m_{\pi^0}}}\right)^2 + \chi^2_{\rm Vertex}, \tag{4.5}$$

were $\chi^2_{\rm Vertex}$ is the vertex likelihood returned by the `TreeFitter` algorithm. We select the correct B candidate 48.02% of the time when more than one candidate is present.

4.1.8 Selection Efficiency

The efficiencies of the selection and reconstruction requirements placed on $B^0 \to K^+\pi^-\pi^0$ candidates are summarized in Table 4.2. The efficiency to reconstruct and select a true $B^0 \to K^+\pi^-\pi^0$ decay is 22.45%, while the efficiency to reconstruct a continuum event passing the `BToCPP` skim, as signal is 0.05%.

Table 4.2: Selection efficiencies relative to the previous cut with binomial errors for signal MC, on-peak and off-peak data.

Cuts	Relative Efficiencies (%)		
	$\varepsilon_{\text{Signal MC}}$	$\varepsilon_{\text{off-peak}}$	$\varepsilon_{\text{on-peak}}$
Reconstruction	57.48 ± 0.02	20.97 ± 0.02	38.39 ± 0.01
`KaonLHTight` PID	78.79 ± 0.02	48.98 ± 0.06	49.13 ± 0.01
`PionLHTight` PID	90.52 ± 0.00	65.43 ± 0.00	66.17 ± 0.00
0.6<NN	80.86 ± 0.03	9.36 ± 0.06	10.53 ± 0.01
$m(\pi^0)_\chi$ <3	92.03 ± 0.02	79.27 ± 0.26	80.44 ± 0.06
$\cos\theta^*_{\pi^0}$ <0.95	98.06 ± 0.01	95.83 ± 0.15	95.83 ± 0.03
$-2.1 < \Delta E' < 2.1$	83.44 ± 0.03	42.99 ± 0.37	42.98 ± 0.08
5.272< Best B m_{ES} <5.2875	89.91 ± 0.03	23.80 ± 0.48	14.77 ± 0.09
Total Efficiency	22.45 ± 0.02	0.049 ± 0.001	0.064 ± 0.000

The selection criteria applied to the skimmed on-peak data set yield a sample of 23268 events distributed over the Dalitz plot as shown in Fig. 4.6.

4.2 Dalitz Coordinates

Since the B is much more massive than the K and π mesons the accessible phase space of charmless three-body B decays is very large. Most contributing resonances have masses much lower than the B mass, consequently signal events cluster along the Dalitz plot boundaries. This is also true for background events. Previous *BABAR* analyses have shown that another set of variables, m', θ' defined by the mapping

$$\begin{aligned} dx\ dy &\longrightarrow dm'\ d\theta', \\ m' &\equiv \frac{1}{\pi}\arccos\left(2\frac{m-m_{\rm min}}{m_{\rm max}-m_{\rm min}}-1\right),\ \theta' \equiv \frac{1}{\pi}\theta_H, \end{aligned} \tag{4.6}$$

are well suited to such configurations. These coordinates define the *Square Dalitz Plot* (SDP) where m $(=\sqrt{x})$ and θ_H are the invariant mass and helicity angle of the $K^\pm\pi^\mp$ system, respectively. The variables, $m_{\rm max} = m_B - m_{\pi^0}$ and $m_{\rm min} = m_{K^+} + m_{\pi^-}$, are the kinematic limits of m. The new variables both range between 0 and 1. The standard and square Dalitz plot of the selected events is shown in Fig. 4.6. The determinant of the Jacobian of the transformation in Eq. (4.6) is given by

$$|\det J| = 2\pi^2|\vec{p}||\vec{q}|m(m_{\rm max}-m_{\rm min})\sin(\pi m')\sin(\pi\theta'), \tag{4.7}$$

where $\vec{p}$ and $\vec{q}$ are the momenta of the π^0 and K^+ in the $K^+\pi^-$ rest frame (See Section 2.5.1).

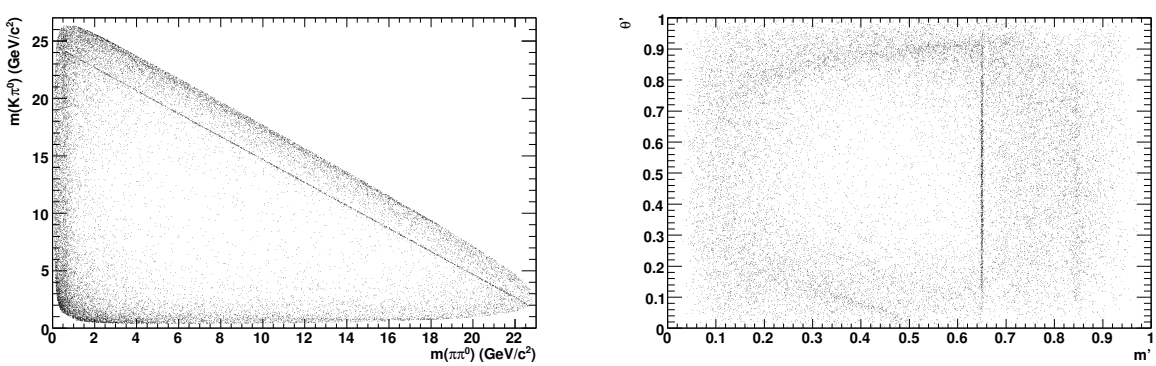

Figure 4.6: The standard (left) and square (right) Dalitz plots of the selected data sample of 23683 events. The intermediate resonances are more spread out in the square Dalitz plot. The $\overline{D}^0 \to K^+\pi^-$ narrow band is preserved with the choice made for the m' variable.

4.3 Mis-Reconstructed Signal Events

High statistics signal MC is used to distinguish between correctly reconstructed signal and SCF events. A correctly reconstructed event where the three particles of the B candidate match the generated ones, is called a truth-matched (TM) event. A SCF event contains a B meson which decays to the signal mode, but one or more reconstructed particles in the B candidate are not actually from the decay of that B. Misreconstruction is primarily due to the presence of low momentum π^0s and $\pi^\pm$s. Consequently, the efficiency $\varepsilon(m', \theta')$ to reconstruct an event either correctly or incorrectly varies across the Dalitz plot. The fraction of SCF events $f_{\rm SCF}(m', \theta')$ is high, where the quality of the reconstruction is poor, namely the slow π^0, $\pi^\pm$ corners of the Dalitz plot. Since it is important to keep a high efficiency in the Dalitz plot corners where the low-mass vector resonances interfere, we cannot treat SCF events as background in the analysis. Variations in the efficiency for TM and SCF events over the Dalitz plot can be seen in Fig. 4.7 computed using high statistics MC samples. The average efficiency over the Dalitz plot, for signal events (See Table 2.5) $\langle\epsilon\rangle_{\rm DP}$, is 21%. The SCF fraction, averaged over the Dalitz plot, $\langle f_{\rm SCF}\rangle_{\rm DP}$ is typically 9%.

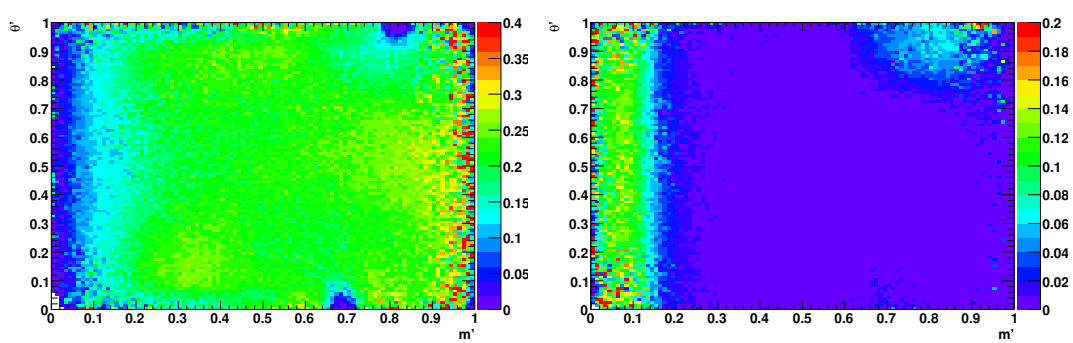

Figure 4.7: Selection efficiency, ϵ for TM events (left) and SCF events (right). The maximum efficiency is 1.

4.4 B-Related Backgrounds

In order to maintain sensitivity to interference over the entire Dalitz plot, no restrictions on any two-body invariant mass of the final state particles is imposed. Consequently, large cross-feed backgrounds from other B decays occur. MC samples are used to study these backgrounds. We make conservative assumptions for decay modes with unknown branching fractions. Inclusive and exclusive B decays are grouped into 19 classes to be used in the fit. Those backgrounds whose contributions are expected to be large (200 or more events) are allowed to float in the fitting procedure while all others are fixed. PDFs describing the $m_{\rm ES}$, ΔE, Neural Network, and Dalitz distributions for the 19 classes of B-background are shown in Appendix B. Branching fractions, topological and kinematical similarities are studied to define the B-background classes as follows:

- Class 1: Contains the modes $B^0 \to K^{*0}\gamma$, $B^0 \to X_{sd}\gamma$, and $B^+ \to K^{*+}\gamma$. These decays are mis-reconstructed where either a π^0 or π^+ from the opposite B has been included in the reconstruction. Consequently, this background has a characteristically high ΔE distribution. The Dalitz distribution is sharply peaked around the K^* resonance (See Fig. B.1).

- Class 2: Contains both resonant (from the ρ) and non-resonant contributions for $B^+ \to \pi^+\pi^0\pi^0$. This decay is typically mis-reconstructed by substituting a K for a slow π^0. Consequently, this mode exhibits an upward sloping ΔE distribution and its Dalitz distribution is concentrated in the slow π^0 and K regions (See Fig. B.2).

- Class 3: Contains resonant contributions from both K^{*+} and f^0 for $B^+ \to K^+\pi^0\pi^0$. Since this mode is mis-reconstructed by substituting a π^0 for a slow $\pi^\pm$ the Dalitz distribution is concentrated in that region. See Fig. B.3

- Class 4: Contains both resonant (from the K^{*+}) and non-resonant contributions for $B^0 \to K^+K^-\pi^0$. This decay is mis-reconstructed by substituting a charged pion for one of the kaons in the reconstruction. The ΔE distribution is low as a result. The K^{*+} resonance is visible in the Dalitz distribution (See Fig. B.4).

- Class 5: This mode is mis-reconstructed with a slow π^0 and K from the opposite B in the Dalitz decay $B^+ \to \pi^+\pi^+\pi^-$. The Dalitz distribution populates the slow π^0 region (See Fig. B.5).

- Class 6: This mode is mis-reconstructed with a slow π^0 from the opposite B in the Dalitz decay $B^+ \to K^+\pi^+\pi^-$. The Dalitz distribution populates the slow π^0 region (See Fig. B.6).

- Class 7: This mode is mis-reconstructed with an additional slow $\pi^\pm$ from the opposite B in the decay $B^+ \to K^+\pi^0$. Its Dalitz distribution populates the slow $\pi^\pm$ region. Since the mis-reconstruction adds a particle to the true decay, the ΔE distribution slopes sharply upward (See Fig. B.7).

- Class 8: Similar to Class 7, this mode is mis-reconstructed with an additional slow π^0 from the opposite B in the decay $B^0 \to K^+\pi^-$. Its Dalitz distribution populates the slow π^0 region. Since the mis-reconstruction adds a particle to the true decay, the ΔE distribution slopes sharply upward (See Fig. B.8).

- Class 9: This mode is mis-reconstructed by substituting a K from the opposite B for a charged pion in the decay $B^0 \to \pi^+\pi^-\pi^0$. Since the K is more massive than the pion it replaces, the ΔE distribution slopes upward (See Fig. B.9).

- Class 10: Includes the non-signal final state of the decays $B^0 \to D^0\pi^0, D\rho$, where $D^0 \to K^+K^-, K^+\pi^-\pi^0$ which are typically mis-reconstructed by omitting a K or pion from the decay. Consequently, the ΔE distribution slopes downward. The D resonance is visible in the Dalitz distribution (See Fig. B.10). The yield of this background contribution is floated in the fit.

- Class 11: Includes the non-signal final state of the decays $B^0 \to D^-\pi^+, D^{*-}\pi^+$, where D^*, $D^{*-} \to \pi^0 D^-, \pi^-\overline{D}^0$ which are typically mis-reconstructed by substituting a slow kaon or π^0 from the opposite B. The Dalitz distribution populates those regions. See Fig. B.11 The yield of this background contribution is floated in the fit.

- Class 12: This mode is mis-reconstructed by substituting a slow pion from the opposite B for the ρ and a_1 in the decays $B^0 \to K^{*0}\rho^0, K^+a_1^-$. Its Dalitz distribution populates the slow π^0 region (See Fig. B.12).

- Class 13: This mode mis-identifies the η as a π^0 in the decay $B^0 \to K^+\eta\pi^-$. Since the η is about 5 times the mass of the π^0, the Dalitz distribution populates a region above a certain π^0 momentum threshold (See Fig. B.13).

- Class 14: The decay $B^+ \to K^+\eta^{'}$ is mis-reconstructed by substituting a slow π^0 for the $\eta^{'}$ and including an additional $\pi^\pm$ from the opposite B. The Dalitz distribution of this background populates the slow π^0 region (See Fig. B.14).

- Class 15: The decays $B^0 \to a_1^+\pi^-, \rho^+\rho^-$ are mis-reconstructed with an additional slow kaon from the opposite B to create this background. The Dalitz distribution of this background populates the slow K region (See Fig. B.15).

- Class 16: The decay $B^+ \to K^{*0}\rho^+$ is mis-reconstructed by substituting a π^0 from the opposite B for the ρ^+. The K^* resonance is visible in the Dalitz distribution (See Fig. B.16).

- Class 17: Mis-reconstructed decays of $B^0 \to K^{*0}\eta, K^{*+}\rho^-, K^+a_1^-, a_1^0K^+$ populate the slow π^0 and π^- regions of the Dalitz plot. This background is mis-reconstructed by substituting either a slow π^0 or $\pi^\pm$ for a more massive particle and exhibits a downward sloping ΔE distribution (See Fig. B.17).

- Class 18: Mis-reconstructed decays of $B^+ \to a_1^0(K,\pi), \rho^+\rho^0, a_1^+\pi^0, \pi^0\pi^+K_s, \pi^0 l\nu$ generally include an additional slow K from the opposite B and their Dalitz distribution populates that region (See Fig. B.18).

- Class 19 (Generics): Contains numerous many body decays of the B generated from generic B^0 and $B^\pm$ simulation production. The result is an irregularly populated Dalitz plot and relatively flat ΔE and m_{ES} distributions. See Fig. B.19

The B-backgrounds and their expected yields are summarized in Table 4.3.

SP#	Class	Description	Eff.(%)	$\mathcal{B}$ ($\times 10^{-6}$)	Expected Yield
1710	1	$B^0 \to K^{*0}(\to K^+\pi^-)\gamma$	0.55	28.7 ± 2.7	71.5 ± 6.7
6456	1	$B^0 \to X_{sd}\gamma$	0.07	355 ± 37	114.2 ± 11.9
1713	1	$B^+ \to K^{*+}(\to K^+\pi^0)\gamma$	0.03	12.7 ± 1.7	1.7 ± 0.2
1940	2	$B^+ \to \rho^+\pi^0$	0.19	10.9 ± 1.5	9.4 ± 1.3
1938	2	$B^+ \to \pi^+\pi^0\pi^0$ (NR)	0.10	4.0 ± 4.0	1.9 ± 1.9
1941	3	$B^+ \to K^{*+}(\to K^+\pi^0)\pi^0$	2.41	2.3 ± 0.8	25.2 ± 8.8
5068	3	$B^+ \to f_0(980)(\to \pi^0\pi^0)K^+$	1.67	3.0 ± 1.0	22.7 ± 7.6
1945	4	$B^0 \to K^{*+}(\to K^+\pi^0)K^-$	2.07	1.0 ± 1.0	9.4 ± 9.4
1221	4	$B^0 \to K^+K^-\pi^0$ (NR)	1.81	0.5 ± 0.5	4.1 ± 4.1
6944	5	$B^+ \to \pi^+\pi^+\pi^-$ (Dalitz)	0.10	16.2 ± 1.5	7.9 ± 0.7
6846	6	$B^+ \to K^+\pi^+\pi^-$ (Dalitz)	0.66	54.8 ± 2.9	163.9 ± 8.7
1587	7	$B^+ \to K^+\pi^0$	1.12	12.8 ± 0.6	65.2 ± 3.1
1028	8	$B^+ \to K^+\pi^-$	0.60	19.4 ± 0.6	53.1 ± 1.6
6948	9	$B^0 \to \pi^+\pi^+\pi^0$ (Dalitz)	0.92	26.0 ± 3.0	109.4 ± 12.6
	10	States with a D^0			522.1 ± 40.4
	11	States with a D^-			310.7 ± 13.8
2359	12	$B^0 \to K^{*0}(\to K^+\pi^-)\rho^0$	0.26	3.9 ± 1.1	4.6 ± 1.3
7042	12	$B^0 \to K^+a_1^-(\to \rho^0\pi^-)$	0.13	6.7 ± 2.0	4.1 ± 1.2
5575	13	$B^0 \to K^+\eta(\to \gamma\gamma)\pi^-$	0.14	12.5 ± 1.2	7.9 ± 0.8
1508	14	$B^+ \to K^+\eta'(\to \rho^0\gamma)K^-$	0.23	20.6 ± 0.2	21.7 ± 0.2
2498	15	$B^0 \to \rho^+\rho^-$	0.18	23.1 ± 3.3	18.9 ± 2.7
4157	15	$B^0 \to a_1^+\pi^-$	0.05	31.7 ± 3.7	8.0 ± 0.9
2244	16	$B^+ \to K^{*0}(\to K^+\pi^-)\rho^+$	0.31	6.1 ± 1.0	8.7 ± 1.4
4960	17	$B^0 \to a_1^+(\to \rho^+\pi^0)K^-$	0.39	6.7 ± 2.0	11.9 ± 3.6
2499	17	$B^0 \to K^{*+}(\to K^+\pi^0)\rho^-$ (long.)	0.67	1.8 ± 1.3	5.5 ± 4.0
4874	17	$B^+ \to a_1^0K^+$	0.23	3.4 ± 3.4	3.6 ± 3.6
2390	18	$B^+ \to \rho^+\rho^0$	0.19	18.2 ± 3.0	15.5 ± 2.6
1058	18	$B^+ \to \pi^0 l\nu$	0.02	150 ± 60	12.4 ± 5.0
7073	18	$B^+ \to \pi^0\pi^-K_s$ (Dalitz)	0.08	30.0 ± 30.0	11.5 ± 11.5
4156	18	$B^+ \to a_1^0\pi^+$	0.08	20.4 ± 5.8	7.8 ± 2.2
3584	18	$B^+ \to a_1^+\pi^0$	0.12	5.0 ± 5.0	2.7 ± 2.7
	19	Generic B			425.4 ± 425.4

Table 4.3: Exclusive neutral B background modes. Modes from each category are taken as a single PDF, as a weighted sum of the individual contributions. Branching fractions ($\mathcal{B}$) are taken from the PDG [13] and, when available, from HFAG [34]. In the cases where only an upper limit exists, we take it as the central value with 100% error.

4.5 The Maximum Likelihood Fit

The selected on-peak data sample consists of signal, continuum-background and B-background components, separated by the flavor (charge sign of the K) and B-tagging category of the tag side. We use $m_{\rm ES}$, $\Delta E'$, the NN, and the Dalitz distribution to discriminate signal from background. The Dalitz plot measurement permits the determination of the relative phases and amplitudes among different intermediate resonances. The signal likelihood consists of the sum of a TM and SCF component. The fit strategy attempts to determine as many continuum shape and asymmetry parameters as possible simultaneously with the signal parameters. This reduces systematic effects from the description of the dominant background. The likelihood $\mathcal{L}_i^c$ for a single event i in tagging category c is the sum of the PDFs of all components:

$$\begin{aligned}\mathcal{L}_i^c \;\equiv\;& N_{\rm sig} f_{\rm sig}^c \left[(1-\left\langle f_{\rm SCF}\right\rangle_{\rm DP}^c)\mathcal{P}_{{\rm sig-TM},i}^c + \left\langle f_{\rm SCF}\right\rangle_{\rm DP}^c \mathcal{P}_{{\rm sig-SCF},i}^c\right] \\ &+ N_{q\bar{q}}^c \frac{1}{2}\left(1+q_{{\rm tag},i}A_{q\bar{q},\,{\rm tag}}\right)\mathcal{P}_{q\bar{q},i}^c \\ &+ \sum_{j=1}^{19} N_{Bj} f_{Bj}^c \frac{1}{2}\left(1+q_{{\rm tag},i}A_{B,\,{\rm tag},j}\right)\mathcal{P}_{B,ij}^c,\end{aligned} \tag{4.8}$$

where $N_{\rm sig}$ is the total number of $B^0 \to K^+\pi^-\pi^0$ signal events in the data sample; $f_{\rm sig}^c$ is the fraction of signal events that are tagged in category c; $\left\langle f_{\rm SCF}\right\rangle_{\rm DP}^c$ is the fraction of SCF events in tagging category c, averaged over the DP; $N_{q\bar{q}}^c$ is the number of continuum events that are tagged in category c; $q_{{\rm tag},i}$ is the tag flavor of the event, and is equal to the charge of the kaon from the B^0 decay; $A_{q\bar{q},\,{\rm tag}}$ parametrizes possible tag asymmetry in continuum events; $\mathcal{P}_{q\bar{q},i}^c$ is the continuum PDF for tagging category c; $N_{B,j}$ is the number of expected events in the B-background class j; $f_{B,j}^c$ is the fraction of B-background events of class j that are tagged in category c; $A_{B,\,{\rm tag},j}$ describes a possible tag asymmetry in the B-background class j; $\mathcal{P}_{B,ij}^c$ is the B-background PDF for tagging category c and B-background class j.

The PDFs $\mathcal{P}_X^c$ ($X = {\rm sig-TM},\ {\rm sig-SCF},\ q\bar{q},\ B$) are the product of the four

PDFs of the discriminating variables [3], $P^c_{X,i(j)}(x_k)$ where $x_1 = m_{\rm ES}$, $x_2 = \Delta E'$, $x_3 =$ NN output and $x_4 = \{m', \theta'\}$ describes the Dalitz distribution. Explicitly we have

$$\mathcal{P}^c_{X,i(j)} \equiv \prod_{k=1}^{4} P^c_{X,i(j)}(x_k) \ , \tag{4.9}$$

where i is the event index and j is a B-background class. The extended likelihood over all tagging categories is given by

$$\mathcal{L} \equiv \prod_{c=1}^{7} e^{-\overline{N}^c} \prod_{i}^{\overline{N}^c} \mathcal{L}^c_i \ , \tag{4.10}$$

where $\overline{N}^c$ is the total number of events expected in tagging category c. Parametrization of the PDFs and corrections for their relative correlations are discussed in Section 4.6.

4.6 PDF Parametrization

In this section we describe the $m_{\rm ES}$, $\Delta E'$, NN, and Dalitz PDFs in Eq. (4.9) used in this analysis. The likelihood model relies on the assumption that the variables used in its construction are uncorrelated. Violation of this assumption will result in biases of the fitted parameters. Where correlations exist, they are explicitly corrected for in the relevant PDFs as discussed below.

It is often the case that a parametric description of a given PDF cannot be found or would be too time consuming to create. In these cases we use a gaussian kernel estimation (smoothing) [35] to generate the PDF. The smoothing describes the data as a sum of gaussian PDFs centered at each data point with width h. Once the sum of gaussians has been tabluated we generate a finely binned smoothed histogram PDF from the kernel estimation. We adjust the smoothing parameter (proportional to h) to achieve a satisfactory fit to the data. Unless otherwise noted the PDFs

[3] Not all the PDFs depend on the tagging category. The general notations $P^c_{X,i(j)}$ and $\mathcal{P}^c_{X,i(j)}$ are used for simplicity.

for the 19 classes of B-background are modeled with smoothed histograms shown in Appendix B.

4.6.1 Dalitz Plot PDFs

Since the decay $B^0 \to K^+\pi^-\pi^0$ is flavor-specific (the charge of the kaon identifies the B flavor), the B^0 and $\overline{B}^0$ Dalitz plots are independent. However, because the backgrounds are essentially flavor blind, we get a more robust procedure by fitting them simultaneously. We define the total amplitude,

$$\mathcal{A} = \sum_k a_k e^{i\Phi_k} f_k(m', \theta'), \tag{4.11}$$

where k runs over all of resonances in the model described in Section 2.5. It is enough to describe only the B^0 Dalitz plot PDF. A change from $\mathcal{A}$ to $\overline{\mathcal{A}}$ accompanied by the interchange of the charges of the kaon and pion gives the $\overline{B}^0$ PDF. The amplitudes and phases are measured relative to the $\rho^-(770)K^+$ amplitude so that the phases $\Phi_{\rho^-K^+}$ and $\overline{\Phi}_{\rho^+K^-}$ are fixed to 0 and the isobar amplitude, $\overline{a}_{\rho^-K^+}$ is fixed to 1.

For an event i, we have

$$\mathcal{P}_{\mathrm{sig-TM},i} = \varepsilon_i \left(1 - f_{\mathrm{SCF},i}\right) |\det J_i| \, \frac{|\mathcal{A}_i|^2}{|N_{\mathrm{TM}}|^2} \ , \tag{4.12}$$

$$\mathcal{P}_{\mathrm{sig-SCF},\,i} = \varepsilon_i \, f_{\mathrm{SCF},i} \frac{[|\det J||\mathcal{A}|^2 \otimes R_{\mathrm{SCF}}]_i}{|N_{\mathrm{SCF}}|^2 \otimes R_{\mathrm{SCF}}} \ , \tag{4.13}$$

where $\otimes R_{\mathrm{SCF}}$ denotes convolution with a resolution function described below. J is the Jacobian matrix of the transformation to the square Dalitz plot. The normalization constants $|N_{\mathrm{TM}}|^2$ and $|N_{\mathrm{SCF}}|^2$ are given by:

$$|N_{\mathrm{TM}}|^2 = \mathrm{Re} \sum_{\kappa,\sigma} a_\kappa a_\sigma e^{i(\Phi_\kappa - \Phi_\sigma)} \langle \varepsilon \left(1 - f_{\mathrm{SCF}}\right) |\det J| \, f^\kappa f^{\sigma *} \rangle \ , \tag{4.14}$$

$$|N_{\mathrm{SCF}}|^2 = \mathrm{Re} \sum_{\kappa,\sigma} a_\kappa a_\sigma e^{i(\Phi_\kappa - \Phi_\sigma)} \langle \varepsilon \, f_{\mathrm{SCF}} \, |\det J| \, f^\kappa f^{\sigma *} \rangle \ , \tag{4.15}$$

where the indices κ, σ run over all resonances of the signal model. The expectation values occurring in Eq. (4.14) and Eq. (4.15) are model-dependent and are computed with high statistics MC integration over the square Dalitz plot:

$$\langle \varepsilon\,(1 - f_{\rm SCF})\,|\det J|\,f^{\kappa} f^{\sigma *}\rangle \;=\; \frac{\int_0^1\int_0^1 \varepsilon\,(1 - f_{\rm SCF})\,|\det J|\,f^{\kappa} f^{\sigma *}\,dm'd\theta'}{\int_0^1\int_0^1 \varepsilon\,|\det J|\,f^{\kappa} f^{\sigma *}\,dm'd\theta'}\;, \tag{4.16}$$

and similarly for $\langle \varepsilon f_{\rm SCF},\,|\det J|\,f^{\kappa} f^{\sigma *}\rangle$, where all quantities in the integrands are Dalitz plot dependent. Note that the integral in Eq. (4.16) depends on the line shape parameters (mass, width, spin, ect.) assumed for the signal model. If these parameters are determined from a fit to data, the evaluation of Eq. (4.16) would iterative and time consuming. As a result, the parameters of the resonance line shapes are held constant in the fit given that they have been previously well measured [13].

SCF Fractions

Eq. (4.8) invokes the DP-averaged SCF fraction $\langle f_{\rm SCF}\rangle_{\rm DP}$ which is decay dynamics-dependent, since it is obtained from an integral of the decay amplitude-squared over the Dalitz plot

$$\langle f_{\rm SCF}\rangle_{\rm DP} \;=\; \frac{\int_0^1\int_0^1 \varepsilon\,f_{\rm SCF}\,|\det J|\,(|\mathcal{A}|^2 + |\overline{\mathcal{A}}|^2)\,dm'd\theta'}{\int_0^1\int_0^1 \varepsilon\,|\det J|\,(|\mathcal{A}|^2 + |\overline{\mathcal{A}}|^2)\,dm'd\theta'}\;. \tag{4.17}$$

In principle $\langle f_{\rm SCF}\rangle_{\rm DP}$ must be computed iteratively, though the remaining systematic uncertainty after one iteration step is expected to be small. We determine the SCF fractions separately for each tagging category from simulation using Eq. (4.17). The fraction of total signal events and the DP-averaged SCF fraction are shown Table 4.4 for each tagging category.

Resolution

Studies in simulation have shown that the experimental resolutions of m' and θ' need not be introduced in the TM signal PDF. However, mis-reconstructed events

Tagging Category	$f_{\rm sig}$ (%)	$\langle f_{\rm SCF}\rangle_{\rm DP}$ (%)
`Lepton`	8.81	4.70
`KaonI`	10.89	7.07
`KaonII`	17.26	8.54
`KaonPion`	13.66	9.23
`Pion`	14.20	9.43
`Other`	9.48	9.88
`NoTag`	25.70	10.22

Table 4.4: The fraction of total signal events ($f_{\rm sig}$) and the DP-averaged SCF fraction ($\langle f_{\rm SCF}\rangle_{\rm DP}$) in each tagging category. The fraction of total signal events is determined from a fit to a subset of the *BABAR* data where both B mesons are fully reconstructed known as the BReco dataset.

often incur large migrations, *i.e.* the reconstructed coordinates m'_r, θ'_r are far from the true values m'_t, θ'_t. As shown in Fig. 4.8, migrations of 2.5% of the square Dalitz coordinates are typically observed. This corresponds to a broadening of resonances by 800 MeV/c, much larger than their widths. We introduce a rank-4 resolution tensor, $R_{\rm SCF}(m'_r, \theta'_r; m'_t, \theta'_t)$, which represents the probability to reconstruct at the coordinates (m'_r, θ'_r) an event that has the true coordinate (m'_t, θ'_t). The tensor obeys the unitarity condition

$$\int_0^1 dm'_r \int_0^1 d\theta'_r R_{\rm SCF}(m'_r, \theta'_r; m'_t, \theta'_t) = 1 \ \forall \ m'_t, \theta'_t. \tag{4.18}$$

In practice the resolution tensor is implemented as an array of 2-dimensional histograms which store the probabilities as a function of the Dalitz coordinates. We find that an array of 100×100 histograms representing bins of the true Dalitz coordinate in m', θ', adequitely models the resolution of SCF events on the DP. $R_{\rm SCF}$ is convoluted with the signal model in the expression of $\mathcal{P}_{\rm SCF}$ in Eq. (4.13) to correct for broadening of the SCF events.

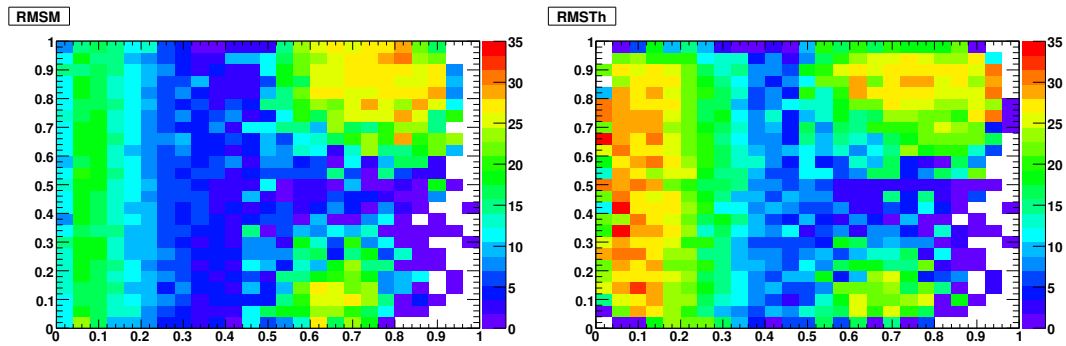

Figure 4.8: The width (RMS) of $m'_{\rm reco} - m'_{\rm truth}$ for SCF events over the Dalitz plot (left). The width (RMS) of $\theta'_{\rm reco} - \theta'_{\rm truth}$ for SCF events over the Dalitz plot (right). The units of the color axis are in 10^{-3}.

Backgrounds

Except for events coming from exclusive $B \to D$ decays, all background Dalitz PDF are modeled with smoothed, 2-dimensional histograms. The continuum distributions are extracted from a combination of off resonance data and a sideband ($5.20 < m_{\rm ES} < 5.25\,{\rm GeV}/c^2$) of the on-resonance data from which the B-background has been subtracted. The square Dalitz plot is divided into eight regions where different smoothing parameters are applied in order to optimally reproduce the observed wide and narrow structures by using a 2-dimensional kernel estimation technique [35]. For $0.64 < m' < 0.66$ and all θ', a finely binned, unsmoothed histogram is used to follow the peak from the narrow D^0 continuum production. The B-background (See Table 4.3) Dalitz PDFs are obtained from the MC simulation. For the components which model $b \to c$ decays with real D^0 mesons, a fine grained binning around the D mass is used to construct unsmoothed histograms.

4.6.2 Kinematic PDFs

The $m_{\rm ES}$ distribution for TM events is parametrized as

$$f(x = m_{\rm ES}) = \exp\left[-\frac{(x-m)^2}{2\sigma_\pm^2 + \alpha_\pm(x-m)^2}\right], \tag{4.19}$$

where m, the mean and $\sigma_\pm$, the high and low side widths, are floated in the fit. For

SCF events we use a smoothed histogram taken from the MC simulation.

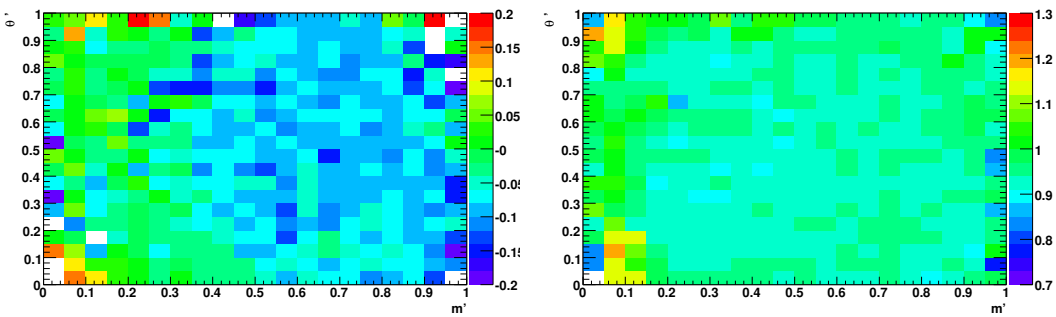

Figure 4.9: The mean (left) and RMS (right) of $\Delta E'$ for TM signal events as a function of the Dalitz Plot.

$\Delta E'$ is correlated with the Dalitz plot variables for TM events. The source of this correlation is the underestimation of $\sigma_{\Delta E}$ for slow π^0s and is illustrated in Fig. 4.2. Though $\Delta E'$ was developed explicitly to correct for this correlation, the fundamentally non-Gaussian shape of $\Delta E/\sigma_{\Delta E}$ is difficult to uncorrelated form the Dalitz Plot perfectly as shown in Fig. 4.9. To account for the remaining correlation, we choose the combination of a Gaussian and 1st order polynomial PDF for $\Delta E'$:

$$
\begin{aligned}
f(x = \Delta E') &= \exp\left[-\frac{(x-m)^2}{2\sigma^2}\right] + ax + b, \\
m = m_0 + m_1 m_{K^+\pi^-},\ \sigma &= \sigma_0 + \sigma_1 m_{K^+\pi^-}, \\
a = a_0 + a_1 m_{K^+\pi^-},\ b &= b_0 + b_1 m_{K^+\pi^-}.
\end{aligned}
\tag{4.20}
$$

The mean and standard deviation of the Gaussian and slope of the polynomial vary linearly with $m^2_{K^\pm\pi^\mp}$ as shown in Eq. (4.20). The intercept and slope parameters, $a_{0,1}, b_{0,1}, m_{0,1}, \sigma_{0,1}$ are floated in the fit. A non-parametric shape taken from the MC simulation is used as the SCF $\Delta E'$ PDF.

Backgrounds

We use the Argus function [36]

$$f(x = \frac{m_{\rm ES}}{m_{\rm ES}^{\rm max}}) \propto x\sqrt{1-x^2}e^{-\xi(1-x^2)}, \tag{4.21}$$

as the continuum $m_{\rm ES}$ PDF. The endpoint $m_{\rm ES}^{\rm max}$ is fixed to $5.2897\,{\rm GeV}/c^2$ and ξ is free in the fit. The $\Delta E'$ PDF is a linear polynomial whose slope is free to vary in the fit. We use smoothed non-parametric distributions taken from the MC to describe $m_{\rm ES}$, and $\Delta E'$ for the B-background classes.

4.6.3 Neural Network PDFs

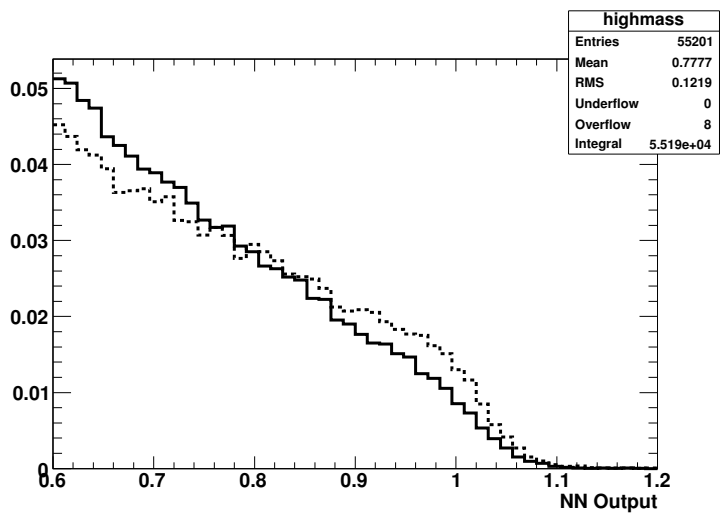

Figure 4.10: The NN output for events at low (solid) and high (dashed) $\Delta_{\rm Dalitz}$.

The NN PDFs for TM, SCF and B-background events are non-parametric distributions taken from the MC. The shape of the NN distribution for continuum is correlated with the event location in the Dalitz plot. The source of the NN correlation with the Dalitz plot is the fact that events close to the borders of the Dalitz plot are more jet like than those in the center of the Dalitz plot, where the three Mandelstam variables (invariant mass pairs) are of similar magnitude. Since the latter have kinematics closer to a typical multi-body B-decay, they lead to increased (*i.e.*, more

signal-like) NN outputs than the former as shown in Fig. 4.10. The continuum NN is thus correlated with the closest distance between the Dalitz position the event and the boundary of the standard Dalitz plot, Δ_{Dalitz}:

$$\begin{aligned}\mathcal{P}(NN;\Delta_{\text{Dalitz}}) = \quad & (1-NN)^{k_1} \\ & \times(k_2 NN^2 + k_3 NN + k_4), \\ & k_i = q_i + p_i \cdot \Delta_{\text{Dalitz}}.\end{aligned} \tag{4.22}$$

The k_i are linear functions of Δ_{Dalitz} where the q_i and p_i are varied in the likelihood fit.

PDF parameters

The parameters of the PDFs are determined from a series of fits to the selected dataset as described in Section D.4. The fitted parameters are shown in Table 4.5.

4.7 Fit Validation

Before fitting to data, the analysis is validated by fitting to pure toy MC samples generated from the PDF models supplied by the analysts and embedded toy MC samples generated with full detector simulation. Fits are performed to MC samples generated with the expected yields of signal, continuum, and B-backgrounds, fluctuated with Poisson uncertainties. For an ensemble of fits, the average value of a fitted parameter should be equal to the generated value. The distribution of the normalized residual (pull)

$$p_x = \frac{x - m_x}{\sigma_x}, \tag{4.23}$$

is plotted for all fitted parameters x where m_x is the generated value of the parameter and σ_x is the per event error calculated from the minimization algorithm. Nominally the definition of p_x implies a Gaussian distribution of mean 0 and width 1. A mean value of p_x different from 0 indicates a bias in the fitting procedure, while a width

Table 4.5: PDF shape parameters determined from fits to data.

Parameter Name	Fit Result
$m_0(\Delta E')$ `Signal`	0.06 ± 0.05
$m_1(\Delta E')$ `Signal`	-0.01 ± 0.004
$\sigma_0(\Delta E')$ `Signal`	1.011 ± 0.041
$\sigma_1(\Delta E')$ `Signal`	-0.002 ± 0.004
$a_0(\Delta E')$ `Signal`	-0.008 ± 0.027
`Slope`$(\Delta E')$ `Continuum`	-0.017 ± 0.007
$m(m_{\rm ES})$ `Signal`	5279.21 ± 0.16 MeV/c^2
$\sigma_-(m_{\rm ES})$ `Signal`	2.41 ± 0.14 MeV/c^2
$\sigma_+(m_{\rm ES})$ `Signal`	2.92 ± 0.12 MeV/c^2
`Argus Slope`$(m_{\rm ES})$ `Continuum`	-9.97 ± 5.84
$q_1(NN)$ `Continuum`	4.00 ± 0.12
$p_1(NN)$ `Continuum`	-0.18 ± 0.11
$q_2(NN)$ `Continuum`	0.21 ± 0.01
$p_2(NN)$ `Continuum`	-0.067 ± 0.003
$q_3(NN)$ `Continuum`	-0.10 ± 0.06
$p_3(NN)$ `Continuum`	0.034 ± 0.039
$q_4(NN)$ `Continuum`	2.56 ± 0.23
$p_4(NN)$ `Continuum`	-0.63 ± 0.14

different from 1 indicates that the error of the parameter is mis-estimated. Fits to pure toy data sets guarantee that there is no bias intrinsic to the fitting machinery developed for this analysis. Embedded toy data set fits ensure that the PDFs used in the analysis are indeed good models of the distributions of the fit variables, and that no un-corrected correlations exist among those variables. The `MIGRAD` routine of the `MINUIT` minimization algorithm is employed to perform all fits in this analysis. The `HESSE` routine is used for a calculation of the error matrix with non-gaussian errors.

4.7.1 Validation in Samples of Pure Toy MC

We generated 262 samples of pure toy events scaled to the full Runs 1-6 statistics and expected resonance parameters. We fit each sample 20 times with randomized initial parameters and select the fit with the lowest likelihood. The compiled results of the fits, in terms of the fit fractions of resonances contributing to the Dalitz model,

are summarized in Table 4.6. We observe slight pulls in the $(K\pi)^*_0\pi$ amplitudes, and include them as a systematic error. The excited states, $\rho(1450)$ and $\rho(1700)$ are not included in the model used to study pure toy fits.

Amplitude	Generated Fit Fraction (%)	μ_{Pull}	σ_{Pull}	$\langle\sigma\rangle$ (%)
$\rho^+(770)K^+$	22.8	-0.02	1.25	1.0
$K^{*+}(892)\pi^-$	7.7	0.04	0.95	1.0
$K^{*0}(892)\pi^0$	6.7	0.01	0.83	0.9
$(K\pi)^{*+}_0\pi^-$	36.7	0.24	0.80	2.3
$(K\pi)^{*0}_0\pi^0$	16.1	-0.23	0.97	1.6
NR	10.0	-0.14	1.05	1.5

Table 4.6: Summary of fit fractions for the resonant amplitudes from 262 toy datasets. μ_{Pull} and σ_{Pull} denote the mean and width of the pull distribution respectively, while the average error is denoted by $\langle\sigma\rangle$.

4.7.2 Validation of the Fit Using Embedded MC

B-background samples are created by selecting events randomly from the background SP modes listed in Table 4.3 and adding their expected yields. Due to limited statistics only 100 such samples could be created with statistics corresponding to the expected yields, without severe over sampling. Since sufficient MC is unavailable for the Generic B-background (Class 19), these events are generated as pure toy. The B-background samples are then added to SP samples of signal events and pure toy continuum, to create a 100 fully embedded samples. The results of fits to the fully embedded datasets are summarized in Table 4.7. Plots of the pulls and errors for the amplitudes and phases are shown in Fig. 4.11 - Fig. 4.17. Only small pulls are observed for a few of the isobar parameters and these are quoted as systematic errors. There is some indication that the errors returned from the fitting algorithm are underestimated for the isobar amplitudes in which case the quoted statistical uncertainty of the measurement is conservative.

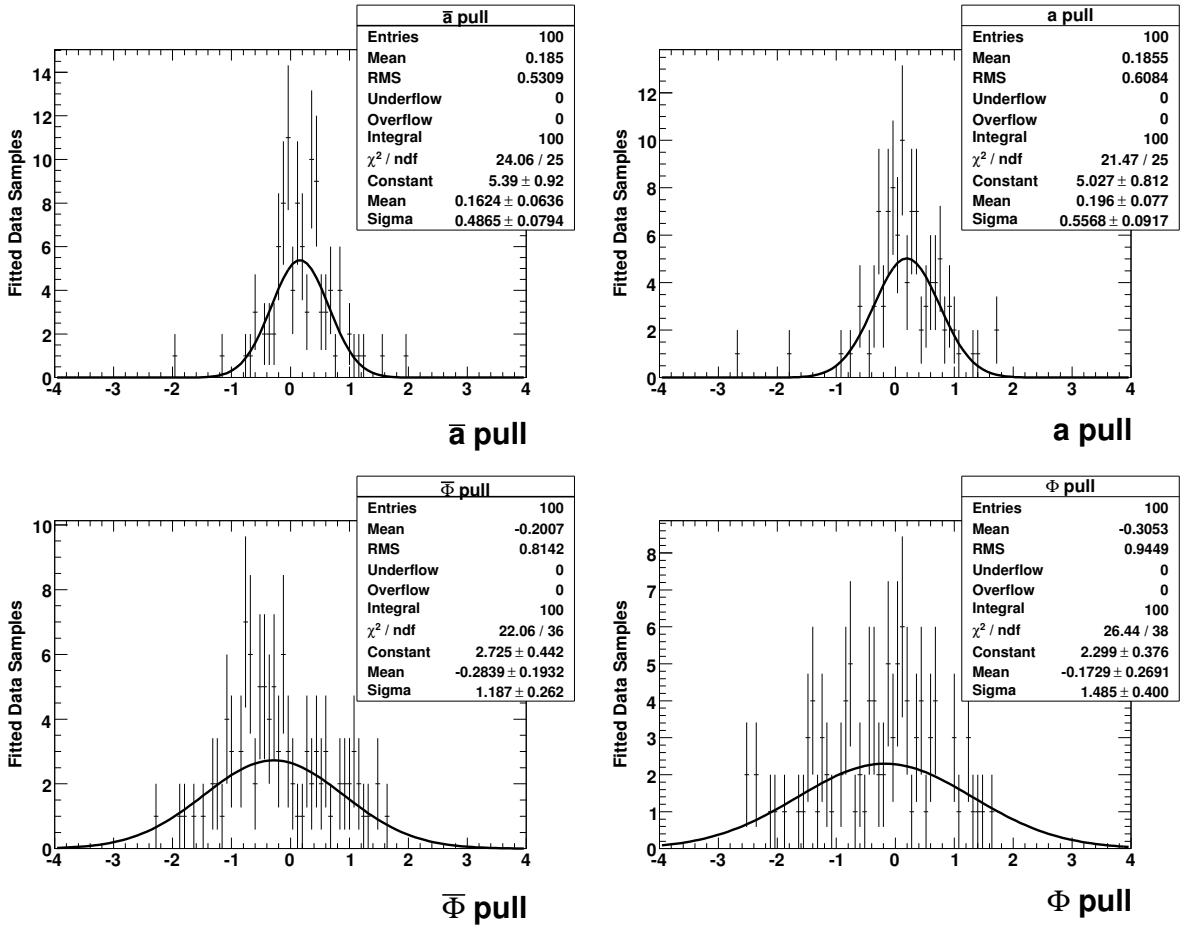

Figure 4.11: $(K\pi)_0^{*+}\pi^-$ $\overline{a}$ (upper left), $\overline{\Phi}$ (lower left), a (upper right) $\overline{a}$ (lower right) Pull distributions of embedded toy fits with Gaussian curves overlaid.

Amplitude	Parameter	Generated Value	μ_{Pull}	σ_{Pull}	$\langle\sigma\rangle$
$(K\pi)_0^{*+}\pi^-$	a	35.36	0.11	0.61	7.42
	$\overline{a}$	37.98	0.11	0.53	7.87
	Φ	-2.28	-0.32	0.94	0.34
	$\overline{\Phi}$	-2.96	-0.25	0.81	0.44
$(K\pi)_0^{*0}\pi^0$	a	28.71	-0.07	0.59	6.05
	$\overline{a}$	24.21	-0.03	0.65	5.06
	Φ	0.19	-0.10	0.91	0.33
	$\overline{\Phi}$	0.40	0.03	0.89	0.46
$K^{*+}(892)\pi^-$	a	0.75	0.09	0.60	0.16
	$\overline{a}$	0.56	0.04	0.64	0.13
	Φ	0.68	-0.28	0.96	0.39
	$\overline{\Phi}$	0.58	-0.20	0.84	0.53
$K^{*0}(892)\pi^0$	a	0.66	0.09	0.58	0.20
	$\overline{a}$	0.57	0.05	0.60	0.17
	Φ	0.37	0.03	0.97	0.35
	$\overline{\Phi}$	0.72	-0.04	0.83	0.51
NR	a	11.30	0.34	0.73	2.84
	$\overline{a}$	13.41	0.10	0.66	3.03
	Φ	1.69	0.01	1.05	0.36
	$\overline{\Phi}$	1.02	0.05	0.86	0.45
$\rho^-(1450)K^+$	a	1.77	0.08	0.71	0.53
	$\overline{a}$	1.39	-0.04	0.60	0.73
	Φ	-0.99	0.05	0.93	0.39
	$\overline{\Phi}$	-1.44	-0.12	0.77	0.68
$\rho^-(1700)K^+$	a	0.83	-0.11	0.70	0.35
	$\overline{a}$	0.61	-0.32	0.63	0.31
	Φ	-2.18	-0.15	0.98	0.47
	$\overline{\Phi}$	-2.14	0.01	0.69	0.87
$\rho^+(770)K^+$	a	0.83	-0.04	0.56	0.19

Table 4.7: Summary of fit results for the resonant amplitudes from 100 fully embedded toy samples. μ_{Pull} and σ_{Pull} denote the mean and width of the pull distribution respectively, while the average error is denoted by $\langle\sigma\rangle$. The phases are given in radians.

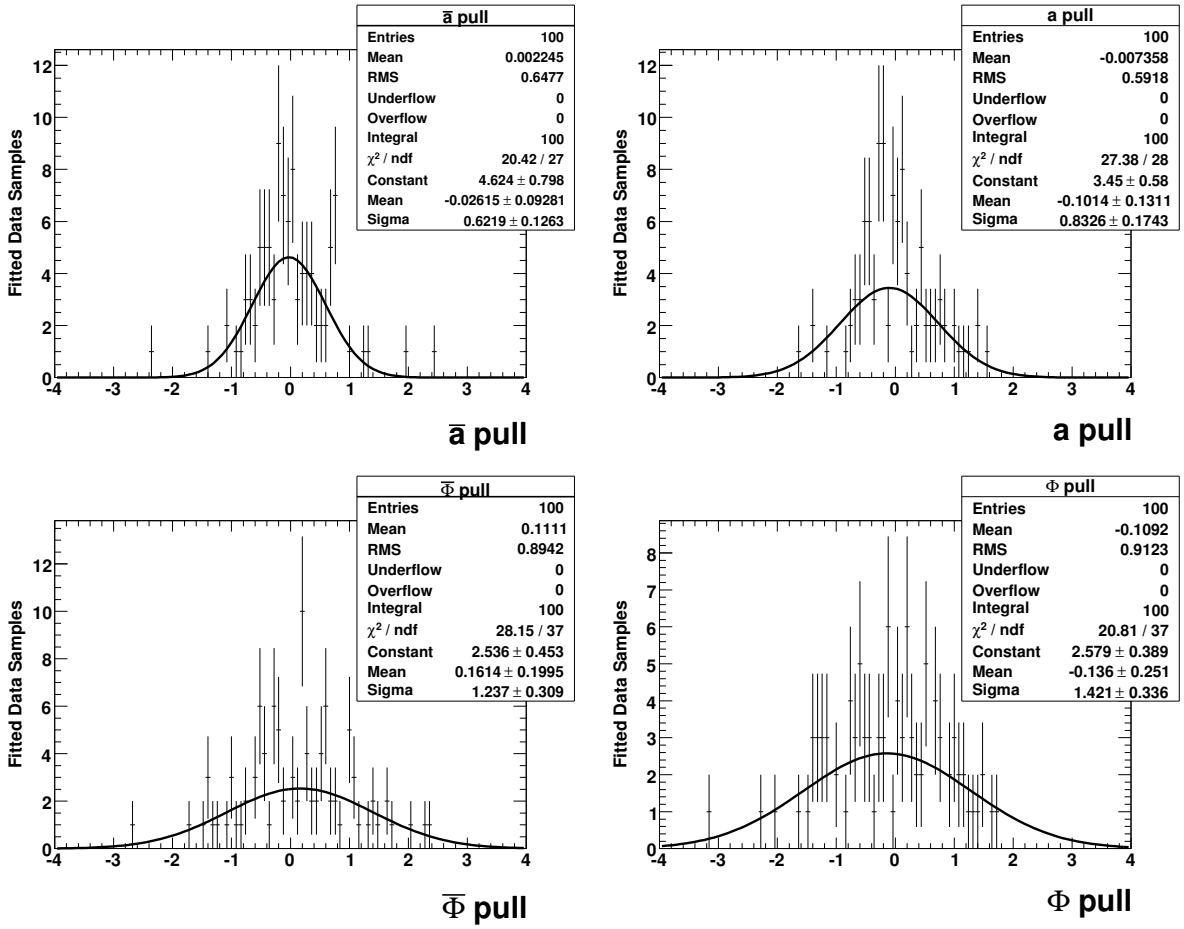

Figure 4.12: $(K\pi)_0^{*0}\pi^0$ $\overline{a}$ (upper left), $\overline{\Phi}$ (lower left), a (upper right) $\overline{a}$ (lower right) Pull distributions of embedded toy fits with Gaussian curves overlaid.

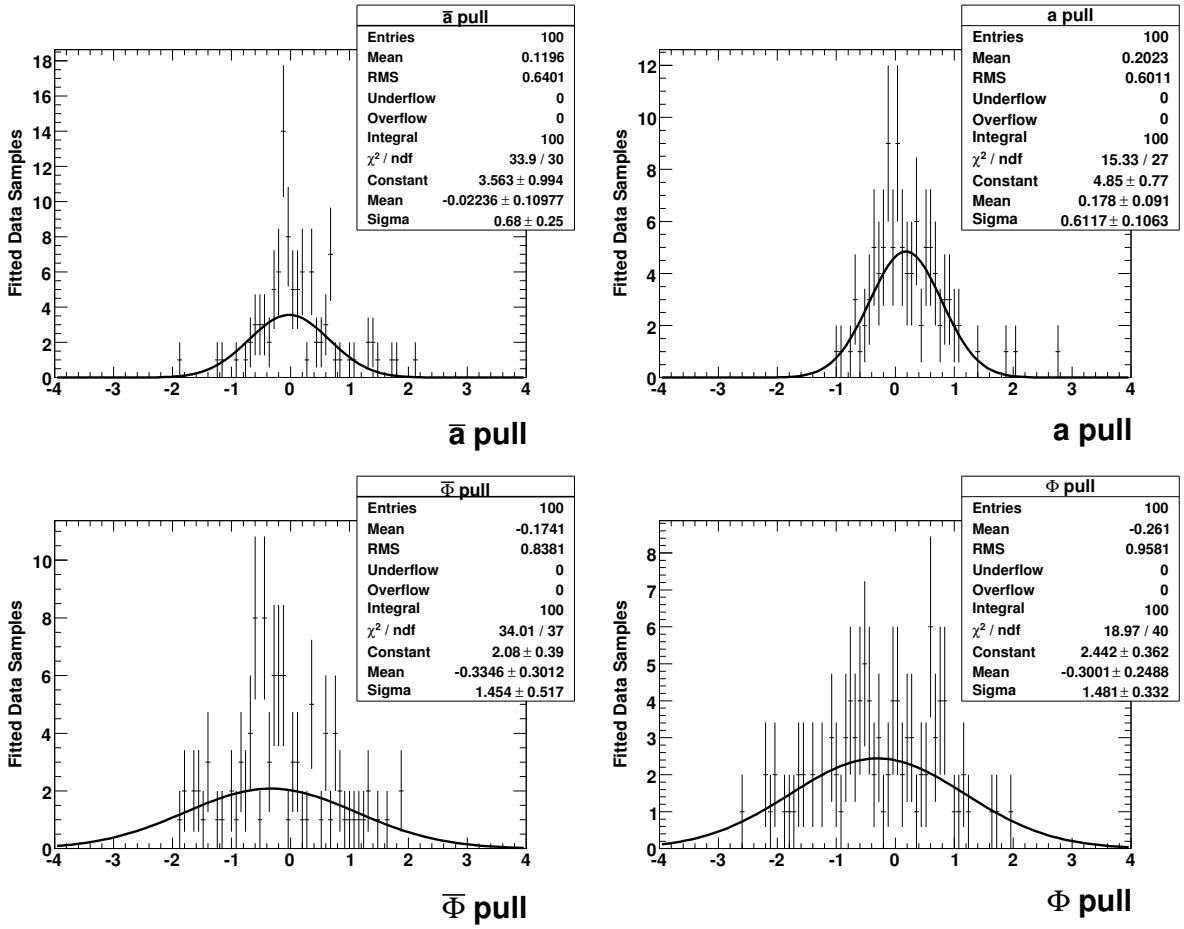

Figure 4.13: $K^{*+}(892)\pi^-$ $\overline{a}$ (upper left), $\overline{\Phi}$ (lower left), a (upper right) $\overline{a}$ (lower right) Pull distributions of embedded toy fits with Gaussian curves overlaid.

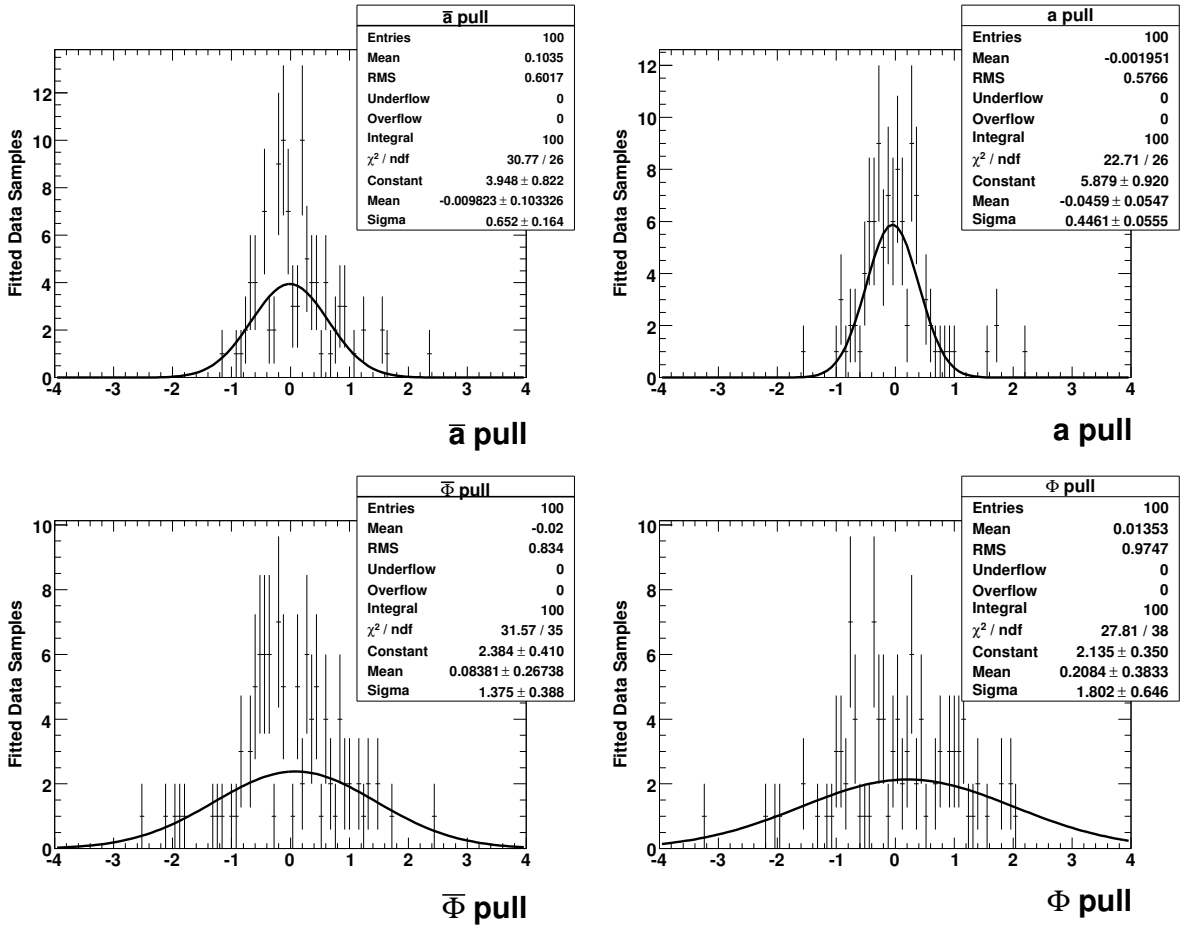

Figure 4.14: $K^{*0}(892)\pi^0$ $\overline{a}$ (upper left), $\overline{\Phi}$ (lower left), a (upper right) $\overline{a}$ (lower right) Pull distributions of embedded toy fits with Gaussian curves overlaid.

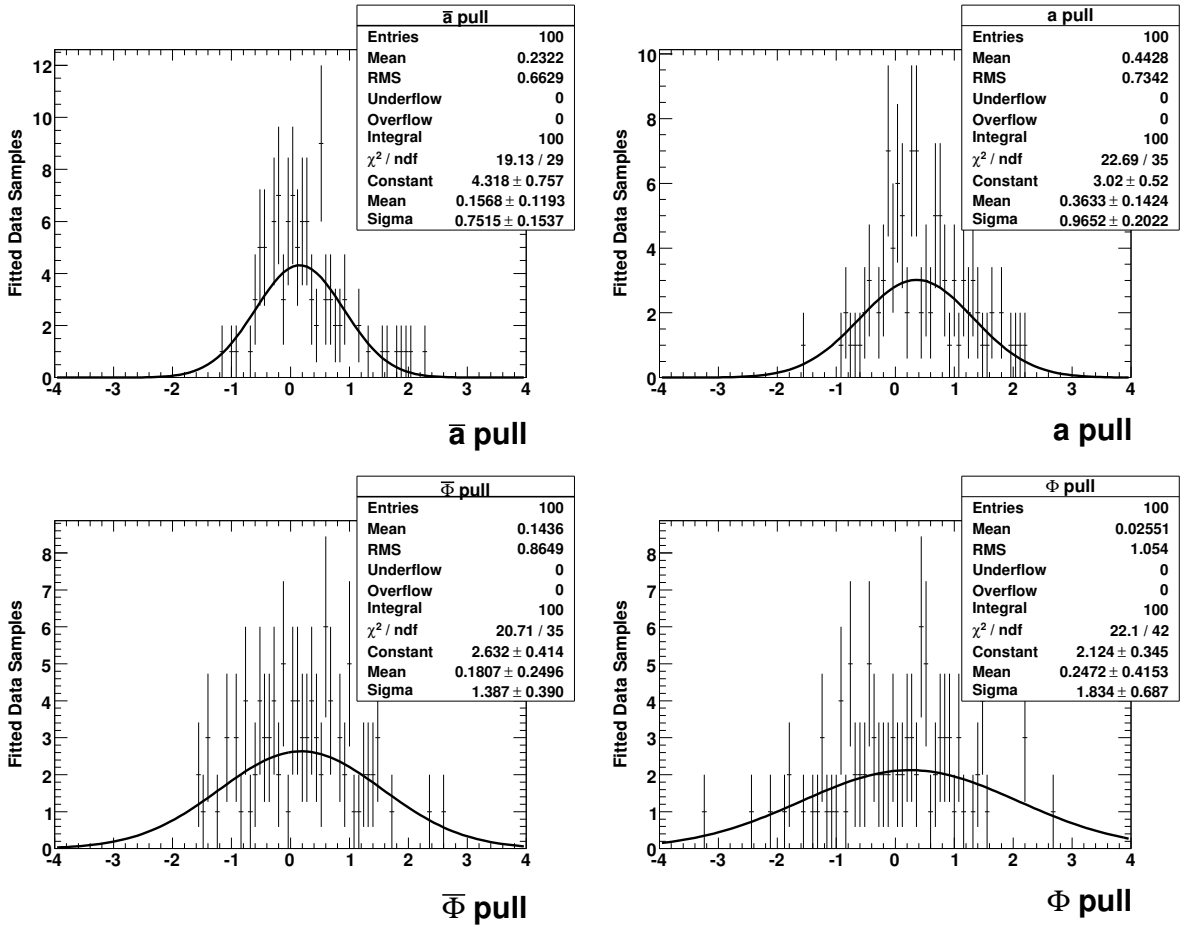

Figure 4.15: NR $\overline{a}$ (upper left), $\overline{\Phi}$ (lower left), a (upper right) $\overline{a}$ (lower right) Pull distributions of embedded toy fits with Gaussian curves overlaid.

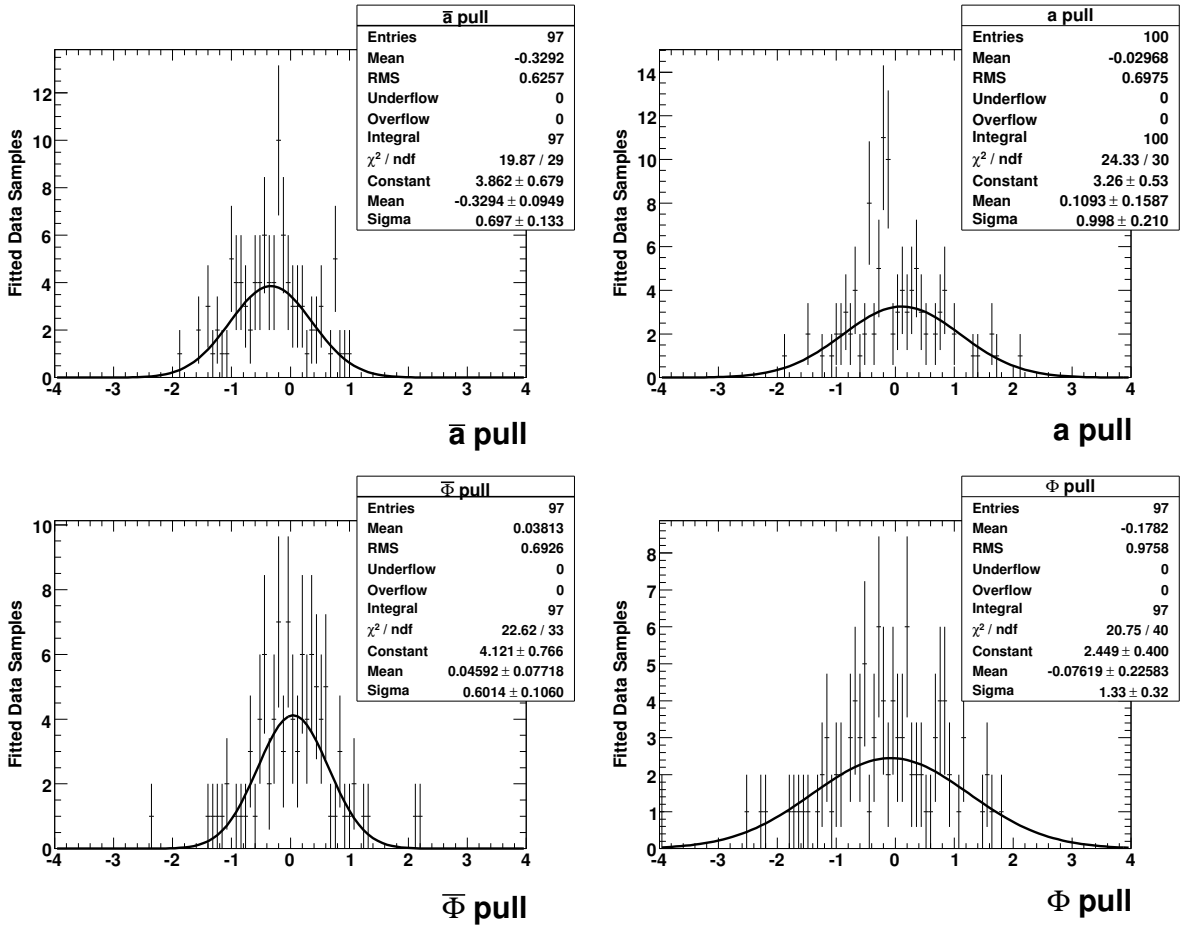

Figure 4.16: $\rho^-(1700)K^+$ $\overline{a}$ (upper left), $\overline{\Phi}$ (lower left), a (upper right) $\overline{a}$ (lower right) Pull distributions of embedded toy fits with Gaussian curves overlaid.

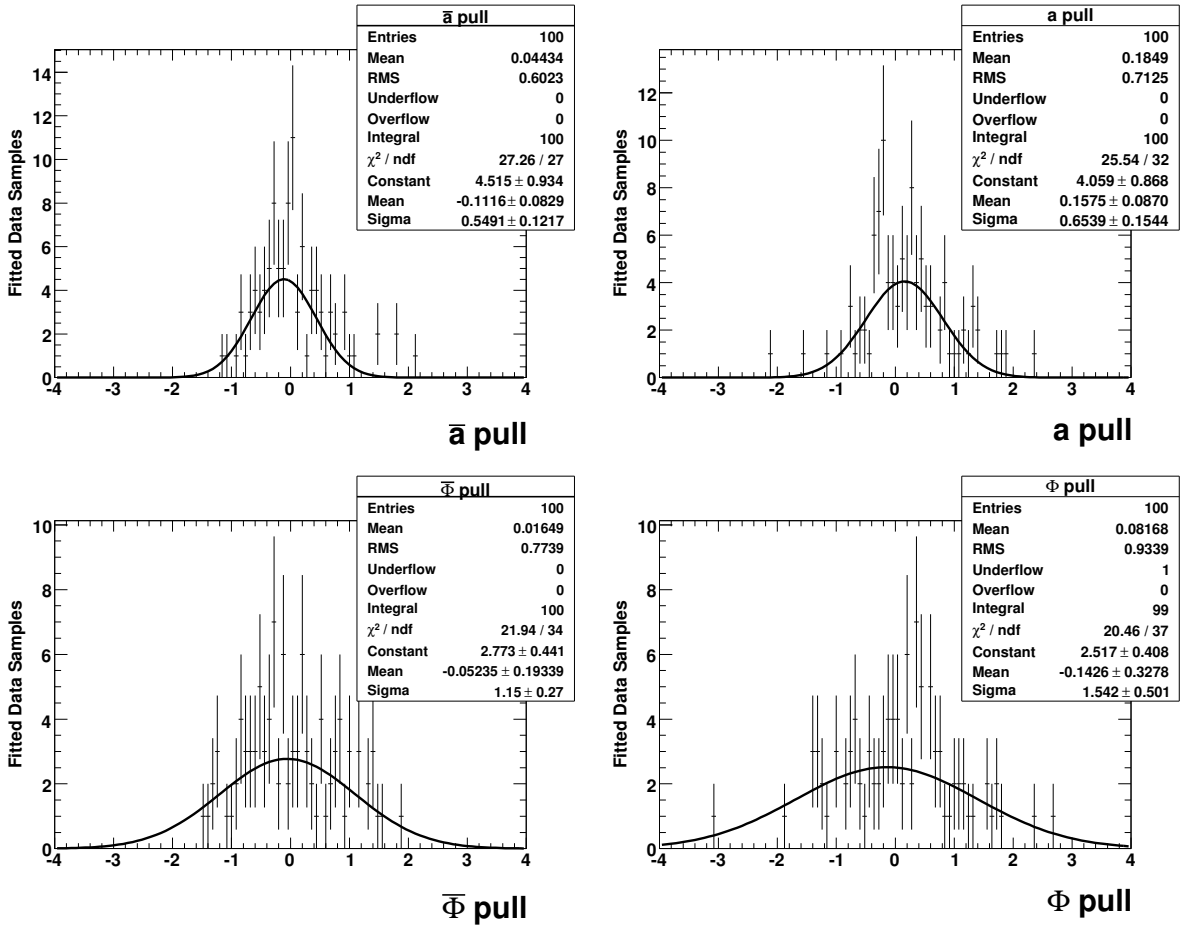

Figure 4.17: $\rho^-(1450)K^+$ $\overline{a}$ (upper left), $\overline{\Phi}$ (lower left), a (upper right) $\overline{a}$ (lower right) Pull distributions of embedded toy fits with Gaussian curves overlaid.

4.8 Fit Results

The maximum likelihood fit to the sample of 23268 selected B decays determines the values of 34 amplitudes and phases, which include $B^0 \to D^-K^+$ and $B^0 \to \overline{D}^0\pi^0$ events, 18 PDF shape parameters (See Table 4.5), and the yields of signal, continuum, and B-background (classes $9, 10, 19$ only) events. Those B-backgrounds not determined in the fit are fixed to their expected yields and varied systematically as an additional source of systematic error. The fit is repeated 1000 times, starting from input parameter values randomly chosen within wide ranges of one order of magnitude above and below the nominal values for the amplitudes and within the $[-\pi, \pi]$ interval for the phases. Four solutions corresponding to different arrangements of interference among the resonances in the Dalitz model are found. The best solution is separated by 5.43 units of NLL (3.3σ) from the next best solutions. The fitted phases Φ, $\overline{\Phi}$, CP asymmetries and fit fractions are given in Table 4.9 for the four solutions. The fitted event yields for the best solution is given in Table 4.8.

Table 4.8: Fitted event yields for the best solution. Errors are statistical only. The continuum background yields are separated by tagging category.

Parameter Name	Fit Result
`NLL`	-203025.722
`N(`$B^0 \to K^+\pi^-\pi^0$`)`	4583 ± 107
`N(class 10)`	598 ± 56
`N(class 11)`	424 ± 77
`N(class 19)`	564 ± 112
`N(cont-KaonI)`	725 ± 32
`N(cont-KaonII)`	2194 ± 53
`N(cont-KaonPion)`	1982 ± 51
`N(cont-Lepton)`	54 ± 11
`N(cont-NoTag)`	7053 ± 92
`N(cont-Other)`	1896 ± 48
`N(cont-Pion)`	2380 ± 55

The validity of the fit is checked by generating 100 toy experiments with the fitted yields and isobars of the best solution and observing that the NLL of the data fit is consistent with the distribution of NLLs in the toy experiments. The distribution

of likelihood ratios for data and toy experiments are in good agreement as shown in Fig. 4.18. The goodness of fit to the Dalitz distribution is calculated with a χ^2 of 772 for 644 bins where at least 25 events are guaranteed to exits in each bin.

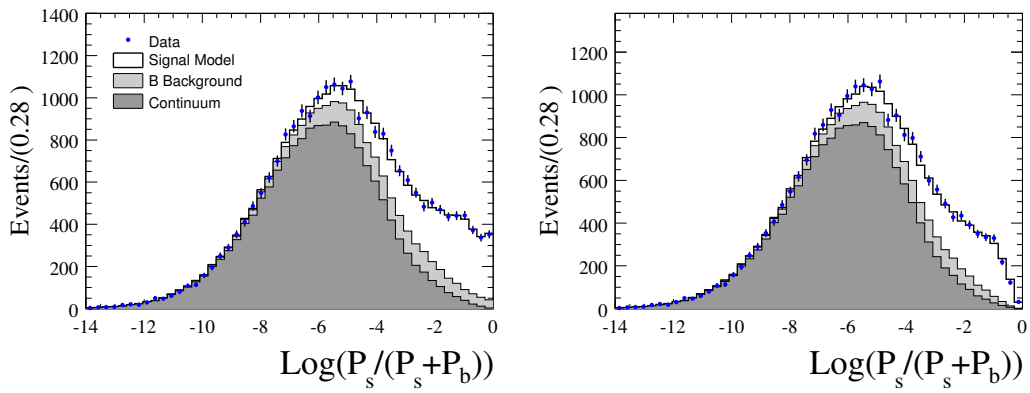

Figure 4.18: Distributions of the log likelihood for all events (left) and for events excluding the D region $1.8 < m_{K^+\pi^-} < 1.9$ GeV (right). The data are shown as points with error bars. The solid histograms show the projection of the fit result where the signal model includes both TM and SCF contributions.. The dark and light gray shaded areas represent the B background and continuum, respectively.

The Dalitz plot mass distributions are shown in Fig. 4.23. The ρ^-, K^{*+}, and K^{*0} are clearly visible in an enlargement of the low-mass resonance region (masses below 2.0 GeV/c^2) in the $m_{\pi^-\pi^0}$, $m_{K^+\pi^0}$, $m_{K^+\pi^-}$ distributions respectively. The distributions of the discriminating variables ($m_{\rm ES}$, $\Delta E'$and NN) are shown in Fig. 4.19 and projections of the Dalitz coordinates are shown in Fig. 4.20.

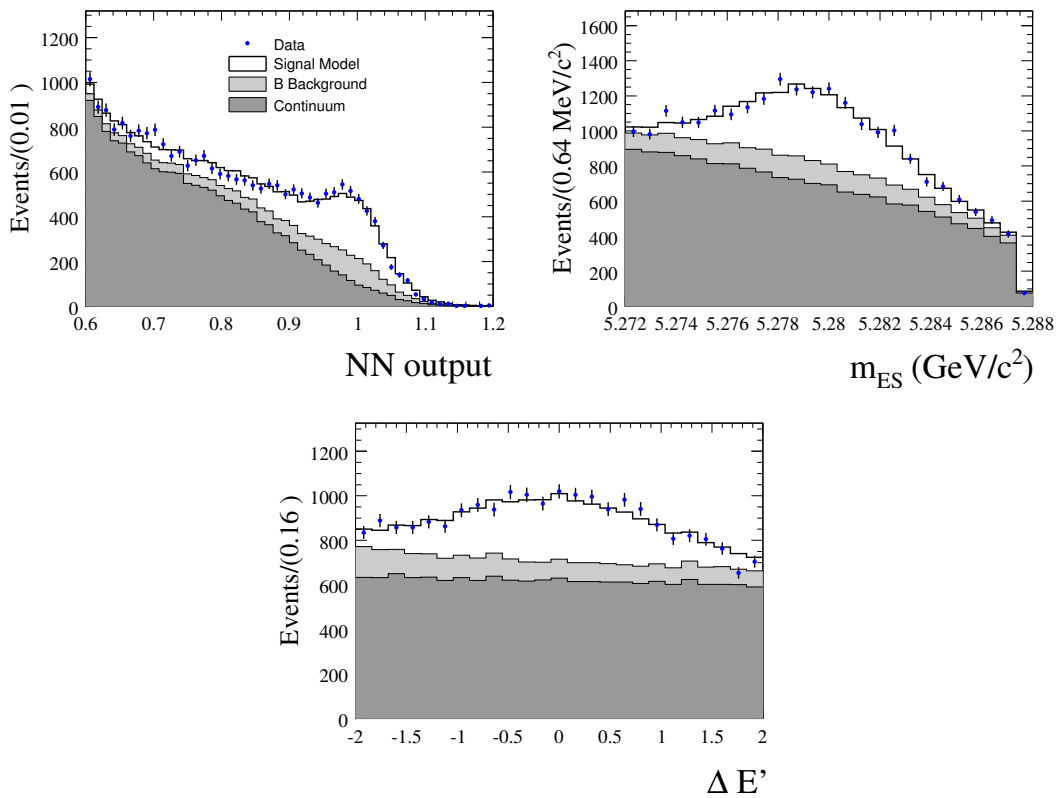

Figure 4.19: NN distributions (top left) $m_{\rm ES}$ (top right) and $\Delta E'$ (bottom). The data are shown as points with error bars. The solid histograms show the projection of the fit result where the signal model includes both TM and SCF contributions. The dark and light gray shaded areas represent the B-background and continuum, respectively.

Table 4.9: Results of the four solutions of the fit. The fractions are the CP-averaged isobar fractions (FF_k). The phases Φ for the B^0 decays and $\overline{\Phi}$ for the $\overline{B}^0$ decays are measured relative to $B^0(\overline{B}^0) \to \rho^{\mp}\pi^{\pm}$ in radians. The uncertainties are statistical only. The correlation matrix for Solution-I is given in Appendix C

Amplitude	Parameter	Solution-I	Solution-II	Solution-III	Solution-IV
	NLL	-203025.722	-203020.2928	-203018.6791	-203013.3964
$\rho^-(770)K^+$	FF (%)	13.77 ± 0.91	13.78 ± 1.56	13.42 ± 1.30	13.44 ± 2.29
	$A_{\rm CP}$	0.20 ± 0.09	0.19 ± 0.11	0.18 ± 0.09	0.17 ± 0.12
	$\overline{\Phi}$	0 (fixed)	0 (fixed)	0 (fixed)	0 (fixed)
	Φ	0 (fixed)	0 (fixed)	0 (fixed)	0 (fixed)
$\rho^-(1450)K^+$	FF (%)	4.96 ± 2.17	4.18 ± 3.02	5.09 ± 1.49	4.29 ± 3.29
	$A_{\rm CP}$	-0.10 ± 0.32	0.09 ± 0.54	-0.09 ± 0.33	0.10 ± 0.55
	$\overline{\Phi}$	1.30 ± 0.33	1.29 ± 0.32	1.25 ± 0.35	1.24 ± 0.37
	Φ	2.20 ± 0.43	1.57 ± 0.39	2.20 ± 0.43	1.56 ± 0.38
$\rho^-(1700)K^+$	FF (%)	1.31 ± 1.18	0.54 ± 1.51	1.12 ± 0.88	0.32 ± 1.54
	$A_{\rm CP}$	-0.36 ± 0.57	0.61 ± 1.72	-0.62 ± 0.50	0.36 ± 2.37
	$\overline{\Phi}$	0.32 ± 0.63	0.30 ± 0.61	-0.27 ± 0.83	-0.29 ± 0.99
	Φ	0.87 ± 0.67	0.61 ± 2.86	0.88 ± 0.60	0.60 ± 2.78
$K^{*+}(892)\pi^-$	FF (%)	5.51 ± 0.79	5.53 ± 0.72	5.87 ± 1.01	5.89 ± 0.67
	$A_{\rm CP}$	-0.29 ± 0.11	-0.29 ± 0.11	-0.21 ± 0.11	-0.21 ± 0.11
	$\overline{\Phi}$	0.58 ± 0.38	0.57 ± 0.38	3.01 ± 0.35	3.00 ± 0.37
	Φ	0.68 ± 0.43	2.72 ± 0.44	0.68 ± 0.43	2.73 ± 0.44
$K^{*0}(892)\pi^0$	FF (%)	4.59 ± 0.75	4.61 ± 0.68	4.65 ± 0.86	4.66 ± 0.63
	$A_{\rm CP}$	-0.15 ± 0.12	-0.16 ± 0.12	-0.14 ± 0.12	-0.14 ± 0.12
	$\overline{\Phi}$	0.51 ± 0.32	0.50 ± 0.32	0.16 ± 0.32	0.16 ± 0.33
	Φ	0.30 ± 0.35	0.29 ± 0.37	0.29 ± 0.36	0.28 ± 0.37
$(K\pi)_0^{*+}\pi^-$	FF (%)	23.69 ± 1.57	24.88 ± 2.25	24.90 ± 2.31	26.11 ± 1.27
	$A_{\rm CP}$	0.07 ± 0.14	0.02 ± 0.15	0.12 ± 0.05	0.07 ± 0.05
	$\overline{\Phi}$	-2.92 ± 0.28	-2.93 ± 0.28	-0.66 ± 0.31	-0.67 ± 0.34
	Φ	-2.27 ± 0.38	-0.34 ± 0.44	-2.27 ± 0.38	-0.33 ± 0.43
$(K\pi)_0^{*0}\pi^0$	FF (%)	11.96 ± 1.58	17.86 ± 1.76	16.67 ± 1.61	22.71 ± 1.48
	$A_{\rm CP}$	-0.15 ± 0.10	-0.43 ± 0.08	0.18 ± 0.07	-0.13 ± 0.06
	$\overline{\Phi}$	0.22 ± 0.29	0.22 ± 0.30	0.01 ± 0.24	0.01 ± 0.25
	Φ	0.18 ± 0.30	0.36 ± 0.30	0.17 ± 0.30	0.36 ± 0.30
NR	FF (%)	5.86 ± 1.11	4.06 ± 0.83	5.25 ± 1.07	3.45 ± 1.02
	$A_{\rm CP}$	0.10 ± 0.16	0.62 ± 0.20	-0.01 ± 0.22	0.53 ± 0.24
	$\overline{\Phi}$	0.84 ± 0.25	0.83 ± 0.25	-1.13 ± 0.27	-1.14 ± 0.29
	Φ	1.52 ± 0.36	-1.07 ± 0.39	1.52 ± 0.36	-1.06 ± 0.38
$\overline{D}^0\pi^0$	FF (%)	20.86 ± 3.69	20.71 ± 2.03	20.66 ± 1.10	20.51 ± 0.99
	$A_{\rm CP}$	0.02 ± 0.04	0.03 ± 0.14	0.01 ± 0.11	0.02 ± 0.04
D^-K^+	FF (%)	0.94 ± 0.26	0.98 ± 0.28	1.00 ± 0.29	1.03 ± 0.28
	$A_{\rm CP}$	0.19 ± 0.27	0.15 ± 0.25	0.23 ± 0.23	0.20 ± 0.24

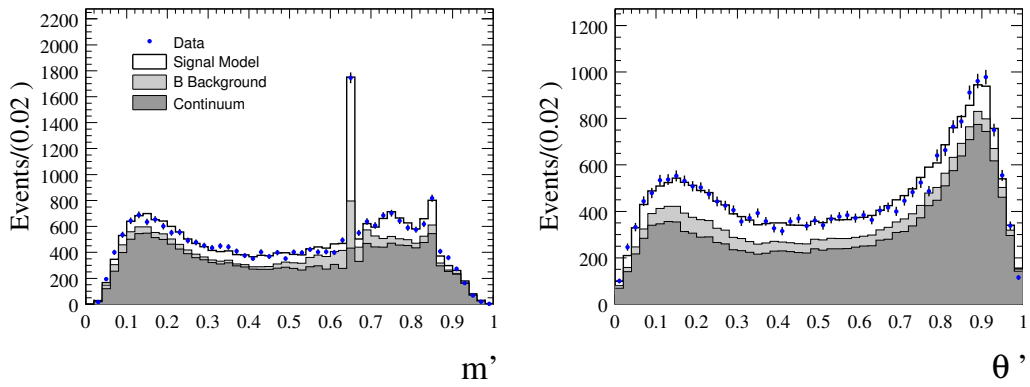

Figure 4.20: Dalitz projections for: m'(left), θ'(right). The data are shown as points with error bars. The solid histograms show the projection of the fit result where the signal model includes both TM and SCF contributions. The dark and light gray shaded areas represent the B-background and continuum, respectively.

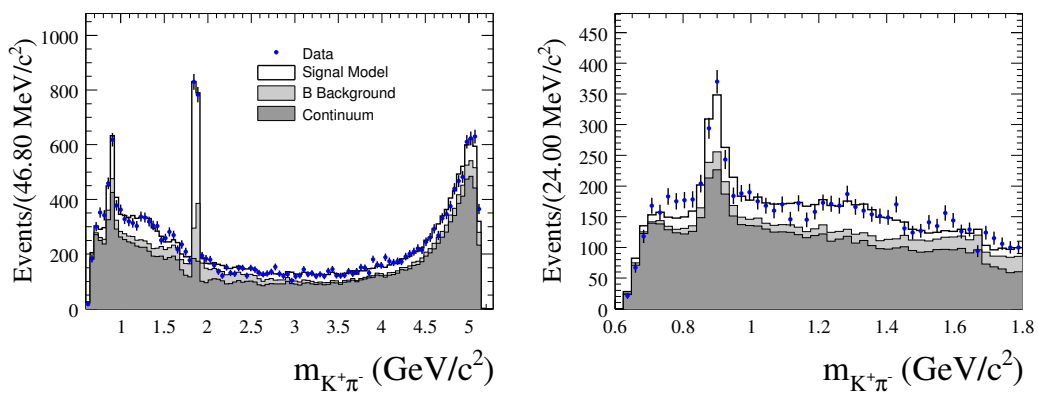

Figure 4.21: $m_{K^+\pi^-}$ mass distributions for all events (left) and for events in $m_{K^+\pi^-} < 1.8\,\mathrm{GeV}/c^2$ (right). The data are shown as points with error bars. The solid histograms show the projection of the fit result where the signal model includes both TM and SCF contributions. The dark and light gray shaded areas represent the B-background and continuum, respectively.

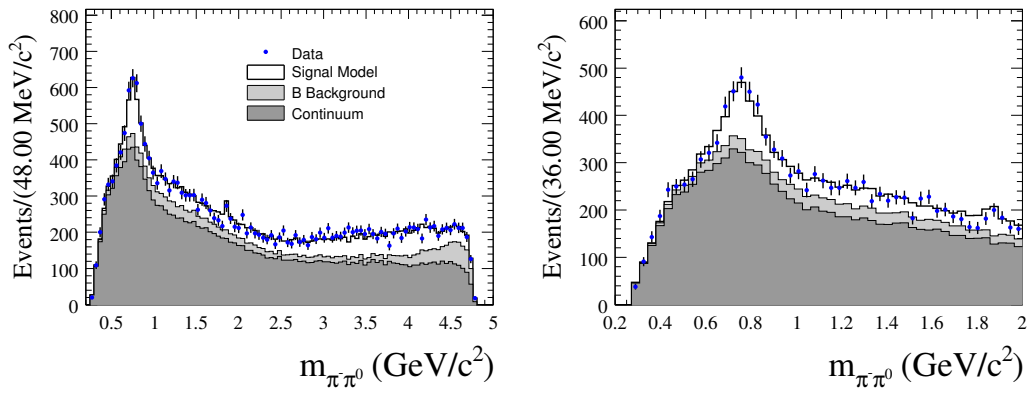

Figure 4.22: $m_{\pi^-\pi^0}$ mass distributions for all events (left) and $m_{\pi^-\pi^0} < 2\,\mathrm{GeV}/c^2$ (right). The data are shown as points with error bars. The solid histograms show the projection of the fit result where the signal model includes both TM and SCF contributions. The dark and light gray shaded areas represent the B background and continuum, respectively.

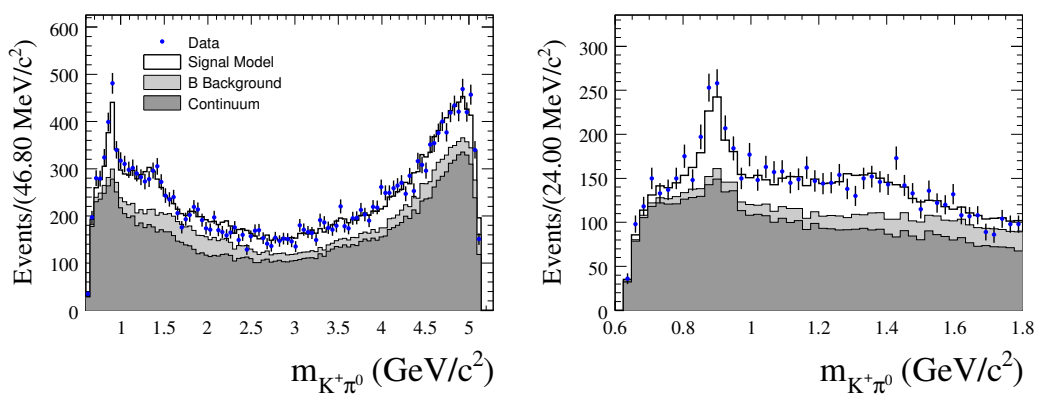

Figure 4.23: $m_{K^+\pi^0}$ mass distributions for all events (left) and $m_{K^+\pi^0} < 1.8\,\mathrm{GeV}/c^2$ (right). The data are shown as points with error bars. The solid histograms show the projection of the fit result where the signal model includes both TM and SCF contributions. The dark and light gray shaded areas represent the B background and continuum, respectively.

4.9 Estimation of Systematic Uncertainty

In order to estimate the systematic uncertainty inherent in the analysis ansatz we perform a series of fits to the dataset with models which vary from those in the nominal fitting procedure. For each parameter of interest (FF, $A_{\rm CP}$, Φ), the positive (negative) deviations from each effect are summed in quadrature to obtain total upward (downward) systematic errors. We vary the number of resonances contributing to the signal model, the line shape parameters of the resonances in the signal model, the yields of the nominally fixed B-backgrounds, and the shape of the modeled continuum Dalitz distribution. The intrinsic bias of the fit as measured in MC studies, is also included as a source of systematic error. Tables of the systematic uncertainties are shown in Table 4.12 - Table 4.14.

4.9.1 Dalitz Model

In addition to the resonances contributing to the nominal Dalitz model (Section 2.5.1) it is also possible for the $K_2^{*0}(1430)\pi^0$, $K_2^{*+}(1430)\pi^-$, $K^{*0}(1680)\pi^0$ and $K^{*+}(1680)\pi^-$ intermediate decay amplitudes to contribute to the $K^+\pi^-\pi^0$ final state. Since these decays have small branching fractions and since the amount of time required for a fit to data to converge is a rapidly increasing function of the number of fitted parameters, we choose not to include them in the nominal Dalitz model. We estimate the effect of excluding the contributions of the additional excited K^* resonances by generating a sample of 100 pure toy datasets including models of the additional K^* contributions and fitting these datasets with only the nominal Dalitz model.

In order to obtain the values of the amplitudes and phases for the additional K^* states used to generate the toy samples, we perform a single fit to the dataset where the additional K^* states have been included. The FF, $A_{\rm CP}$, and phases determined from this fit for the additional resonances are shown in Table 4.11. The improvement in the NLL of the fit shown in Table 4.11 is due to the presence of the additional resonances in the Dalitz model and is not due to the discovery of a more likely interference pattern of the nominal resonances. The significant improvement in likelihood is observed only when all of the additional resonances are included in the fit and does

Table 4.10: The line shape parameters of the additional $K_2^{*0}(1430)$, $K_2^{*+}(1430)$, $K^{*0}(1680)$ and $K^{*+}(1680)$ resonances.

Resonance	Line Shape	Parameters
	Spin-$J = 1$	
$K^{*0}(1680)$	RBW	$M = 1717$ MeV/c^2
		$\Gamma^0 = 322$ MeV
		$R = 1.5$ (GeV)$^{-1}$
$K^{*+}(1680)$	RBW	$M = 1717$ MeV/c^2
		$\Gamma^0 = 322$ MeV
		$R = 1.5$ (GeV)$^{-1}$
	Spin-$J = 2$	
$K_2^{*0}(1430)$	RBW	$M = 1432$ MeV/c^2
		$\Gamma^0 = 109$ MeV
		$R = 1.5$ (GeV)$^{-1}$
$K_2^{*+}(1430)$	RBW	$M = 1425$ MeV/c^2
		$\Gamma^0 = 98.5$ MeV
		$R = 1.5$ (GeV)$^{-1}$

not reflect observation of any single resonant contribution.

We use the magnitues and phases for the $K_2^{*0}(1430)\pi^0$, $K_2^{*+}(1430)\pi^-$, $K^{*0}(1680)\pi^0$ and $K^{*+}(1680)\pi^-$ amplitudes given in Table 4.11 to generate 100 pure toy datasets including these resonant contributions. We then fit these data sets with only the nominal model of resonances. The average observed shifts in the nominal magnitudes and phases are recorded as *Dalitz Model* systematic uncertainties.

4.9.2 Line Shapes

Since recomputing the numerical Dalitz plot integrals in Section 4.6.1 is time consuming, we fix the parameters of the line shapes to the values given in Table 2.5 in fits to data. We vary the masses and widths of the nominal resonances within their measured uncertainties [13] in a series of fits to data by $\pm 1\sigma$ to estimate the uncertainty due to not fitting for the resonant masses and widths. Observed shifts in the

Table 4.11: Results of the fit to data including the $K_2^{*0}(1430)\pi^0$, $K_2^{*+}(1430)\pi^-$, $K^{*0}(1680)\pi^0$ and $K^{*+}(1680)\pi^-$ amplitudes. The fractions are the CP-averaged isobar fractions (FF_k). The phases Φ for the B^0 decays and $\overline{\Phi}$ for the $\overline{B}^0$ decays are measured relative to $B^0(\overline{B}^0) \to \rho^\mp\pi^\pm$ in radians. The uncertainties are statistical only.

Amplitude	Parameter	Additional K^* Solution
	NLL	-203049.546
$K^{*+}(1680)\pi^-$	FF (%)	0.84 ± 0.70
	$A_{\rm CP}$	-1.00 $^{+2.00}_{-0.00}$
	$\overline{\Phi}$	-1.96 ± 3.14
	Φ	-2.14 ± 0.47
$K^{*0}(1680)\pi^0$	FF (%)	0.66 ± 0.39
	$A_{\rm CP}$	-0.02 ± 0.51
	$\overline{\Phi}$	1.34 ± 0.99
	Φ	1.42 ± 0.57
$K_2^{*+}(1430)\pi^-$	FF (%)	1.00 ± 0.80
	$A_{\rm CP}$	-0.47 ± 0.67
	$\overline{\Phi}$	-0.51 ± 0.55
	Φ	-0.21 ± 0.37
$K_2^{*0}(1430)\pi^0$	FF (%)	0.81 ± 0.59
	$A_{\rm CP}$	-0.70 ± 0.52
	$\overline{\Phi}$	2.16 ± 0.74
	Φ	2.18 ± 0.35

physical parameters are recorded as *Line Shape* systematic uncertainties.

4.9.3 B-backgrounds

Unless otherwise noted, the yields of the B-background contributions to the dataset are fixed to their expected values given the measured branching fractions and efficiencies shown in Table 4.3. To estimate the systematic uncertainty due to fixing these yields, we float each of the B-background contributions in a series of fits to data. We record the varations in the physical parameters as *B-background* systematic uncertainties.

4.9.4 Continuum Dalitz Model

Continuum events are the dominant background contributing 69% of the total 23468 selected events. Consequently, mis-modeling of the continuum Dalitz distribution is an important source of systematic uncertainty in the measured amplitudes and phases of the contributions to the signal Dalitz model. We estimate the systematic uncertainty due to continuum Dalitz distribution mis-modeling due to both the kinematic differences between events selected inside and outside the $m_{\rm ES}$ signal region and mis-estimation of the true Dalitz distribution from the smoothing procedure.

Due to the limited amount of off-peak events recorded at *BABAR* the continuum Dalitz distribution is modeled from the $m_{\rm ES}$ sideband as described in Section 4.6.1. Events in the $m_{\rm ES}$ sideband are necessarily higher momentum than those near the signal peak and hence have a different Dalitz distribution. To quantify the effect of modeling the $m_{\rm ES}$ on-peak continuum Dalitz distribution with off-peak events we use a high statistics sample of $q\overline{q}$ MC to create a model of the continuum Dalitz distribution from the $m_{\rm ES}$ signal region. We then generate a sample of 100 toy datasets with the $m_{\rm ES}$ signal region continuum Dalitz model and fit each of these with both the signal region and off-peak models of the continuum Dalitz distribution. The average difference observed in the physical parameters between fits with each of the continuum Dalitz models is recorded as the *Continuum Dalitz* systematic uncertainty.

In order to study the effect of mis-modeling of the shape of the continuum Dalitz distribution with the nominal smoothing parameter, we recreate the continuum Dalitz PDF with smoothing parameters, 0.1 and 0.5. We refit the data using these alternate continuum Dalitz PDFs and record the variations in the physical resonance parameters as a *PDF Shape Parameter* systematic.

4.9.5 SCF Fraction

The SCF fractions listed in Table 4.4 are determined from high statistics samples of MC which may not perfectly reflect the fraction of mis-reconstructed events in data. We estimate effect of mis-estimating the SCF fractions in MC by are varying their nominal values by $\pm 10\%$ in a pair of fits to data. The average shift in the physical

parameters is recorded as a *SCF Fraction* systematic.

4.9.6 PID

The efficiency to identify a particle correctly (See Fig. 3.12) is slightly different for MC and data. Since the efficiency across the Dalitz plot is measured in MC events we must apply a weighting ($\epsilon_{\rm Data}/\epsilon_{\rm MC}$) to each reconstructed event in order to produce a corrected Dalitz plot efficiency. We refit the data with the PID corrected Dalitz plot efficiecy and record the shift in the physical parameters as a *PID* systematic.

4.9.7 Fit Bias

The correlations between variables in the fit cannot be perfectly removed and result in a small *Fit Bias* intrinsic to the analysis procedure. We record the pulls in physical parameters shown in Table 4.7 as a source of systematic uncertainty.

Table 4.12: Summary of systematic uncertainties associated with the $B^0 \to \rho^- K^+$ amplitudes. Uncertainties in the phases are given in radians

Amplitude		Fit Fraction (%)	$A_{\rm CP}$	Φ	$\overline{\Phi}$
$\rho^-(770)K^+$	DalitzModel	0.742	0.071	fixed	fixed
	B Backgrounds	0.048	0.005	fixed	fixed
	PDF Shape Parameters	0.459	0.022	fixed	fixed
	SCF Fraction	0.007	0.004	fixed	fixed
	PID Systematics	0.084	0.009	fixed	fixed
	LineShapes	0.232	0.013	fixed	fixed
	Fit Bias	0.436	0.007	fixed	fixed
	Continuum Dalitz	0.180	0.008	fixed	fixed
	Total	**1.024**	**0.076**	**fixed**	**fixed**
$\rho^-(1450)K^+$	DalitzModel	0.778	0.016	0.444	0.084
	B Backgrounds	0.148	0.009	0.009	0.016
	PDF Shape Parameters	0.371	0.042	0.010	0.038
	SCF Fraction	0.122	0.008	0.007	0.020
	PID Systematics	0.200	0.026	0.013	0.008
	LineShapes	0.496	0.044	0.092	0.094
	Fit Bias	0.125	0.049	0.027	0.076
	Continuum Dalitz	0.005	0.030	0.017	0.055
	Total	**1.040**	**0.090**	**0.455**	**0.164**
$\rho^-(1700)K^+$	DalitzModel	0.239	0.067	0.285	0.214
	B Backgrounds	0.071	0.012	0.034	0.060
	PDF Shape Parameters	0.075	0.033	0.046	0.008
	SCF Fraction	0.019	0.011	0.008	0.016
	PID Systematics	0.028	0.021	0.026	0.007
	LineShapes	0.411	0.169	0.183	0.149
	Fit Bias	0.523	0.124	0.074	0.013
	Continuum Dalitz	0.079	0.021	0.005	0.072
	Total	**0.720**	**0.225**	**0.352**	**0.278**

Table 4.13: Summary of systematic uncertainties associated with the $B^0 \to K^*\pi$ amplitudes. Uncertainties in the phases are given in radians

Amplitude		Fit Fraction (%)	$A_{\rm CP}$	Φ	$\overline{\Phi}$
$K^{*+}(892)\pi^-$	DalitzModel	0.045	0.008	0.281	0.327
	B Backgrounds	0.038	0.001	0.016	0.017
	PDF Shape Parameters	0.076	0.014	0.053	0.020
	SCF Fraction	0.002	0.001	0.014	0.012
	PID Systematics	0.041	0.000	0.006	0.015
	LineShapes	0.077	0.007	0.165	0.076
	Fit Bias	0.052	0.013	0.109	0.106
	Continuum Dalitz	0.081	0.001	0.035	0.023
	Total	**0.162**	**0.022**	**0.350**	**0.354**
$(K\pi)_0^{*+}$	DalitzModel	1.082	0.003	0.324	0.626
	B Backgrounds	0.093	0.001	0.013	0.015
	PDF Shape Parameters	0.488	0.002	0.056	0.014
	SCF Fraction	0.013	0.001	0.015	0.012
	PID Systematics	0.277	0.001	0.002	0.009
	LineShapes	0.207	0.005	0.144	0.060
	Fit Bias	0.724	0.000	0.106	0.111
	Continuum Dalitz	0.698	0.002	0.077	0.093
	Total	**1.597**	**0.007**	**0.382**	**0.646**
$K^{*0}(892)\pi^0$	DalitzModel	0.098	0.035	0.038	0.005
	B Backgrounds	0.037	0.002	0.013	0.013
	PDF Shape Parameters	0.061	0.004	0.023	0.011
	SCF Fraction	0.012	0.001	0.002	0.004
	PID Systematics	0.043	0.003	0.016	0.002
	LineShapes	0.103	0.009	0.067	0.071
	Fit Bias	0.244	0.013	0.023	0.012
	Continuum Dalitz	0.197	0.006	0.112	0.083
	Total	**0.354**	**0.040**	**0.141**	**0.112**
$(K\pi)_0^{*0}$	DalitzModel	0.544	0.020	0.242	0.158
	B Backgrounds	0.112	0.006	0.014	0.020
	PDF Shape Parameters	0.026	0.008	0.025	0.023
	SCF Fraction	0.123	0.005	0.004	0.008
	PID Systematics	0.129	0.004	0.001	0.005
	LineShapes	0.370	0.026	0.065	0.099
	Fit Bias	0.624	0.008	0.022	0.023
	Continuum Dalitz	0.900	0.024	0.106	0.070
	Total	**1.295**	**0.044**	**0.274**	**0.202**

Table 4.14: Summary of systematic uncertainties associated with the NR amplitude and non-interfering D contributions. Uncertainties in the phases are given in radians

Amplitude		Fit Fraction (%)	$A_{\rm CP}$	Φ	$\overline{\Phi}$
NR	DalitzModel	0.131	0.016	0.226	0.018
	B Backgrounds	0.057	0.002	0.010	0.015
	PDF Shape Parameters	0.296	0.018	0.019	0.051
	SCF Fraction	0.007	0.001	0.007	0.020
	PID Systematics	0.086	0.003	0.000	0.009
	LineShapes	0.270	0.025	0.138	0.073
	Fit Bias	0.375	0.066	0.010	0.033
	Continuum Dalitz	0.243	0.006	0.024	0.044
	Total	**0.623**	**0.075**	**0.267**	**0.109**
$\overline{D}^0\pi^0$	DalitzModel	0.233	0.000	-	-
	B Backgrounds	0.053	0.000	-	-
	PDF Shape Parameters	1.065	0.000	-	-
	SCF Fraction	0.062	0.000	-	-
	PID Systematics	0.026	0.000	-	-
	LineShapes	0.225	0.000	-	-
	Fit Bias	0.457	0.002	-	-
	Continuum Dalitz	0.401	0.000	-	-
	Total	**1.271**	**0.002**	**-**	**-**
D^-K^+	DalitzModel	0.011	0.000	-	-
	B Backgrounds	0.002	0.000	-	-
	PDF Shape Parameters	0.048	0.000	-	-
	SCF Fraction	0.003	0.000	-	-
	PID Systematics	0.001	0.000	-	-
	LineShapes	0.010	0.000	-	-
	Fit Bias	0.314	0.051	-	-
	Continuum Dalitz	0.018	0.000	-	-
	Total	**0.318**	**0.051**	**-**	**-**

Chapter 5

Results

In this section we combine the results of the $B^0 \to K^+\pi^-\pi^0$ and $B^0 \to K_S\pi^+\pi^-$ Dalitz analyses to produce a constraint on the CKM triangle and measurement of the $K^{*+}(892)\pi^-$ CP asymmetry. The $B^0 \to K_S\pi^+\pi^-$ Dalitz analysis using the *BABAR* dataset is presented in [31]. We summarize the results of the $B^0 \to K^+\pi^-\pi^0$ Dalitz analysis and proceed to produce a measurement of $\Delta\phi_{\frac{3}{2}}$. This result is combined with measurements of $\Delta\phi_{K^*\pi}$ [31] and $r_{\frac{3}{2}}$ (See Appendix A) to constrain the CKM triangle. Measurements of the $K^{*+}(892)\pi^-$ CP asymmetry from the $B^0 \to K^+\pi^-\pi^0$ and $B^0 \to K_S\pi^+\pi^-$ Dalitz analyses are combined to show evidence of direct CP violation in $B^0 \to K^{*+}(892)\pi^-$ decays.

The results of the $B^0 \to K^+\pi^-\pi^0$ Dalitz analysis are summarized in Table 5.1. The total branching fractions are calculated from the fit fractions via the relationship

$$\mathcal{B}_k = FF_k \times \frac{N_{\text{Sig}}}{N_{B\overline{B}}\langle\epsilon\rangle_{DP}}, \tag{5.1}$$

where we assume isospin symmetry in $K^* \to K\pi$ decays. In addition to the systematic errors described in Section 4.9 we account for a 1.1% systematic error from B counting, a 2% systematic from π^0 efficiency, and a 0.236% systematic from tracking efficiency in the calculation of the branching fraction systematic uncertainties. When contributions from $B^0 \to D^-K^+$ and $B^0 \to \overline{D}^0\pi^0$ decays are excluded, we measure a signal yield of 3670 ± 96 (stat.) $\pm\, 94$ (syst.) events corresponding to a $B^0 \to K^+\pi^-\pi^0$

branching fraction of $\mathcal{B}(B^0 \to K^+\pi^-\pi^0) = 38.5 \pm 1.0$ (stat.) $\pm$ 3.9 (syst.) $\times 10^{-6}$.

Table 5.1: The branching fractions are the CP-averaged branching fractions ($\mathcal{B}_k$) defined with the CP asymmetries, $A_{\rm CP}$ in Eq. (2.32). The phases Φ for the B^0 decays and $\overline{\Phi}$ for the $\overline{B}^0$ decays are measured relative to $B^0(\overline{B}^0) \to \rho(770)^{\mp}K^{\pm}$. The first error is statistical and the second is systematic. When the elastic range term is separated from the $K\pi$ S-wave we determine the total NR branching fraction $\mathcal{B}_{\rm NR} = 7.6 \pm 0.5$ (stat.) $\times 10^{-6}$ and the resonant $K_0^*(1430)\pi$ branching fractions $\mathcal{B}_{K_0^*(1430)^+\pi^-} = 27.8 \pm 2.5$ (stat.) $\times 10^{-6}$, $\mathcal{B}_{K_0^*(1430)^0\pi^0} = 7.0 \pm 0.5$ (stat.) $\times 10^{-6}$.

Isobar Amplitude	$\mathcal{B}$ ($\times 10^{-6}$)	$\overline{\Phi}$ [°]	Φ [°]	$A_{\rm CP}$
$\rho(770)^-K^+$	$6.6 \pm 0.5 \pm 0.8$	0 (fixed)	0 (fixed)	$0.20 \pm 0.09 \pm 0.08$
$\rho(1450)^-K^+$	$2.4 \pm 1.0 \pm 0.6$	$75 \pm 19 \pm 9$	$126 \pm 25 \pm 26$	$-0.10 \pm 0.32 \pm 0.09$
$\rho(1700)^-K^+$	$0.6 \pm 0.6 \pm 0.4$	$18 \pm 36 \pm 16$	$50 \pm 38 \pm 20$	$-0.36 \pm 0.57 \pm 0.23$
$K^*(892)^+\pi^-$	$8.0 \pm 1.1 \pm 0.8$	$33 \pm 22 \pm 20$	$39 \pm 25 \pm 20$	$-0.29 \pm 0.11 \pm 0.02$
$K^*(892)^0\pi^0$	$3.3 \pm 0.5 \pm 0.4$	$29 \pm 18 \pm 6$	$17 \pm 20 \pm 8$	$-0.15 \pm 0.12 \pm 0.04$
$(K\pi)_0^{*+}\pi^-$	$34.2 \pm 2.4 \pm 4.1$	$-167 \pm 16 \pm 37$	$-130 \pm 22 \pm 22$	$0.07 \pm 0.14 \pm 0.01$
$(K\pi)_0^{*0}\pi^0$	$8.6 \pm 1.1 \pm 1.3$	$13 \pm 17 \pm 12$	$10 \pm 17 \pm 16$	$-0.15 \pm 0.10 \pm 0.04$
NR	$2.8 \pm 0.5 \pm 0.4$	$48 \pm 14 \pm 6$	$90 \pm 21 \pm 15$	$0.10 \pm 0.16 \pm 0.08$

5.1 Constraint on the Apex of the CKM triangle

The expression for $\Delta\phi_{\frac{3}{2}}$ in Eq. (2.45) is used to impose a constraint in a series of fits to the selected $B^0 \to K^+\pi^-\pi^0$ dataset. Values of $\Delta\phi_{\frac{3}{2}}$ are constrained in increments of 3.6° where 30 fits for randomized initial values of the isobars are completed for each point. The minimum value of the NLL for the 30 fits is recorded at each point and twice the change in the NLL relative to the most likely value of $\Delta\phi_{\frac{3}{2}}$ is plotted against the constrained values of $\Delta\phi_{\frac{3}{2}}$ (See Fig. 5.1). The amplitudes $A_{K^{*0}\pi^0}$ and $A_{K^{*+}\pi^-}$ represent the total amplitudes for K^* decays. The $B^0 \to K^+\pi^-\pi^0$ Dalitz analysis reconstructs only the final state $K^+\pi^-\pi^0$ so we must relate the partial amplitudes measured, to the total amplitude via isospin in order to evaluate Eq. (2.45) correctly.

$$\sqrt{\frac{2}{3}}A_{K^{*0}} = A_{K^{*0}\to K^+\pi^-} \qquad (5.2)$$
$$\sqrt{\frac{1}{3}}A_{K^{*+}} = A_{K^{*+}\to K^+\pi^0}$$

We measure $\Delta\phi_{\frac{3}{2}} = -7^{+15}_{-18}$ (stat.) $\pm$ 15 (syst.)°. It should be noted that the value of $\Delta\phi_{K^*\pi}$ reported in [31] does not remove the mixing phase contribution $2\beta = 42.2°$ [34] which must be subtracted in order to measure $\Phi_{\frac{3}{2}}$. The likelihood scans of $\Delta\phi_{\frac{3}{2}}$ and $\Delta\phi_{K^*\pi}$ are combined using Eq. (2.44) to produce a likelihood scan of the phase $\Phi_{\frac{3}{2}}$ in Fig. 5.1. We exclude the range $-81° < \Phi_{\frac{3}{2}} < -35°$ at the level of 2σ.
At present we do not use Eq. (2.47) to measure $\Phi_{\frac{3}{2}}$ from $B^0 \to \rho K$ decay amplitudes, however we do produce scans of the phase difference between ρK and $K^*\pi$ amplitudes, $\Delta\Phi_{\rho^-K^+} = \Phi_{\rho^-K^+} - \Phi_{K^{*+}\pi^-}$ and $\Delta\overline{\Phi}_{\rho^+K^-} = \overline{\Phi}_{\rho^+K^-} - \overline{\Phi}_{K^{*-}\pi^+}$ using the $B^0 \to K^+\pi^-\pi^0$ Dalitz analysis in Fig. 5.2. We measure $\Delta\Phi_{\rho^-K^+} = -33 \pm 22$ (stat.) $\pm$ 20 (syst.)° and $\Delta\overline{\Phi}_{\rho^+K^-} = -39 \pm 25$ (stat.) $\pm$ 20 (syst.)° (See Table 5.1).

Finally, we use the measurement of $\Phi_{\frac{3}{2}}$ shown in Fig. 5.1, the measurement of $r_{\frac{3}{2}}$, and Eq. (2.27) to produce a constraint on the apex of the CKM triangle. Two degenerate bands of likelihood are clearly visible as a result of the statistical degeneracy in the measurement of $\Delta\phi_{K^*\pi}$ in the $B^0 \to K_S\pi^+\pi^-$ analysis. The addition of data from the BELLE experiment could eliminate this degeneracy significantly improving

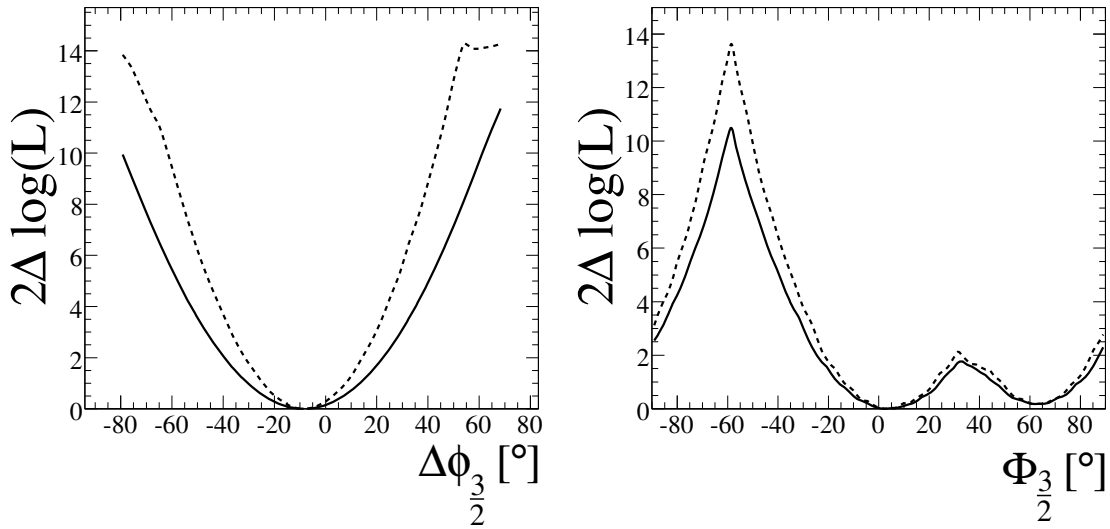

Figure 5.1: Likelihood Scans for $\Delta\phi_{\frac{3}{2}}$ (left) and $\Phi_{\frac{3}{2}}$ (right). The statistical uncertainty is shown in dashed lines and the total uncertainty is shown in solid. We measure $\Delta\phi_{\frac{3}{2}} = -7^{+15}_{-18}$ (stat.) $\pm$ 15 (syst.)$^\circ$ and exclude the range $-81^\circ < \Phi_{\frac{3}{2}} < -35^\circ$ at the level of 2σ.

the constraint.

5.2 Evidence of direct CP violation in $B^0 \to K^{*+}\pi^-$ decays

Measurements of direct CP violation are made from analyses of both the $B^0 \to K^+\pi^-\pi^0$ and $B^0 \to K_S\pi^+\pi^-$ Dalitz plots. Since these analyses are independent up to small detector effects the measurements of $A_{\rm CP}$ may be combined for intermediate resonances common to both. The combined measurement of direct CP violation for $B^0 \to K^{*+}(892)\pi^-$ decays is found to be $A_{\rm CP}(K^{*+}\pi^-) = -0.24 \pm 0.07$ (stat.) $\pm$ 0.02 (syst.). Likelihood scans illustrating the measurement of $A_{\rm CP}(K^{*+}\pi^-)$ in $B^0 \to K^+\pi^-\pi^0$ and the combined result including the measurement in $B^0 \to K_S\pi^+\pi^-$ are shown in Fig. 5.4.

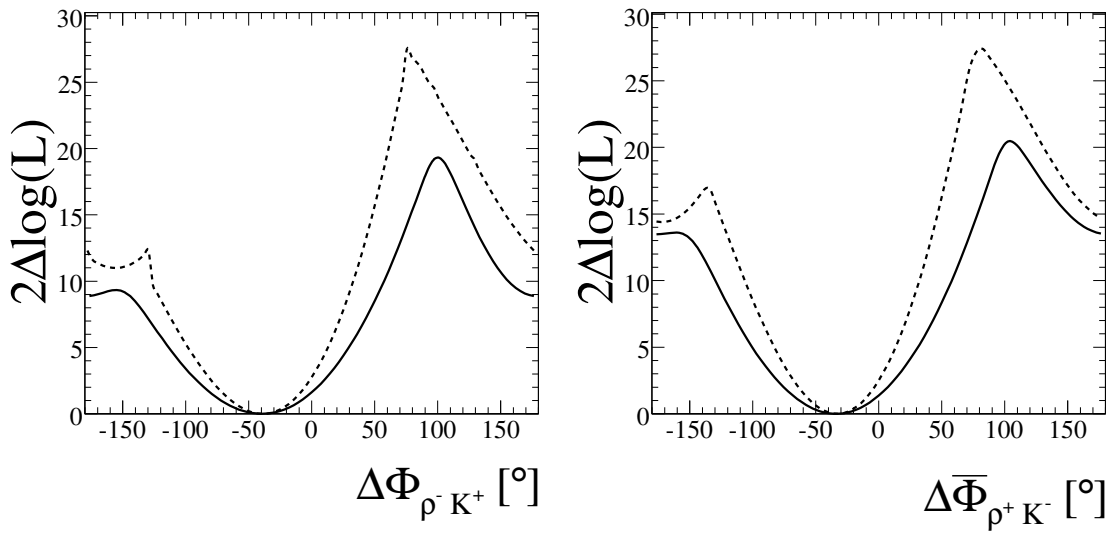

Figure 5.2: Likelihood Scans for $\Delta\Phi_{\rho^- K^+}$ (left) and $\Delta\overline{\Phi}_{\rho^+ K^-}$ (right). The statistical uncertainty is shown in dashed lines and the total uncertainty is shown in solid. We measure $\Delta\Phi_{\rho^- K^+} = -33 \pm 22$ (stat.) ± 20 (syst.)$^\circ$ and $\Delta\overline{\Phi}_{\rho^+ K^-} = -39 \pm 25$ (stat.) $\pm$ 20 (syst.)$^\circ$.

5.3 Conclusions

In summary, we analyze the Dalitz distribution for $B^0 \to K^+\pi^-\pi^0$ decays from a sample of 454 million $B\overline{B}$ pairs. We determine the branching fractions, CP asymmetries and phase differences of seven intermediate resonances in addition to a NR contribution. Combining this information with the phase difference $\Delta\phi_{K^*\pi}$ [31] we exclude the range $-81^\circ < \Phi_{\frac{3}{2}} < -35^\circ$ at the level of 2σ, via $K^*(892)\pi$ amplitudes. We additionally measure the ratio of hadronic matrix elements $r_{\frac{3}{2}} = (0.21 \pm 0.13$ (stat.) $\pm$ 0.77 (syst.) ± 0.06 (theo.)) $\pm\, i(1.45 \pm 0.35$ (stat.) ± 0.77 (syst.) ± 0.44 (theo.)) as described in Appendix A. We combine the measurements of $\Phi_{\frac{3}{2}}$ and $r_{\frac{3}{2}}$ to produce a constraint on the CKM triangle. We observe a constraint consistent with the existing world average. Finally, we find evidence of direct CP violation in $B^0 \to K^{*+}\pi^-$ decays, $A_{\rm CP}(K^{*+}\pi^-) = -0.24 \pm 0.07$ (stat.) ± 0.02 (syst.), combining measurements from the $B^0 \to K^+\pi^-\pi^0$ and $B^0 \to K_S\pi^+\pi^-$ [31] Dalitz analyses.

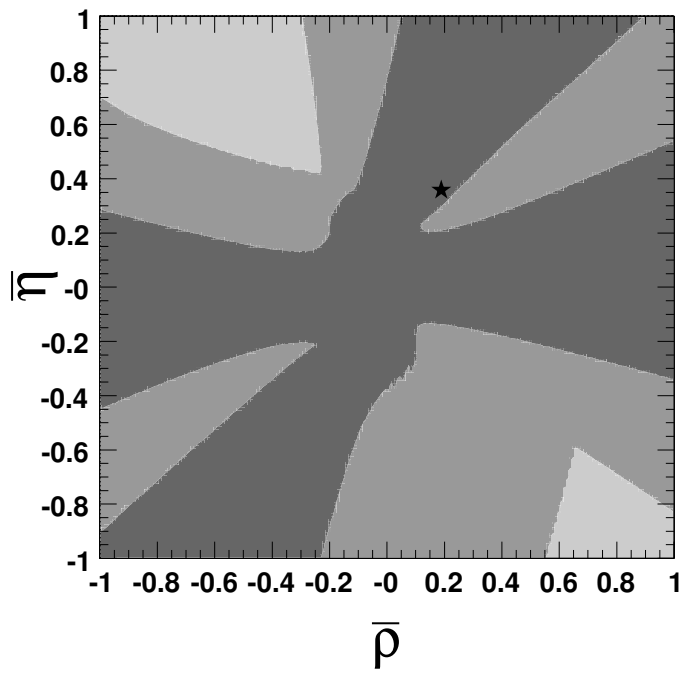

Figure 5.3: The constraint of the apex of the CKM triangle given in Eq. 2.27 for the measured values of $\Phi_{\frac{3}{2}}$ and $r_{\frac{3}{2}}$ in $\sqrt{2\log(L)} = 1, 2$ contours (darkest to lightest). The $\star$ indicates the world average value of the apex of the CKM triangle [7].

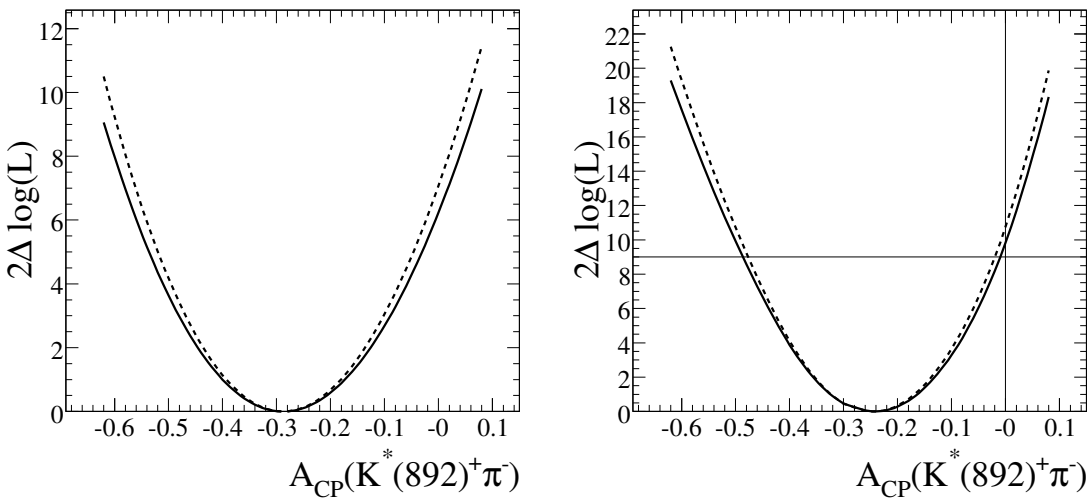

Figure 5.4: Likelihood Scans for $A_{\rm CP}(K^{*+}(892)\pi^-)$ using only the $B^0 \to K^+\pi^-\pi^0$ analysis (left) and the combined measurement with the $B^0 \to K_S\pi^+\pi^-$ analysis (right). The statistical uncertainty is shown in dashed lines and the total uncertainty is shown in solid. We measure $A_{\rm CP}(K^{*+}\pi^-) = -0.24 \pm 0.07$ (stat.) $\pm$ 0.02 (syst.) combining measurements from both $B^0 \to K^+\pi^-\pi^0$ and $B^0 \to K_S\pi^+\pi^-$ analyses (left).

Appendix A

Measurement of $r_{\frac{3}{2}}$

In this section we present a measurement of the ratio of hadronic matrix elements $r_{\frac{3}{2}}$, necessary to produce a constraint on the CKM triangle from measurements of $\Phi_{\frac{3}{2}}$. The expression given in Eq. (2.30) relates $r_{\frac{3}{2}}$ to measurable B^+ decay amplitudes. It is important to note that for a general $K^*\pi$ intermediate state, Eq. (2.30) must be modified by replacing the $B^+ \to (\rho\pi)^+$ amplitudes with $B^+ \to (\rho'\pi)^+$ amplitudes, where the ρ' are the $I = 1$ states in the same SU(3) octet as the K^*. If a ρK intermediate state is used to measure $\Phi_{\frac{3}{2}}$ then the corresponding value of $r_{\frac{3}{2}}$ is given by mulitiplying the expression in Eq. (2.30) by -1. Branching fractions and asymmetries relevant in evaluating Eq. (2.30) are shown in Table A.1.

A.1 Strategy

The expression for $r_{\frac{3}{2}}$ in terms of B^+ decay amplitudes is given in Eq. (2.30):

$$r_{\frac{3}{2}} = \frac{[A_{\rho^+\pi^0} - A_{\rho^0\pi^+}] - \sqrt{2}[A_{K^{*+}\overline{K}^0} - A_{K^+\overline{K}^{*0}}]}{A_{\rho^+\pi^0} + A_{\rho^0\pi^+}}. \tag{A.1}$$

We seek to measure $r_{\frac{3}{2}}$ via the simplified expression:

$$r_{\frac{3}{2}} \equiv \frac{A_{\rho^+\pi^0} - A_{\rho^0\pi^+}}{A_{\rho^+\pi^0} + A_{\rho^0\pi^+}}, \tag{A.2}$$

Table A.1: CP-averaged Branching fractions ($\mathcal{B}$) and CP asymmetries for $B \to \rho\pi$ and $B \to K^*K$ decays taken from [34]. Upper limits are quoted for those branching ratios consistent with 0.

	Decay Mode	$\mathcal{B}$ ($\times 10^{-6}$)	$A_{\rm CP}$
$B^+ \to$	$\rho^0\pi^+$	$8.3^{+1.2}_{-1.3}$	$0.18^{+0.09}_{-0.17}$
	$\rho^+\pi^0$	$10.9^{+1.4}_{-1.5}$	0.02 ± 0.11
	$K^+\overline{K}^{*0}$	< 1.1	-
	$K_S K_S \pi^+$	< 0.51	-
	$K^+\overline{K}^0\pi^0$	< 24	-
$B^0 \to$	$\rho^\pm\pi^\mp$	23.0 ± 2.3	-
	$\rho^0\pi^0$	2.0 ± 0.1	-

where the amplitude ratio

$$\sqrt{2}\frac{A_{K^{*+}\overline{K}^0} - A_{K^+\overline{K}^{*0}}}{A_{\rho^+\pi^0} + A_{\rho^0\pi^+}}, \tag{A.3}$$

will be estimated as a systematic error for both the real and imaginary parts of $r_{\frac{3}{2}}$. This ansatz is justified since the central value for $\mathcal{B}(B^+ \to K^+\overline{K}^{*0}) = 0.6 \pm 0.3(\text{stat.}) \pm 0.2(\text{syst.}) \times 10^{-6}$ [37] is small compared with the $\rho\pi$ branching fractions. Similarly, the $B^+ \to K^{*+}\overline{K}^0$ branching fraction, calculated from $\mathcal{B}(B^+ \to K_S K_S \pi^+) = 0.25 \pm 0.24(\text{stat.}) \pm 0.09(\text{syst.}) \times 10^{-6}$ [38], is also relatively small.

In order to exploit Eq. A.2 to meausre $r_{\frac{3}{2}}$ we must measure the magnitudes and phase differences of the $B^+ \to (\rho\pi)^+$ amplitudes. Since the amplitudes do not interfere, we can only measure their phase difference indirectly via an isospin pentagon relation:

$$A_{\rho^+\pi^0} + A_{\rho^0\pi^+} = \frac{1}{\sqrt{2}}(A_{\rho^+\pi^-} + A_{\rho^-\pi^+}) + \sqrt{2}A_{\rho^0\pi^0}. \tag{A.4}$$

Eq. A.2 may be used to derive a system of two equations that constrain $r_{\frac{3}{2}}$ in terms of observable amplitudes:

$$\mathrm{Im}(\mathrm{r}_{\frac{3}{2}})^2 + \left(\mathrm{Re}(\mathrm{r}_{\frac{3}{2}}) - \frac{|\mathrm{A}_{\rho^+\pi^0}|^2 + |\mathrm{A}_{\rho^0\pi^+}|^2}{|\mathrm{A}_{\rho^+\pi^0}|^2 - |\mathrm{A}_{\rho^0\pi^+}|^2}\right)^2 = \frac{4|\mathrm{A}_{\rho^+\pi^0}|^2|\mathrm{A}_{\rho^0\pi^+}|^2}{(|\mathrm{A}_{\rho^+\pi^0}|^2 - |\mathrm{A}_{\rho^0\pi^+}|^2)^2}, \tag{A.5}$$

$$\mathrm{Im}(\mathrm{r}_{\frac{3}{2}})^2 + \mathrm{Re}(\mathrm{r}_{\frac{3}{2}})^2 + 1 = \frac{2(|\mathrm{A}_{\rho^+\pi^0}|^2 + |\mathrm{A}_{\rho^0\pi^+}|^2)}{|\mathrm{A}_{\rho^+\pi^0} + \mathrm{A}_{\rho^0\pi^+}|^2}. \tag{A.6}$$

Note that relative phases appear in Eq. (A.6) only where Eq. (A.4) can be exploited to measure the phase difference in $B^0 \to (\rho\pi)^0$ amplitudes. The circular constraints in Eq. (A.5) and Eq. (A.6) intersect in two points symmetric about the real axis, so that $r_{\frac{3}{2}}$ is measured only up to the sign of its phase.

A.2 Measurement

Given the measured $B^+ \to \rho^+\pi^0$ and $B^+ \to \rho^0\pi^+$ branching fractions, (Table A.1) only the right hand side of the isospin amplitude relationship in Eq. A.4 remains to be determined. We perform a maximum likelihood fit to the bilinear interference terms measured in the $B^0 \to (\rho\pi)^0$ Dalitz analysis [39] with the full covariance matrix and systematic uncertainties. The fitted amplitudes and phases are shown in Table A.2.

Table A.2: Fitted magnitudes and phases from the $B^0 \to (\rho\pi)^0$ Dalitz analysis [39]. The phases Φ for the B^0 decays and $\overline{\Phi}$ for the $\overline{B}^0$ decays are measured relative to $B^0 \to \rho^+\pi^-$ in degrees. The error includes both the statistical and systematic errors from [39]. The amplitudes are comparable to the bilinear interference terms in [39] and are not scaled by the branching fractions listed in Table A.1.

	$\lvert A\rvert$	$\lvert\overline{A}\rvert$	$\Phi[^\circ]$	$\overline{\Phi}[^\circ]$
$\rho^+\pi^-$	0.87 ± 0.04	0.49 ± 0.07	0 (fixed)	1 ± 32
$\rho^-\pi^+$	0.69 ± 0.06	0.87 ± 0.05	22 ± 30	-156 ± 30
$\rho^0\pi^0$	0.36 ± 0.07	0.40 ± 0.07	166 ± 40	-102 ± 43

We define the sum of amplitudes $A_\rho = A_{\rho^+\pi^0} + A_{\rho^0\pi^+}$, and perform a series of fits to produce a likelihood contour of $|A_\rho|^2$ vs. $|\overline{A}_\rho|^2$ in Fig. A.1 where the $B^0 \to (\rho\pi)^0$

amplitudes in Table A.2 are scaled by the branching fractions in Table A.1.

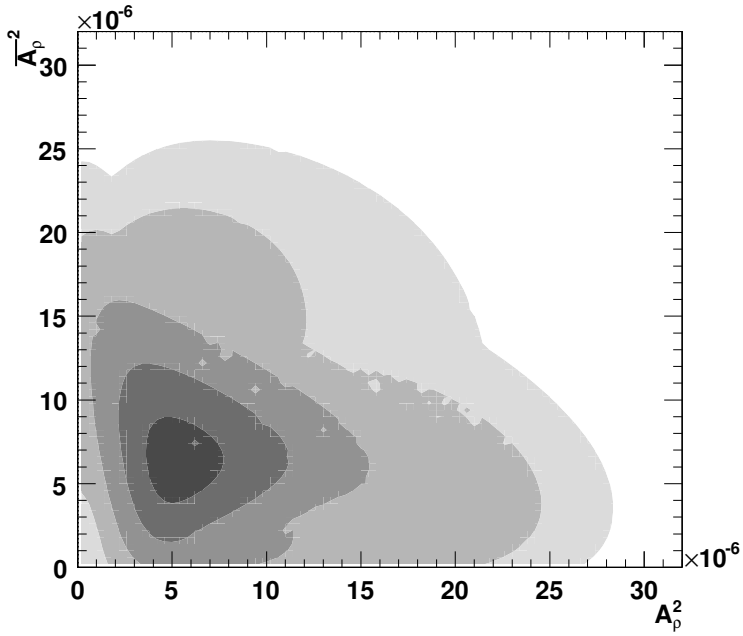

Figure A.1: $\sqrt{2\log(L)} = 1, 2, 3, 4, 5$ contours (darkest to lightest) of $|A_\rho|^2$ vs. $|\overline{A}_\rho|^2$. The units are 10^{-6} and are directly comparable to branching fractions.

The expression for $r_{\frac{3}{2}}$ holds equally well for $B \to \rho\pi$ and $\overline{B} \to \rho\pi$ amplitudes. Consequently, we measure $\mathrm{Re}(\mathrm{r}_{\frac{3}{2}})$ vs. $\mathrm{Im}(\mathrm{r}_{\frac{3}{2}})$ in a series of fits constraining the values of $r_{\frac{3}{2}}$ calculated with amplitudes and their CP conjugates to be the same. We correct the values of $|A_\rho|^2$ and $|\overline{A}_\rho|^2$ for the lifetime ratio $\tau^+/\tau^0 = 1.076$ and include the errors for the branching fractions and CP asymmetries for the $B^+ \to (\rho\pi)^+$ decays listed in Table A.1. Significance contours of $r_{\frac{3}{2}}$ are shown in Fig. A.2.

A.3 Systematics

We estimate the size of the systematic error due to ignoring the $B^+ \to (K^*K)^+$ contributions in the expression for $r_{\frac{3}{2}}$ by generating a distribution of the real and imaginary parts of Eq. (A.3) for 4×10^6, randomly sampled values of the $B^+ \to K^{*+}\overline{K}^0$

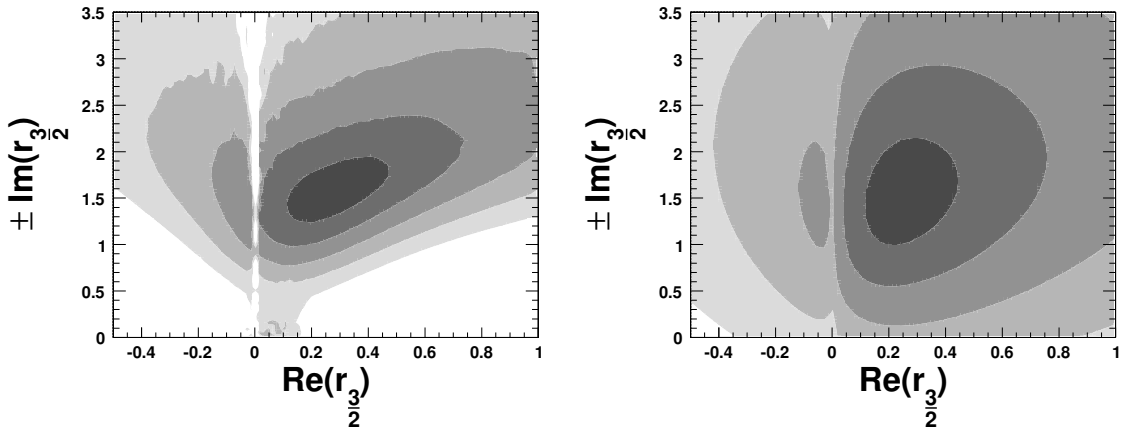

Figure A.2: $\sqrt{2\log(L)} = 1, 2, 3, 4, 5$ contours (darkest to lightest) of $r_{\frac{3}{2}}$. The contour on the right includes statistical errors in addition to a modest estimate of SU(3) breaking ($m_s/m_b \approx 2.5\%$) while the contour on the right illustrates the more conservative $m_s/\Lambda_{\rm QCD} \approx 30\%$ systematic uncertainty [16]. Note the contours are symmetric about the real axis

and $B^+ \to K^+\overline{K}^{*0}$ amplitudes. Since no measurement of the relative phases exists, we generate them with a flat prior distribution. The magnitudes of the $B^+ \to (K^*K)^+$ amplitudes are generated using the central values, for $\mathcal{B}(B^+ \to K^+\overline{K}^{*0})$, $\mathcal{B}(B^+ \to K_S K_S \pi^+)$ with gaussian errors. The value of $|A_\rho|^2$ is generated from the likelihood contour shown in Fig. A.1. The distribution of toy events generated in this way is used to produce a likelihood scan of the size of the systematic error. We plot twice the change in the negative logarithm of the likelihood relative to the minimum for the real and imaginary systematic uncertainty (See Eq. (A.3)) in Fig. A.3. Since the expression of $r_{\frac{3}{2}}$ in terms of B^+ decay amplitudes is the result of an SU(3) expansion of operators and amplitudes, we quote a $m_s/\Lambda_{\rm QCD} \approx 30\%$ theory error due to SU(3) breaking [16].

A.4 Conclusions

Finally, we measure the ratio of hadronic matrix elements:

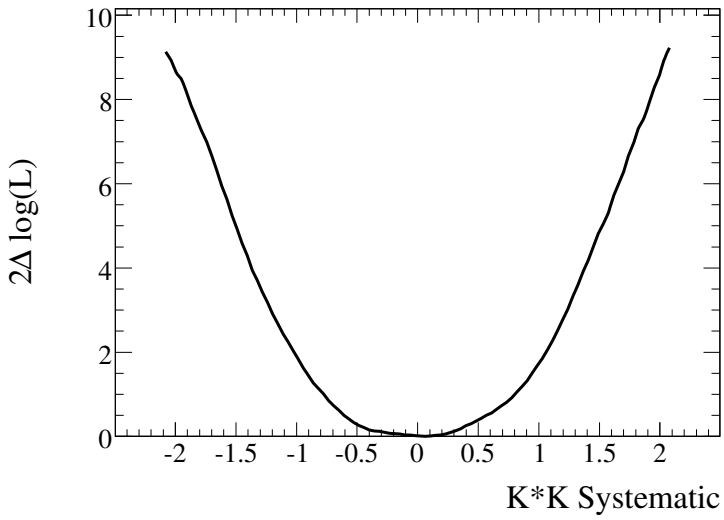

Figure A.3: Likelihood scan of the real part of Eq. (A.3) generated from 4×10^6 randomly sampled $K^{*+}\overline{K}^0$ and $K^+\overline{K}^{*0}$ phases. We take the deviation at 1σ, 0.77 as a systematic error for the real and imaginary parts of $r_{\frac{3}{2}}$.

$$\begin{aligned} \mathrm{Re}(r_{\frac{3}{2}}) &= 0.21 \ \pm 0.13 \ (\mathrm{stat.}) \ \pm 0.77 \ (\mathrm{syst.}) \ \pm 0.06 \ (\mathrm{theo.}), \\ \pm\mathrm{Im}(r_{\frac{3}{2}}) &= 1.45 \ \pm 0.35 \ (\mathrm{stat.}) \ \pm 0.77 \ (\mathrm{syst.}) \ \pm 0.44 \ (\mathrm{theo.}). \end{aligned} \tag{A.7}$$

We use Eq. (2.26) and the values of $C = -0.27 \pm 0.007$ [16] and $\sqrt{\overline{\rho}^2 + \overline{\eta}^2} = .405^{+0.035}_{-0.032}$ [7] to measure the $I = \frac{3}{2}$ ratio of EWP penguin to tree amplitudes:

$$\begin{aligned} \mathrm{Re}(P_{\mathrm{EWP}}/T) &= -0.21 \ \pm 0.13 \ (\mathrm{stat.}) \ \pm 0.29 \ (\mathrm{syst.}) \ \pm 0.16 \ (\mathrm{theo.}), \\ \pm\mathrm{Im}(P_{\mathrm{EWP}}/T) &= -0.54 \ \pm 0.05 \ (\mathrm{stat.}) \ \pm 0.29 \ (\mathrm{syst.}) \ \pm 0.04 \ (\mathrm{theo.}). \end{aligned} \tag{A.8}$$

The K^*K systematic is the dominant source of error in this measurement and can only be eliminated by measuring the $K^{*+}\overline{K}^0$ and $K^+\overline{K}^{*0}$ relative phases, though it may be improved if smaller limits on the $B^+ \to K_S K_S \pi^+, K^+\overline{K}^{*0}$ branching fractions

are set. A Dalitz analysis of the decay $B^+ \to K^+\overline{K}^0\pi^0$ would permit the measurement of the relevant phase differences via the interference of the $K^{*+}\pi^0$, $\overline{K}^{*0}\pi^0$, and $\rho^+(1700)\pi^0$ intermediate states. Unfortunately, the small branching fractions for decays via these states as shown in Table A.1, combined with the difficulty of efficiently reconstructing the $K^+\overline{K}^0\pi^0$ final state make such an analysis impossible with the existing *BABAR* dataset. It is also not possible at this time to exploit measurements of $\Phi_{\frac{3}{2}}$ via the $K^*(1430)\pi$ intermediate state since the $B \to a_0(1450)\pi$ amplitudes have not been measured.

Appendix B

B background PDFs

The classification of the B-backgrounds that contribute to the reconstructed $K^+\pi^-\pi^0$ final state is described in Section 4.4. The PDFs in each of the discriminating variables for these backgrounds are described by smoothed histograms with the exception of those backgrounds whose Dalitz distribution contains a narrow resonance. The composite PDF for each class is created by adding the event weighted contributions from each of the decays contributing to that category.

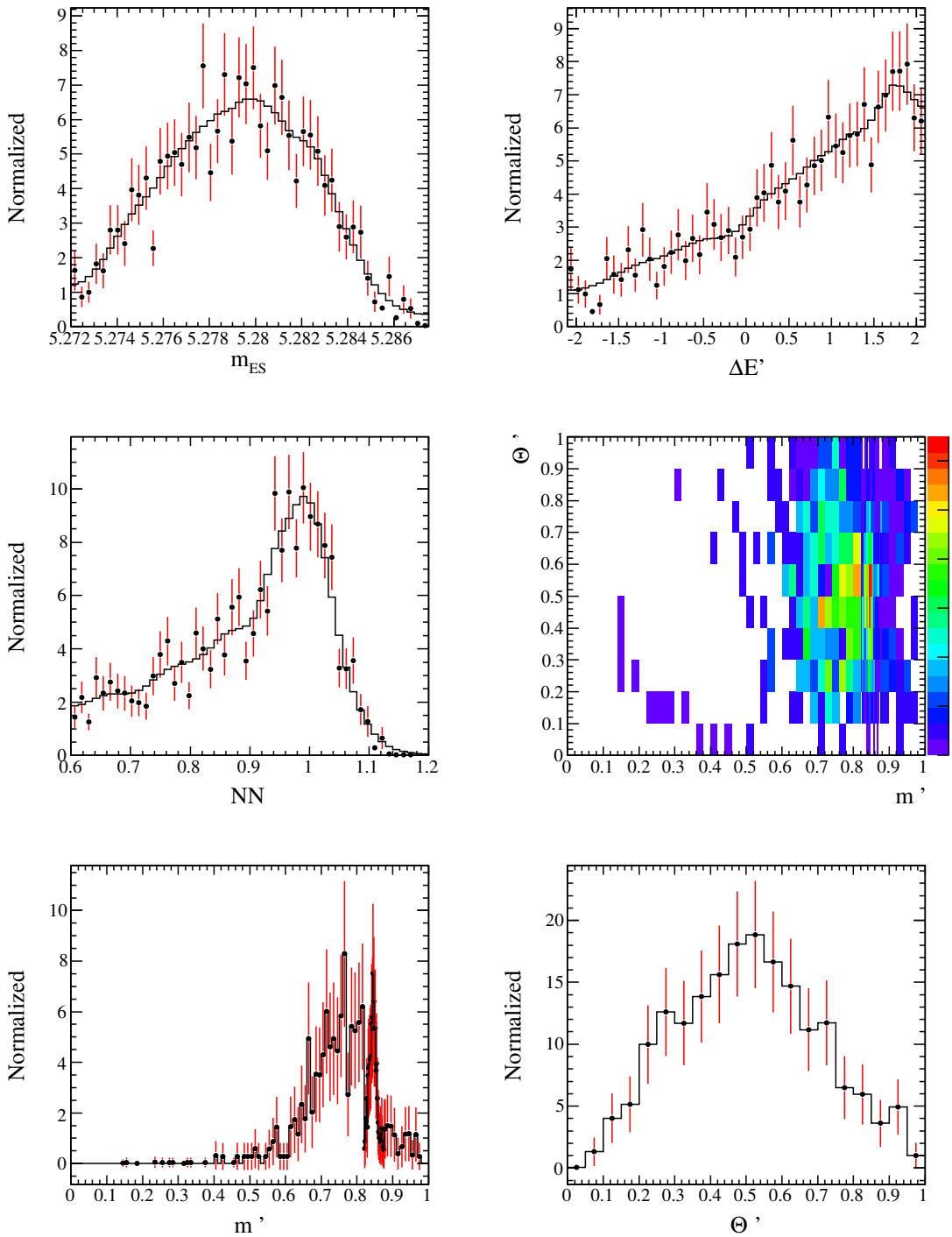

Figure B.1: Class 1 PDFs for m_{ES} (upper left), $\Delta E'$ (upper right), NN output (middle left), Dalitz Distribution (middle right), m' Dalitz projection (lower left), θ' Dalitz projection (lower right). Histogram PDFs are displayed in solid black. Event weighted MC is shown with red error bars.

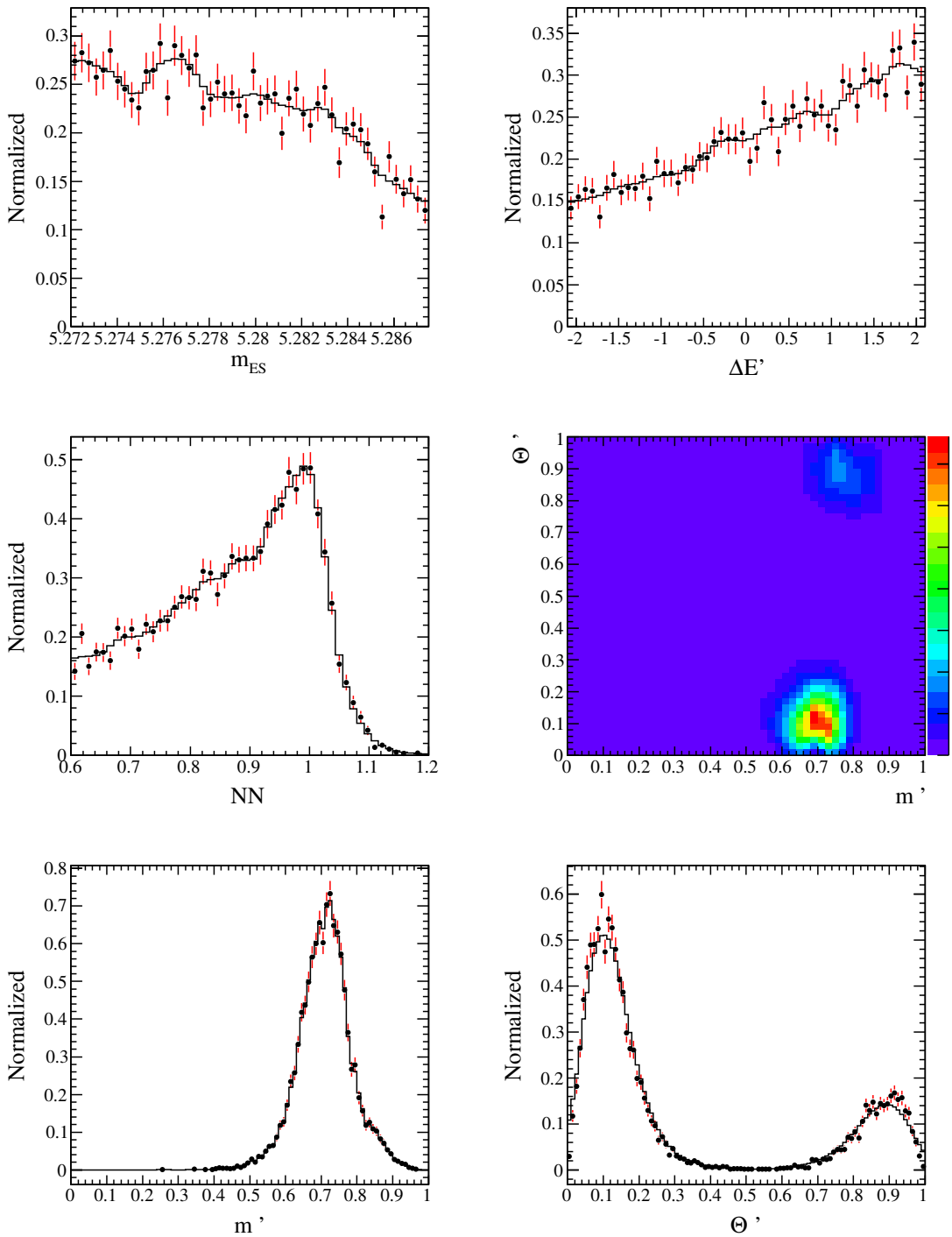

Figure B.2: Class 2 PDFs for m_{ES} (upper left), $\Delta E'$ (upper right), NN output (middle left), Dalitz Distribution (middle right), m' Dalitz projection (lower left), θ' Dalitz projection (lower right). Histogram PDFs are displayed in solid black. Event weighted MC is shown with red error bars.

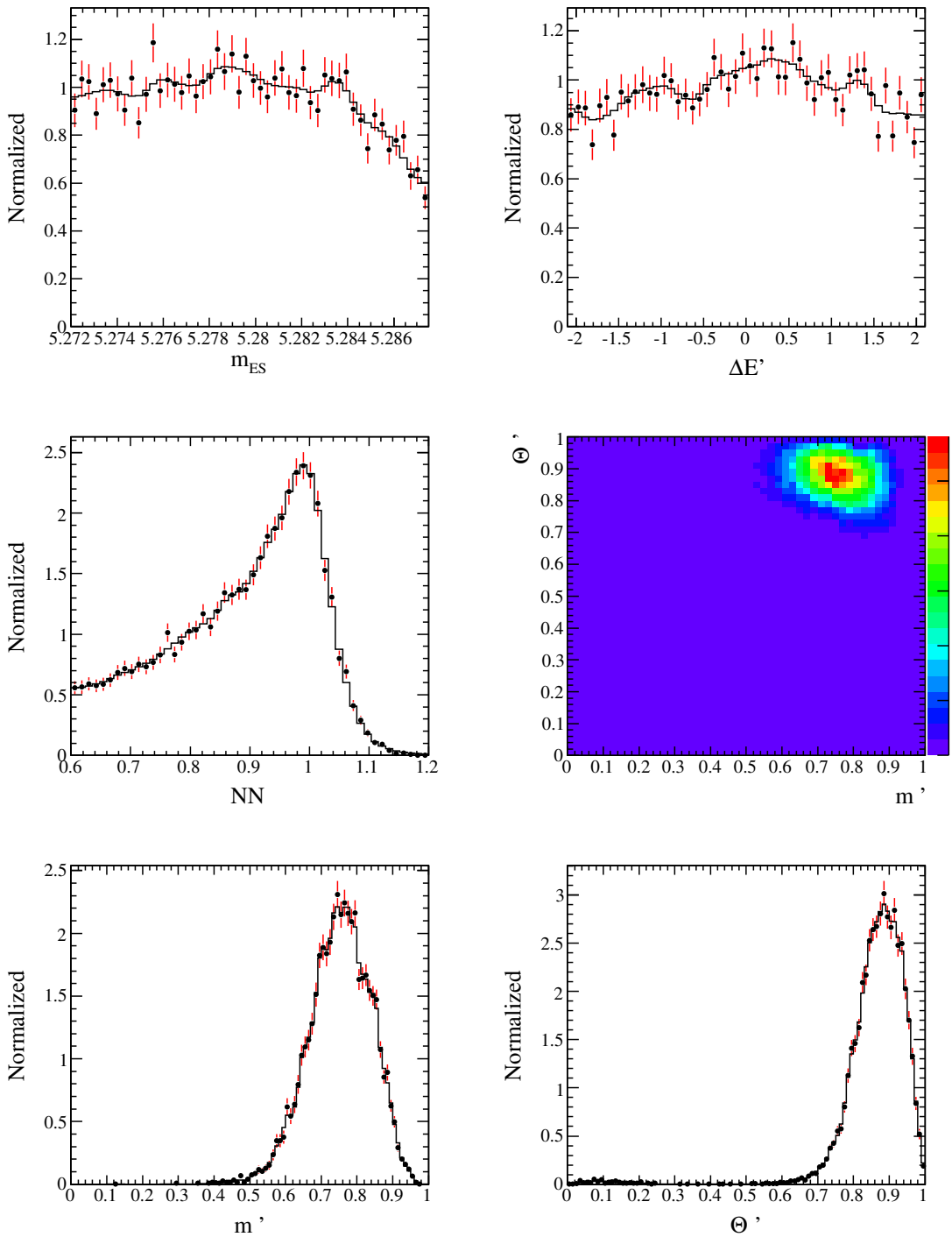

Figure B.3: Class 3 PDFs for m_{ES} (upper left), $\Delta E'$ (upper right), NN output (middle left), Dalitz Distribution (middle right), m' Dalitz projection (lower left), θ' Dalitz projection (lower right). Histogram PDFs are displayed in solid black. Event weighted MC is shown with red error bars.

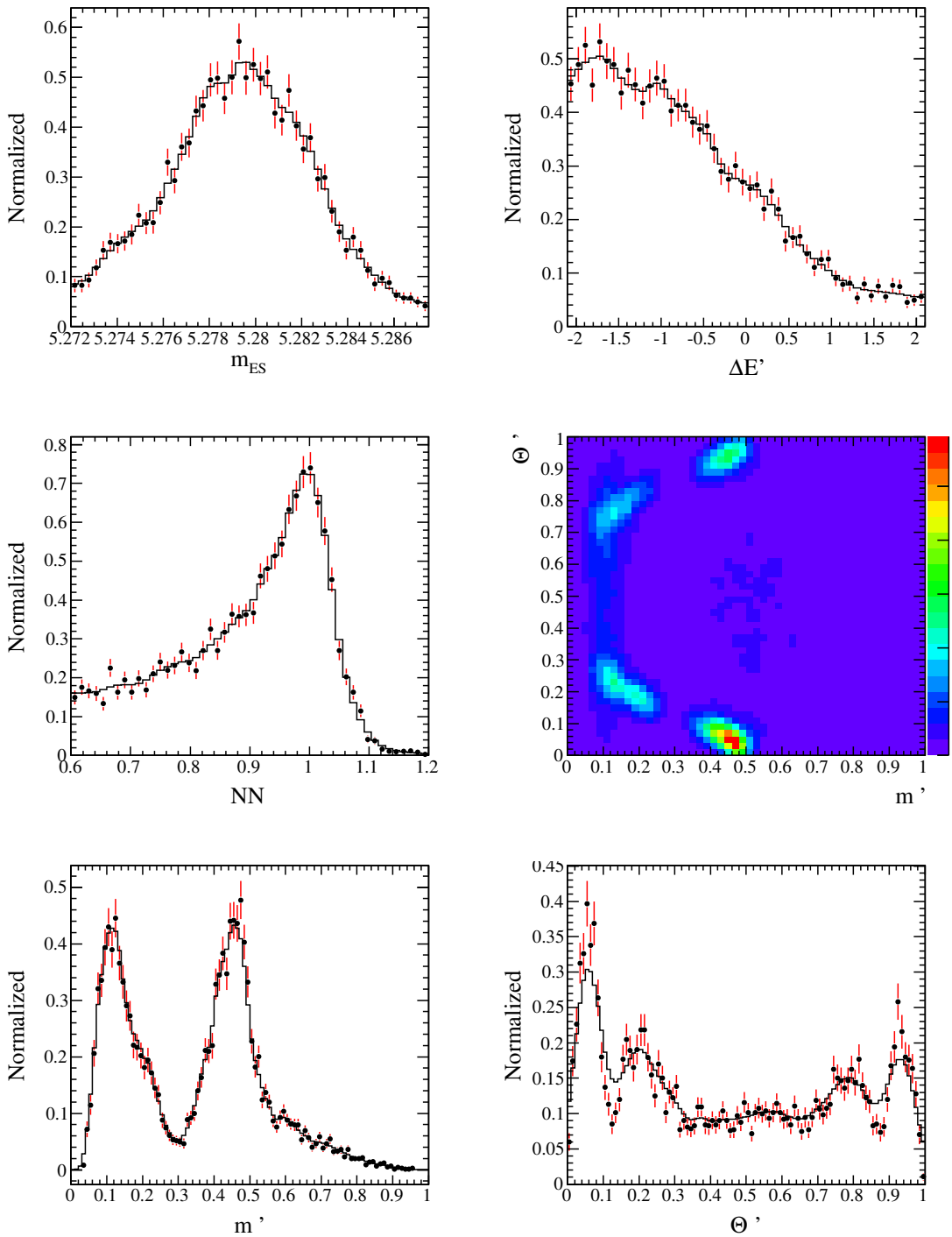

Figure B.4: Class 4 PDFs for m_{ES} (upper left), $\Delta E'$ (upper right), NN output (middle left), Dalitz Distribution (middle right), m' Dalitz projection (lower left), θ' Dalitz projection (lower right). Histogram PDFs are displayed in solid black. Event weighted MC is shown with red error bars.

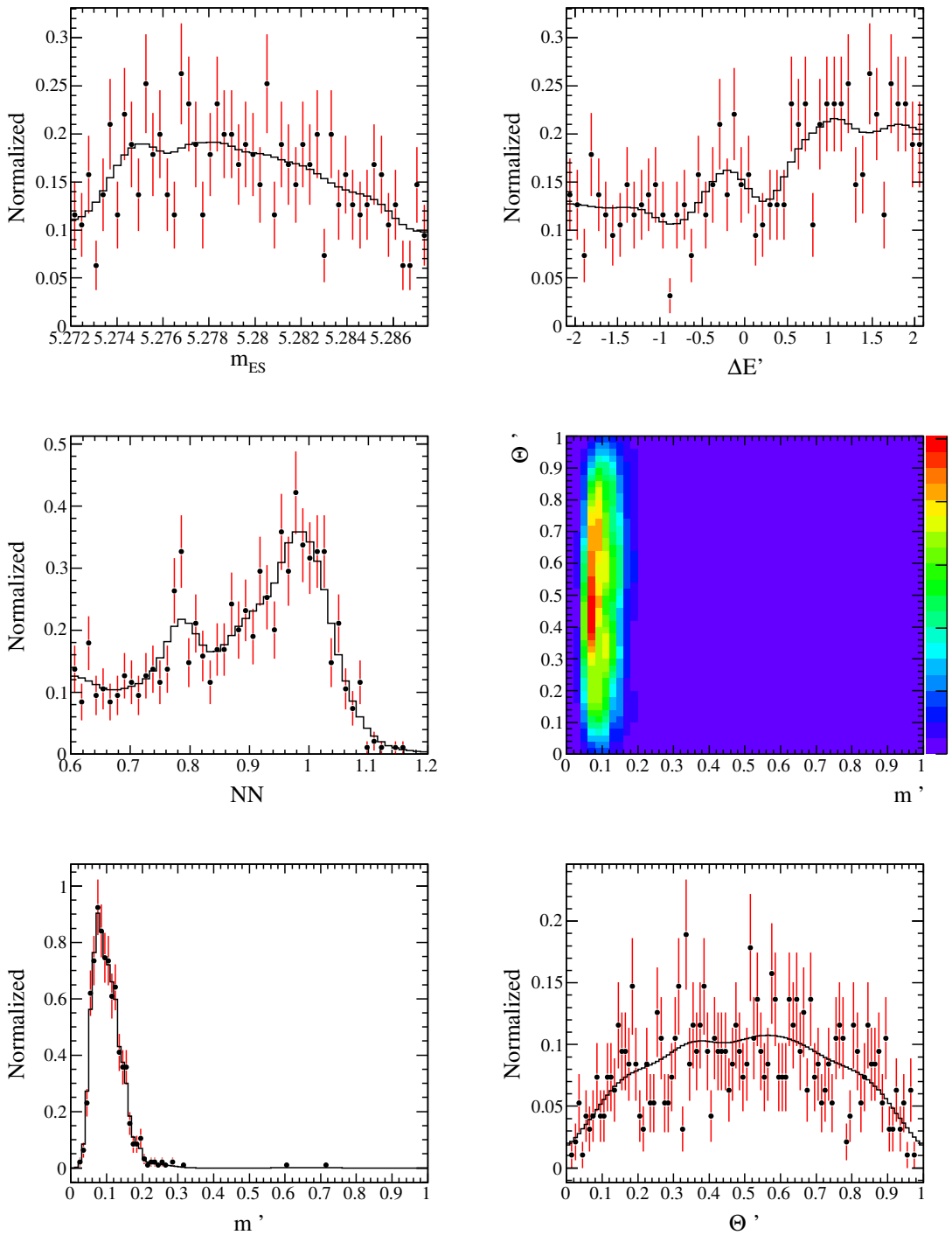

Figure B.5: Class 5 PDFs for m_{ES} (upper left), $\Delta E'$ (upper right), NN output (middle left), Dalitz Distribution (middle right), m' Dalitz projection (lower left), θ' Dalitz projection (lower right). Histogram PDFs are displayed in solid black. Event weighted MC is shown with red error bars.

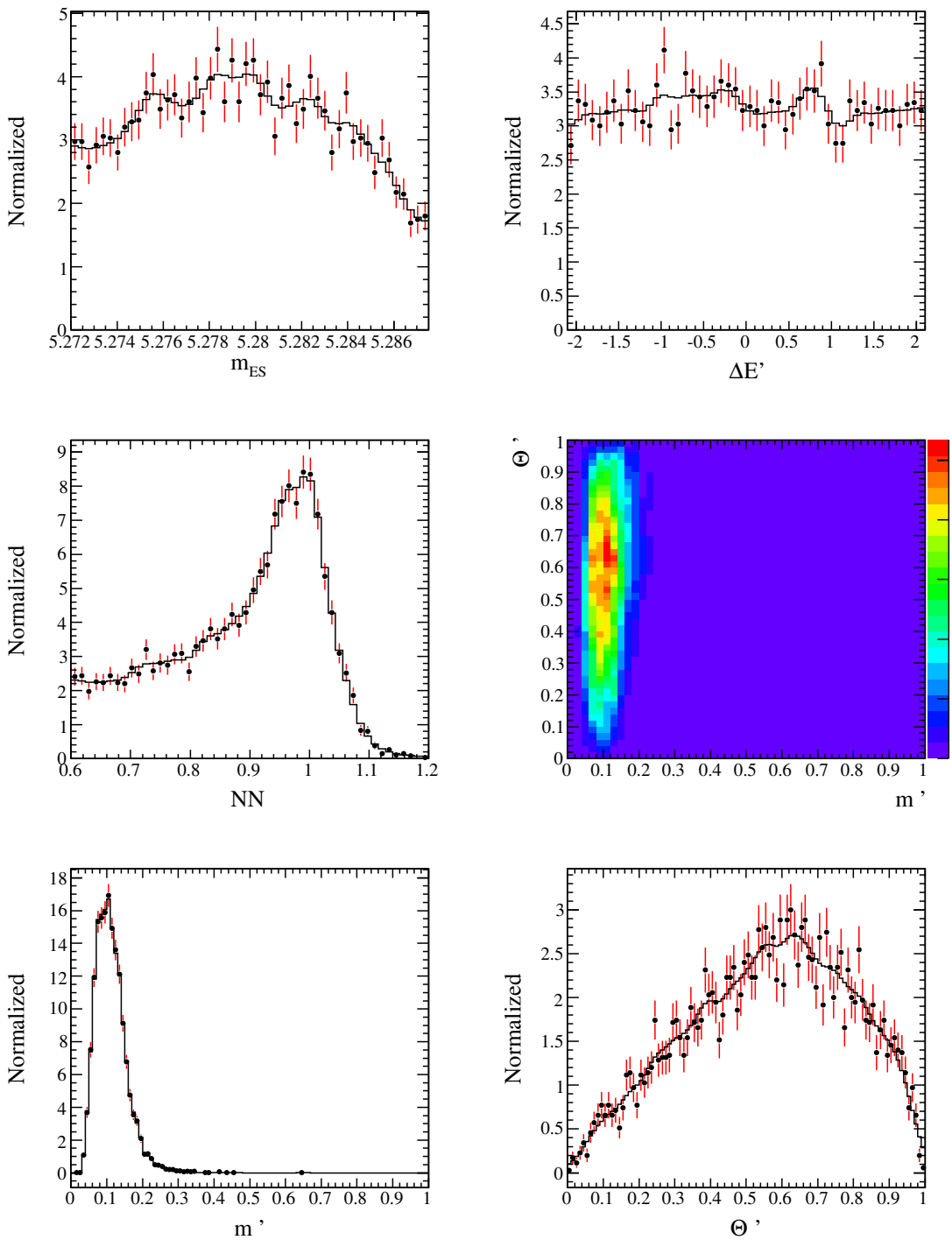

Figure B.6: Class 6 PDFs for m_{ES} (upper left), $\Delta E'$ (upper right), NN output (middle left), Dalitz Distribution (middle right), m' Dalitz projection (lower left), θ' Dalitz projection (lower right). Histogram PDFs are displayed in solid black. Event weighted MC is shown with red error bars.

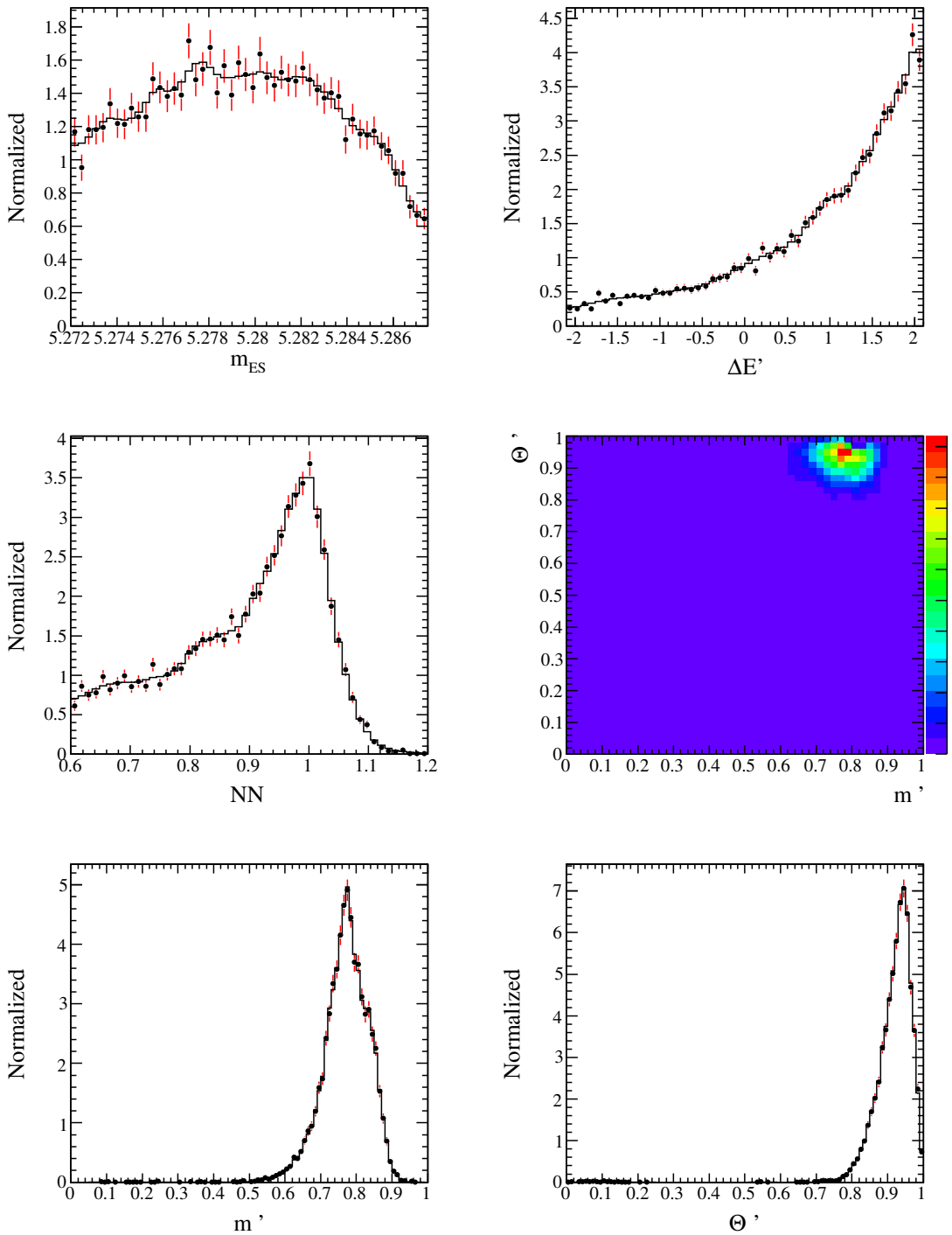

Figure B.7: Class 7 PDFs for m_{ES} (upper left), $\Delta E'$ (upper right), NN output (middle left), Dalitz Distribution (middle right), m' Dalitz projection (lower left), θ' Dalitz projection (lower right). Histogram PDFs are displayed in solid black. Event weighted MC is shown with red error bars.

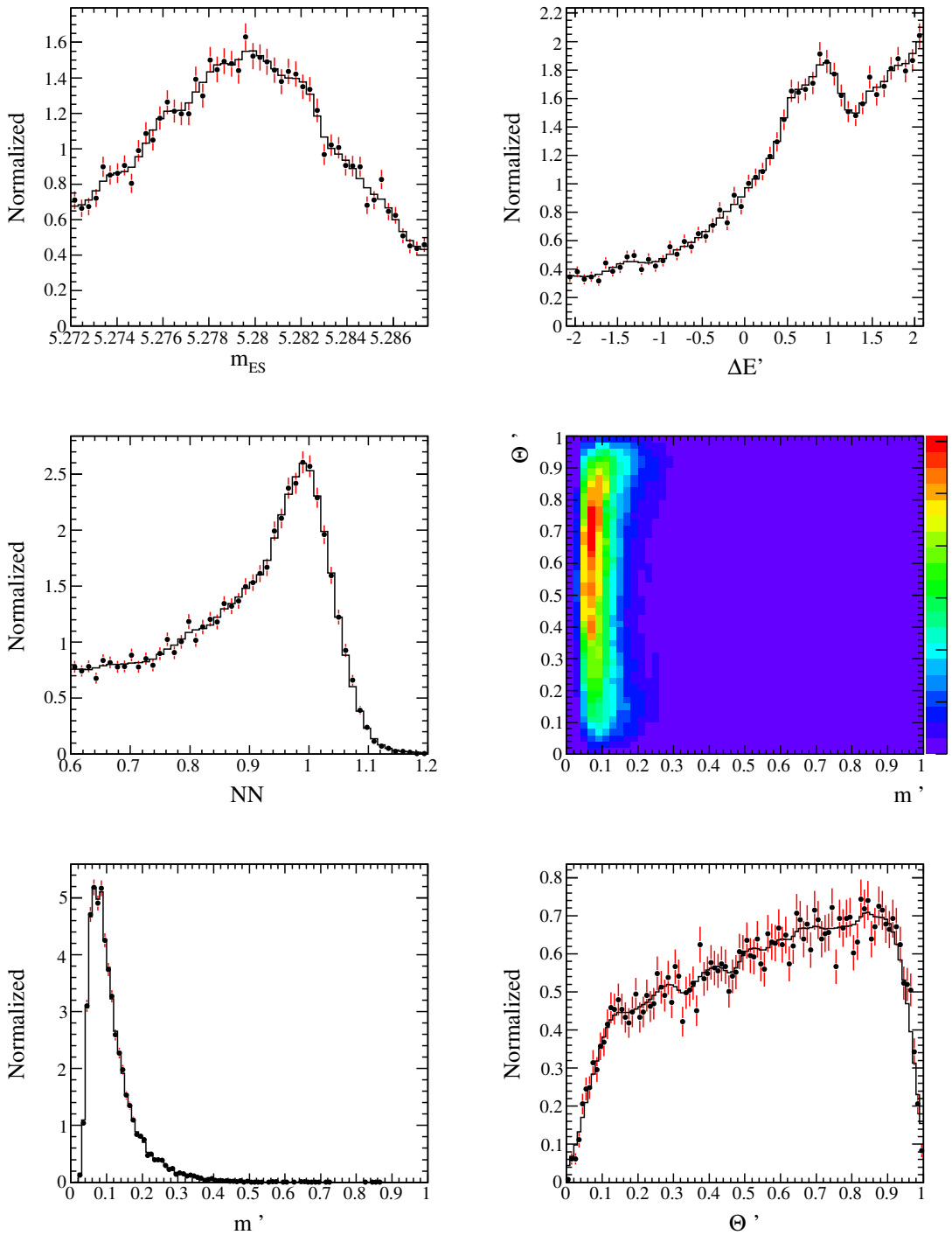

Figure B.8: Class 8 PDFs for m_{ES} (upper left), $\Delta E'$ (upper right), NN output (middle left), Dalitz Distribution (middle right), m' Dalitz projection (lower left), θ' Dalitz projection (lower right). Histogram PDFs are displayed in solid black. Event weighted MC is shown with red error bars.

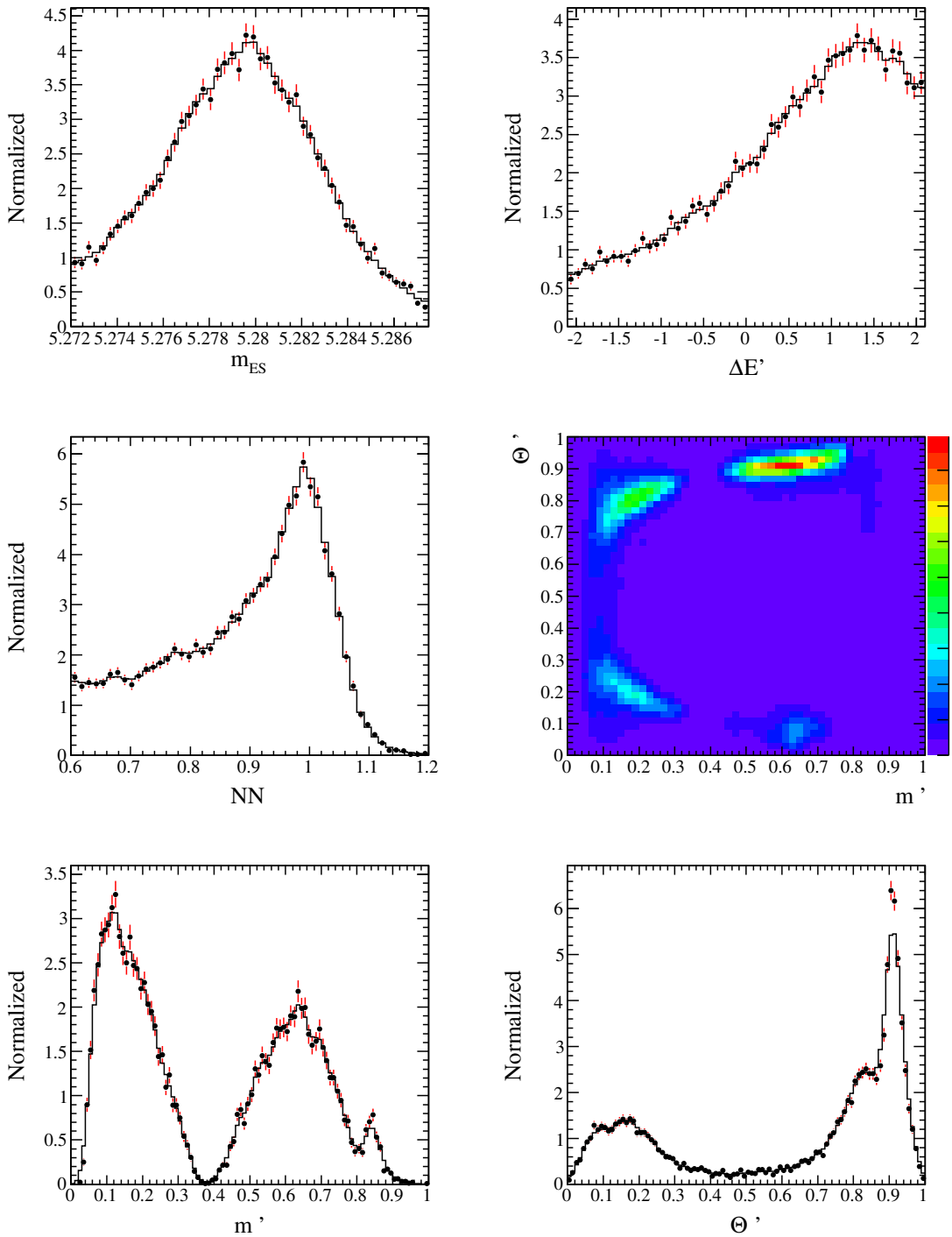

Figure B.9: Class 9 PDFs for m_{ES} (upper left), $\Delta E'$ (upper right), NN output (middle left), Dalitz Distribution (middle right), m' Dalitz projection (lower left), θ' Dalitz projection (lower right). Histogram PDFs are displayed in solid black. Event weighted MC is shown with red error bars.

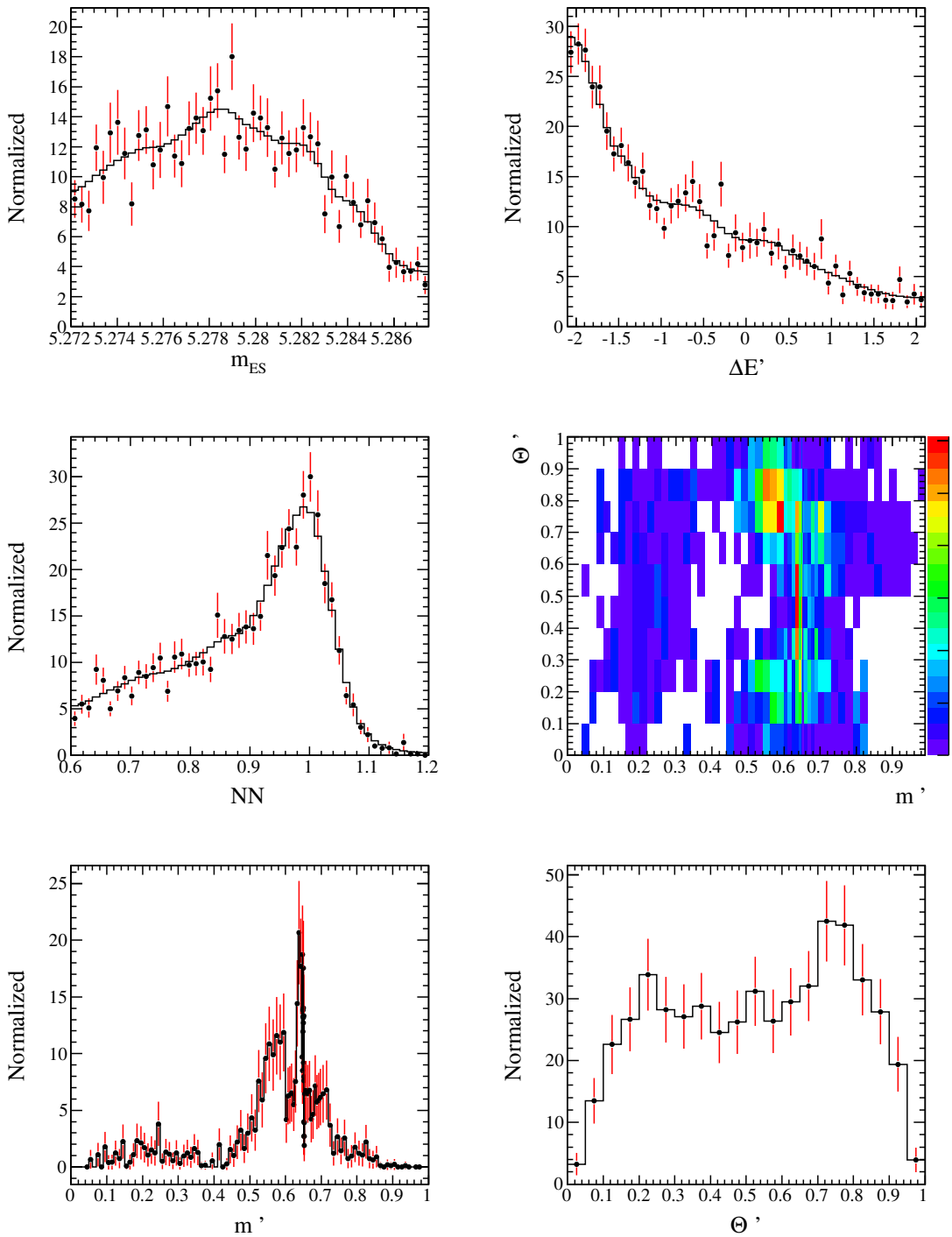

Figure B.10: Class 10 PDFs for m_{ES} (upper left), $\Delta E'$ (upper right), NN output (middle left), Dalitz Distribution (middle right), m' Dalitz projection (lower left), θ' Dalitz projection (lower right). Histogram PDFs are displayed in solid black. Event weighted MC is shown with red error bars.

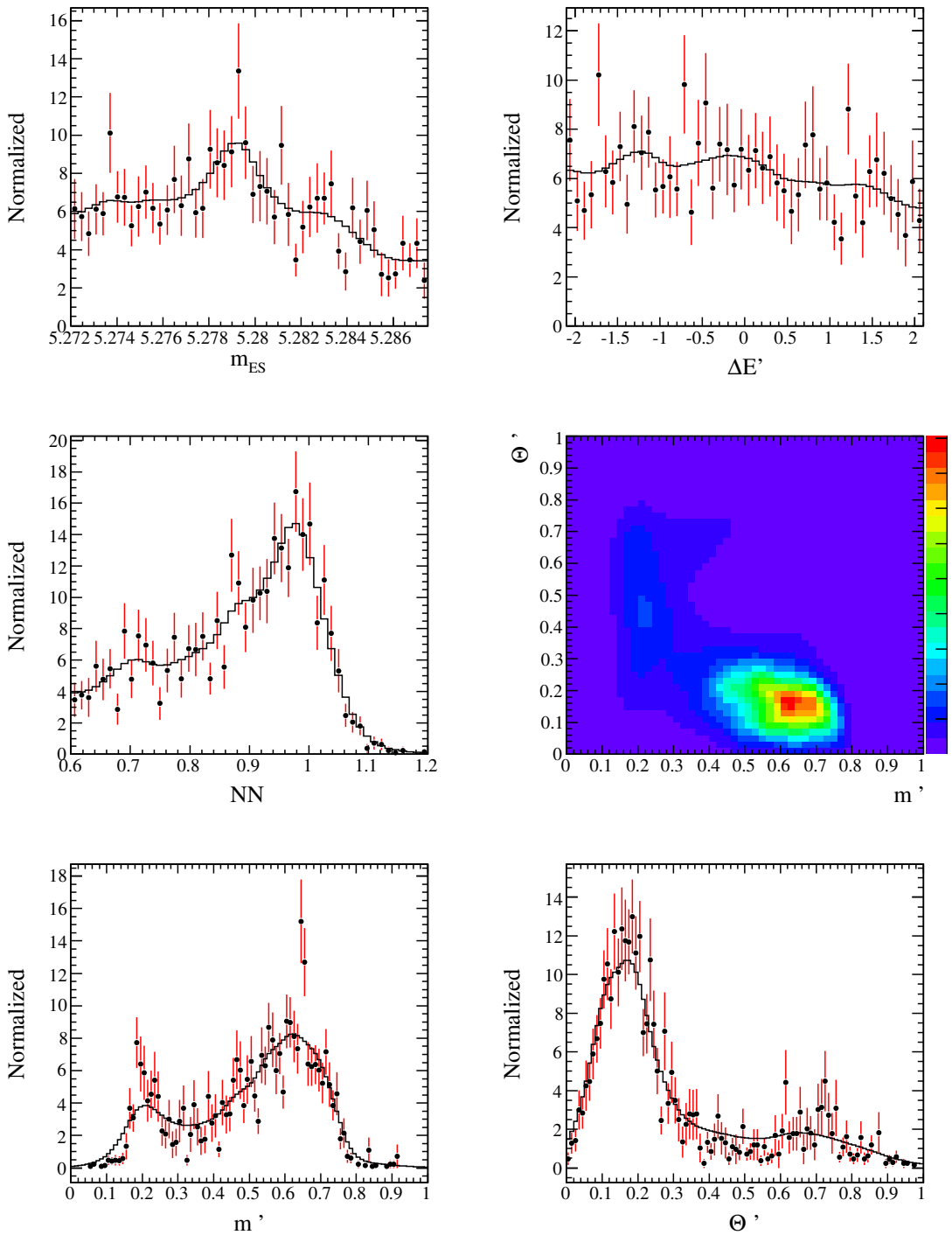

Figure B.11: Class 11 PDFs for m_{ES} (upper left), $\Delta E'$ (upper right), NN output (middle left), Dalitz Distribution (middle right), m' Dalitz projection (lower left), θ' Dalitz projection (lower right). Histogram PDFs are displayed in solid black. Event weighted MC is shown with red error bars.

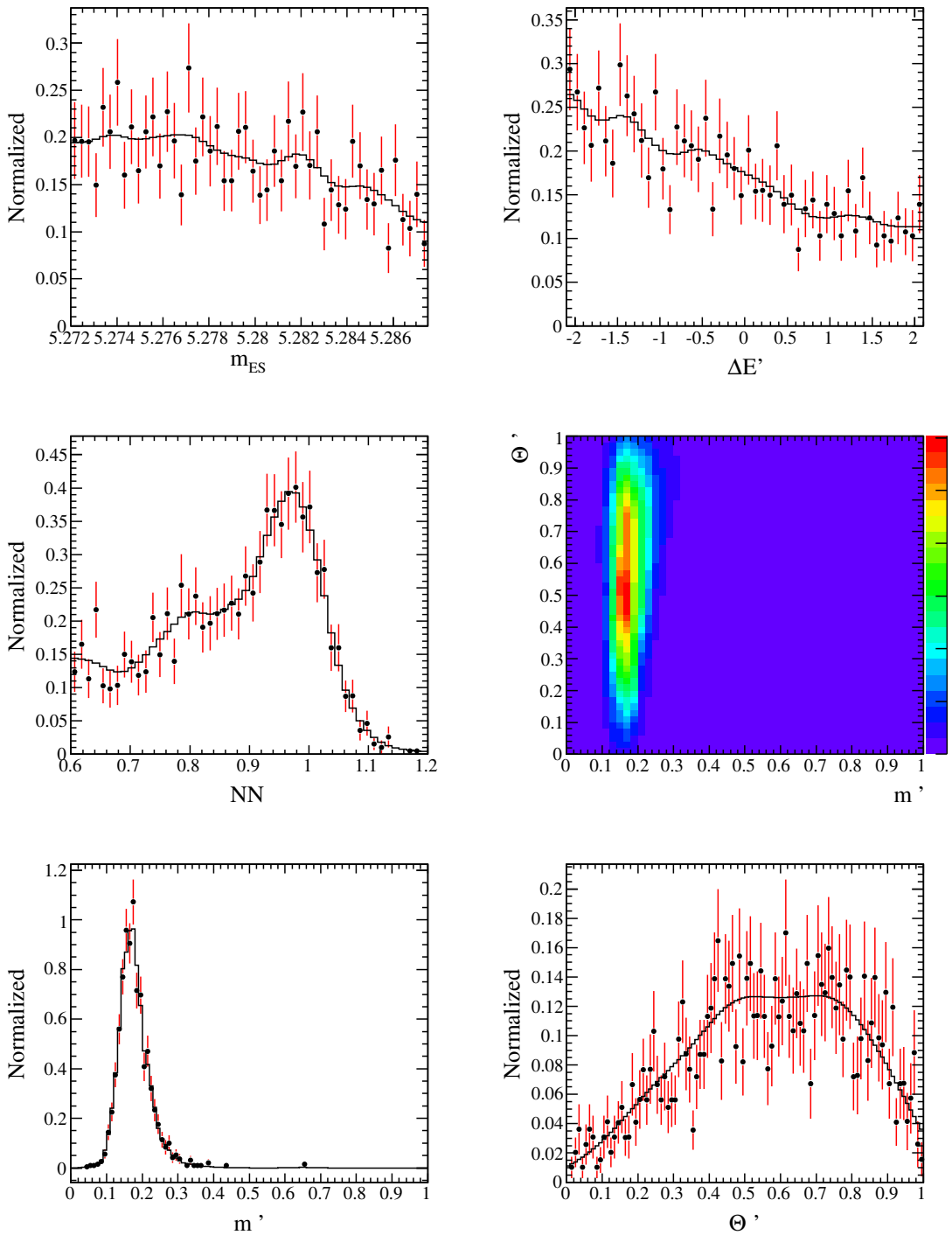

Figure B.12: Class 12 PDFs for m_{ES} (upper left), $\Delta E'$ (upper right), NN output (middle left), Dalitz Distribution (middle right), m' Dalitz projection (lower left), θ' Dalitz projection (lower right). Histogram PDFs are displayed in solid black. Event weighted MC is shown with red error bars.

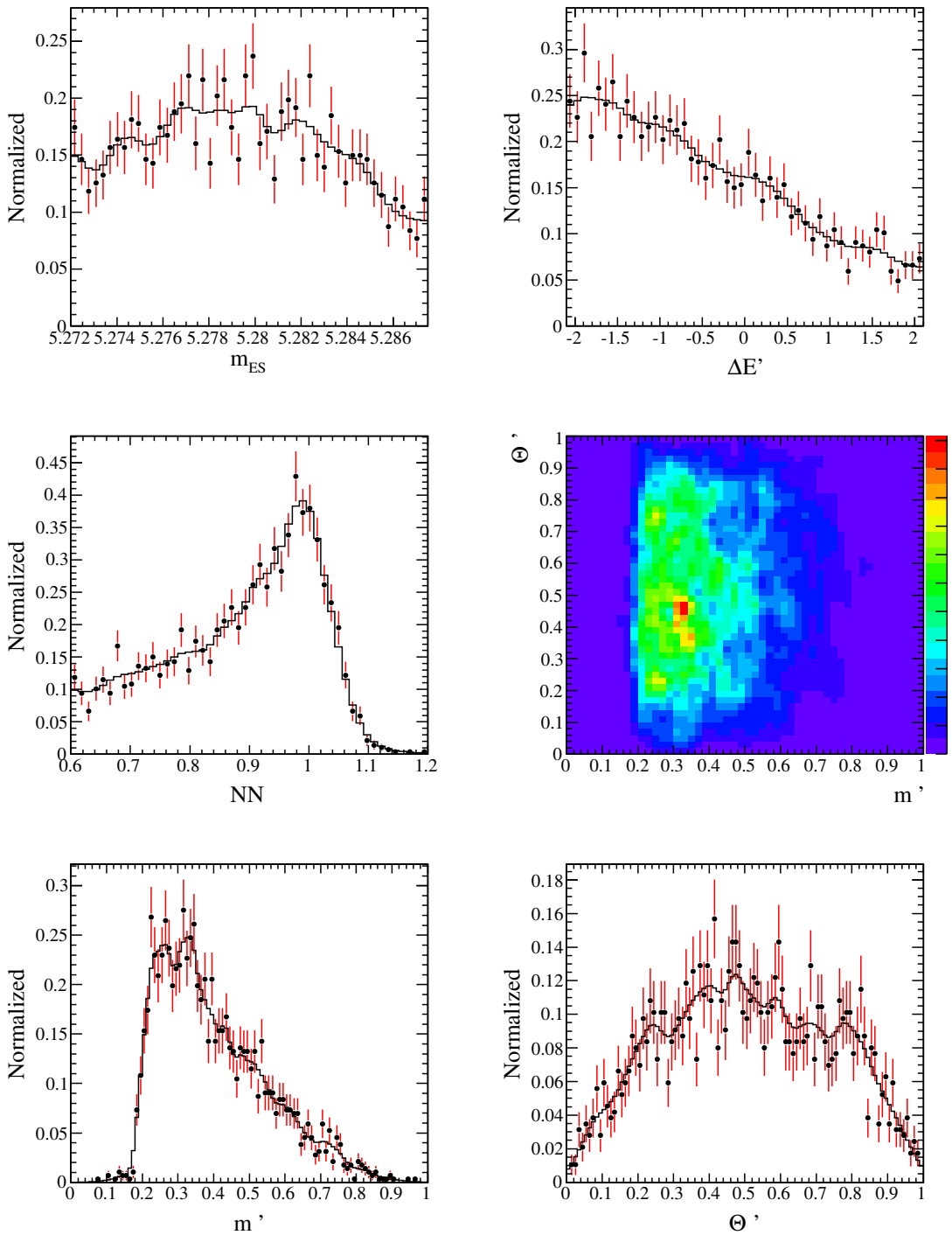

Figure B.13: Class 13 PDFs for m_{ES} (upper left), $\Delta E'$ (upper right), NN output (middle left), Dalitz Distribution (middle right), m' Dalitz projection (lower left), θ' Dalitz projection (lower right). Histogram PDFs are displayed in solid black. Event weighted MC is shown with red error bars.

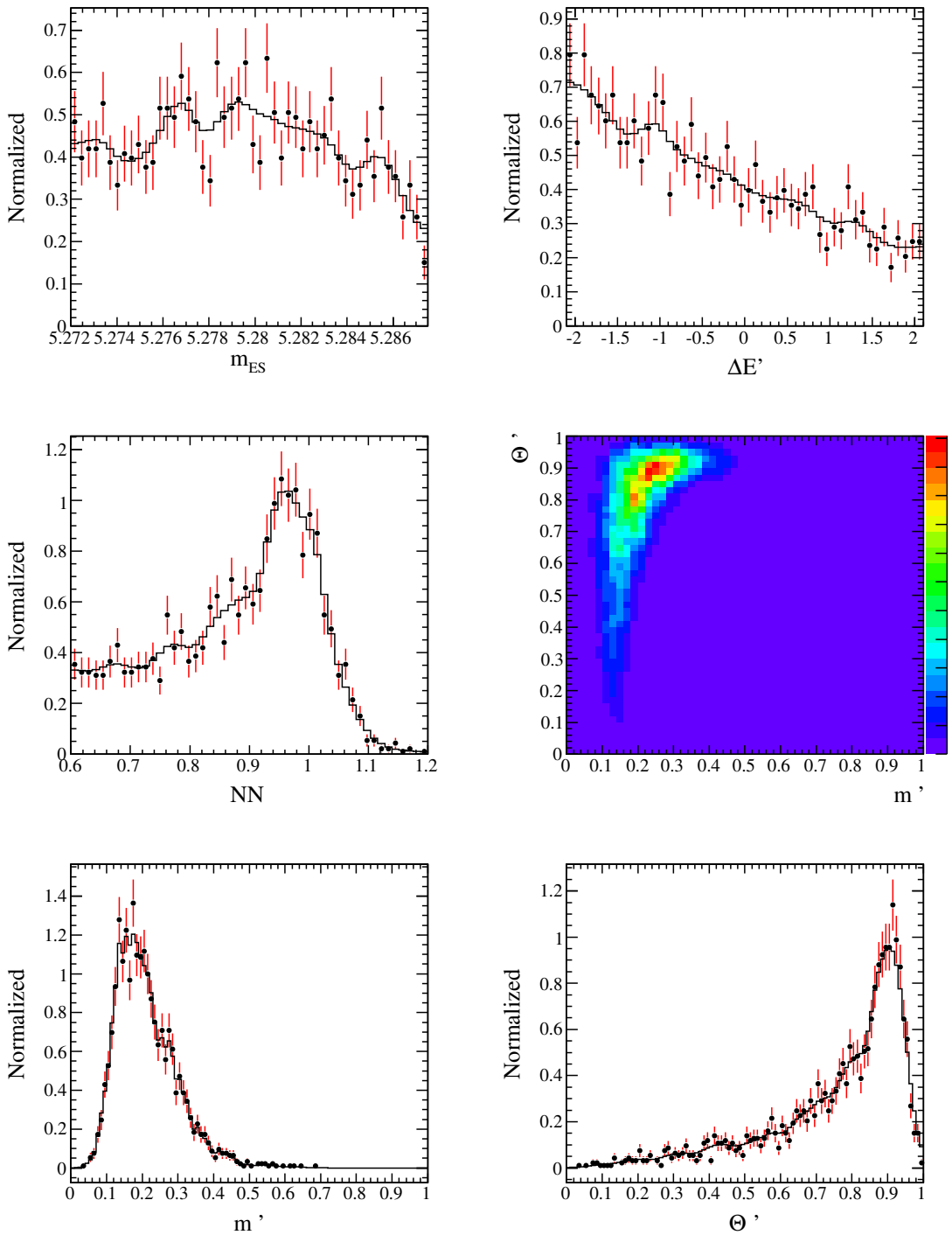

Figure B.14: Class 14 PDFs for m_{ES} (upper left), $\Delta E'$ (upper right), NN output (middle left), Dalitz Distribution (middle right), m' Dalitz projection (lower left), θ' Dalitz projection (lower right). Histogram PDFs are displayed in solid black. Event weighted MC is shown with red error bars.

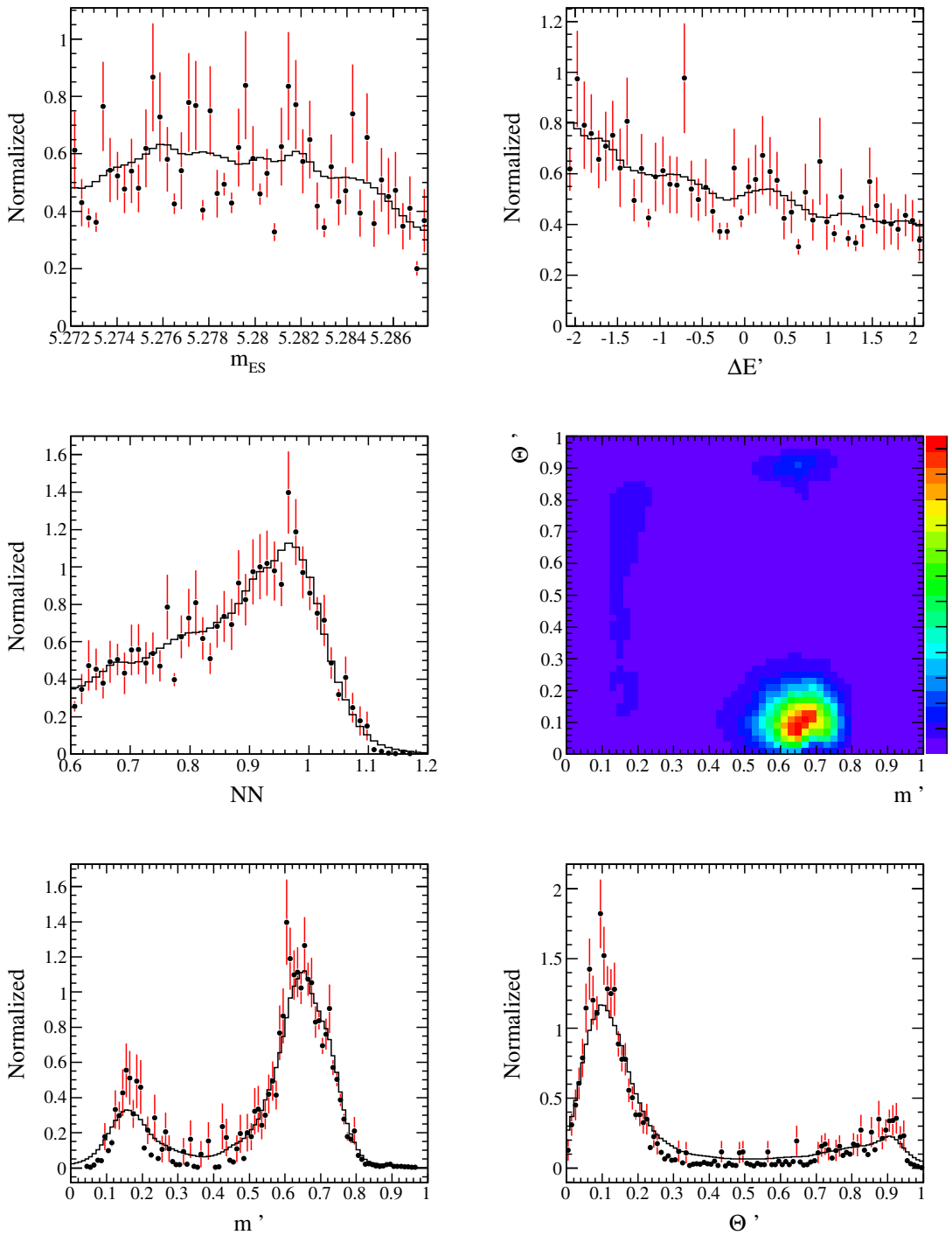

Figure B.15: Class 15 PDFs for m_{ES} (upper left), $\Delta E'$ (upper right), NN output (middle left), Dalitz Distribution (middle right), m' Dalitz projection (lower left), θ' Dalitz projection (lower right). Histogram PDFs are displayed in solid black. Event weighted MC is shown with red error bars.

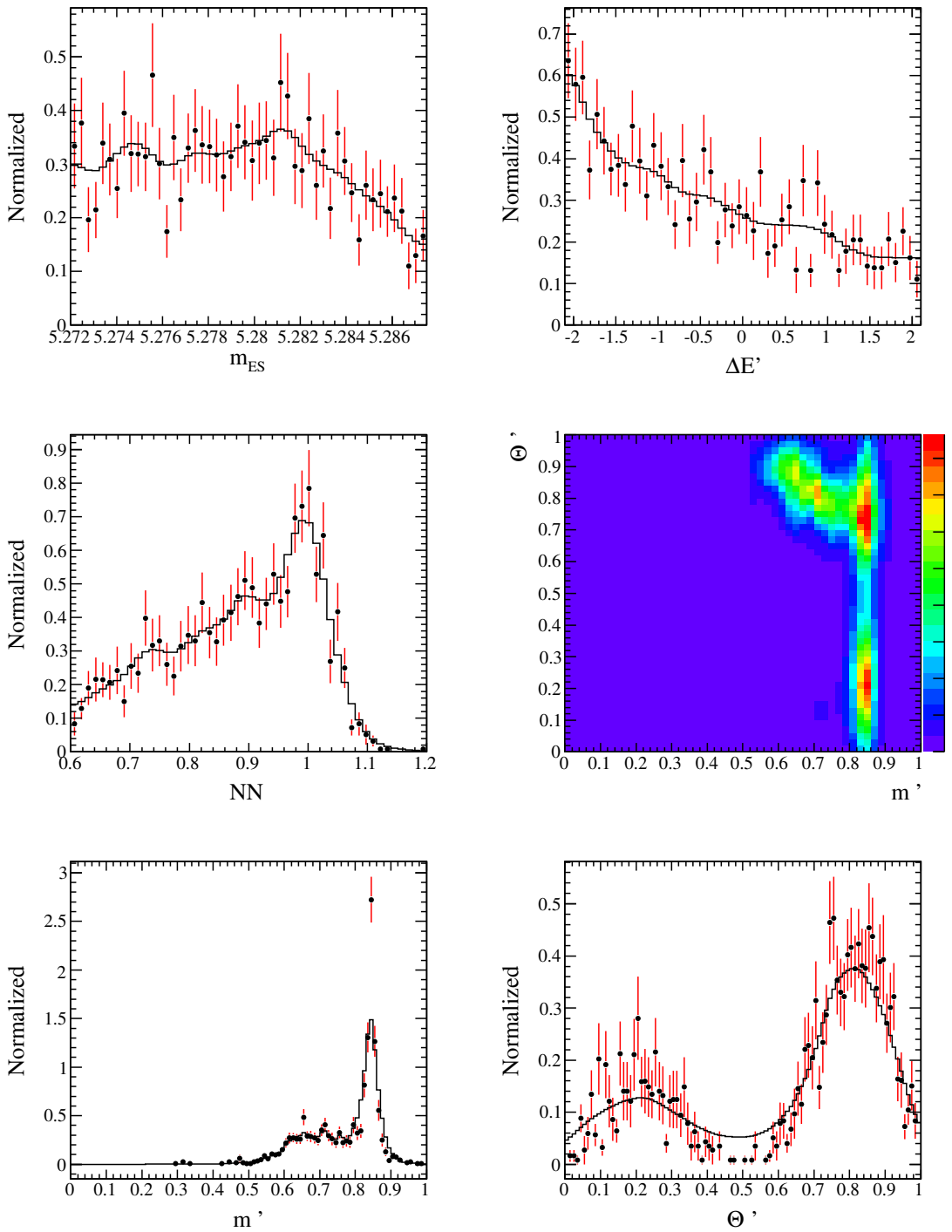

Figure B.16: Class 16 PDFs for m_{ES} (upper left), $\Delta E'$ (upper right), NN output (middle left), Dalitz Distribution (middle right), m' Dalitz projection (lower left), θ' Dalitz projection (lower right). Histogram PDFs are displayed in solid black. Event weighted MC is shown with red error bars.

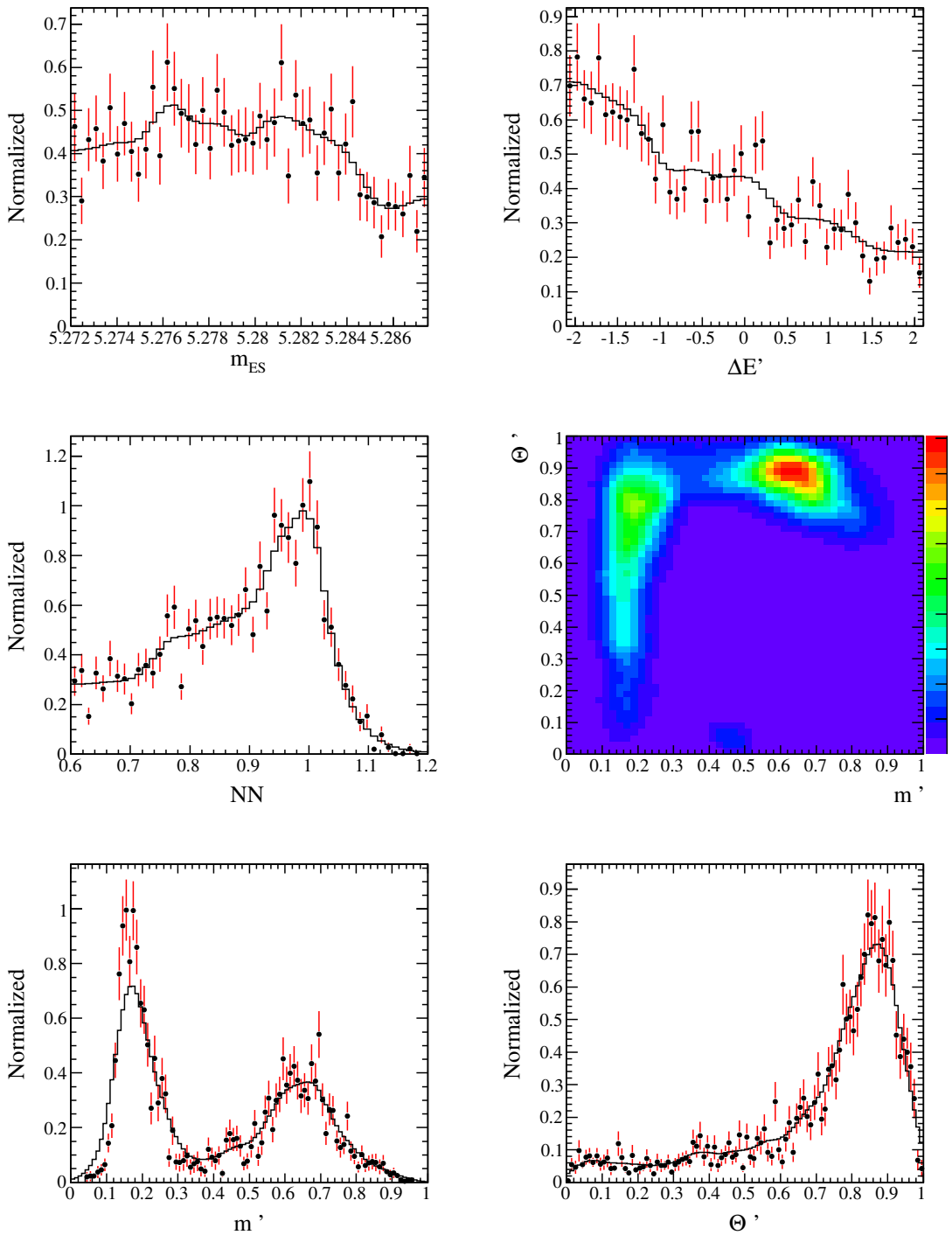

Figure B.17: Class 17 PDFs for m_{ES} (upper left), $\Delta E'$ (upper right), NN output (middle left), Dalitz Distribution (middle right), m' Dalitz projection (lower left), θ' Dalitz projection (lower right). Histogram PDFs are displayed in solid black. Event weighted MC is shown with red error bars.

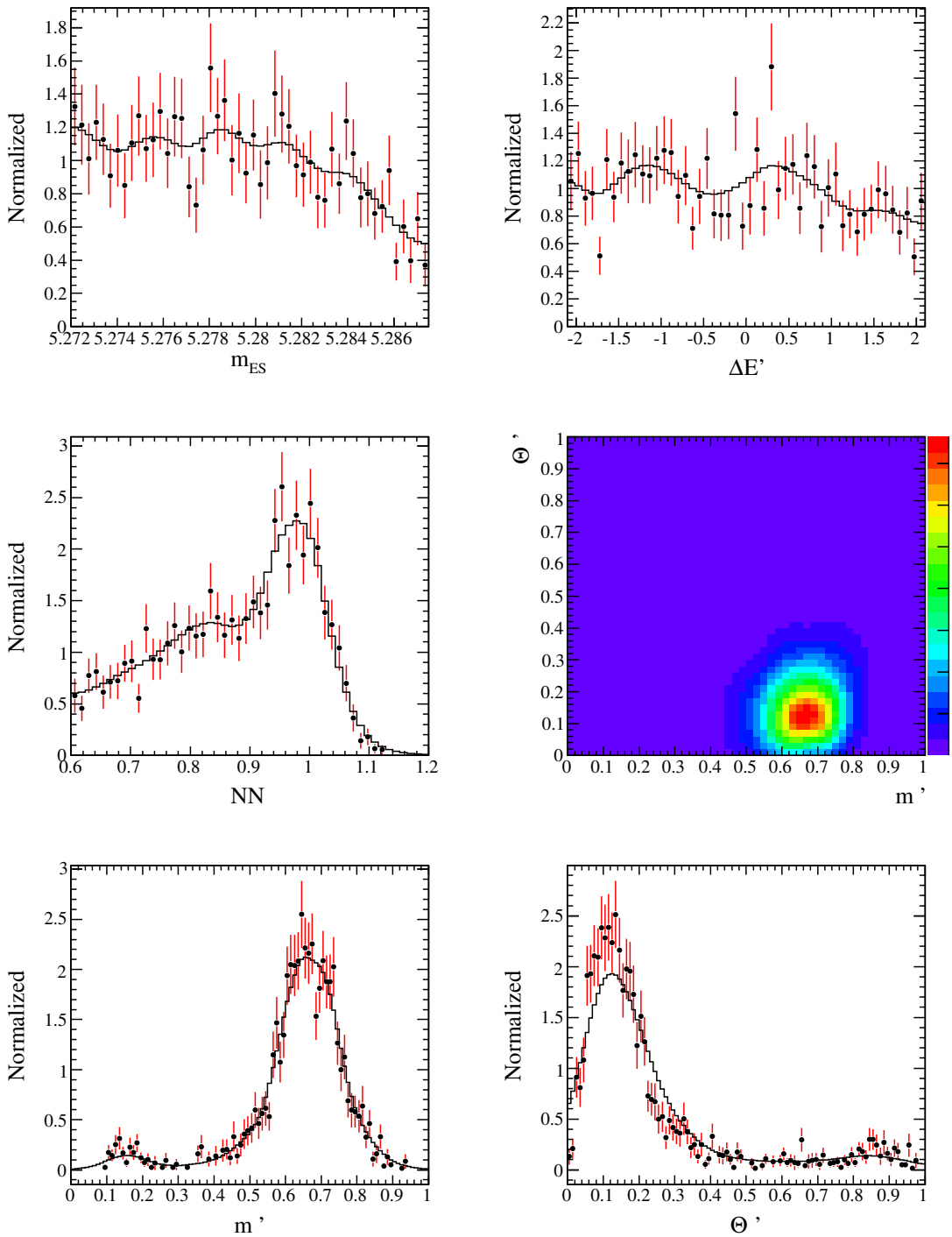

Figure B.18: Class 18 PDFs for m_{ES} (upper left), $\Delta E'$ (upper right), NN output (middle left), Dalitz Distribution (middle right), m' Dalitz projection (lower left), θ' Dalitz projection (lower right). Histogram PDFs are displayed in solid black. Event weighted MC is shown with red error bars.

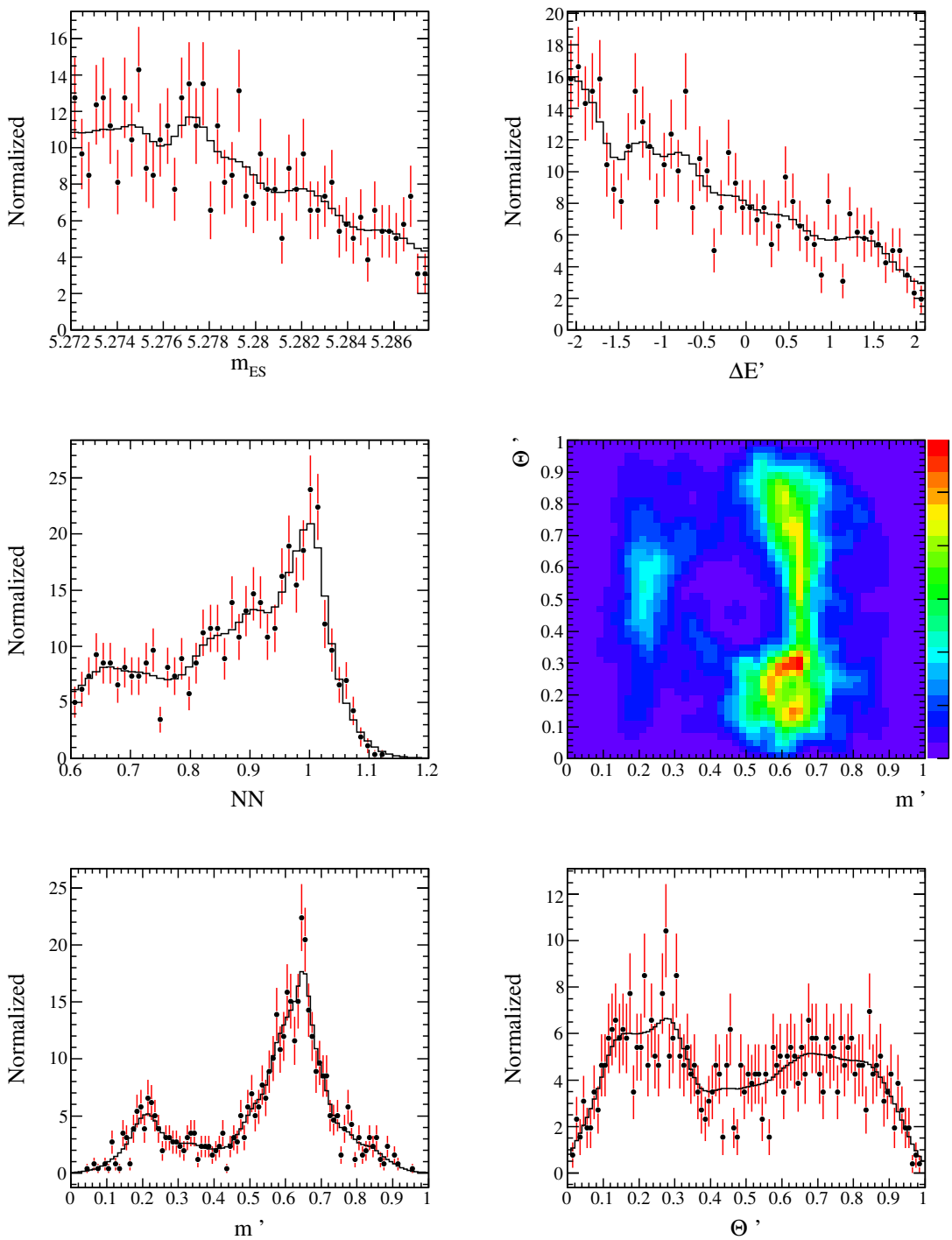

Figure B.19: Class 19 PDFs for m_{ES} (upper left), $\Delta E'$ (upper right), NN output (middle left), Dalitz Distribution (middle right), m' Dalitz projection (lower left), θ' Dalitz projection (lower right). Histogram PDFs are displayed in solid black. Event weighted MC is shown with red error bars.

Appendix C

Correlation Matrix

The correlation coefficients between the floated event yields and isobar parameters as determined by the `MINUIT` minimization algorithm, are given in this section. These coefficients correspond to the correlations for Solution-I in Table 4.9.

Table C.1: Correlation coefficients between the floated event yields and the B-background and Signal yields.

		B-backgrounds			Signal
		class 10	class 11	class 19	$B^0 \to K^+\pi^-\pi^0$
B-backgrounds	class 10	1.00	0.10	-0.39	-0.12
	class 11	0.10	1.00	-0.54	-0.09
	class 19	-0.39	-0.54	1.00	-0.14
Continuum	KaonI	-0.01	-0.02	-0.05	-0.09
	KaonII	0.00	-0.04	-0.07	-0.10
	KaonPion	0.03	-0.01	-0.12	-0.08
	Lepton	0.01	0.00	-0.07	-0.07
	NoTag	0.02	-0.02	-0.09	-0.11
	Other	0.02	0.01	-0.10	-0.07
	Pion	0.00	-0.05	-0.05	-0.09
Signal	$B^0 \to K^+\pi^-\pi^0$	-0.12	-0.09	-0.14	1.00

Table C.2: Correlation coefficients between the floated event yields and the continuum background yields.

		Continuum						
		KaonI	KaonII	KaonPion	Lepton	NoTag	Other	Pion
B-backgrounds	class 10	-0.01	0.00	0.03	0.01	0.02	0.02	-0.00
	class 11	-0.02	-0.04	-0.01	0.00	-0.02	0.01	-0.05
	class 19	-0.05	-0.07	-0.12	-0.07	-0.09	-0.10	-0.05
Continuum	KaonI	1.00	0.03	0.03	0.02	0.03	0.02	0.03
	KaonII	0.03	1.00	0.04	0.02	0.04	0.03	0.03
	KaonPion	0.03	0.04	1.00	0.03	0.04	0.03	0.03
	Lepton	0.02	0.02	0.03	1.00	0.03	0.02	0.02
	NoTag	0.03	0.04	0.04	0.03	1.00	0.03	0.04
	Other	0.02	0.03	0.03	0.02	0.03	1.00	0.03
	Pion	0.03	0.03	0.03	0.02	0.04	0.03	1.00
Signal	$B^0 \to K^+\pi^-\pi^0$	-0.09	-0.10	-0.08	-0.07	-0.11	-0.07	-0.09

Table C.3: Correlation coefficients among the floated isobar parameters for B decays.

		D^-K^+	$\overline{D}^0\pi^0$	$(K\pi)_0^{*+}\pi^-$		$(K\pi)_0^{*0}\pi^0$		$K^{*+}(892)\pi^-$	
		a	a	a	Φ	a	Φ	a	Φ
D^-K^+	a	1.00	-0.28	0.26	0.08	0.28	0.08	0.22	0.07
$\overline{D}^0\pi^0$	a	-0.28	1.00	-0.78	0.03	-0.69	0.01	-0.63	0.03
$(K\pi)_0^{*+}\pi^-$	a	0.26	-0.78	1.00	-0.07	0.65	-0.01	0.51	-0.06
	Φ	0.08	0.03	-0.07	1.00	0.17	0.56	0.03	0.94
$(K\pi)_0^{*0}\pi^0$	a	0.28	-0.69	0.65	0.17	1.00	0.17	0.52	0.15
	Φ	0.08	0.01	-0.01	0.56	0.17	1.00	-0.01	0.51
$K^{*+}(892)\pi^-$	a	0.22	-0.63	0.51	0.03	0.52	-0.01	1.00	0.03
	Φ	0.07	0.03	-0.06	0.94	0.15	0.51	0.03	1.00
$K^{*0}(892)\pi^0$	a	0.19	-0.56	0.56	0.01	0.36	-0.04	0.42	0.00
	Φ	0.05	0.01	0.00	0.51	0.17	0.86	-0.01	0.46
NR	a	0.11	-0.43	0.43	-0.38	0.15	0.02	0.37	-0.36
	Φ	0.09	0.03	0.07	0.63	0.18	0.68	-0.05	0.53
$\rho^-(1450)K^+$	a	-0.04	-0.34	0.31	-0.19	0.14	-0.13	0.20	-0.20
	Φ	0.07	-0.04	0.06	0.52	0.11	0.58	0.04	0.46
$\rho^-(1700)K^+$	a	-0.13	-0.25	0.23	-0.28	0.06	-0.20	0.14	-0.27
	Φ	0.14	0.09	-0.12	0.62	0.10	0.56	-0.03	0.56
$\rho^-(770)K^+$	a	0.27	-0.57	0.56	0.17	0.56	0.20	0.45	0.16

Table C.4: Correlation coefficients among the floated isobar parameters for B decays.

		$K^{*0}(892)\pi^0$		NR		$\rho^-(1450)K^+$		$\rho^-(1700)K^+$		$\rho^-(770)K^+$
		a	Φ	a	Φ	a	Φ	a	Φ	a
D^-K^+	a	0.19	0.05	0.11	0.09	-0.04	0.07	-0.13	0.14	0.27
$\overline{D}^0\pi^0$	a	-0.56	0.01	-0.43	0.03	-0.34	-0.04	-0.25	0.09	-0.57
$(K\pi)_0^{*+}\pi^-$	a	0.56	0.00	0.43	0.07	0.31	0.06	0.23	-0.12	0.56
	Φ	0.01	0.51	-0.38	0.63	-0.19	0.52	-0.28	0.62	0.17
$(K\pi)_0^{*0}\pi^0$	a	0.36	0.17	0.15	0.18	0.14	0.11	0.06	0.10	0.56
	Φ	-0.04	0.86	0.02	0.68	-0.13	0.58	-0.20	0.56	0.20
$K^{*+}(892)\pi^-$	a	0.42	-0.01	0.37	-0.05	0.20	0.04	0.14	-0.03	0.45
	Φ	0.00	0.46	-0.36	0.53	-0.20	0.46	-0.27	0.56	0.16
$K^{*0}(892)\pi^0$	a	1.00	-0.09	0.25	0.09	0.27	0.18	0.24	-0.10	0.42
	Φ	-0.09	1.00	0.00	0.65	-0.15	0.54	-0.14	0.50	0.20
NR	a	0.25	0.00	1.00	-0.26	0.24	-0.05	0.21	-0.23	0.27
	Φ	0.09	0.65	-0.26	1.00	-0.16	0.71	-0.22	0.63	0.24
$\rho^-(1450)K^+$	a	0.27	-0.15	0.24	-0.16	1.00	0.02	0.70	-0.67	-0.10
	Φ	0.18	0.54	-0.05	0.71	0.02	1.00	0.16	0.46	0.36
$\rho^-(1700)K^+$	a	0.24	-0.14	0.21	-0.22	0.70	0.16	1.00	-0.61	-0.01
	Φ	-0.10	0.50	-0.23	0.63	-0.67	0.46	-0.61	1.00	0.27
$\rho^-(770)K^+$	a	0.42	0.20	0.27	0.24	-0.10	0.36	-0.01	0.27	1.00

Table C.5: Correlation coefficients among the floated isobar parameters for $\overline{B}$ decays.

		D^+K^-	$D^0\pi^0$	$(K\pi)_0^{*-}\pi^+$		$(K\pi)_0^{*0}\pi^0$		$K^{*-}(892)\pi^+$	
		$\overline{a}$	$\overline{a}$	$\overline{a}$	$\overline{\Phi}$	$\overline{a}$	$\overline{\Phi}$	$\overline{a}$	$\overline{\Phi}$
D^+K^-	$\overline{a}$	1.00	0.25	0.23	-0.05	-0.19	-0.07	-0.15	-0.03
$D^0\pi^0$	$\overline{a}$	0.25	1.00	0.78	0.01	-0.54	0.01	-0.50	0.03
$(K\pi)_0^{*-}\pi^+$	$\overline{a}$	0.23	0.78	1.00	0.09	-0.44	0.05	-0.39	0.10
	$\overline{\Phi}$	-0.05	0.01	0.09	1.00	0.01	0.35	0.12	0.86
$(K\pi)_0^{*0}\pi^0$	$\overline{a}$	-0.19	-0.54	-0.44	0.01	1.00	0.47	0.34	0.02
	$\overline{\Phi}$	-0.07	0.01	0.05	0.35	0.47	1.00	0.02	0.28
$K^{*-}(892)\pi^+$	$\overline{a}$	-0.15	-0.50	-0.39	0.12	0.34	0.02	1.00	0.14
	$\overline{\Phi}$	-0.03	0.03	0.10	0.86	0.02	0.28	0.14	1.00
$\overline{K}^{*0}(892)\pi^0$	$\overline{a}$	-0.16	-0.50	-0.49	0.01	0.24	0.03	0.31	-0.01
	$\overline{\Phi}$	-0.05	0.06	0.07	0.34	0.34	0.80	-0.02	0.28
NR	$\overline{a}$	-0.11	-0.46	-0.49	-0.25	0.25	0.02	0.30	-0.23
	$\overline{\Phi}$	-0.04	0.06	-0.09	0.33	-0.11	0.45	-0.08	0.18
$\rho^+(1450)K^-$	$\overline{a}$	-0.13	-0.67	-0.63	-0.19	0.41	-0.17	0.35	-0.18
	$\overline{\Phi}$	-0.03	0.00	0.02	0.48	0.02	0.50	0.02	0.37
$\rho^+(1700)K^-$	$\overline{a}$	0.04	-0.43	-0.37	-0.17	0.24	-0.13	0.22	-0.16
	$\overline{\Phi}$	0.01	0.29	0.30	0.49	-0.19	0.36	-0.14	0.39

Table C.6: Correlation coefficients among the floated isobar parameters for $\overline{B}$ decays.

		$\overline{K}^{*0}(892)\pi^0$		NR		$\rho^+(1450)K^-$		$\rho^+(1700)K^-$	
		$\overline{a}$	$\overline{\Phi}$	$\overline{a}$	$\overline{\Phi}$	$\overline{a}$	$\overline{\Phi}$	$\overline{a}$	$\overline{\Phi}$
D^+K^-	$\overline{a}$	-0.16	-0.05	-0.11	-0.04	-0.13	-0.03	0.04	0.01
$D^0\pi^0$	$\overline{a}$	-0.50	0.06	-0.46	0.06	-0.67	0.00	-0.43	0.29
$(K\pi)_0^{*-}\pi^+$	$\overline{a}$	-0.49	0.07	-0.49	-0.09	-0.63	0.02	-0.37	0.30
	$\overline{\Phi}$	0.01	0.34	-0.25	0.33	-0.19	0.48	-0.17	0.49
$(K\pi)_0^{*0}\pi^0$	$\overline{a}$	0.24	0.34	0.25	-0.11	0.41	0.02	0.24	-0.19
	$\overline{\Phi}$	0.03	0.80	0.02	0.45	-0.17	0.50	-0.13	0.36
$K^{*-}(892)\pi^+$	$\overline{a}$	0.31	-0.02	0.30	-0.08	0.35	0.02	0.22	-0.14
	$\overline{\Phi}$	-0.01	0.28	-0.23	0.18	-0.18	0.37	-0.16	0.39
$\overline{K}^{*0}(892)\pi^0$	$\overline{a}$	1.00	-0.05	0.25	0.05	0.35	0.03	0.23	-0.16
	$\overline{\Phi}$	-0.05	1.00	-0.01	0.49	-0.23	0.49	-0.18	0.35
NR	$\overline{a}$	0.25	-0.01	1.00	-0.05	0.31	0.01	0.23	-0.20
	$\overline{\Phi}$	0.05	0.49	-0.05	1.00	-0.21	0.57	-0.23	0.45
$\rho^+(1450)K^-$	$\overline{a}$	0.35	-0.23	0.31	-0.21	1.00	-0.24	0.57	-0.72
	$\overline{\Phi}$	0.03	0.49	0.01	0.57	-0.24	1.00	0.13	0.47
$\rho^+(1700)K^-$	$\overline{a}$	0.23	-0.18	0.23	-0.23	0.57	0.13	1.00	-0.49
	$\overline{\Phi}$	-0.16	0.35	-0.20	0.45	-0.72	0.47	-0.49	1.00

Appendix D

Corrections to EMC Resolution in Simulation

D.1 Introduction

In order to accurately select signal from continuum background events, the distribution of ΔE (See Eq. (4.1)) must be correctly modeled in Monte Carlo (MC). In many exclusive analyses of B meson decays with neutral particles in the final state, it was noticed that the ΔE distribtion in the MC does not describe the data distribution very well. In order to select a clear sample to study this effect, the $B^0 \to K^{*0} \to K^{\pm}\pi^{\mp}\gamma$ decay was chosen, since it has just one high energetic γ ($E_{\gamma}^{B} \approx 2.6$ GeV) as the only neutral particle and hence has a clear separation of tracking and calorimeter effets. Since only one neutral particle is involved, the effect of asymmetric resolution functions is not obscured by the convolution of different asymmetric functions, so it can be studied directly.

When comparing the ΔE distributions in the $K^*\gamma$ sample in data and MC in all available calibrations of the EMC, the `MkIIComboCalibrator` and the `PhotonClusterCalibrator` in its versions before December 2006, a shift in the ΔE distribution in the MC of -10 to -5 MeV with respect to the data can be observed. Additionally, the MC distributoin appeared too steep on the positive side of ΔE. Hence the idea was born to smear the MC events asymmetrically, in order to both

shift the overall distribution upward and smear it out more on the upward side. Since the $K^*\gamma$ should be retained as a control sample, and since it has not the most optimal statistics due to the small $B \to K^*\gamma$ BF, another control sample was used for the determination of the best smearing function and the calculation of the best smearing parameters.

The $\mu\mu\gamma$ sample is used for this study because of the large number of events with low background and the presence of an isolated photon. For each event the photon's energy E_{meas} is determined from the calorimeter. In addition, the muon momenta together with the energy and momentum constraints are used to infer the photon's energy without using calorimeter information; this quantity is called E_{fit}. We then look at distributions of the ratio

$$x = \frac{E_{\text{meas}}}{E_{\text{fit}}} \ . \tag{D.1}$$

Distributions of this ratio show significant discrepancies between data and Monte Carlo. In particular, the data distributions have a tail extending to high values of x. Here we describe a technique by which the MCenergies are smeared in such a way that the distributions of x are in better agreement with the data.

It should be noted that this study requires that the measured photon energy be > 1GeV. A separate study in π^0s is used to correct the MCenegy below 1 GeV.

The document is organized as follows: Section D.2 gives an overview over the data sample used for the development of the smearing and the selection cuts applied. Section D.3 describes the mathematical framework used for the optimization of the smearing. Section D.4 shows the comparisons of the smeared MC with the data for the most optimal smearing fuction. In Section D.5 we describe the validation of the smearing with the independent sample of $B^0 \to K^{*0}\gamma$ decays and in Section D.6 we summarize the results.

D.2 Data sample

This analysis is based on data and MC processed in release 18 for run cylces 1 through 5. The data are taken from the `AllEvents` skim list. The MC sample (SP5244) requires that $E_\gamma > 500\,\mathrm{MeV}$. Events used in this study pass the following quality cuts:

Table D.1: Selection cuts on the $\mu\mu\gamma$ sample applied before smearing

Cuts Applied
`Tau11` = `true`
`ExclusiveIsr` = `true`
$0 <$ `nlLen`
`SumE` < 0.1
$0.425 <$ `btamfittheta` < 2.4
$0.4 < E_{\mathrm{miss}}^{\mathrm{nofit}}$
$0.05 <$ `btamfitprob`

The variables used for the selection of the $\mu\mu\gamma$ events are listed in Table D.1. The tag bits `Tau11` and `ExclusiveIsr` select a clean sample of events with exactly two oppositely charged tracks. `Tau11` allows for an ISR photon going down the beam pipe, while `ExclusiveIsr` requires the existence of a photon candidate consistent with an ISR photon. For the kinematic range $E_\gamma^{\mathrm{lab}} > 1$ GeV under study here, the sample is almost entirely `ExclusiveIsr` = `true`.

In order to select clean $\mu\mu\gamma$ events, where the reconstructed photon is the true ISR photon, and where we have no large contribution from beam backgrounds, photon splitting or FSR, the following cuts are applied in addition to the tag bits: $0 <$ `nlLen` requires at least one neutral cluster on `GoodPhotonLoose` list, `SumE` < 0.1 requires that the sum of the neutral energy in the detector apart from the highest energetic neutral cluster does not exceed 100 MeV. The cut on `btamfittheta` requires that the ISR photon actually lies in the fiducial volume of the detector. The cut on the missing energy against the muon pair $E_{\mathrm{miss}}^{\mathrm{nofit}}$ before the kinematic fit excludes soft ISR. Then, a kinematic fit of the two muons to the beam spot with the constraint that the

missing momentum must have $m = 0$ is performed, and a cut on the fit probability `btamfitprob` is applied.

D.3 Smearing method

This section describes the determination of parameters for a function that can be used to smear the Monte Carlo. Figure D.1 illustrates the discrepency between data and MCin the E/E_{fit} distribution of the $\mu\mu\gamma$ sample.

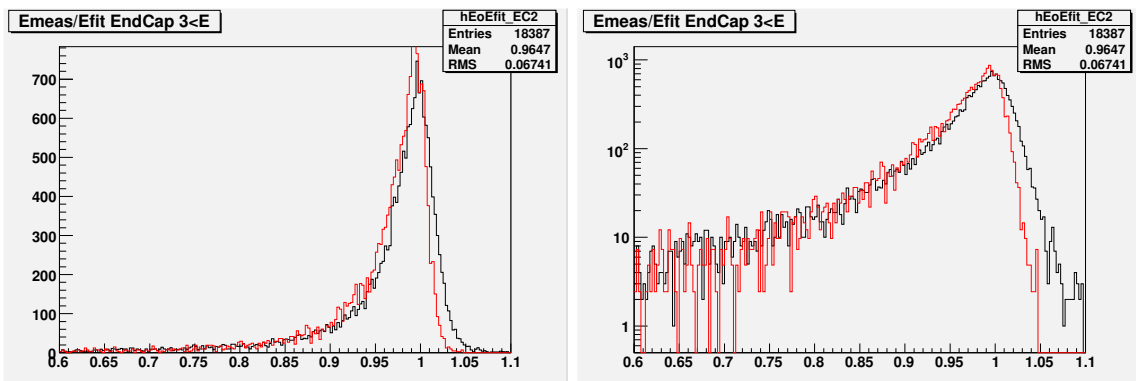

(a) (b)

Figure D.1: E/E_{fit} distributions for MC(red) and data (black) without smearing for the calorimeter endcap. (a) shows the distribution on a linear scale, (b) the same distribution on a logarithmic scale.

The general shape needs to be altered, and particular attention has to be paid to the peak position, which needs to be shifted to higher values, and the high-side tail, where the monte Carlo falls short. Here we present the analytical technique used to determine the parameters of an appropriate smearing function.

The ratios of E_{meas} to E_{fit} in data and MC are called x and y, respectively:

$$x = (E_{\text{meas}}/E_{\text{fit}})_{\text{data}}, \tag{D.2}$$

$$y = (E_{\text{meas}}/E_{\text{fit}})_{\text{MC}}. \tag{D.3}$$

The variables x and y follow probability density functions $f(x)$ and $g(y)$, respectively.

The disagreement between data and MC is essentially the statement that the distributions $f(x)$ and $g(y)$ have different shapes. The goal of this study is to define a new variable z, with a pdf $s(z)$, such that the sum $x' = y + z$ has the same pdf as that of x. That is, the variable z is used to smear the MC value y such that their sum has the same distribution as that of the data.

The histogram of data values is a set of numbers $\vec{n} = (n_1, \ldots, n_N)$ where n_i is the number of entries in the ith bin. The corresponding histogram for MC is represented by another set of numbers $\vec{\mu} = (\mu_1, \ldots, \mu_N)$. The μ_i are scaled so that the data and MC histograms have the same area. The smeared histogram, i.e., the distribution of $x' = y + z$, is a third set of numbers $\vec{\nu} = (\nu_1, \ldots, \nu_N)$.

Now because x' is defined as the sum $y+z$, its distribution is given by the Fourier convolution,

$$f(x') = \int s(x' - y)\, g(y)\, dy \; . \tag{D.4}$$

In addition we can express $f(x')$ in terms of the conditional probability for x' given y, $s(x'|y)$, as

$$f(x') = \int s(x'|y)\, g(y)\, dy \; . \tag{D.5}$$

Because here x' is the sum $y + z$, one has that the conditional pdf $s(x'|y)$ is equal to the pdf $s(z) = s(x' - y)$.

In order to express these integral equations in terms of the histograms we define the conditional probability to have x in bin i given that y is in bin j,

$$S_{ij} = P(x \text{ in bin } i \,|y \text{ in bin } j) \approx s(x_i|y_j)\Delta x_i \; , \tag{D.6}$$

where x_i and y_j are the centers of the bins and Δx_i is the bin width. We can therefore relate the histograms of x' and y by

$$\nu_i(\vec{\theta}) = \sum_{j=1}^{N} S_{ij}(\vec{\theta})\mu_j \; , \tag{D.7}$$

where $\vec{\theta}$ represents a set of parameters that characterize the pdf $s(z)$. We estimate

the parameters $\vec{\theta}$ by minimizing

$$\chi^2(\vec{\theta}) \equiv -2 \ln \lambda(\vec{\theta}) = 2 \sum_{i=1}^{N} \left(n_i \ln \frac{n_i}{\nu_i(\vec{\theta})} + \nu_i(\vec{\theta}) - n_i \right). \tag{D.8}$$

Now the aim is to discover an $S_{ij}(\vec{\theta})$ that can accomodate the high-side tail and easily be applied as a correction within the *BABAR* framework. Three possible asymmetric functions were found which were thought to be able to perform the smearing accurately. These were the Johnson's function, the Student's t, a and a Left/Right Asymmetric Gaussian. a symmetric Gaussian was used as a cross-check. The asymmetric gaussian and the Student's t provided the most accurate smearing, the functional form of these distributions is shown below:

$$S_{ij}(\vec{\theta}) = \begin{cases} \sqrt{\frac{2}{\pi}} \frac{1}{\sigma_1+\sigma_2} e^{-(i-j-\epsilon)^2/2\sigma_1^2} \\ \sqrt{\frac{2}{\pi}} \frac{1}{\sigma_1+\sigma_2} e^{-(i-j-\epsilon)^2/2\sigma_2^2} \end{cases} \qquad \text{Asymmetric Gaussian.} \tag{D.9}$$

where $\vec{\theta} = (\epsilon, \sigma_1, \sigma_2)$. In the case of the Student's t, ν controls the extent of the tails, as ν goes to infinity the tail approaches a Gaussian form, and if ν is 1 then the tail is that of a Cauchy distribution:

$$S_{ij}(\vec{\theta}) = \frac{1}{\lambda} \frac{\Gamma((\nu+1)/2)}{\sqrt{\nu\pi}\Gamma(\nu/2)} (1 + \frac{t^2}{\nu})^{-(\nu+1)/2} \qquad \text{Student's } t. \tag{D.10}$$

where $t = \frac{i-j-e}{\lambda}$ and, $\vec{\theta} = (\epsilon, \lambda, \nu)$. For the smearing with the Student's t function, the suppression of large smearings to the positive side is softer than for a gaussian. Hence, in order to avoid unphysiacally large smearing for a small number of events, the Student's t function was truncated at a value of $\pm 12\,\%$ smearing. One example for the smearing functions with physical parameters is shown in Figure D.2.

D.4 Results

The Left/Right asymmetric gaussian and the Student's t showed the most accurate results and so further work was then proposed on these two distributions.

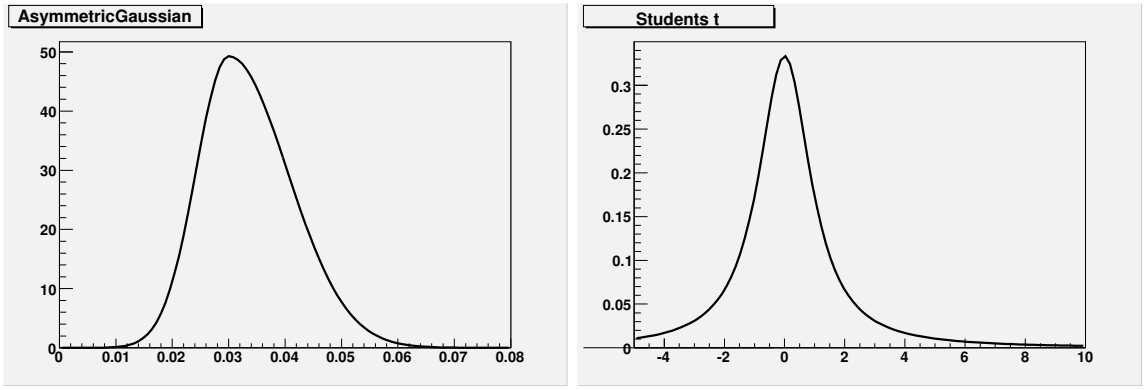

(a) (b)

Figure D.2: Example smearing functions for (a) the left-right asymmetric gaussian and (b) the Student's t function.

The smearing was optimized in bins of run cycle, energy and theta of the photon cluster, to accomodate the effect of different inaccuracies in the detector description across the whole calorimeter. Angular binning was split into three regions, the End Cap, the Forward Barrel, and the Backward Barrel. The energy binning differed in different theta regions so as to get a large enough number of events to fit to.

A detailed comparison in terms of the χ^2 values of the fitted MC of the smearing with the asymmetric gaussian and the Student's t is given in Table D.2. This comparison has been performed with the September 2006 version of the `PhotonClusterCalibrator` calibration. The results show that both distributions reasonably smear the MC to the data, with a certain advantage for the Student's t function especially in the calorimeter endcap and for small or very large photon energies.

Figures D.3 to D.5 show the unsmeared MC, the smeared MC and the data on a logarithmic scale for all binned regions and energies. The final smearing parameters have been developed on analysis release R22.0.0d and R18 data. All smearing is performed after the December 2006 calibration is applied.

The plots shown on the previous pages are all the plots from Run 5 from the angular binned and theta binned smearings that were produced. The Student's t function seems to perform an accurate smearing. The table below shows the goodness-of-fit χ^2

Table D.2: χ^2 values for the fits of the MC to the data in E/E_{fit} for a saymmetric gaussian and a Student's t function. For all fits, the number of d.o.f is 203.

Region (GeV)	Student's t	Asymmetric Gaussian
End Cap, $1 < E < 3$	698	963
End Cap, $3 < E$	304	369
Forward Barrel, $1 < E < 2$	250	201
Forward Barrel, $2 < E < 3$	267	250
Forward Barrel, $3 < E < 4$	255	280
Forward Barrel, $4 < E < 5$	244	206
Forward Barrel, $5 < E$	230	556
Backward Barrel, $1 < E < 2$	223	321
Backward Barrel, $2 < E < 3$	267	265
Backward Barrel, $3 < E < 4$	217	234
Backward Barrel, $4 < E$	94	152

values for each binned smearing function; there are occasions where the asymmetric gaussian does do slightly better but generally the Student's t performs more accurately and some of these are significant improvements over the asymmetric gaussian. After consultation with EMC and Neutrals Group it was therefore decided to implement the Student's t smearing into the next simulation production as a Neutrals correction.

D.5 Validation of the Smearing using $B^0 \to K^{*0}\gamma \to K^+\pi^-\gamma$

The smearing derived in the previous paragraphs has ben validated on the $B \to K^*\gamma$ sample using the decay $B^0 \to K^{*0}\gamma \to K^\pm\pi^\mp\gamma$ described in Section D.1. Figure D.6 shows the ΔE distributions for the MC and the data without neutrals corrections. Edge corrections are applied. The December 2006 version of `PhotonClusterCalibrator` has been used. This version of the calibration for the first time avoids the -5 MeV shift of the MC with respect to the data, which was

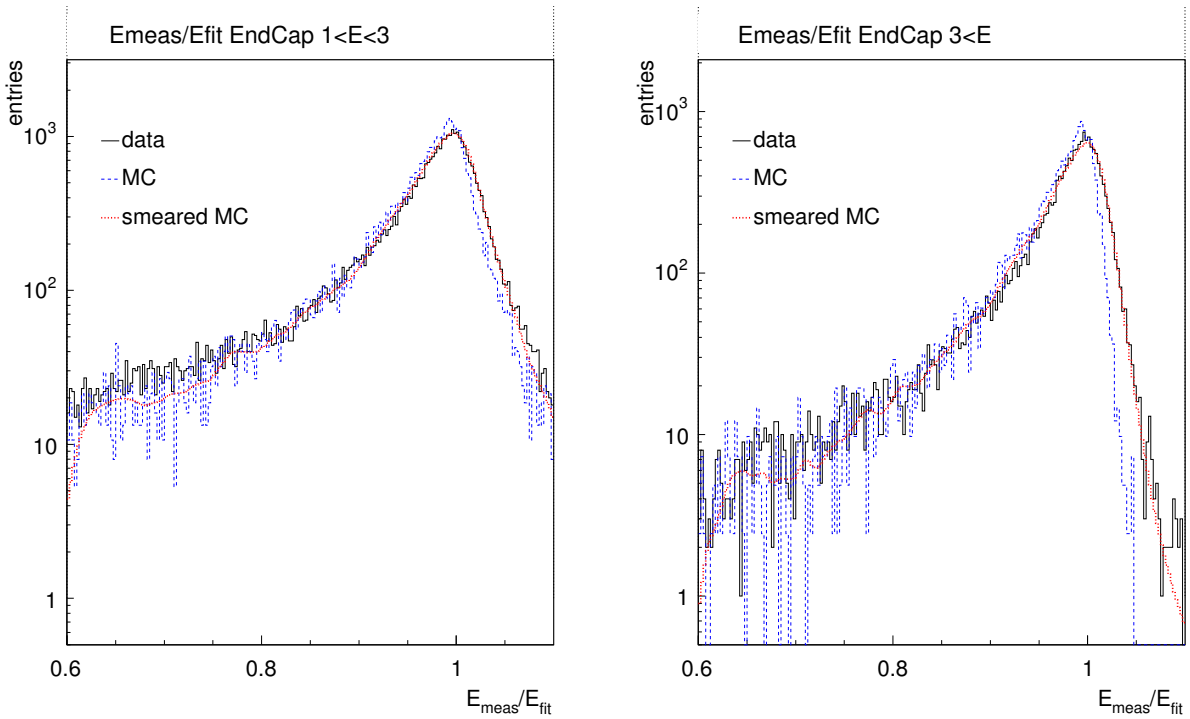

Figure D.3: E/E_{fit} resolution plots of unsmeared MC, smeared MC and data for Run 5 for the two energy bins of the calorimeter endcap.

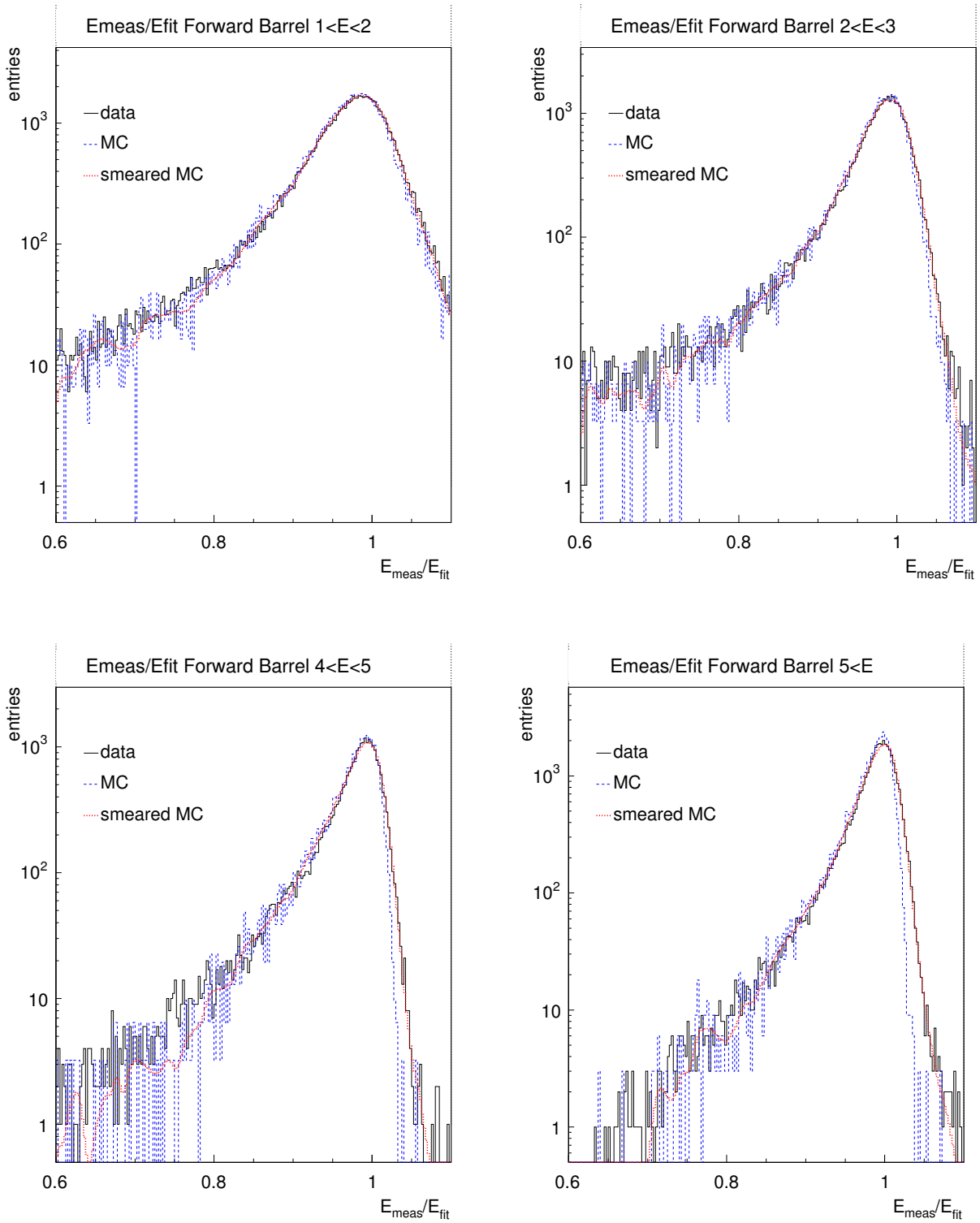

Figure D.4: E/E_{fit} resolution plots of unsmeared MC, smeared MC and data for Run 5 for different energy bins of the forward barrel.

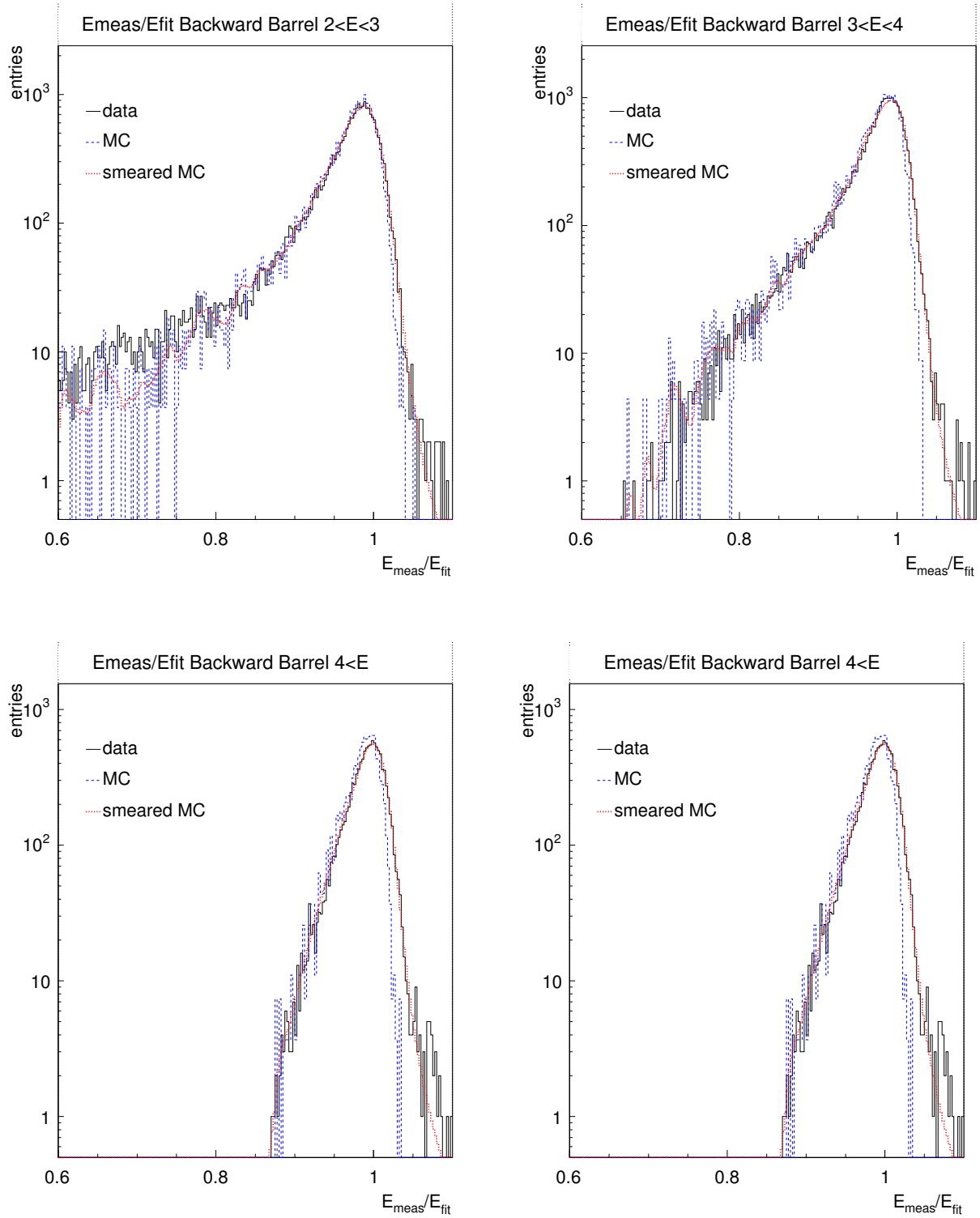

Figure D.5: E/E_{fit} resolution plots of unsmeared MC, smeared MC and data for Run 5 for different energy bins of the backward barrel.

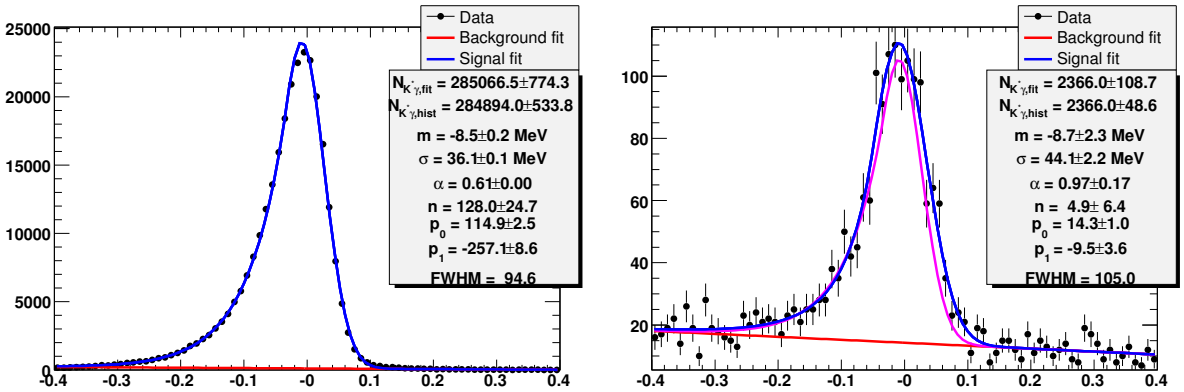

(a) (b)

Figure D.6: Distributions of ΔE for the process $B^0 \to K^{*0}\gamma \to K^+\pi^-\gamma$ in (a) MC and (b) Run1 to Run5 data. The December 2006 `PhotonClusterCalibrator` calibration and the edge corrections are applied. No neutrals corrections are used on the MC.

described in Section D.1. Figure D.6 (a) shows the MC distribution with a linear function for the background and a Crystall Ball (CB) function for the signal fitted in a binned ML fit. The most important fit parameters derived from that fit are the mean of the gaussian part of the CB function of $\mu_{MC} = -8.5 \pm 0.2$ MeV and the width of the gaussian part of $\sigma_{MC} = 36.1 \pm 0.1$ MeV. This can be compared with the parameters for the fit to Run 1 to Run 5 data in Figure D.6 (b), with a good agreement in the mean of $\mu_{DATA} = -8.7 \pm 2.3$ MeV and a very suboptimal agreement in the width of $\sigma_{DATA} = 44.1 \pm 2.2$ MeV. The MC signal shape (magenta) is overlayed to the fitted data line (blue), also showing the poor agreement.

The effect of the smearing is obvious from the comparison of the smeared MC distribution with the data in Figure D.7. The same MC and data samples, calibration and edge correction as in the unsmeared example above have been used. The MC has a mean of $\mu^s_{MC} = -6.7 \pm 0.2$ MeV and a width of $\sigma^s_{MC} = 46.0 \pm 0.1$ MeV. This is both within 1 σ od the data values quoted above. Figure D.7 (b) shows the very good agreement of the data distribution (fitted in blue) with the overlayed MC distribution (magenta).

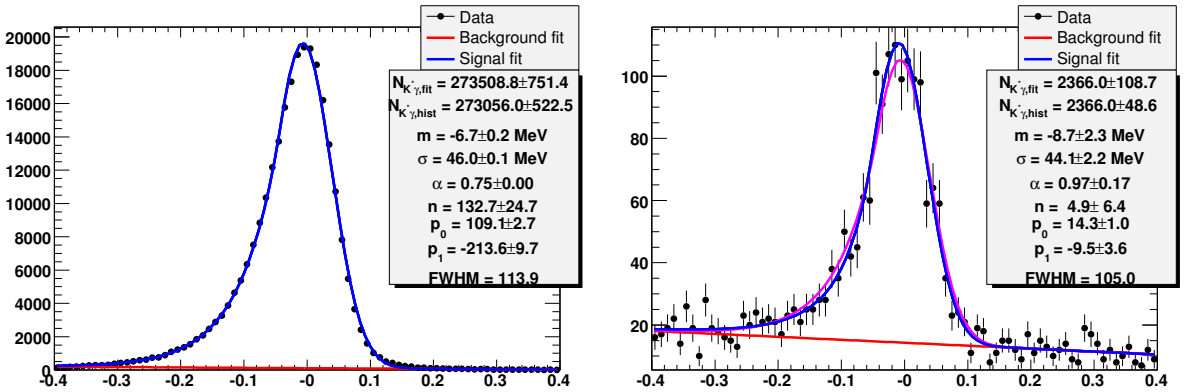

(a) (b)

Figure D.7: Distributions of ΔE for the process $B^0 \to K^{*0}\gamma \to K^+\pi^-\gamma$ in (a) MC and (b) Run1 to Run5 data. The December 2006 `PhotonClusterCalibrator` calibration and the edge corrections are applied. The neutrals corrections including the smearing algorithm are used on the MC.

D.6 Conclusions

The asymmetric energy smearing of neutral clusters in the EMC cruciually improves the MC simulation in the cluster energy range above 1 GeV. It has been motivated by $B \to K^*\gamma$ decays and developed on a $\mu\mu\gamma$ control sample. Different asymmetric smearing functions have been tested. The best results have been achieved for a Student's t distribution with truncated tails, with parameters fitted independently for different runs, energy ranges and polar angle. It has been shown that the smeared distributions achieve a strong improvement in the MC simulation both for $\mu\mu\gamma$ and $B \to K^*\gamma$. With this improvement, systematic studies of the uncertainties on selection efficiencies between data and MC and the evaluation of fits to variables like ΔE are going to be strongly improved and simplified in the future.

Bibliography

[1] M. Kobayashi and T. Maskawa, Prog. Theor. Phys. **49**, 652 (1973).

[2] *BABAR* Collaboration, *The BABAR Physics Book* (P. Harrison and H. Quinn eds. (SLAC-R-0504), 1999).

[3] M. Gronau and D. Wyler, Phys. Lett. B **265**, 172 (1991).

[4] M. Gronau and D. London, Phys. Lett. B **253**, 483 (1991).

[5] D. Atwood, I. Dunietz, and A. Soni, Phys. Rev. Lett. **78**, 3257 (1997).

[6] A. Giri, Y. Grossman, A. Soni, and J. Zupan, Phys. Rev. D **68**, 054018 (2003).

[7] J. Charles *et al.*, Eur. Phys. Jour. C **41**, 1 (2005). Updates available at **http://ckmfitter.in2p3.fr**.

[8] A. D. Sakharhov, Pisma Zh. Eksp. Teor. Fiz. **5**, 32 (1967).

[9] T. D. Lee and Y. C. N., Prog. Theor. Phys. **104**, 254 (1956).

[10] C. S. Wu, E. Ambler, R. W. Hayward, D. D. Hoppes, and R. P. Hudson, Phys. Rev. **105**, 1413 (1957).

[11] N. Cabibbo, Phys. Rev. Lett. **10**, 531 (1963).

[12] L. Wolfenstein, Phys. Rev. Lett. **51**, 1945 (1983).

[13] W. M. Yao *et al.*, Journal of Physics G **33**, 1 (2006).

[14] J. Thompson, P.h. D. Dissertation, Stanford University (2008).

[15] M. Ciuchini, M. Pierini, and L. Silvestrini, Phys. Rev. D **74**, 051301(R) (2006).

[16] M. Gronau, D. Pirjol, A. Soni, and J. Zupan, Phys. Rev. D **75**, 014002 (2007).

[17] G. Buchalla, A. Buras, and M. Lautenbacher, Rev. Mod. Phys. **68**, 1125 (1996).

[18] G. Paz, SU(3)-Flavor Symmetry in $B \to VP$ Decays, **arXiv:hep-ph/0206312** (2002).

[19] *BABAR* Collaboration, B. Aubert *et al.*, Phys. Rev. D **72**, 072003 (2005). Erratum. Phys. Rev. D **74**, 099903(E) (2006); *BABAR* Collaboration, B. Aubert *et al.*, Phys. Rev. D **78**, 012004 (2008).

[20] J. Blatt and V. E. Weisskopf, *Theoretical Nuclear Physics* (J. Wiley (NewYork), 1952).

[21] C. Zemach, Phys. Rev. **133**, B1201 (1964).

[22] D. Asner, Charm Dalitz Analysis Formalism, **arXiv:hep-ex/0410014** (2003).

[23] G. J. Gounaris and J. J. Sakurai, Phys. Rev. Lett. **21**, 244 (1968).

[24] CDM2 Collaboration, R. R. Akhmetshin *et al.*, Phys. Lett. B **257**, 161 (2002).

[25] DM2 Collaboration, D. Bisello *et al.*, Phys. Lett. B **220**, 321 (1989).

[26] P. Estabrooks, Phys. Rev. D **19**, 2678 (1979).

[27] LASS Collaboration, D. Aston *et al.*, Nucl. Phys. B **296**, 493 (1988).

[28] *BABAR* Collaboration, B. Aubert *et al.*, Nucl. Instrum. Meth. A **479**, 1 (2002).

[29] S. Agostinelli *et al.*, Nucl. Instrum. Meth. A **506**, 250 (2003).

[30] *BABAR* Collaboration, B. Aubert *et al.*, Phys. Rev. D **78**, 052005 (2008).

[31] *BABAR* Collaboration, B. Aubert *et al.*, Phys. Rev. D **80**, 112001 (2009).

[32] W. Hulsbergen, A Kalman Filter for *BABAR* Decay Chain Fitting, **http://www.slac.stanford.edu/BFROOT/www/Physics/Tools/Vertex/treefitter/kalman.ps** (2004).

[33] P. Gay, B. Michel, J. Proriol, and O. Deschamps, New computing techniques in physics research, Pisa 725 (1995).

[34] Heavy Flavor Averaging Group (HFAG), E. Barberio *et al.*, **arXiv:hep-ex/0704.3575**.

[35] K. S. Cranmer, Comput. Phys. Commun. **136**, 198 (2001).

[36] Argus Collaboration, H. Albrecht *et al.*, Z Phys. C **48**, 543 (1990).

[37] *BABAR* Collaboration, B. Aubert *et al.*, Phys. Rev. D **76**, 071103 (2007).

[38] *BABAR* Collaboration, B. Aubert *et al.*, Phys. Rev. D **79**, 051101 (2009).

[39] *BABAR* Collaboration, B. Aubert *et al.*, Phys. Rev. D **76**, 012004 (2007).